State-selective transport of single neutral atoms

Dissertation

zur
Erlangung des Doktorgrades (Dr. rer. nat.)
der
Mathematisch-Naturwissenschaftlichen Fakultät
der
Rheinischen Friedrich-Wilhelms-Universität Bonn

vorgelegt von
Michał Karski
aus
Białystok (Polen)

Bonn 2010

Angefertigt mit Genehmigung
der Mathematisch-Naturwissenschaftlichen Fakultät
der Rheinischen Friedrich-Wilhelms-Universität Bonn

1. Gutachter: Prof. Dr. Dieter Meschede
2. Gutachter: Prof. Dr. Reinhard F. Werner

Tag der Promotion: 20.10.2010

Erscheinungsjahr: 2010

Diese Dissertation ist auf dem Hochschulschriftenserver der ULB Bonn
`http://hss.ulb.uni-bonn.de/diss_online` elektronisch publiziert

Summary

The present work investigates the state-selective transport of single neutral cesium atoms in a one-dimensional optical lattice. It demonstrates experimental applications of this transport, including a single atom interferometer, a quantum walk and controlled two-atom collisions. The atoms are stored one by one in an optical lattice formed by a standing wave dipole trap. Their positions are determined with sub-micrometer precision, while atom pair separations are reliably inferred down to neighboring lattice sites using real-time numerical processing. Using microwave pulses in the presence of a magnetic field gradient, the internal qubit states, encoded in the hyperfine levels of the atoms, can be separately initialized and manipulated. This allows us to perform arbitrary single-qubit operations and prepare arbitrary patterns of atoms in the lattice with single-site precision.

Chapter 1 presents the experimental setup for trapping a small number of cesium atoms in a one-dimensional optical lattice. Chapter 2 is devoted to fluorescence imaging of atoms, discussing the imaging setup, numeric methods and their performance in detail. Chapter 3 focuses on engineering of internal states of trapped atoms in the lattice using optical methods and microwave radiation. It provides a detailed investigation of coherence properties of our experimental system. Finally manipulation of individual atoms with almost single-site resolution and preparation of regular strings of atoms with predefined distances are presented.

In Chapter 4, basic concepts, the experimental realization and the performance of the state-selective transport of neutral atoms over several lattice sites are presented and discussed in detail. Coherence properties of this transport are investigated in Chapter 5, using various two-arms single atom interferometer sequences in which atomic matter waves are split, delocalized, merged and recombined on the initial lattice site, while the interference contrast and the accumulated phase difference are measured. By delocalizing a single atom over several lattice sites, possible spatial inhomogeneities of fields along the lattice axis in the trapping region are probed.

In Chapter 6, experimental realization of a discrete time quantum walk on a line with single optically trapped atoms is presented as an advanced application of multiple path quantum interference in the context of quantum information processing. Using this simple example of a quantum walk, fundamental properties of and differences between the quantum and classical regimes are investigated and discussed in detail. Finally, by combining preparation of atom strings, position-dependent manipulation of qubit states and state-selective transport, in Chapter 7, two atoms are deterministically brought together into contact, forming a starting point for investigating two-atom interactions on the most fundamental level. Future prospects and suggestions are finally presented in Chapter 8.

Parts of this thesis have been published in the following journal articles:

1. M. Karski, L. Förster, J.-M. Choi, W. Alt, A. Widera and D. Meschede, *Nearest-Neighbor Detection of Atoms in a 1D Optical Lattice by Fluorescence Imaging*, Phys. Rev. Lett. **102**, 053001 (2009)

2. M. Karski, L. Förster, J.-M. Choi, A. Steffen, W. Alt, D. Meschede and A. Widera, *Quantum Walk in Position Space with Single Optically Trapped Atoms*, Science **325**, 174 (2009)

3. M. Karski, L. Förster, J.-M. Choi, A. Steffen, N. Belmechri, W. Alt, D. Meschede and A. Widera, *Imprinting patterns of neutral atoms in an optical lattice using magnetic resonance techniques*, to appear in New. J. Phys. (2010)

Contents

Introduction

In the course of the 20th century, scientific understanding of phenomena in the microscopic world has revolutionarily changed by the developments in quantum theory. While in the second half of the century the experimental effort has been primarily focused on the demonstration and systematic investigation of such phenomena, on the dawn of the new millennium a paradigm change has taken place. Leaving the role of the passive observer a new direction has been pursued, focusing on controlled isolation and manipulation of elementary quantum mechanical processes. Stimulated by the technological progress, control over isolated quantum systems has been increasingly gained, initiating investigations of their possible use in practical applications. In this context, a new interdisciplinary research field — quantum information theory — has evolved, picking up and combining concepts of classical information theory, mathematics, communication science and physics. The most prominent goal of this field is the realization of a universal quantum computer [1], from which efficient solution of complex problems and a wide range of possible applications is expected in the future. The interest on a quantum computer is encouraged by the trend towards miniaturization in the semiconductor technology, which sooner or later approach a fundamental limit of atomic dimensions. By then at the latest, engineering and control of quantum mechanical processes will be unavoidable.

The basic unit of quantum information is the quantum bit, or in short qubit, encoded in a quantum two-level system. In contrast to its classical counter part, which can take just one of two distinct basis states $|0\rangle$ or $|1\rangle$, a qubit can be prepared in a superposition of these states. Tensor products of qubits are called quantum registers, in analogy to the classical processor registers. Superpositions of quantum register states are commonly referred to as entangled states having no classical equivalent. Analogous to the classical case, in which information is typically processed using logical gates, quantum information can be processed by so-called quantum gates — coherent unitary transformations typically operating on a single qubit (single-qubit gates) or a pair of qubits (two-qubit gates).

Alternatively to the traditional gate-based quantum computing [2], quantum walks have been recently proposed [3–6]. The quantum walk is a quantum mechanical analogue of the classical random walk with remarkably different properties, which arise from its particular ability of quantum interference. This characteristic ability is primarily used to design quantum algorithms, which mostly outperform their classical counterparts for the same problem [7]. Random walks have already proven useful in different fields, including computer science [8], physics, chemistry [9], biology [10], economics [11], and other fields relying on random pro-

cesses in time [12]. By translating random walks to their quantum mechanical counterparts, new efficient quantum algorithms are hoped to be found in the future.

In recent years, tremendous progress has been made in developing and experimentally realizing concepts of quantum information theory. From the theoretical side, for instance, an increased efficiency in solving of particular problems has been reported [13–15] while various approaches for universal quantum computing have been proposed [16–18]. The experimental realization, however, turns out to be by far more difficult, due to high requirements on the possible two-level quantum system regarding the scalability, manipulation and isolation from its environment [19]. There are currently only few systems, which partially meet these requirements, including ions in Paul traps [20], nuclei in molecules [21], and cooper-pairs in Josephson junctions [22]. In some of them notable progress have been achieved. By coupling ions through their collective motional degrees of freedom, entangled states have been deterministically generated [23, 24] and employed for implementation of quantum gates and the Deutsch-Jozsa algorithm [25]. Using nuclei in molecules a simple Grover's search [13] for a system with four states [26] and Shor's algorithm [14, 15] on the number 15 has been experimentally demonstrated [27].

Neutral atoms in optical lattices provide a further promising two-level quantum system [28–30]. Their isolation from the environment and easily accessible long-living internal states make them ideally suited for use in quantum information processing. Two-qubit gates can be realized either through exchange of photons in high-finesse cavities [31–33], Rydberg blockade interactions [34–36] or coherent cold collisions in state-selective optical lattices [37]. So far, state-selective optical lattices have been realized for large ensembles of Rubidium atoms in a Mott insulating state [38, 39], impressively demonstrating controlled and coherent delocalizing of an atomic wave function over a defined number of lattice sites [40] and generating large-scale entanglement [41]. However, controlling each individual atom of such ensemble and a quantitative measurement for the size of the entangled many-body state has been not feasible so far.

For this reason, another approach has been followed in our research group over the years. Instead of starting from a large ensemble and working towards full control of its individual parts ("top-down" approach), following Ref. [42] we rather prefer to investigate small well-controllable systems of few atoms and extending them atom-by-atom to larger system ("bottom-up" approach).

This thesis continues the tradition of the bottom-up approach, focusing on quantum state engineering with unprecedented resolution and precision and the experimental realization of a state-selective transport of single neutral atoms and its applications in a one-dimensional optical lattice. For this purpose, an experimental setup has been designed and constructed from scratch which allows to trap a small number of cesium atoms in the lattice, determine their position with sub-micrometer precision and reliably infer atom pair separations down to neighboring lattice sites using real-time numerical processing of fluorescence images with a markedly improved quality and reduced noise. Previous restrictions imposed by the diffraction

limit [43] are overcome by a precise knowledge of the transfer function of the optical system. The increased reliability is achieved by taking the signal-noise relation in the numerical method into account. Both, the transfer function and signal-noise relation can by directly and precisely deduced from fluorescence images of atoms alone. Recently, single-site detection and addressability using focused electron beams from an ultra-high vacuum compatible electron gun [44, 45] has been reported. However, this technique is not easily integrated in many neutral atoms experiments, in which, in contrast, optical imaging by fluorescence light is widely established.

The internal states of individual atoms in the optical lattice are manipulated using microwave radiation [46–48] and detected by projection measurements [49]. Most of these methods originate from nuclear magnetic resonance originally developed for solid-state systems and recently found their way into quantum optics experiments using cooled trapped atoms [21]. I present the technical implementation of these methods, analyze their performance and investigate the coherence properties of our system. Using a magnetic field gradient along the lattice axis, individual atoms are coherently manipulated with almost single-site resolution. This ability is used to prepare regular strings of atoms with predefined distances, which form the starting point for experiment relying on controlled two-atom collisions.

The central topic of this thesis is the state-selective transport of single thermal atoms in a one-dimensional optical lattice. I present its basic concepts, our experimental realization and technical limitations, and finally, experimental results, from which the transport efficiency is inferred. So far, the question whether coherent transport can be adapted to a thermal ensemble of atoms and to which extent coherence properties are then maintained, remained unanswered. We aim to close this gap, investigating coherence properties of the transport using a two-arm single atom interferometer in which atomic matter waves are split, delocalized, merged and recombined on the initial lattice site, while the interference contrast and the accumulated phase difference is measured. Delocalizing a single atom over several lattice sites allows us in principle to probe spatial inhomogeneities of fields along the lattice axis in the trapping region.

As an advanced application of multiple path quantum interference in the context of quantum information processing, following the proposal of Ref. [50], the experimental realization of discrete time quantum walk in position space with single optically trapped atoms is presented. This basic example of a walk provides all of the relevant features necessary to understand the fundamental properties of and differences between the quantum and classical regimes. Simultaneous detection of internal state and the atomic position in the lattice by our imaging techniques allows for local quantum state tomography of the wave function. In contrast to other recent implementations of quantum walks [51, 52], it theoretically augurs implementations with up to several hundred steps [50].

Finally, by combining preparation of atom strings, position-dependent manipulation of qubit states and state-selective transport, two atoms are brought together into contact, forming a starting point for investigating two-atom interactions on

the most fundamental level. By this, unbiased insights into details of two-atom interactions are anticipated, which can be used for implementing two-qubit gates in the future [37, 41, 53–55].

1. Trapping of single atoms

Quantum engineering on single atom scale requires a fully controllable system of individual atoms, which are well isolated from their environment. Since the invention of laser cooling in 1975 [56, 57] and magneto-optical trap in 1987 [58], such systems are commonly realized by capturing neutral atoms from a dilute gas at room temperature, cooling them down to sub-millikelvin temperatures and transferring them into a periodic array of conservative trapping potentials of a so-called optical lattice. The latter rely on an off-resonant interaction of polarizable particles with the light field [59–61] formed by interference patterns of laser light.

Neutral atoms in optical lattices have been extensively studied over the past decades, impressively demonstrating a variety of new experimental possibilities in quantum optics, quantum information processing, and even in condensed matter physics. For a general review, see Refs. [28–30] and references therein. Extensive studies performed in our research group, which are closely related to this thesis, can be found in Refs. [47, 62–67].

In this chapter, the basic concepts of the magneto-optical trap and the standing wave dipole trap are shortly summarized, introducing the terminology and defining relevant parameters, which will be frequently used throughout this thesis. Both traps are routinely employed to prepare initial configurations of well-localized individual atoms, which form the starting point of each experiment presented. The main purpose of this chapter is rather to give a brief overview over the experimental setup, which has been designed and constructed from scratch during this thesis. Parts of this setup are discussed in detail in subsequent chapters or a parallel thesis [68].

1.1. A magneto-optical trap

A magneto-optical trap (MOT) is a widely used tool to capture neutral atoms from a dilute gas at room temperature, cool these atoms to sub-millikelvin temperatures while keeping them confined for long times. It relies on the three-dimensional Doppler cooling [56,57], extending this concept by an inhomogeneous magnetic field, or more precisely a magnetic field gradient which provides a position-dependent radiation pressure [58]. In our experiment, we use the MOT as a source of precooled cesium atoms, the average number of which can be adjusted by the strength of the field gradient.

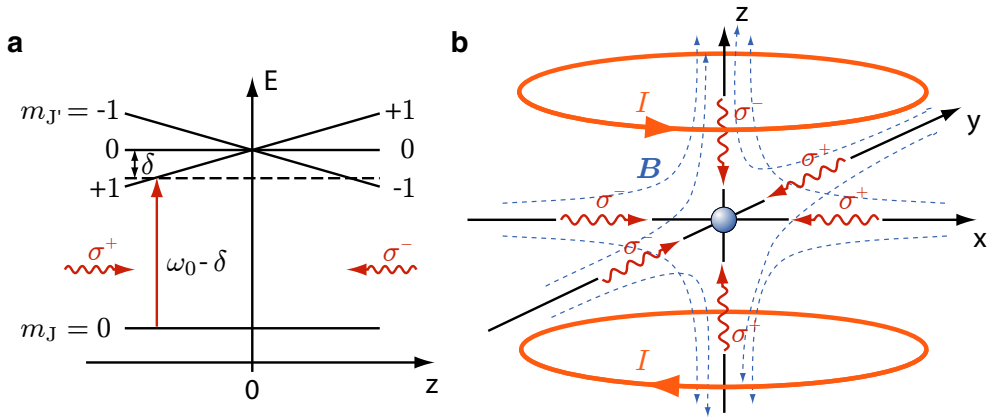

Figure 1.1.: Principle of operation of a magneto-optical trap (MOT). (**a**) Simplified one-dimensional model to illustrate the origin of the position-dependent restoring force. A linear magnetic field gradient lifts the degeneracy of the sublevels of the excited state $J' = 1$. For an atom displaced to the left from the trap center, the $m_J = 0 \rightarrow m_{J'} = 1$ transition is shifted into resonance. Being only excited by the σ^+-polarized light field from the left, the atom is pushed back to the center. (**b**) Schematics of a three-dimensional MOT. Three mutually orthogonal pairs of counterpropagating circularly polarized laser beams form the optical molasses. In presence of a quadrupole magnetic field $\boldsymbol{B}$ generated by a pair of anti-Helmholtz coils, these beams exert cooling and position-dependent restoring forces which confine the atoms in the center of the trap.

1.1.1. Principle of operation

The operation of a MOT relies on a velocity-dependent cooling force and a position-dependent restoring force to provide spatial confinement of the atoms. The former is realized by three mutually orthogonal pairs of counterpropagating laser beams which are slightly red-detuned with respect to the atomic resonance. An atom moving within the intersection region of the laser beams preferentially absorbs photons coming from the opposite direction of its motion, because their frequency is Doppler-shifted closer to the atomic resonance. Since the subsequent spontaneous reemission of photons is anisotropic, the net force resulting from the momentum transfer slows the atom down, cooling it to a finite equilibrium temperature, the so-called *Doppler limit* or *Doppler temperature* [69, 70] given by

$$T_\mathrm{D} = \frac{\hbar\Gamma}{2k_\mathrm{B}}\,. \tag{1.1}$$

Here Γ denotes the natural line width of the atom and k_B the Boltzmann constant. The Doppler limit is imposed by the momentum kicks of absorbed and spontaneously reemitted photons which result in heating of the atom. For the commonly employed D_2 transition of a cesium atom at $\lambda = 852.3\,\mathrm{nm}$, it is $\Gamma = 2\pi \times 5.2\,\mathrm{MHz}$ and thus $T_\mathrm{D} = 125\,\mu\mathrm{K}$. Note that the multi-level structure of the atom and properly set polarization of the light fields can permit sub-Doppler cooling mechanisms

which may lead to temperatures below the Doppler limit [71]. Because of the analogy to a viscous friction force for atoms moving in arbitrary directions, the three-dimensional Doppler cooling is also referred to as *optical molasses*.

A position-dependent restoring force for spatial confinement of atoms is obtained by circularly polarizing the light of the optical molasses and adding a quadrupole magnetic field which is usually generated by a pair of anti-Helmholtz coils centered with the intersecting cooling beams, see Fig. 1.1(b). The quadrupole field vanishes at the center of the optical molasses and increases linearly in all directions, lifting the degeneracy of the excited states due to the Zeeman effect and providing a level splitting proportional to the distance from the center. This principle is illustrated in Fig. 1.1(a) for a simplified one-dimensional model in which the relevant atomic states are characterized by the angular momentum quantum numbers J and m_J: For red-detuned, orthogonally circularly polarized counterpropagating laser beams, an atom displaced from the center of the quadrupole field is shifted closer into resonance with that laser beam which pushes it back to the center. This principle is easily extendible to three-dimensions, see Fig. 1.1(b).

Standard MOTs usually trap $10^3 - 10^{11}$ atoms. Smaller numbers down to a single atom can be captured using high magnetic field gradients which reduce the trap radius and the capturing rate of atoms from a thermal background gas [62, 72].

1.1.2. Vacuum system

Experiments with optically trapped atoms have to be performed under ultra-high vacuum (UHV) conditions to minimize the probability of collisions between these atoms and particles from the thermal background gas. Such collisions limit the lifetime of atoms in the trap, which in principle is the longer, the lower the residual gas pressure. The primary goal in designing the UHV system is therefore to provide the lowest possible pressure. Additionally, a variety of considerations have to be taken into account, to which I will shortly refer in the following.

Glass cell

Not long ago, experiments with neutral atoms have been usually performed in stainless steel vacuum chambers with many windows for optical access. This concept, however, has some major practical and economical disadvantages: Since imaging optics with high numerical apertures require to be positioned close to the trapping region of the atoms, the respective elements need to be placed inside the chamber, which make them difficult to align from the outside. The same applies for magnetic coils which have to be preferably mounted close to the atoms to minimize the dissipated power and the currents required for operation. Apart from the fact that coated vacuum windows with a flatness of less than $\lambda/4$ per inch are comparatively expensive, using many windows increase not only the complexity of the vacuum setup, but also the risk of vacuum leakage which increases with the number of flanges required to mount them.

Instead, we use a cuboid glass cell which permits a compact design and free optical access almost over its entire extent. The glass cell is made from Vycor glass (Corning, VYCOR 7913) — a 96% silica glass which is typically used for high temperature applications. Its outer dimensions are 30 mm × 30 mm × 125 mm with a wall thickness of 5 mm providing low diffusion leak rates. The surfaces of the glass cell are optically polished to a flatness of $\lambda/4$ per inch and broadband antireflection coated at the outside ($770 - 870$ nm, 22.5°, $R < 0.3\%$).[1] Due to the compact design, coating at the inside of the glass cell was technically not possible. The inner surfaces thus only provide a reflectivity of $R \approx 4\%$ in the relevant wavelength range. Despite of this disadvantage, the compact design allows to place all imaging optics and magnetic coils outside the vacuum, see Sec. 2.2.1 and Sec. 1.1.4, respectively.

The glass cell is fused to a tubular graded seal quartz-to-metal adaptor (Larson Electronic Glass Inc., SQ-100-F2) with an inner diameter of 19 mm. The latter is flanged to the vacuum chamber by a CF40 flange, see Fig. 1.2. In contrast to conventional quartz-to-metal seals, which rather use Kovar to match the coefficients of expansion, the adaptor is entirely made from nonmagnetic materials, the magnetic permeability of which is less than 1.005. By this, magnetization of the adaptor is effectively suppressed, allowing a high long-term stability of magnetic fields in the trapping region of the atoms located in the center of the glass cell. This stability is absolutely essential for working with magnetically sensitive internal states of the atoms, see Chap. 3.

Vacuum apparatus

The vacuum apparatus comprises a custom-made vacuum chamber which has been adapted exactly to the experimental requirements and manufactured in the institute's own workshops. It is designed to maintain an ultra-high vacuum in the attached glass cell, reduce the effect of magnetic distortions in the trapping region by employing nonmagnetic materials and placing magnetic sources in larger distances from the trap center while keeping the design compact. The vacuum chamber is made from nonmagnetic, forged stainless steel of grades ANSI 316LN ESR (all CF flanges) and ANSI 316L (main pipe and pipe sockets), both providing a magnetic permeability of less than 1.005. Apart from this property, these steel grades are characterized by highest purity, homogenous structure and low outgassing rates. After the welding and manufacturing process, the vacuum chamber has been vacuum-annealed at 1050 C for one hour. This established heat treatment procedure not only removes residual impurities from the manufacturing process, but also reduces the hydrogen amount in the steel and thus further decreases its outgassing rates.

[1] Note that the vacuum setup has been designed for optically cooling and trapping of both rubidium and cesium atoms. The chosen wavelength range of the antireflection coating thus comprises all required wavelengths for this purpose. The coating angle of incidence of 22.5° sufficiently suppress reflections of commonly used beams, the incident angles of which range from 0° to 45°.

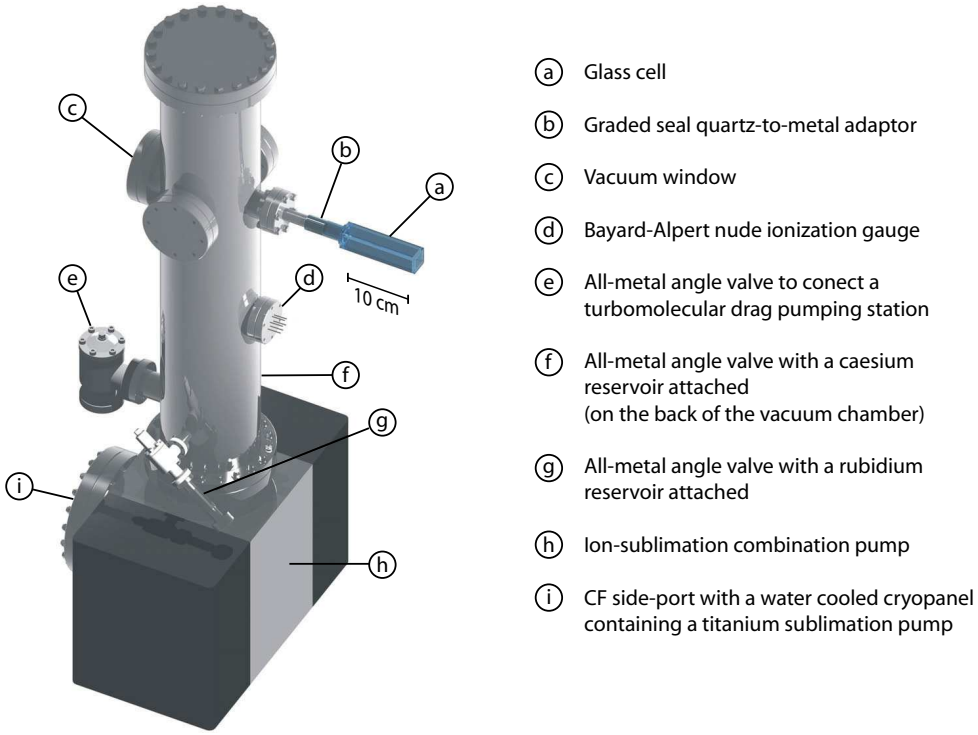

Figure 1.2.: Three-dimensional model of the vacuum apparatus.

In Figure 1.2, a three-dimensional model of the vacuum apparatus is shown. The main pipe connects the glass cell to an ion-sublimation combination pump (Varian, VacIon Plus 300 combination pump with StarCell elements). The latter provides a side-mounted CF port to which a water-cooled cryopanel (Varian, model 919-0180) containing a titanium sublimation pump (Varian, model 916-0050) is flanged. The length of the main pipe ensures a sufficiently large distance between the glass cell and the permanent magnets of the ion pump, so that their stray magnetic field can be easily compensated in the trapping region ($|\boldsymbol{B}_\mathrm{S}| < 0.5\,\mathrm{G}$). The cross section of the pipe is adapted to that of the ion pump, ensuring an optimum pump performance. Both, the cesium and rubidium reservoirs are attached through all-metal angle valves (VAT, "Easy-close" series 540) to the side-mounted CF16 ports which are located close to the ion pump. A further CF40 port with an all-metal angle valve seals the vacuum chamber against the atmosphere. To this valve, a turbomolecular drag pumping station (Pfeiffer, TSU 071 E) has been temporarily flanged to bring the pressure down to the operation region of the ion pump.

To unbiasedly measure the pressure, a Bayard-Alpert nude ionization gauge (Varian, UHV-24p) is flanged deep into the vacuum chamber. By this, heating of its inner walls during measurement is avoided, which otherwise would increase the out-

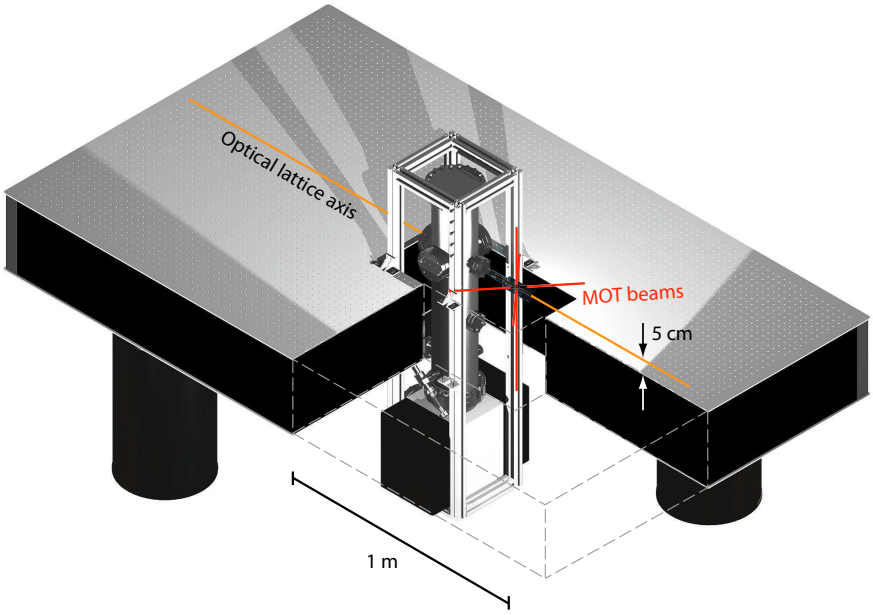

Figure 1.3.: Three-dimensional model showing the mounting of the vacuum apparatus into a rectangular opening of a custom-made optical table. For a better overview, a part of the table and supporting elements attached to the upper CF port of the vacuum chamber have been hidden in the model.

gassing rate. The ionization gauge has been frequently used in the early stage of the experiment, i.e. until the desired pressure has been reached. Afterwards, we estimate the pressure from the lifetime of the atoms in the dipole trap.

A CF63 port opposite to the glass cell holds a diffusion bounded quartz vacuum window (Spectrosil 2000) which provides a flatness of $\lambda/4$ per inch and is antireflection coated on both sides ($770 - 870\,\mathrm{nm}$, $0°$, $R < 0.3\%$). Two additional CF63 ports on both sides at the same height leave room for possible extensions.

The entire vacuum apparatus is rigidly mounted in an aluminum cage and placed into a rectangular opening ($60\,\mathrm{cm} \times 30\,\mathrm{cm}$) of a custom-made optical table (Thorlabs) in such a way, that the vertical position of the glass cell is situated 5 cm above the surface of the table, see Fig. 1.3. This table is made from nonmagnetic stainless steel (ANSI 316L). It is seismically mounted on active, self-leveling vibration isolation supports, which prevent the coupling of ambient background vibration in the building (typically in the $4 - 100\,\mathrm{Hz}$ range). By placing the bulky vacuum components below the table, we not only save space on its surface, but also improve the stability of the entire experimental setup by lowering the center of gravity of the vacuum system. Otherwise, systems with a high center of gravity experience stability problems, if they are supported on active self-leveling pneumatic isolators.

The vacuum apparatus has been baked at $200\,°\mathrm{C}$ for one week. At full pump

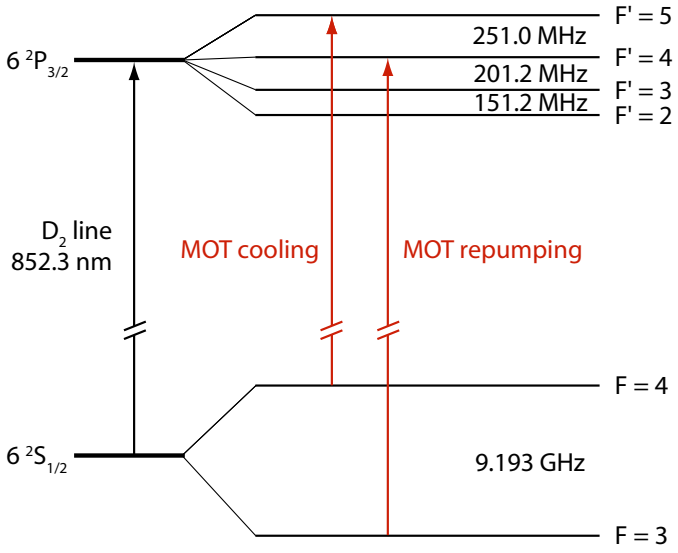

Figure 1.4.: Hyperfine level scheme of the D_2 line of cesium. Red arrows indicate the cooling and repumping transitions.

power, i.e. operating the ion pump and the titanium sublimation pump simultaneously, final pressures of less than 5×10^{-12} mbar have been achieved. Since then, only the ion pump and the cryopanel are permanently operated. Including the residual cesium gas, we typically achieve a pressure of 3×10^{-11} mbar.

1.1.3. Laser system

Laser cooling and trapping of atoms in a MOT usually requires a closed cycling transition. We therefore operate the cooling laser on the $F = 4 \rightarrow F' = 5$ transition of the D_2 line (852.3 nm), see Fig. 1.4, where throughout the thesis primed (non-primed) quantum numbers refer to the $6^2P_{3/2}$ ($6^2S_{1/2}$) electronic state of cesium. However, because of a small probability of off-resonantly exciting an atom to the $F' = 4$ level, from where it can spontaneously decay to the $F = 3$ ground state, an additional repumping laser operated on the $F = 3 \rightarrow F' = 4$ transition is required to pump the atom back into the cooling cycle. Both, the cooling and repumping laser are external cavity diode lasers in Littrow configuration [73] (partially self-development,[2] operated with a Toptica DC110 controller unit). They are actively stabilized to atomic transitions using Doppler-free polarization spectroscopy [75,76], resulting in line widths of approximately 1 MHz. Details on experimental setup and performance, and further references can be found in Refs. [77, 78].

The cooling laser is locked to the crossover signal of the $F = 4 \rightarrow F' = 3$ and $F = 4 \rightarrow F' = 5$ transition, the frequency of which is red-detuned by 225 MHz with

[2] An image of the diode laser design can be found in Ref. [74].

respect to the $F = 4 \rightarrow F' = 5$ cycling transition. This detuning is partially compensated using an acousto-optical modulator in double pass configuration. The latter shifts the laser frequency by $2 \times 110\,\mathrm{MHz}$ towards the cycling transition, allowing us to control the power and detuning of the cooling laser beams electronically. The repumping laser is directly locked to the signal of the $F = 3 \rightarrow F' = 4$ transition.

To save space on the main optical table, both diode lasers and the respective spectroscopies are set up on a separate table. Single mode, polarization-maintaining optical fibers guide the laser light to the main table close to the glass cell, see Fig. 1.7 in Sec. 1.2.3. Right after the fiber coupler, each of the three incident MOT beams is circularly polarized and focused to a waist radius of 1.4 mm in the trapping region. The retro-reflected beams, the polarizations of which are changed by passing through a quarter-wave plate twice, are focused slightly tighter to compensate for the losses from passing the uncoated surfaces of the glass cell. The repumping beam of the MOT is overlapped with the vertical cooling beam. Once the MOT beams are properly aligned, this compact setup requires almost no maintenance over several months.

1.1.4. Magnetic coil system

Trapping a small number of well-localized atoms in a MOT and transferring them into an optical lattice to manipulate their electronic states requires a switchable magnetic field gradient of the order of 300 G/cm. Such gradient can be generated by a pair of magnetic coils in anti-Helmholtz configuration which for practical reasons are placed outside the UHV glass cell. The design of these coils should be primarily adapted to the geometrical constraints imposed by the dimensions of the glass cell and the optical access required, for instance, for three mutually orthogonal pairs of counterpropagating molasses beams and the imaging optics, see Sec. 2.2.1. It should also consider the limited power for their operation, heat dissipation, additional space for water cooling, stability and suppression of eddy currents for fast-switching purposes, either by proper choice of materials or a clever design.

To provide the required field strength for an affordable power supply and meet the geometrical constrains, the bobbins of the MOT coils have to be placed close to the trapping region, aligned parallel to the surfaces of the glass cell. Taking the intended paths of the MOT beams into account (see Fig. 1.3), their symmetry axes have to coincide with the vertical MOT beam.

Besides operating a single atom MOT, we aim to employ a magnetic field gradient to position-dependently manipulate electronic state of individual atoms trapped in a one-dimensional optical lattice, see Sec. 3.4. Due to the geometry and confinement of the optical lattice, such manipulations prefer the symmetry axis of the coils to coincide with the lattice axis [79] since the field gradient of anti-Helmholtz coils in their center is twice as strong along the symmetry axis compared to that along a perpendicular axis. A stronger field gradient along the lattice axis improves both the selectivity and efficiency of position-dependent manipulation of the atoms, see

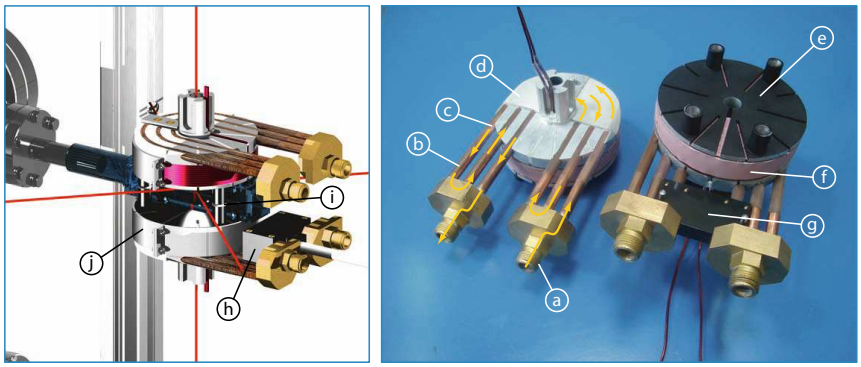

Figure 1.5.: Three-dimensional model (**left**) and manufactured parts (**right**) of the MOT coils. Special cooling water supply connections (**a**) serially connect the cooper pipes (**b**) ensuring identical flow pressure in each pipe and thus protecting them from clogging by calcification. Ultra-thin, thermally conductive and electrically resistant shrimp tubes (**c**), and epoxy potting compounds (**d**) electrically isolate the coil bobbins from the cooper pipes. Bobbins sides facing the glass cell (**e**) are painted black. Thermally conductive gel-like pads (**f**) fill the gap between the outer wire layer and the brackets (**j**). A build-in docking station (**g**) allows mounting a box with magnetic field sensors (**h**). Teflon bolts (**l**) support the bobbins for a high stability.

Sec. 3.4. In our case, the lattice axis is perpendicular to the vertical MOT beam. Consequently, a further pair of anti-Helmholtz coils is required, which we will refer to as addressing coils. Finally, we need three pairs of mutually orthogonal Helmholtz coils to compensate magnetic DC-fields and for application of guiding fields.

The dimensions of each coil pair have been numerically optimized to meet the requirements and take the above constraints into account, including space requirement of other coils and their holders. Additionally, simple estimations of heat dissipation have been performed. It turned out that not all optimum solutions could be technically realized. For this reason, the final design has been developed in cooperation with the institute's own workshop, in which the coil system has been finally manufactured. In the following, I will shortly present its main parts.

MOT coils

Each of the MOT coils has an inner diameter of 26 mm, an outer diameter of 106 mm and a height of 20 mm. It is wound with a flat, highly heat-resistant enameled copper wire (2.00 mm × 1.25 mm, type W 200, thermal class 200 C) and epoxy-molded on a single-block milled-aluminum bobbin with integrated water cooling copper pipes, see Fig. 1.5. The thermally conductive and electrically resistant epoxy potting compound (Duralco 128) fixes the wire while ensuring ideal heat dissipation by filling gaps between individual windings and provide a direct contact to the water-cooled bobbin. To prevent induction of eddy currents during switching

of the coils, each bobbin comprises a main slit from the center to the outside and 10 supporting slits segmenting the conductive material. Electrically bypassing of the slits through the integrated cooper pipes is prevented by partially covering these pipes with ultra-thin, thermally conductive and electrically resistant shrink tubes. For stability reasons, both bobbins are supported against each other by Teflon bolts to interrupt eddy currents around the glass cell between them. The bobbin sides facing the glass cell are painted black to reduce stray light. Heat from the outer winding layer is conducted to the water-cooled region using brackets. A thin, thermally conductive and electrically resistant film electrically isolates the brackets from each other and the slit bobbin. Highly compliant, gel-like pads (Bergquist, Gap Pad VO Ultra Soft) fill the gap between the outer wire layer and the brackets to support heat dissipation.

It should be mentioned that the entire coil design employs nonmagnetic materials, including bolts and screws. The strength of the field gradient along the symmetry axis of the MOT coils has been measured using a Hall-probe mounted on a translation stage, yielding $(16.1 \pm 0.1)\,\mathrm{G/cm\ A}$. The coils have been tested to sustain continuous currents up to 12.5 A (201 G/cm) and even 45 A for short times.

Addressing coils

A single addressing coil has an inner diameter of 148 mm, an outer diameter of 188 mm and a height of 40 mm. It is wound with two separated wires, each forming an independent coil. By this, part of the addressing coils can be operated in anti-Helmholtz configuration to generate strong quadrupole fields whereas another part can be optionally operated in Helmholtz configuration at the same time to provide a strong guiding field. For both coils, we use the same enameled wire as for the MOT coils, which is also epoxy-molded on a single-block milled-aluminum bobbin. Water cooling copper pipes are integrated close to the outer winding layer for optimum heat dissipation. Unlike the MOT coils, the addressing coils have to sustain high currents for long times maintaining a constant temperature. Because of thermal expansion of the bobbins, the center of the quadrupole field may measurably shift by a distance of approximately $2\,\mu$m (see e.g. Fig. 7.1 in Sec. 7.1.2) if their temperature changes on the order of one degree. This shift would affect the position-dependent manipulation of the atoms. For this reason, besides maximizing the strength of the field gradient, the coil design, including the winding geometry has been primarily focused on heat dissipation. Suppression of eddy currents has been merely considered by slitting the bobbins once.

In Figure 1.6(a), a three-dimensional model and the manufactured parts of the addressing coils are shown. The strength of the field gradient along the symmetry axis (lattice axis) is $(2.8 \pm 0.1)\,\mathrm{G/cm\ A}$ (measured with a Hall-probe). It agrees well with the value inferred from the position-dependent Zeeman shift of the measured atomic transition frequency, see Sec. 3.4.1, which gives $(2.74 \pm 0.01)\,\mathrm{G/cm\ A}$. The coils have been tested to sustain continuous currents up to 45 A (123 G/cm) for the time intervals of interest. The optional Helmholtz coils provide a guiding field

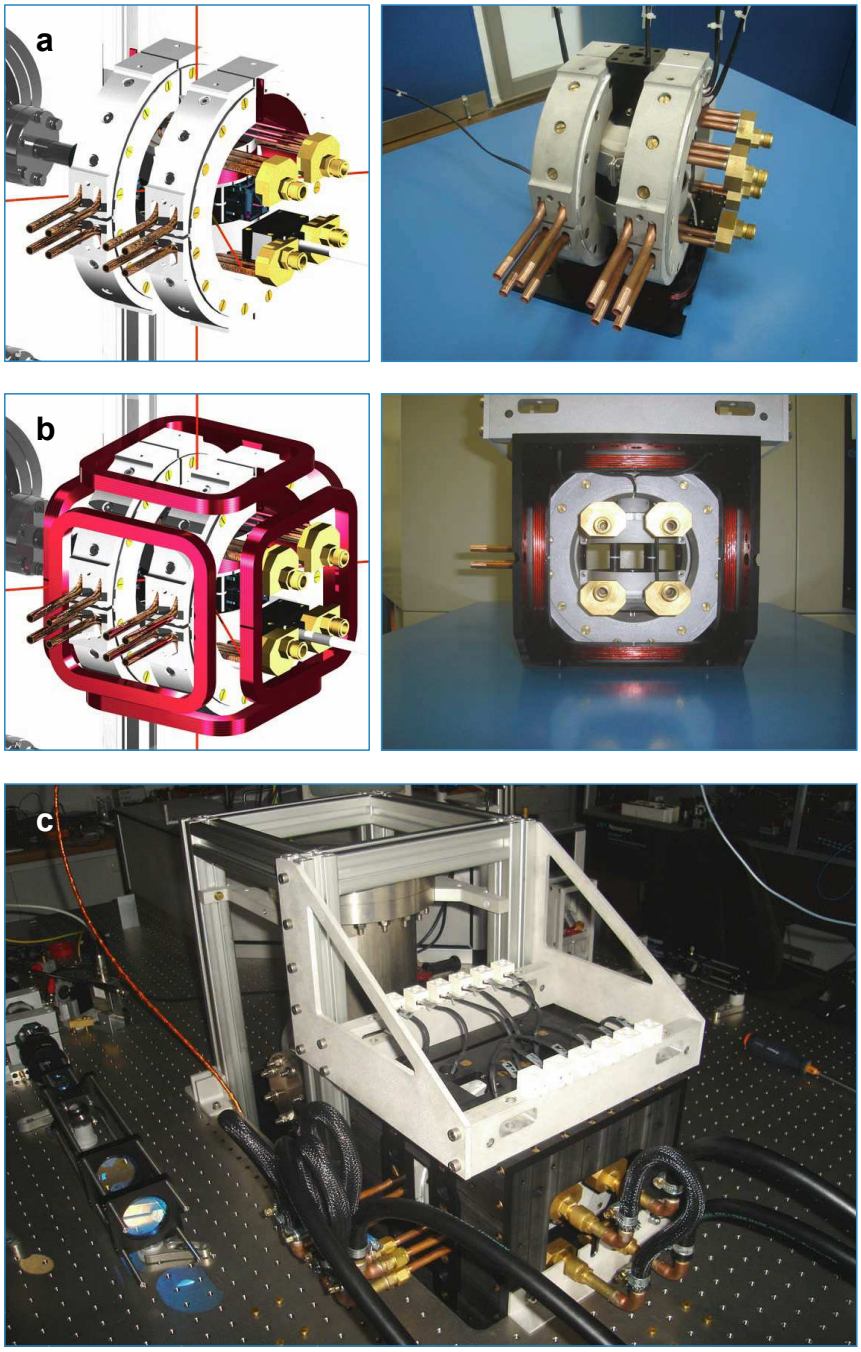

Figure 1.6.: Three-dimensional model (**left**) and manufactured parts (**right**) of (**a**) the addressing coils, and (**b**) the compensation and guiding field coils. For a better overview, the bobbins (black plastic) are hidden in the model in (**b**), whereas the front coil bobbin has been removed in the image of manufactured parts. An image taken at an early stage of the experiment (**c**), shows the cube-shaped coil system mounted to the aluminum cage and the optical table.

of $(22.6 \pm 0.1)\,\mathrm{G/A}$, resulting in a maximum field strength of 1000 G using the currently available power supply, see below.

Compensation and guiding field coils

Compensation and guiding fields are generated by three pairs of mutually orthogonal, rectangular coils in Helmholtz configuration. They are wound with the same enameled wire as the MOT coils. Each rectangular coil is epoxy-molded on a bobbin which is milled from a durable hard plastic. This material is also used to support the entire coil system, see Fig. 1.6(b), reducing the inductance of eddy currents. The compensation and guiding field coils are air-cooled. Each pair provides a field strength of 1.8 G/A.

The cube-shaped coil system is finally mounted to the aluminum cage which supports the vacuum apparatus. It is partially placed into the opening of the optical table, see Fig. 1.6(c). The upper and lower side of the cube provide additional holes around the beam axis which are compatible with 30 mm cage system (Thorlabs) for optical mounts. This allows us to mount the optics of the vertical MOT beam directly on the cube.

Power supplies

The MOT coils and addressing coils share a common power supply (Delta Elektronika, SM 70-45 D) with a built-in isolated amplifier card (option P145) for analog programming, providing up to 70 V and 45 A. It is connected to a custom-made switching box which permits fast switching of (and between both) coils via a TTL input within milliseconds. Parts of its electric circuit design are based on the switching device of Ref. [77], whereas instead of the power MOSFETs[3], IGBT[4] modules have been employed while capacitors and resistors for power dissipation have been adjusted to the inductance of our coils.

The compensation and guiding field coils are driven by a triple-output power supply (Toellner TOE 8733-1), which provides two outputs with up to 16 V and 2 A, and a single output with up to 7 V and 5 A. All outputs provide a residual ripple of 50 μA.

1.2. A one-dimensional optical lattice

Selective manipulation of individual atoms in specific electronic states requires that the atoms are well localized and separated, while any perturbation changing their electronic states is sufficiently suppressed on the relevant timescales. Meeting the latter two requirements, however, is inherently impossible in a MOT since the trapped atoms are spatially inseparable whereas continuous scattering of photons

[3]MOSFET: Metal-Oxide-Semiconductor Field-Effect Transistor.
[4]IGBT: Insulated-Gate Bipolar Transistor.

continually changes their electronic states. Instead, the precooled atoms are transferred into a one-dimensional optical lattice — a periodic array of conservative trapping potentials, generated by interaction of a far-detuned standing wave light field with the atomic dipole moment. The separation between individual trapping potentials forming the sites of the optical lattice is defined by the periodicity of the standing wave, whereas photon scattering rates are only a few photons per second, meeting the requirements stated above.

1.2.1. Classical model of a dipole potential

Besides an intuitive understanding, a classical model of a dipole potential provides a good approximation to the quantum-mechanical treatment, characterizing its essential properties and dependencies on experimental parameters. It relies on the Lorentz model of a classical damped oscillator driven by an external, monochromatic electric field $\boldsymbol{E}(\boldsymbol{r},t) = (\boldsymbol{E}_0(\boldsymbol{r})\exp(-i\omega t) + \text{c.c.})/2$ [28]. According to this model, the induced dipole moment of the atom $\boldsymbol{d}(\boldsymbol{r},t)$ obeys the equation of motion

$$\ddot{\boldsymbol{d}}(\boldsymbol{r},t) + \Gamma_\omega \dot{\boldsymbol{d}}(\boldsymbol{r},t) + \omega_0^2 \boldsymbol{d}(\boldsymbol{r},t) = \frac{e^2}{m_\mathrm{e}} \boldsymbol{E}(\boldsymbol{r},t) \tag{1.2}$$

with the resonance frequency of the oscillator ω_0 and the energy damping rate due to classical dipole radiation [80]

$$\Gamma_\omega = \frac{e^2\omega^2}{6\pi\varepsilon_0 m_\mathrm{e} c^3}\,, \tag{1.3}$$

where m_e and e are the rest mass and electric charge of the electron, respectively, and ε_0 the electric constant.

The induced dipole moment is related to the electric field through the complex atomic polarizability $\alpha(\omega)$

$$\boldsymbol{d}(\boldsymbol{r},t) = \alpha(\omega)\boldsymbol{E}(\boldsymbol{r},t)\,. \tag{1.4}$$

From the stationary solution of Eq. (1.2), we obtain

$$\alpha(\omega) = \frac{e^2}{m_\mathrm{e}} \frac{1}{\omega_0^2 - \omega^2 - i\omega\Gamma_\omega} = \frac{6\pi\varepsilon_0 c^3 (\Gamma/\omega_0^2)}{\omega_0^2 - \omega^2 - i\omega^3(\Gamma/\omega_0^2)}\,, \tag{1.5}$$

where in the last step, the on-resonance damping rate $\Gamma \equiv \Gamma_{\omega_0} = (\omega_0/\omega)^2\Gamma_\omega$ and Eq. (1.3) have been employed. The former is determined from a simple quantum mechanical model of a two-level atom rather than from Larmor's formula [28], extending the initial classical model of a dipole potential to a semiclassical approach.

The time-averaged (denoted as $\langle\ldots\rangle$) interaction energy between the induced dipole and its driving field finally results in a dipole potential

$$U_\mathrm{dip}(\boldsymbol{r}) = -\frac{1}{2}\langle \boldsymbol{d}(\boldsymbol{r},t)\boldsymbol{E}(\boldsymbol{r},t)\rangle = -\frac{1}{2\varepsilon_0 c}\mathrm{Re}\left\{\alpha(\omega)\right\} I(\boldsymbol{r}) \tag{1.6}$$

with the field intensity $I(\boldsymbol{r}) = c\varepsilon_0|\boldsymbol{E_0}(\boldsymbol{r})|^2/2$. Another important quantity is the photon scattering rate which imposes a limit on the lifetime of internal states [64]. This rate is determined analogously from the absorbed power P_{abs}, yielding

$$R_{\mathrm{s}}(\boldsymbol{r}) = \frac{P_{\mathrm{abs}}(\boldsymbol{r})}{\hbar\omega} = \frac{1}{\hbar\omega}\langle\dot{\boldsymbol{d}}(\boldsymbol{r},t)\boldsymbol{E}(\boldsymbol{r},t)\rangle = \frac{1}{\hbar\varepsilon_0 c}\mathrm{Im}\left\{\alpha(\omega)\right\}I(\boldsymbol{r})\,. \tag{1.7}$$

In our experiment, the detuning of the light field $\Delta = \omega - \omega_0$ is much larger than the natural line width ($|\Delta| \gg \Gamma$). On the other hand, the detuning is much smaller than the optical resonance frequency ω_0, so that $|\Delta| \ll \omega_0$ and thus $\omega/\omega_0 \approx 1$. Therefore, we can rewrite Eqs. (1.6) and (1.7) in the rotating wave approximation as [28]

$$U_{\mathrm{dip}}(\boldsymbol{r}) = \frac{3\pi c^2}{2\omega_0^3}\frac{\Gamma}{\Delta}I(\boldsymbol{r})\,, \tag{1.8}$$

$$R_{\mathrm{s}}(\boldsymbol{r}) = \frac{3\pi c^2}{2\hbar\omega_0^3}\frac{\Gamma^2}{\Delta^2}I(\boldsymbol{r})\,. \tag{1.9}$$

From these equations, the basic properties of dipole trapping and photon scattering in far-detuned, monochromatic light fields can be inferred, which remain valid even in a quantum mechanical treatment of a multi-level atom: First, both the dipole potential and photon scattering rate scale linearly with the intensity of the light field. Second, while the dipole potential depends linearly on the reciprocal of detuning, the respective dependency of the scattering rate is quadratically. Therefore, to minimize the photon scattering rate, it is preferable to work with a large detuning while compensating the decreasing potential depth by higher intensities. Finally, the sign of the detuning determines the nature of the corresponding conservative dipole force $\boldsymbol{F}_{\mathrm{dip}}(\boldsymbol{r}) = -\nabla U_{\mathrm{dip}}(\boldsymbol{r})$ exerted on the atom by the light field. In case of blue detuning ($\Delta > 0$), the dipole potential is positive, yielding a repulsive dipole force, whereas for red detuning ($\Delta < 0$), it is negative and the corresponding force is attractive.

Remarks on multi-level atoms

The above semiclassical model provides a simple expression for the dipole potential. However, it neither takes the multi-level structure of the atom nor the polarization of the electromagnetic field into account. In general, the dipole potential depends on the particular state of the atom, including atomic fine, hyperfine and even Zeeman substates. The latter are differently affected by the polarization of the light field, see Sec. 4.1. To understand these properties, a full quantum mechanical treatment of the atom-light field interaction is required which takes all relevant atomic substates into account. Such quantum mechanical description provides AC-Stark shifts (also referred to as "light shift") of every atomic level. For cesium atoms, the AC-Stark shift of the $6^2\mathrm{S}_{1/2}$, $6^2\mathrm{P}_{1/2}$ and $6^2\mathrm{P}_{3/2}$ electronic states have been extensively studied in our group, see e.g. Ref. [47,49,78] and references therein. Throughout this thesis, I will merely refer to some results of these studies.

For a linearly polarized light field, the multi-level structure of cesium can be approximately taken into account by applying the semiclassical model to the D_1 and D_2 transition separately and adding up the resulting contributions weighted with each transition's oscillator strength [77]. This yields a similar expression as in Eq. (1.8), albeit with an "effective" detuning

$$\frac{1}{\Delta_{\text{eff}}} = \frac{1}{3}\left(\frac{1}{\Delta_{D_1}} + \frac{2}{\Delta_{D_2}}\right) . \tag{1.10}$$

The so calculated dipole potential differs only marginally from a quantum mechanical calculation.

1.2.2. Periodic array of trapping potentials

According to previous considerations, a periodic array of confined trapping potentials requires a periodic intensity pattern of monochromatic light, the frequency of which is far detuned from the transition frequencies of the atom. In the one-dimensional case, such a pattern can be realized by interference of two focused counterpropagating, linearly polarized Gaussian laser beams. For $\Delta_{\text{eff}} < 0$, atoms are attracted to the maxima of the resulting standing wave intensity distribution.

Let $\boldsymbol{E}_1(\boldsymbol{r},t)$ and $\boldsymbol{E}_2(\boldsymbol{r},t)$ be the electric fields of two counterpropagating, linearly polarized Gaussian beams, the polarization of which is given by $\boldsymbol{e}_{\text{lin}}$. In cylindrical coordinates ($\boldsymbol{r} = (\rho, z, \varphi)$), they can be written as

$$\boldsymbol{E}_1(\boldsymbol{r},t) = A(\boldsymbol{r})\cos(\omega t - f(\boldsymbol{r}))\cdot\boldsymbol{e}_{\text{lin}}\,, \tag{1.11}$$
$$\boldsymbol{E}_2(\boldsymbol{r},t) = A(\boldsymbol{r})\cos(\omega t + f(\boldsymbol{r}))\cdot\boldsymbol{e}_{\text{lin}} \tag{1.12}$$

with the auxiliary functions

$$A(\boldsymbol{r}) = E_0\frac{w_0}{w(z)}e^{-\frac{\rho^2}{w^2(z)}} \quad \text{and} \quad f(\boldsymbol{r}) = kz + \frac{k\rho^2}{2R(z)} - \eta(z)\,, \tag{1.13}$$

corresponding to an amplitude and phase, respectively. Here, $w(z) = w_0\sqrt{1+z^2/z_0^2}$ denotes the beam radius with the waist radius w_0 and the Rayleigh length $z_0 = \pi w_0^2/\lambda$, $R(z) = z(1+z_0^2/z^2)$ the radius of curvature of the wavefronts and $\eta(z) = \arctan(z/z_0)$ the Gouy phase. The contributions of the latter two can in principle be neglected in the trapping region ($|z| \ll z_0$), yielding $f(\boldsymbol{r}) \approx kz$. The standing wave intensity distribution of both interfering beams is then given by

$$\begin{aligned} I(\boldsymbol{r}) \quad &= \quad c\varepsilon_0\langle[\boldsymbol{E}_1(\boldsymbol{r},t)+\boldsymbol{E}_2(\boldsymbol{r},t)]^2\rangle = 2c\varepsilon_0 A^2(\boldsymbol{r})\cos^2(f(\boldsymbol{r})) \\ &\overset{|z|\ll z_0}{\approx} \quad I_{\max}\frac{w_0^2}{w^2(z)}e^{-\frac{2\rho^2}{w^2(z)}}\cos^2(kz) \end{aligned} \tag{1.14}$$

with the peak intensity $I_{\max} = 4P/\pi w_0^2$ characterized by the power of a single laser beam P. Using Eq. (1.8), we finally get the dipole potential of a one-dimensional

optical lattice

$$U_{\mathrm{dip}}(\boldsymbol{r}) = -U_0 \frac{w_0^2}{w^2(z)} e^{-\frac{2\rho^2}{w^2(z)}} \cos^2(kz)\,, \tag{1.15}$$

where U_0 denotes its maximum depth, also referred to as trap depth. This potential is thus periodic along the beam propagation axis, the so-called lattice axis. Its minima in which atoms are trapped will be also referred to as potential wells or lattice sites. The periodicity of the lattice, $\lambda/2$, is determined by the laser wavelength λ. Radially, i.e. perpendicular to the lattice axis, the dipole potential has a Gaussian profile. It provides a transversal confinement of the atoms determined by the waist radius of the laser beams.

Each potential well of the optical lattice can be well approximated by a cylindrically symmetric harmonic oscillator, e.g. by a Taylor series expansion of Eq. (1.15) at $(\rho, z) = (0, 0)$. In this harmonic approximation, the oscillation frequencies of a trapped atom in the axial and radial direction are given by

$$\Omega_{\mathrm{ax}} = 2\pi \sqrt{\frac{2U_0}{m_{\mathrm{Cs}}\lambda^2}} \tag{1.16}$$

and

$$\Omega_{\mathrm{rad}} = \sqrt{\frac{4U_0}{m_{\mathrm{Cs}} w_0^2}}\,, \tag{1.17}$$

respectively, where m_{Cs} denotes the mass of the cesium atom. They are also referred to as axial and radial trapping frequencies.

1.2.3. Experimental setup

To generate the light field of the optical lattice, we use a commercial (Coherent Monolithic Block Resonator, MBR-110) tunable ring titanium:sapphire (Ti:S) laser, pumped with a solid-state laser system (Verdi V-18, 532 nm) which provides a maximum output power of 18 W. The Ti:S laser can be operated in a range from 700 nm to 1020 nm depending on the built-in optics set. It can be locked to a stabilized internal reference cavity, providing a Gaussian (TEM_{00}) transverse mode with linear polarization and a maximum output power of 3.4 W at a wavelength of $\lambda = 865.9\,\mathrm{nm}$.[5]

In Figure 1.7, a schematic overview of the optical lattice setup is shown. After passing through an optical isolator (Linos FI 660/110-8 SI), the output beam is actively power-stabilized using an acousto-optic modulator (AOM) based feedback loop. It allows us to control the laser power and thus the lattice depth using an analog input voltage, providing a bandwidth of 30 kHz. The pointing stability of the laser beam is passively stabilized by shortening the free beam path using a fiber line

[5] The choice of this wavelength is discussed in Sec. 4.1.

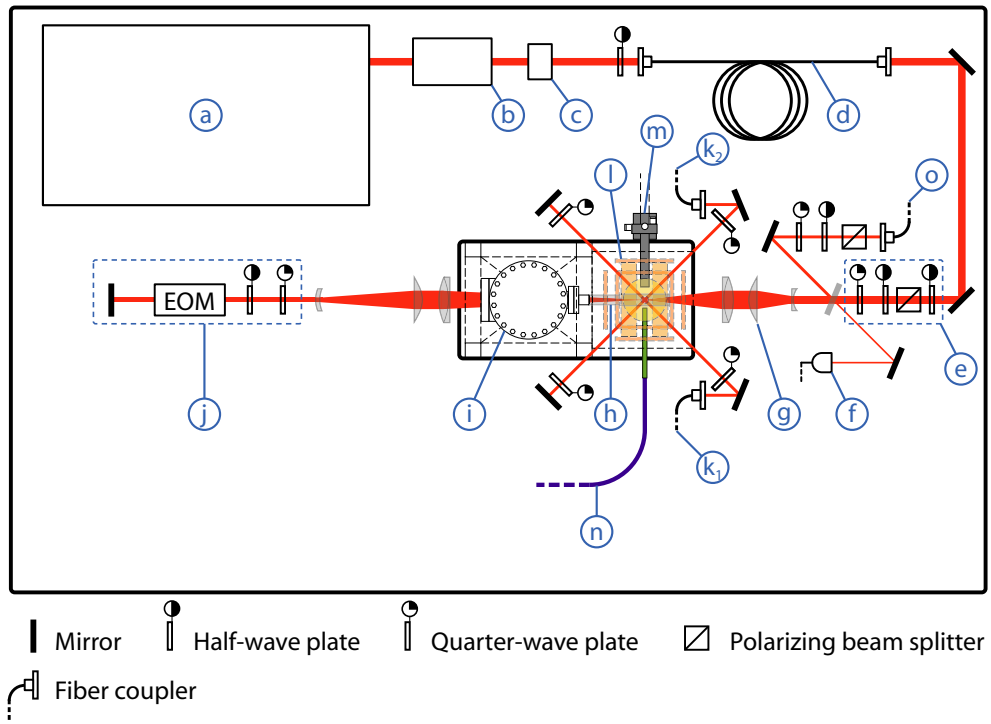

Figure 1.7.: Schematic overview of the optical lattice setup. The incident laser beam from a Ti:S laser (**a**) passes through an optical isolator (**b**) and an AOM (**c**) used for power control and stabilization, the output signal for feedback of which is measured by a fast photodiode (**f**). The beam passes a fiber line (**d**), a setup for precompensation of polarization distortions (**e**), a system of lenses (**g**) and finally the glass cell (**h**) and vacuum chamber (**i**) before entering the polarization control setup (**j**, see Sec. 4.3) and being retro-reflected. ($\mathbf{k}_1$) and ($\mathbf{k}_2$) indicate two of three MOT beams. The missing beam is perpendicular to the image plane. For overview reasons, the coil system (**l**, see Sec. 1.1.4), parts of the imaging system (**m**, see Sec. 2.2.1), the microwave setup (**n**, see Sec. 3.2.2) and optical pumping setup (**o**, see Sec. 3.1.1) are shown.

and enclosing the entire optical table by a PVC[6] strip curtain. The latter protects the mounted optical elements from dust and acoustic vibrations while preventing draft and reducing temperature variations.

To ensure linear polarization of the laser beam in the trapping region of the atoms, polarization distortions from optical elements in the beam path are precompensated using a combination of a polarizer, a half- and a quarter-wave plate. The laser is finally focused to a waist radius of 20 μm in the trapping region of the atoms by a system of lenses, which has been previously simulated and optimized using an optical design software. Details on the lens system can be found in Ref. [68].

After passing through the vacuum chamber and its window, the laser beam is fi-

[6]PVC: Polyvinyl Chloride.

nally retro-reflected, passing the polarization control setup twice. The latter allows to rotate the polarization angle of the retro-reflected linearly polarized beam. Rotation of polarization, however, is only employed for the state-selective transport and its applications and will be therefore discussed in detail in Chap. 4. Unless stated otherwise, throughout this thesis the polarization of the retro-reflected beam is identical to that of the incident beam.

For the sake of completeness and illustrative reasons, parts of the magneto-optical trap and the optical pumping setup and their positions on the main optical table are also shown in Fig. 1.7. The optical pumping setup will be presented and discussed in detail in a subsequent chapter, see Sec. 3.1.1. The same applies for the imaging setup to detect fluorescence of the atoms (see Sec. 2.2.1) and the microwave setup to manipulate their internal states, see Sec. 3.2.2.

1.3. Computer control system

The entire experiment, its parameters, experimental sequences and acquired data are controlled and processed by a single personal computer (PC) and self-developed software, which I have developed during this thesis. The software is adapted to the multi-threading and multi-core capability of the CPU[7]. By this we avoid communication delays, which would otherwise occur if several computers are employed. The computer comprises two high-speed, multifunction data acquisition boards (National Instruments PCIe-6259), each providing four 16 bit analog outputs ($-10\,\mathrm{V}$ to $+10\,\mathrm{V}$) and 48 digital outputs with a full scale settling time of $2\,\mu\mathrm{s}$ defining the maximum time resolution. Both cards use the PCI[8] Express bus and contain six DMA[9] channels each to maximize the data throughput without using the computer's processing time. They are synchronized via the RTSI[10] bus.

The computer additionally comprises a static analog output board (National Instruments PCI-6723), a high-performance GPIB[11] board (National Instruments PCI-GPIB) and a PCI controller for the camera, see Sec. 2.2.2. The former provides 32 additional analog outputs ($-10\,\mathrm{V}$ to $+10\,\mathrm{V}$) and 8 digital outputs which are rather used as fixed voltage sources. The GPIB interface is used to upload waveforms to the arbitrary waveform generators employed in the microwave (see Sec. 3.2.2) and the polarization control setup (see Sec. 4.3).

A detailed description of the self-developed software for controlling experimental sequences ("Control Center"), uploading arbitrary waveforms ("WaveGen") and controlling the camera ("iXacq") is given in App. A, whereas methods for processing of acquired images are partially discussed in Sec. 2.3 and Sec. 4.5.3.

[7] CPU: Central Processing Unit.
[8] PCI: Peripheral Component Interconnect.
[9] DMA: Direct Memory Access.
[10] RTSI: Real-Time System Integration.
[11] GPIB: General Purpose Interface Bus.

2. Fluorescence detection of neutral atoms in an optical lattice

Detection and manipulation of individual atoms on neighboring sites of an optical lattice has recently come to the fore of various applications of quantum information science [16, 81–83], providing a technical challenge for lattice site separations in the optical wavelength domain. In a different regime, where lattice sites are separated by several micrometers, single atoms could be optically resolved [84, 85]. This approach, however, has currently proved to be inapplicable for most already established schemes, which favor site separations in the optical wavelength regime.

Recently, single-site detection and addressability using focused electron beams from an ultra-high vacuum compatible electron gun [44,45] has been reported. However, this technique is not easily integrated in many neutral atoms experiments, in which, in contrast, optical imaging by fluorescence light is widely established. Upgrading existing experimental setups with high resolution imaging optics encounters difficulties, due to spatial constraints imposed by vacuum components and the optical access. In this work, I follow a different approach which builds up on the success of other research fields, including astronomy and biology. I overcome the previous restrictions imposed by the diffraction limit [43] with a markedly improved data quality and reduced noise, together with advanced numerical processing of fluorescence images.

2.1. The deconvolution problem

Every acquired image is blurred whenever the optical system used has a finite resolving power. This process can be mathematically expressed as a convolution of the original light distribution with the *Point Spread Function* (PSF) of the image — a characteristic intensity distribution of an ideal point source imaged by the optical system. Assuming the PSF to be shift-invariant (isoplanatic[1]) and considering the fact that each light distribution can be decomposed into a collection of point sources, the imaging equation can be written as

$$\begin{aligned} I_{2\mathrm{D}}(x,y) &= (P_{2\mathrm{D}} * O_{2\mathrm{D}})(x,y) + \epsilon_{2\mathrm{D}}(x,y) \\ &= \int_{-\infty}^{\infty}\int_{-\infty}^{\infty} P_{2\mathrm{D}}(x-u,y-v)O_{2\mathrm{D}}(u,v)\,\mathrm{d}u\,\mathrm{d}v + \epsilon_{2\mathrm{D}}(x,y)\,, \quad (2.1) \end{aligned}$$

[1] The isoplanatism is not fulfilled in general, see Sec. 2.3.3. However, there are small regions where the PSF is almost shift-invariant. These regions are called *isoplanatic patches*.

where $O_{2D}(x, y)$ and $I_{2D}(x, y)$ denote the original and imaged intensity distributions, $P_{2D}(x, y)$ the area normalized[2] PSF and $\epsilon_{2D}(x, y)$ additive measurement errors (noise) affecting the image. The subscript 2D distinguishes between two- and one-dimensional functions introduced later in this work.

The shape of the PSF primarily depends on the geometry of the optical system and its imperfections, arising from defocusing and optical aberrations. For a diffraction-limited (aberration free) optical system with a circular entrance pupil, the PSF is the well-known Airy pattern [86]. It consists of a bright central Airy disc, encircling 83.8% of the total energy, surrounded by concentric rings of successively decreasing intensity. The radius of the Airy disc sets the limit for the smallest resolvable distance in the lateral plane, called Rayleigh criterion [87].

In addition, image acquisition involves spatial sampling and digitalization whenever digital detectors such as Charge Coupled Devices (CCDs) are used. Therefore, the detected light distribution is only known at regularly spaced sampling points

$$I_{2D}[x_i, y_j] = (P_{2D} * O_{2D})[x_i, y_j] + \epsilon_{2D}[x_i, y_j]\,, \tag{2.2}$$

where x_i and y_j denote the horizontal and vertical position of a sampling point $\{i, j\}$, e.g. a CCD pixel, $\epsilon_{2D}[x_i, y_j]$ incorporates additional noise arising from the digital detection, and squared brackets are used to distinguish discrete from continuous functions. Note that in general $I_{2D}(x_i, y_j) \neq I_{2D}[x_i, y_j]$.

Both, sampling and noise lead to information loss in the acquisition process. The reverse process aiming to reconstruct the unblurred image is called deconvolution, referring to inversion of Eq. (2.2). Being an inverse problem, deconvolution is inherently ill-conditioned. Therefore, no unique solution exists in the presence of noise, since many light distributions, being convolved with the PSF, are compatible within the error bars with the observed image. For this reason, regularization techniques are used to select a plausible solution amongst the family of possible ones.

There are a variety of deconvolution strategies available in the literature. For an overview, see Ref. [88] and references therein. The diversity of strategies reflects different ways of estimating the true signal under various idealizations of its properties. Different assumptions about the PSF and the instrumental noise have to be considered to constrain the solutions and efficiently use the computational resources available. In this work, I use a parametric deconvolution to determine the positions of atoms in an optical lattice. This method assumes the PSF or its derivatives to be analytically known. Furthermore, it requires all distortions of the original signal, e.g. by the stray light, to be reduced to a minimum. By this, the fluorescence signal of the atoms can be modeled in a simple way — as a sum of intensity spikes on a homogeneous background, the positions and fluorescence contributions of which are determined numerically. This idealization enables to reduce the complexity of the problem to a manageable level, since only a small number of parameters has to

[2] $\int_{-\infty}^{\infty}\int_{-\infty}^{\infty} P_{2D}(x, y)\,\mathrm{d}x\,\mathrm{d}y = 1$.

be precisely determined, being supported by a high number of sampling points. By this, determining the positions of the atoms can be performed almost in real-time.

2.2. Imaging setup

Fluorescence detection of atoms in optical lattices has been widely spread over the years, enabling and advancing the control of internal and external degrees of freedom of each individual atom [47, 89]. It puts the highest demands on efficient fluorescence collection, suppression of stray light and the noise performance and sensitivity of the detector. Diffraction and optical aberrations impose a limit on the optical resolution, whereas noise performance of the detector and stray light strongly affect the chances of successfully overcome this limit using numerical post-processing.

2.2.1. Optical setup

The fluorescence light of the atoms is collected by a self-assembled, diffraction-limited microscope objective with a numerical aperture of NA = 0.29, covering a fluorescence fraction of 2.1% of the 4π solid angle [77, 90]. The microscope objective is composed of standard catalog lenses (25.4 mm diameter) to reduce the cost of manufacture. Its lens design was entirely adopted from Ref. [90], meeting the requirements and spatial constraints imposed by the experimental setup. These constrains include a compact design and a long range working distance with a focal length of $f_{\mathrm{obj}} = 36\,\mathrm{mm}$, allowing the objective to be placed and aligned outside the UHV glass cell between the mounting of the magnetic coils. Furthermore, the working distance prevents the stray light stemming from reflections of molasses beams off the non-coated inner surface of the glass cell to enter the entrance pupil of the objective, whereas reflections off the outer surface are directly shielded using beam tubes, see Fig. 2.1. The lens design has been numerically optimized to minimize spherical aberrations, introduced by the glass cell wall of 5 mm thickness. The wavefront deformations of the assembled microscope have been measured with a share-plate interferometer, providing a peak-valley wavefront distortion of less than $\lambda/4$ over 90% of the clear aperture (for details see Ref. [77, 78]).

The microscope objective collimates the fluorescence light of the atoms, which is then imaged by a plan-convex lens with $f_{\mathrm{img}} = 2\,\mathrm{m}$, resulting in a theoretical magnification of $f_{\mathrm{img}}/f_{\mathrm{obj}} \approx 55.6$.[3] All lenses are permanently mounted in a black anodized aluminum tube with an internal thread, preventing the stray light from being reflected on the inner surface of the tube and entering the optical path. The objective is mounted on a three-axis translation stage, providing the relevant degrees of freedom for the everyday alignment. A black flexible welded bellow connects the adjustable objective to an optically shielded system of mirrors and blackened

[3] A precise measurement of the magnification utilizing the periodicity of the optical lattice is given in Sec. 2.4.2

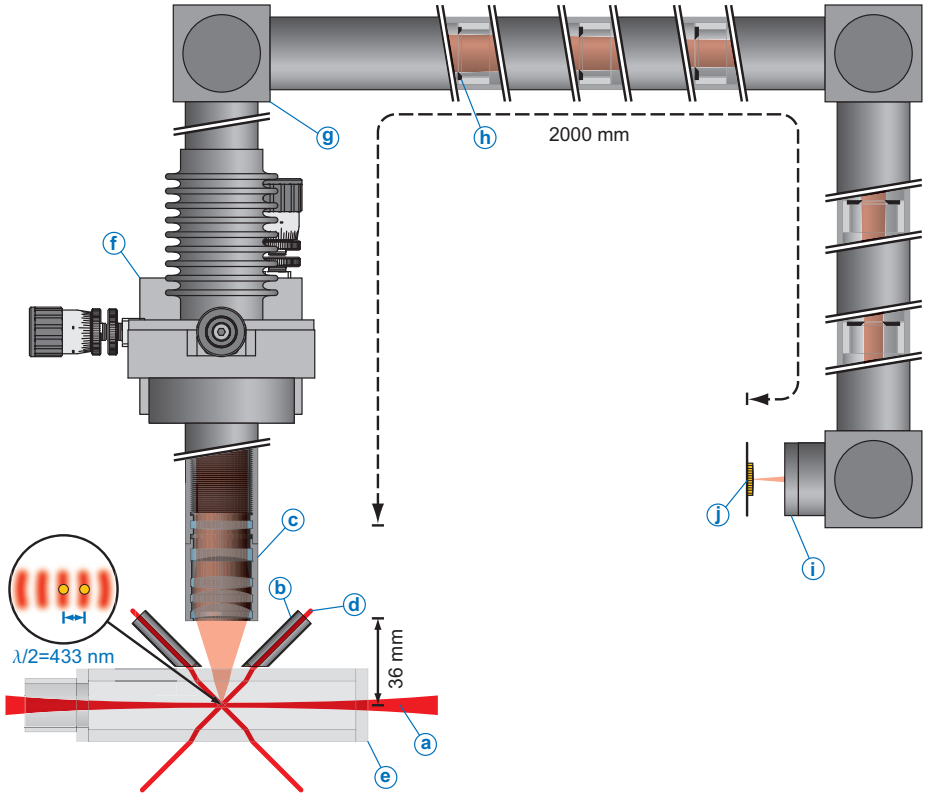

Figure 2.1.: Detail of the imaging setup. Two counterpropagating laser beams (**a**) form the one-dimensional lattice. Beam tubes (**b**) shield the objective (**c**) from stray light of molasses beams (**d**) off the glass cell (**e**). A three-axis translation stage (**f**) allows a precise alignment of the objective. Tubes and mirror cubes (**g**) bridge the distance between the imaging lens and the detector, while built-in apertures (**h**) strongly suppress the remaining stray light. A narrow-band optical filter (**i**) in front of the detector (**j**) filters the stray light from the optical lattice.

tubes, which bridge the 2 m distance and the elevation between the imaging lens and the detector. The tube system comprises a stray light trap consisting of five sooted apertures with gradually decreasing inner diameters of $16, 14, 12, 10$ and 8 mm, which exclude most of the out-of-focus light. Each aperture is made out of steel and mounted in a sliding plastic holder, allowing to smoothly move the apertures along the tube axis from the outside of the tube using magnets. The position of each aperture has been iteratively aligned to minimize the stray light while avoiding obstructions and maintaining the imagining quality of the objective characterized by its line spread function, see Sec. 2.3.3. A narrow-band optical filter (CWL[4] at 850.5 nm, FWHM[5] of 5 nm) with a measured transmission of 82.3% at

[4]Central Wavelength
[5]Full Width at Half Maximum

852.3 nm [78] suppresses the stray light from the optical lattice by more than 37 dB.

2.2.2. The EMCCD detector

The fluorescence signal of the atoms is detected using an *Electron Multiplying Charge Coupled Device* (EMCCD) camera (Andor iXon DV887DCS-FI) which is capable of detecting a single photon without any additional image intensifier and enables imaging with sub-electron noise up to video frame rates. It contains a 512×512 active pixels front-illuminated frame transfer CCD (L3Vision CCD97 [91]) with a pixel size of $16 \times 16\,\mu\mathrm{m}^2$, enabling on-chip charge multiplication before the readout process, while utilizing the full quantum efficiency performance ($\approx 40\%$ at 852 nm) of the CCD. The resolution of the EMCCD is therefore identical to that of the CCD, and thus mainly determined by the pixel size, being only reduced by photons absorbed near the boundary between the pixels. The sensitivity of the CCD, however, is limited by the readout noise arising from the charge-to-voltage and analog-to-digital conversion in the output amplifier and the video chain electronics. This limitation is particularly relevant for low-intensity signals with levels falling beneath the readout noise floor. The EMCCD technology overcomes this limitation [92], by applying a low-noise gain prior the conversion, boosting the signal above the noise floor of the output amplifier. The gain is applied in an additional extended serial register, the *electron multiplication* (EM) register, between the shift register and the output amplifier.

The EM register comprises several hundred of stages (536 for L3Vision CCD97 [91]). By applying a sufficiently high voltage at each stage, the electrons are multiplied by impact ionization, generating secondary electrons in the silicon, similar to a staircase avalanche photodiode. Even though the probability of impact ionization is very low at each individual stage, $p_{\mathrm{imp}} \approx 1.5\%$, due to the high number of stages N, the mean gain of the cascaded multiplication elements $M = (1 + p_{\mathrm{imp}})^N$ reaches values of up to several thousand. This gain mechanism, however, is stochastic and thus introduces an additional system noise component, being evaluated quantitatively as the excess noise factor F — a multiplying factor for the signal noise prior the EM register, e.g. photon and dark current shot noise. The excess factor can be analytically expressed by $F^2 = 2(M-1)M^{-(N+1)/N} + 1/M$ (see Ref. [93]). Thus, for a high number of multiplication stages and a high gain, F^2 tends to 2, effectively halving the quantum efficiency.

The noise performance of the detector strongly affects the quality of the fluorescence signal, imposing the limit of the reliability and accuracy of determining the number and positions of the atoms. Although the latter can be in principle improved if the signal-noise relation is precisely known and properly considered in the parametric deconvolution (see See. 2.3.6), the a priori reduction of noise provides the best strategy for improving the signal quality. In the following, I discuss the dominant noise sources of our detection setup, providing strategies for their reduction within the realms of technical possibilities. Quantitative specifications of the noise sources can be found in Ref. [91].

Readout noise Readout noise arises from the readout of accumulated photoelectrons in each pixel. It can be decomposed into two parts, depending on whether the noise arises before or after the EM register, or rather, whether the noise is affected by the gain process or not. During the readout, the accumulated electrons are shifted on the CCD, yielding some electrons being left behind, jump ahead or even generate additional electrons (clock-induced charges). The resulting noise σ_{shift} scales with the square root of the readout speed. It is subsequently amplified in the EM register. The second part of the readout noise, σ_{conv}, arises from the charge-to-voltage and analog-to-digital conversion, both being carried out after the multiplication process. Therefore, this noise can be effectively reduced by increasing the gain. We operate the EMCCD using the maximum gain[6] of $M \approx 1000$ at a readout rate of 10 MHz, resulting in a total effective readout noise below $0.1\,\mathrm{e}^-$/pixel.

Photon shot noise Photon shot noise arises from statistical fluctuations in the number of incident photons, which translate into a variation of the mean of accumulated photoelectrons S_{signal}. It is a fundamental property of the quantum nature of light and thus unavoidable in the image acquisition process. The photoelectron fluctuations follow Poissonian statistics. Therefore, the corresponding shot noise is given by $\sigma_{\text{shot}} = \sqrt{S_{\text{signal}}}$, being subsequently amplified in the EM register. We reduce the amount of photon shot noise by suppressing the photons not stemming from the fluorescence of the atoms, e.g. additive signal background of the stray light.

Dark current noise Dark current arises from thermally generated electrons in the silicon substrate of the CCD which leak into the pixels during the exposure time. The amount of dark electrons S_{dark} is proportional to the exposure time and exponentially increases with the operation temperature of the CCD [95, 96]. For this reason, we operate the EMCCD at a temperature of $-70\,^\circ\mathrm{C}$, resulting in a dark current of $0.01\,\mathrm{e}^-$/pixel/s for $M = 1$ (no gain). The corresponding dark current shot noise $\sigma_{\text{dark}} = \sqrt{S_{\text{dark}}}$ is subsequently amplified in the EM register. Note that at low temperatures, the multiplication gain is increasingly temperature-dependent and thus affected by temperature stability (typically $\pm 0.01\,^\circ\mathrm{C}$, resulting in a gain stability of $\pm 1\%$).

Photo-response non-uniformity Photo-response non-uniformity (PRNU) describes the difference in pixel response to uniform light sources due to variations in pixel geometry and substrate material across the chip. The corresponding noise σ_{pr} is proportional to the incident pixel illumination, becoming increas-

[6] Note that the EM register suffers from gain aging effects, resulting in a gain fall-off over a period of time [94]. This aging process is even accelerated, by operating the EMCCD at maximum gain. Therefore, using our EMCCD camera for more than one year, we expect the maximum gain to be lower than specified.

ingly prominent for high illumination levels. This noise is amplified in the EM register.

The total noise of the EMCCD per pixel can be modeled by summing the variances of the individual noise sources, while incorporating the influence of the EM register, yielding

$$\sigma^2_{\text{total}} = A^2\sigma^2_{\text{conv}} + A^2M^2F^2\left(\sigma^2_{\text{shift}} + \sigma^2_{\text{shot}} + \sigma^2_{\text{dark}} + \sigma^2_{\text{pr}}\right) , \tag{2.3}$$

where A denotes the total video chain gain, i.e. the electron-to-digital number conversion factor. Therefore, the effective total noise is given by

$$\sigma_{\text{total, eff}} = \sqrt{\sigma^2_{\text{conv,eff}} + F^2\left(\sigma^2_{\text{shift}} + S_{\text{signal}} + S_{\text{dark}} + \alpha^2_{\text{pr}}S^2_{\text{signal}}\right)} , \tag{2.4}$$

where $\sigma_{\text{conv,eff}} = \sigma_{\text{conv}}/M$ and α_{pr} denotes the relative pixel-to-pixel response variability.

2.3. Determining the number and positions of the atoms

The acquisition of fluorescence images of the atoms is typically performed at a lattice depth of $U/k_{\text{B}} = 0.4\,\text{mK}$, for which atom tunneling is negligible. The atoms are illuminated with a red-detuned three-dimensional optical molasses at $\lambda_{\text{f}} = 852\,\text{nm}$ which also provides continuous Doppler cooling and counteracts heating of the atoms. The EMCCD image is typically taken at an exposure time of 1 s. It provides a sampled intensity distribution $I_{\text{2D}}[x_i, y_j]$, where x_i and y_j denote the horizontal and vertical position of pixel $\{i, j\}$, respectively. The intensity distribution of a single atom trapped in the one-dimensional optical lattice shows a characteristic ellipticity, originating from the shape of the trapping potential, see Fig. 2.2(a): The atom is vertically confined to the lattice axis by the Gaussian profile of the laser beams width, whereas its horizontal position depends on the occupied lattice site. The vertical width of the fluorescence spot, i.e., perpendicular to the lattice axis, is primarily given by the spread of the thermal wave packet of the atom in radial direction of the standing wave potential. In axial direction, the atoms are strongly confined: The horizontal $1/\sqrt{e}$ half-width of the fluorescence spot, corresponding to $\sigma^{\text{hor}}_{\text{sp}} = (810 \pm 19)\,\text{nm}$ in the object plane, is mainly caused by diffraction within the imaging optics (with a theoretical value of $\sigma^{\text{hor}}_{\text{diff}} = 647\,\text{nm}$). Compared to this width, thermal motion of the atoms ($\sigma^{\text{hor}}_{\text{th}} = 23\,\text{nm}$) and drifts of the standing wave ($\leq 20\,\text{nm/s}$, see Sec. 2.3.5) can be neglected on the timescale of the exposure time.

To simplify the axial position determination, we bin the acquired intensity distribution vertically $I[x_i] = \sum_j I_{\text{2D}}[x_i, y_j]$, see Fig. 2.2(b). The resulting distribution is related to the unknown source distribution $S(x)$ by a convolution equation

$$I[x_i] = (L * S)[x_i] + \epsilon[x_i] , \tag{2.5}$$

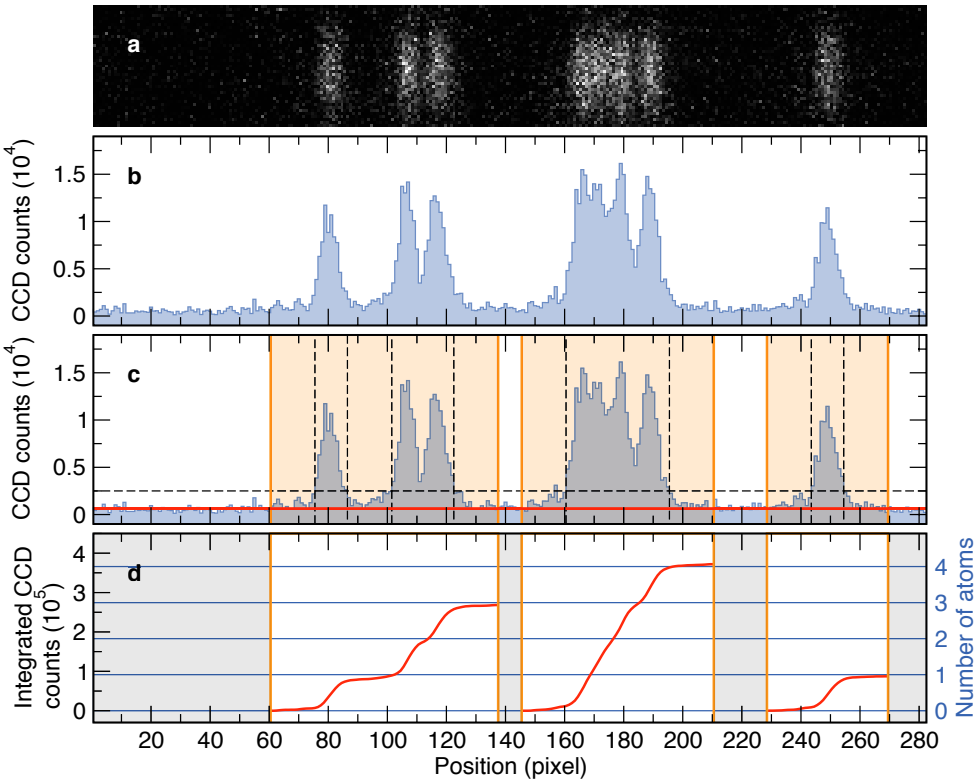

Figure 2.2.: (**a**) Image of atoms in a one-dimensional optical lattice acquired with 1 s exposure time. (**b**) The corresponding binned intensity distribution. (**c**) Segmentation of the binned intensity distribution into regions of interest (shaded regions) and estimation of the background baseline a_0 (horizontal solid line): vertical dashed lines indicate the unextended and unmerged regions in which the binned intensity distributions exceed the threshold (horizontal dashed line). (**d**) Cumulative integration of the binned intensity distribution in each ROI.

where $L(x) = (\delta * P_{\mathrm{2D}})(x)$ is the area normalized *Line Spread Function* (LSF) of our imaging optics (vertically binned PSF[7]), which is assumed to be analytically known and position-independent over the whole acquisition region, and $\epsilon[x_i]$ the additive noise with a variance $\mathrm{Var}(\epsilon[x_i]) = \sigma_i^2$.

The axial confinement of the atoms ($\sigma_{\mathrm{th}}^{\mathrm{hor}} \ll \sigma_{\mathrm{sp}}^{\mathrm{hor}}$) and systematical suppression of the stray light down to a homogeneous background allow us to model the unknown source distribution as

$$S(x) = a_0 + \sum_{j=1}^{N} a_j \delta(x - \xi_j)\,, \tag{2.6}$$

[7]The vertical binning of an continuous sampled 2D function can be mathematically expressed as a convolution with a 1D Dirac delta function $\delta(x)$.

where a_0 denotes the constant baseline of the stray light background, $\delta(x)$ the Dirac delta function representing the strongly confined atom, a_j and ξ_j the fluorescence contributions and the positions of N atoms, respectively.[8] Therefore, the position determination of the atoms in a one-dimensional lattice corresponds to a parameter estimation of the modeled distribution $S(x)$ from the measured intensity distribution

$$I[x_i] = a_0 + \sum_{j=1}^{N} a_j L(x_i - \xi_j) + \epsilon[x_i]\,. \tag{2.7}$$

2.3.1. Counting atoms in an optical lattice

The parametric deconvolution requires the number of parameters to be known, which are directly related to the number of atoms trapped in the optical lattice, see Eq. (2.6). So far, the number of atoms has been determined in the MOT by integrating the detected fluorescence signal in a given time interval and assuming that each trapped atom contributes to the total fluorescence signal by the same amount [46]. To determine the number of atoms in an optical lattice, the atoms have been transferred back to the MOT with a high efficiency [67]. This transfer, however, is destructive, removing the atoms from the optical lattice each time their number has to be determined. Even though the atoms can be retransferred to the optical lattice, their original distribution in the lattice cannot be restored. Thus, the position of the atoms is not maintained by this counting procedure.

In this work, I follow a different approach, reliably inferring the number of atoms directly from the fluorescence signal of atoms trapped in an optical lattice. Compared to atom counting in the MOT, this approach bears two significant advantages: Firstly, the position of the atoms in the optical lattice is not affected by the counting procedure. Furthermore, in combination with the parametric deconvolution, this approach allows a continuous monitoring of both, the number and positions of the atoms, providing a direct insight into the atom dynamics in the optical lattice. Secondly, the reliability to infer the correct number of atoms in the optical lattice is not affected by the transfer efficiency of the atoms between the MOT and the optical lattice. This advantage becomes significant for large numbers of atoms, where the transfer efficiency is reduced by light-induced collisions between the atoms [67]. In spite of all advantages, direct counting of atoms in an optical lattice imposes increasing requirements on the fluorescence detection, including high signal-to-noise ratio and suppression of signal distortion by the stray light. Furthermore, longer exposure times are required for a comparable counting reliability, due to a significantly smaller fluorescence signal of the atoms in an optical lattice compared to the signal of atoms trapped in a MOT.

[8] We define the atomic positions as the center of the thermal wave packets of the atoms.

Image segmentation

The determination of the number of atoms in an optical lattice is performed after a preceding step — the image segmentation. In the image segmentation, we divide the binned intensity distribution, sampled on a discrete interval J, into regions of interest which contain fluorescence from atoms and redundant regions which only contain background. Since parts of the parametric deconvolution are based on Fourier transforms (see Sec. 2.3.5), excluding noise from redundant regions allows us to improve both, the performance and accuracy of our numerical method. For this purpose, we track the regions of the binned intensity distribution exceeding a predefined threshold over a fixed range. The threshold is usually set to 20% of the height of the single atom intensity distribution; the width of the fixed range to half of the width of this distribution at the threshold level. Thresholding allows us to efficiently distinguish real fluorescence contribution of the atoms from possible noise spikes — the characteristic artifacts of the EMCCD detection, see inset of Fig. 2.9 in Sec. 2.3.6. This distinction becomes more relevant for images acquired with shorter exposure times (100–200 ms), e.g. used for the microwave spectroscopy (see Sec. 3.2.3), yielding a low signal-to-noise ratio. The regions exceeding the threshold are extended by a fixed width, which has been previously adjusted to incorporate fluorescence contributions of atoms in the wings of each atom's distribution. Finally, the regions are merged in case of overlap, see Fig. 2.2(c).

Counting of atoms

In the following, let K be the number of regions of interest obtained from an acquired image after the image segmentation. We label the binned intensity distributions of each region of interest (ROI) by the index $k = 1, \ldots, K$, namely $I_k[x_{k,i}]$. The same is done for each sampling interval defining the ROI, $J_k = \{x_{k,1}, \ldots, x_{k,M_k}\} \subset J$, consisting of M_k pixels with positions $x_{k,i}$. We estimate the background baseline a_0 by calculating the mean value of the intensity distribution within the redundant regions, $\{I[x_j] \,|\, x_j \in J \backslash \bigcup_k J_k\}$. For a more precise estimation, optionally the median instead of the mean value is used.[9] Note that this simplified baseline estimation assumes a homogeneous background level, being restricted to a sparely filled optical lattice and a truly homogeneous background.

For each ROI, we determine the number of atoms N_k by integrating the binned intensity distribution $I_k[x_{k,i}]$ above the background baseline a_0 over the corresponding interval J_k. Since each atom contributes equally, the cumulatively integrated distribution exhibits characteristic steps at integer multiples of the averaged single atom fluorescence contribution I_a, see Fig. 2.2(d). Therefore, the atom number for

[9] The noise distribution in low-intensity regions of the binned intensity distribution is positively skewed with outliers pulling the mean to a higher value (see Fig. 2.9 in Sec. 2.3.6) resulting in a small systematical error of the baseline a_0. This error can in principal be reduced using the median instead of the mean value, however, at the expense of performance of the estimation procedure.

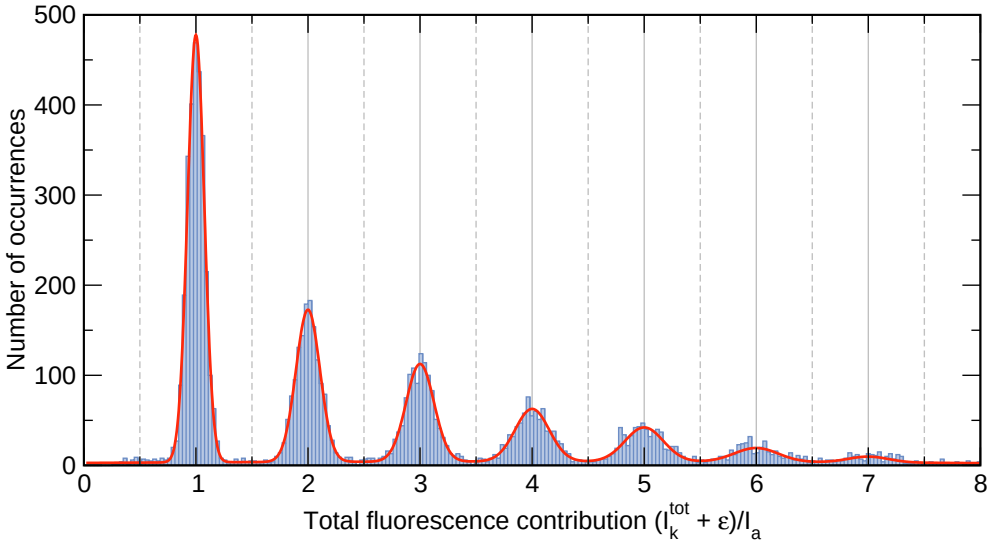

Figure 2.3.: Histogram of the total fluorescence contribution of the atoms I_k^{tot} calculated from the ROIs of approximately 6000 images, each acquired with an exposure time of 1 s. The integer numbers on the rescaled horizontal axis correspond to the number of atoms per ROI. The solid line shows a fit of Eq. (2.9) to the histogram.

each ROI is given by

$$N_k = I_k^{\mathrm{tot}}/I_{\mathrm{a}}\,, \text{ with } \quad I_k^{\mathrm{tot}} = \sum_{i=1}^{M_k} \left(I_k[x_{k,i}] - a_0\right)\,, \tag{2.8}$$

where I_k^{tot} denotes the total fluorescence contribution of the atoms for the kth ROI. The total number of atoms in the image is given by $N = \sum_k N_k$, accordingly.

The reliability and accuracy of the counting procedure strongly depends on the signal-to-noise ratio of the binned intensity distribution, being also affected by the spatial inhomogeneity of atom illumination and detector sensitivity or their fluctuations over the time. To determine the averaged single atom fluorescence contribution I_{a} and estimate the reliability of inferring the correct number of atoms in a ROI, we assume Gaussian distributions of the total fluorescence contributions I_k^{tot} around $\mu_{n\in\mathbb{N}} = nI_{\mathrm{a}} - \varepsilon$ and fit a sum of Gaussian functions

$$\widetilde{f}(x) = P_2(x) + \sum_{n=1}^{7} h_n e^{-(x-\mu_n)^2/(2\sigma_n^2)} \tag{2.9}$$

to the histogram of I_k^{tot} considering the ROIs of approximately 6000 images. The fit parameters h_n and σ_n in Eq. (2.9) denote the heights and the $1/\sqrt{e}$ half-widths (the standard deviations) of the Gaussians, respectively. A second-order polynomial $P_2(x) = b_0 + b_1 x + b_2 x^2$ with $P_2(x) \geq 0$ models the histogram background, arising

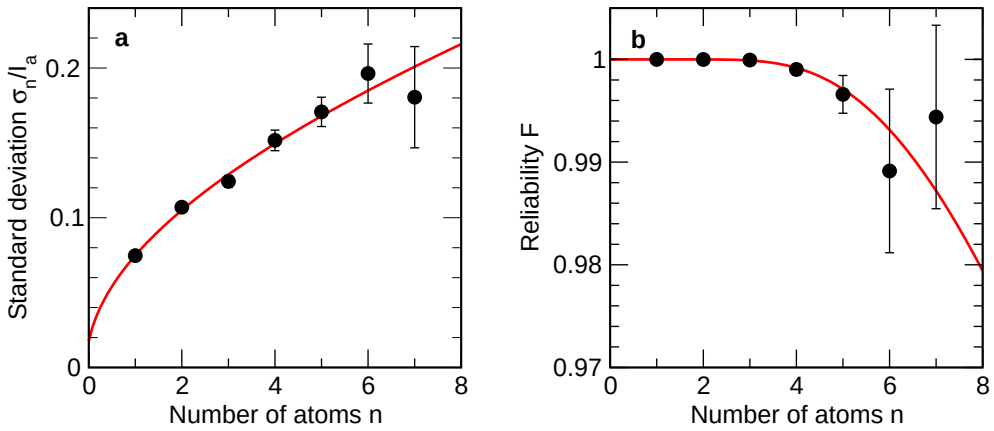

Figure 2.4.: (**a**) Standard deviation σ_n of the total fluorescence contribution for n atoms per ROI as inferred from Fig. 2.3. The solid line shows a fit of the model function $\widetilde{\sigma}(n)$ from Eq. (2.10). (**b**) Reliability of inferring the correct number of atoms in a ROI calculated from the standard deviations σ_n using Eq. (2.11). The solid line shows the reliability as obtained from the model function $\widetilde{\sigma}(n)$.

from fluorescence contributions of atoms which leave the optical lattice during the exposure time, and ε in μ_n compensates the systematic deviation resulting from the simplified estimation of the background baseline a_0 entering Eq. (2.8).

In Figure 2.3, a rescaled histogram of I_k^{tot} and the corresponding fit are shown. The histogram reveals a periodic structure with peaks centered at positive integers n corresponding to the number of atoms in a ROI. From this, we conclude that the model function in Eq. (2.9) and the calculation of the numbers of atoms using Eq. (2.8) is well supported. Using the median for the background baseline estimation, we obtain $\varepsilon/I_{\mathrm{a}} = (2.1 \pm 0.2)\%$ from the fit. This deviation is negligible and thus no sophisticated background baseline estimation is required.

The standard deviation σ_n of the total fluorescence contribution for n atoms per ROI follows a characteristic trend, reflecting the noise characteristics of the image acquisition, see Fig. 2.4(a). According to the noise model of Eq. (2.4), this trend can be modeled by the following function

$$\widetilde{\sigma}(n) = \sqrt{(c_{\mathrm{const}})^2 + \left(c_{\mathrm{sqrt}}\sqrt{n}\right)^2 + \left(c_{\mathrm{lin}}n\right)^2}, \tag{2.10}$$

considering the signal-independent noise contributions, the shot noise contributions ($\propto \sqrt{n}$), and noise contributions with linear signal dependency ($\propto n$). Note that the noise contributions are not directly related to the fit parameters c_{const}, c_{sqrt} and c_{lin}, since the number of atoms is calculated from a difference of the binned intensity signal with its background baseline a_0 which in turn both are affected by the noise. From a fit of the model function $\widetilde{\sigma}(n)$ to the standard deviations σ_n, we obtain $c_{\mathrm{const}}/c_{\mathrm{sqrt}} = 0.2^{+0.3}_{-0.2}$ and $c_{\mathrm{lin}}/c_{\mathrm{sqrt}} = 0.1^{+0.2}_{-0.1}$. Therefore, for small number of atoms per ROI ($n \leq 12$) the $\sqrt{n}$-contribution and thus the shot noise dominates.

In Section 2.3.6, we confirm this conclusion by a standardized and more precise analysis of the signal-noise relation.

The reliability of inferring the correct number of atoms n in a ROI can be deduced from the area of the corresponding (normalized) Gaussian distribution with a standard deviation σ_n within the distinguishability interval $[-I_\mathrm{a}/2, I_\mathrm{a}/2]$

$$F(\sigma_n) = \frac{1}{\sqrt{2\pi}\sigma_n} \int_{-I_\mathrm{a}/2}^{I_\mathrm{a}/2} e^{-x^2/(2\sigma_n^2)}\,\mathrm{d}x\,. \tag{2.11}$$

In Figure 2.4(b), the resulting reliabilities for n atoms per ROI are shown, calculated using the standard deviations σ_n and the model function $\widetilde{\sigma}(n)$, respectively. To estimate the reliability of inferring the correct number of atoms from Eq. (2.8), where in contrast to the definition in Eq. (2.11) the influence of the systematical deviation in the background baseline estimation ε is neglected, we shift the Gaussian distribution in Eq. (2.11) by ε and apply a second-order Taylor series approximation around $\varepsilon/I_\mathrm{a} \ll 1$

$$\begin{aligned}\widetilde{F}(\sigma_n) &= \frac{1}{\sqrt{2\pi}\sigma_n} \int_{-I_\mathrm{a}/2}^{I_\mathrm{a}/2} e^{-(x-\varepsilon)^2/(2\sigma_n^2)}\,\mathrm{d}x \\ &= F(\sigma_n) - \underbrace{\frac{1}{2\sqrt{2\pi}} \frac{I_\mathrm{a}^3}{\sigma_n^3} e^{-I_\mathrm{a}^2/(8\sigma_n^2)}}_{=:C(\sigma_n)} (\varepsilon/I_\mathrm{a})^2 + \mathcal{O}\left((\varepsilon/I_\mathrm{a})^4\right)\,. \end{aligned} \tag{2.12}$$

Since $|C(\sigma_n)| \leq 6\sqrt{6/(\pi e^3)} < 1.86$, for $\varepsilon/I_\mathrm{a} = (2.1 \pm 0.2)\%$ the deviation of $\widetilde{F}(\sigma_n)$ from $F(\sigma_n)$ is negligible ($< 10^{-3}$). Consequently, small systematic errors of the background baseline estimation marginally affect the counting reliability.

In most experiments presented in this work, relying on the determination of the atomic position and therefore on precise knowledge of the number of atoms, a small number of atoms is initially widely distributed over several sites of the optical lattice. This distribution provides images with several isolated ROIs, each containing at most eight atoms. Using the model function $\widetilde{\sigma}(n)$ in Eq. (2.10) a lower limit for the reliability of $F(\widetilde{\sigma}(n \leq 8)) \geq 98\%$ is deduced. The reliability of inferring the total number of atoms within the image is then given by $F(N) = \prod_k F(\widetilde{\sigma}(N_k))$.

2.3.2. Determining the line spread function with sub-pixel accuracy

The analytical description of the LSF constitutes one of the most important prerequisite of the parametric deconvolution. Although, in principle, the measured intensity distribution of an isolated atom yields information on the LSF, a single image does not provide the required resolution and accuracy due to noise and the limited EMCCD resolution. To overcome these limits, we use a method which allows us to reconstruct the LSF with sub-pixel accuracy by simultaneously reducing

the influence of the noise. The additional information content required by the reconstruction process is obtained by considering the intensity distributions of up to hundred of single isolated atoms.

In the following, we assume K binned intensity distributions $I_k[x_{k,i}]$ with $k = 1, \ldots, K$ of images with one isolated atom each. The ROIs are defined by $J_k = \{x_{k,1}, \ldots, x_{k,M}\} \subset J$, each comprising M pixels separated by the pixel distance Δ. The width of each ROI, $M\Delta$, is chosen in such a way that the fluorescence contribution of the atom is completely contained in this region with sufficiently large space on either side. Note that, although the width of the ROI is equal for all considered distributions, the position of the region can vary from image to image. Unless otherwise noted, all positions, distances and derivatives are expressed in length units of CCD pixels in the detection plane ($\Delta = 1\,\text{pixel}$), as originally obtained from the acquired images. The conversion factor to infer the dimensions in the object plane in a standard unit (meter) is determined in Sec. 2.4.2.

Let $L(x)$ be an initial model of the area normalized LSF, which, being amplitude scaled and offset shifted, roughly approximates the shape of the intensity distribution of a single atom, e.g. a Gaussian function. From the fit to each of the sampled single atom intensity distributions $I_k[x_{k,i}]$, we determine the position of the isolated atom ξ_k by minimizing

$$\min_{\{a_k,\xi_k,b_k\}} \sum_{i=1}^{M} \left\{ a_k L(x_{k,i} - \xi_k) + b_k - I_k[x_{k,i}] \right\}^2 , \tag{2.13}$$

where a_k denotes the fluorescence contribution of the atom and b_k the background baseline. Note that ξ_k is not restricted to the sampling points, taking any value within $J_k^{\mathrm{c}} = [x_{k,1}, x_{k,M}]$. An approximation of the continuously sampled representation $I_k(x)$ in J_k^{c} relying on the discretely sampled data $I_k[x_{k,i}]$ can be written as

$$I_k(x) = \sum_{i=1}^{M} I_k[x_{k,i}] R_\Delta(x - x_{k,i}) \tag{2.14}$$

with the rectangular function

$$R_\Delta(x) = \begin{cases} 1 & \text{for} -\Delta/2 < x \leq \Delta/2\,, \\ 0 & \text{else.} \end{cases} \tag{2.15}$$

We superimpose the continuously sampled representations of all considered single atoms intensity distributions as follows

$$\tilde{I}(x) = \frac{1}{K} \sum_{k=1}^{K} I_k(x - \xi_k)\,. \tag{2.16}$$

The resulting distribution $\tilde{I}(x)$ is centered at $x = 0$. It represents the mean single atom distribution in the interval $\tilde{J}^{\mathrm{c}} = [-d, d]$ with $d = \min_k\{\xi_k - x_{k,1}, x_{k,M} - \xi_k\}$.

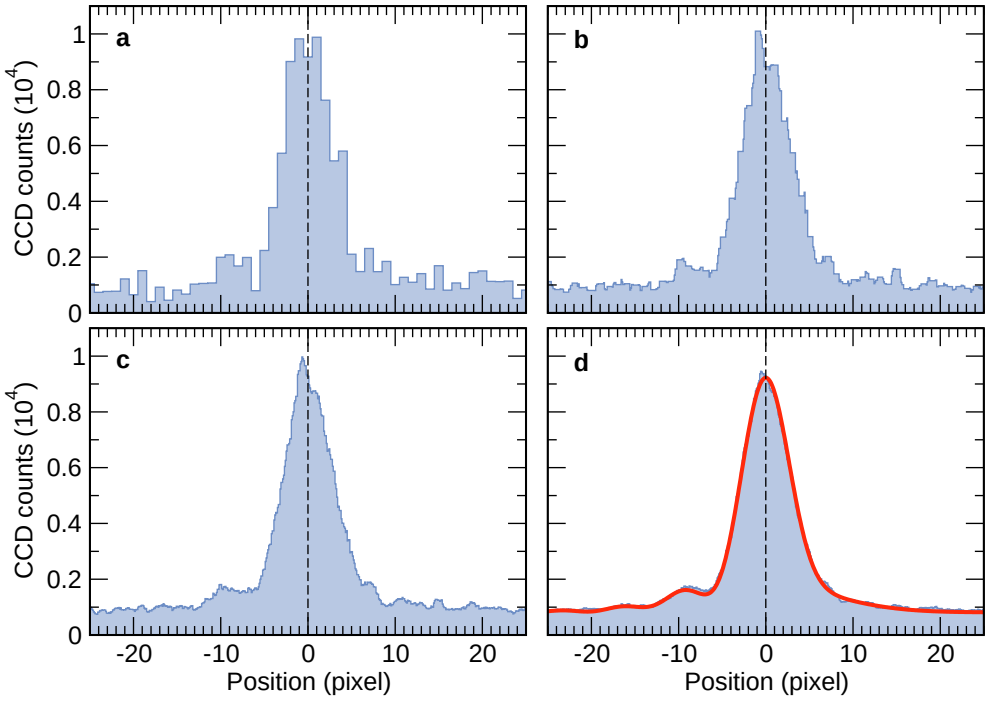

Figure 2.5.: Determination of the line spread function from intensity distributions of isolated atoms with sub-pixel accuracy. (**a**) Intensity distribution of an isolated atom. Superimposed intensity distribution with sub-pixel accuracy (1/10 pixel) of 5 (**b**), 10 (**c**) and 50 (**d**) isolated atoms. The solid line in (**d**) shows the fit of Eq. (2.13), indicating the accuracy of the self-consistent LSF model.

We resample $\tilde{I}(x)$ on a $s \in \mathbb{N}_{>1}$ times denser grid $\tilde{J} = \{\tilde{x}_1, \ldots, \tilde{x}_{sM}\}$ calculating $\tilde{I}[\tilde{x}_j] = \tilde{I}(\tilde{x}_j)$. The distance between the new sampling points is then given by $\tilde{\Delta} = \Delta/s$. For sufficiently large number of considered intensity distributions ($K > s$), an intensity distribution with sub-pixel accuracy is obtained, while the noise is simultaneously reduced by a factor of $\sqrt{K}$, see Fig. 2.5(d). This reconstruction procedure allows us to increase the sampling resolution in a controlled way. The only arbitrariness entering the procedure arises from the initially modeled approximation of the LSF. To successively eliminate this arbitrariness, we use a self-consistency loop, which iteratively improves the modeled LSF until convergence is reached: Based on the sub-pixel sampled and noise-reduced intensity distribution $\tilde{I}[\tilde{x}_j]$ in $\tilde{J}$, we construct an improved model for the LSF $\tilde{L}(x)$, determine its model parameters from a fit, and successively repeat the previous reconstruction procedure with $\tilde{L}(x)$ instead of $L(x)$ until self-consistency is reached. Since in each iteration of the self-consistency loop, the model of the LSF and thus the accuracy of determining the atom positions ξ_k is improved, the reliability of the reconstruction procedure is increased and the arbitrariness is successively eliminated. The self-consistency loop

converges within few iterations resulting in a precise analytical model of the LSF. This model is based on the more resolved data, the higher the factor s is chosen, and is the more accurate, the more sampled intensity distributions (higher K) are considered.

2.3.3. Determining the isoplanatic patch

The isoplanatic patch denotes a region, where the LSF of the optical system is shift-invariant, fulfilling a mandatory requirement for the convolution representation of the imaging process. Therefore, high accuracy and reliability of the parametric deconvolution can only be expected in this region. To determine the isoplanatic patch of our imaging system, we reconstruct the imaged intensity distribution of an isolated atom for different detection regions with sub-pixel accuracy (see Sec. 2.3.2), for each considering more than 50 successively acquired images. For each sub-pixel resolved distribution $\tilde{I}_n[\tilde{x}_j]$, we determine the height h_n and the area A_n in an interval of equal width, large enough to contain the detected fluorescence signal of the atom.[10] The area corresponds to the detected energy fraction (fluorescence and background), reflecting spatial deviations due to inhomogeneous illumination or detector sensitivity, or obstructions by the apertures of the stray light trap. Assuming the area to be constant over the whole detection region, the height of the distribution is directly related to the Strehl ratio (see Sec. 2.3.4), revealing shift-variance of aberrations affecting the shape of the inferred LSF. Higher values of h_n indicate less aberrations resulting in a better resolution.

In Figure 2.6, the resulting intensity distributions for different positions in the detection region and the relative deviations of the corresponding areas and heights from a maximum (optimum) value are shown ($|A_n - A_{\max}|/A_{\max}$ and $|h_n - h_{\max}|/h_{\max}$ with $A_{\max} = \max\{A_n | n = 1, \ldots, N\}$ and $h_{\max} = \max\{h_n | n = 1, \ldots, N\}$). The distributions in Fig. 2.6(a-f) reveal a characteristic shape, consisting of a central peak with sinc^2-like features to the left and a smooth decay to the right. The sinc^2-like features are gradually suppressed close to the borders of the detection region, while the distribution becomes smaller and broader, reflecting degradation of the LSF in these regions, see Fig. 2.6(g,h) and rather weakly Fig. 2.6(a). This degradation is quantitatively visible in the relative areas and heights. Small fluctuations of the area in the central detection region indicate inhomogeneous illumination or detector sensitivity, whereas a significant increase of the deviation close to the right border arises from obstructions by the apertures of the stray light trap. Even though the apertures have been aligned with respect to minimize this effect, a trade-off has been made between the distortion by the stray light and obstructions by the apertures. The relative deviation of the heights reveal a similar trend, almost following the corresponding areas except for a striking deviation close to the right border of the detection region. This deviation most likely arises from field curvature wavefront aberrations, since no deliberate correction of these aberrations has been incorpo-

[10] Note that we determine the area and the height with respect to the zero line, consciously allowing the signal background to affect both parameters.

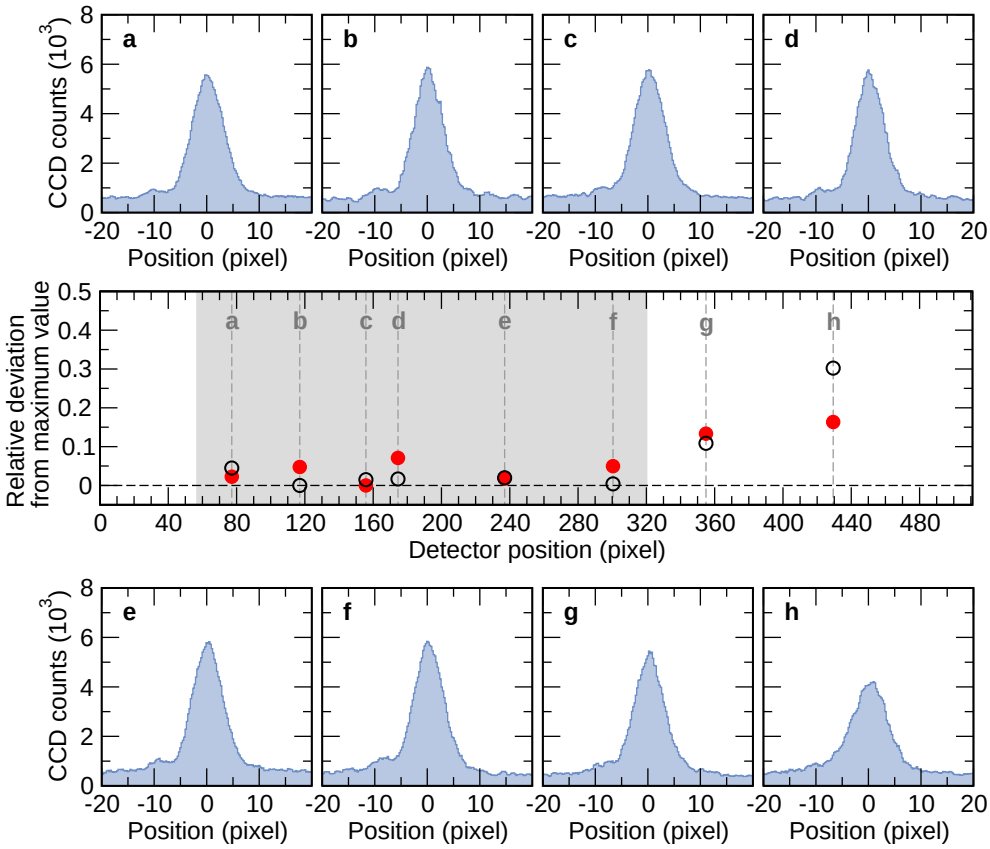

Figure 2.6.: Sub-pixel resolved intensity distributions of an isolated atom at different detector positions (**a**)-(**h**)). From each distribution the area and the height is determined. Solid circles in the central plot indicate the relative deviation of the area from a maximum determined value; open circles, the relative deviation of the height from a maximum value. The shaded region indicates the isoplanatic patch.

rated in the lens design of the objective [90]. From this analysis, we finally infer the position of the isoplanatic patch and its width of 262 pixels (51% of the detection region) corresponding to 77 μm in the object plane (178 lattice sites).

Finally, we model the LSF of the isoplanatic patch, using the method described in Sec. 2.3.2, considering all single atom distributions measured in this region. The resulting shape of LSF can be analytically described by

$$L(x) = \begin{cases} \frac{1}{c_0}\left[c_1 e^{-x^2/(2c_2^2)} + \mathrm{sinc}^2\left(c_3 x\right)\right], & \text{if} \quad x < 0 \\ \\ \frac{1}{c_0}\left[c_1 e^{-x^2/(2c_2^2)} + e^{-x^2/(2c_3^2)}\right], & \text{if} \quad x \geq 0\,. \end{cases} \tag{2.17}$$

where the parameters c_1, c_2 and c_3 are determined from a constrained fit, which

ensures the twice continuously differentiability required by the parametric deconvolution (see Sec. 2.3.5), whereas c_0 normalizes the area of the LSF. The model function in Eq. (2.17) is mainly based on the theoretical LSF of a diffraction-limited objective, being well approximated by a sum of a sinc^2-function and a Gaussian function. The piecewise definition incorporates the asymmetry of the measured LSF arising from coma-type aberrations which among others strongly affect the optical resolution, see Sec. 2.3.4. This model, being scaled and offset shifted, fits well to all sub-pixel reconstructed single atom distributions in the isoplanatic patch. For high accuracy of the parametric deconvolution, especially in determining atom separations beneath the Rayleigh criterion, the LSF has to be reestimated prior the image analysis. This does not necessarily need to be done in a preliminary measurement, if real-time deconvolution is not required. In general, each set of images contains a sufficient number of images with well-isolated atoms, allowing to determine the LSF afterwards for a post-analysis of the data. It turns out that the model parameters in Eq. (2.17) do not significantly change over several months when the objective is only refocused from time to time.

2.3.4. Characterizing the line spread function

Determining the LSF with sub-pixel accuracy enables us a precise quantitive analysis of our optical system, which can be used to identify its imperfections and infer the resulting limits of optical resolution. For this purpose, we introduce the *Optical Transfer Function* (OTF) which is commonly used as an international measuring standard to characterize the image quality of an optical system. The OTF is defined as the Fourier transform (FT) of the area normalized PSF [86], $H_{\mathrm{2D}}(u,v) := \mathrm{FT}\left\{P_{\mathrm{2D}}(x,y)\right\}$, and therefore directly related to the area normalized LSF by

$$H(u) := H_{\mathrm{2D}}(u, v=0) = \mathrm{FT}\left\{\delta(x) * P_{\mathrm{2D}}(x,y)\right\} = \mathrm{FT}\left\{L(x)\right\} . \tag{2.18}$$

The magnitude of this complex function of real variables, $M_{\mathrm{2D}}(u,v) := |H_{\mathrm{2D}}(u,v)|$ ($M(u) = M_{\mathrm{2D}}(u, v=0)$), is referred to as the *Modulation Transfer Function* (MTF), the phase as the *Phase Transfer Function*, accordingly. The MTF is also known as spatial frequency response which describes the ratio of modulation, e.g. of a sinusoidal intensity test pattern, leaving to that entering the optical system over the range of frequencies of interest. It is thus directly related to the resolution and the contrast properties of the optical system. A further commonly used characteristic quantity is the *Strehl Ratio* (SR), which compares the measured MTF of an optical system to that of an optimum, diffraction-limited system $M_{\mathrm{opt}}(u)$

$$\mathrm{SR} = \frac{\int M(u)\mathrm{d}u}{\int M_{\mathrm{opt}}(u)\mathrm{d}u} = \frac{L(0)}{L_{\mathrm{opt}}(0)} . \tag{2.19}$$

The Strehl ratio is directly related to waveform aberrations of an optical system [97], providing a quantitative measure of the imaging quality.

The advantage of analyzing the imaging system in the Fourier domain arises from the convolution theorem, providing that the OTF of a composite optical system is given by the product of OTFs of the subsystems [86]. The same holds for the MTF. For the imaging system presented in Sec. 2.2.1, the overall OTF can be written as

$$H(u) = H_{\mathrm{obj}}(u) H_{\mathrm{det}}(u)\,, \tag{2.20}$$

where $H_{\mathrm{obj}}(u)$ denotes the OTF of the objective, including possible defocusing, and $H_{\mathrm{det}}(u)$ the OTF of the detector. The latter incorporates the shape and the size of the detector and the sampling grid, detector specific properties for diffusion and charge transfer efficiency (for details see Ref. [98]). By restricting the analysis to the isoplanatic patch (see Sec. 2.3.3), the influence of the apertures forming the stray light trap can be neglected. The same holds for the optical narrow-band filter.

Incorporate atomic motion

For a diffraction-limited objective with a circular entrance pupil, the theoretical one-dimensional defocused OTF ($v = 0$) can be approximated by [99]

$$\begin{aligned} H_{\mathrm{obj}}^{\mathrm{dif}}(u, \Delta z) \;=\; & \frac{4}{\pi a} \cos\left(\frac{ab}{2}\right) \\ & \times \left\{ \beta J_1(a) + \sum_{n=1}^{\infty} (-1)^{n+1} \frac{\sin(2n\beta)}{2n} [J_{2n-1}(a) - J_{2n+1}(a)] \right\} \\ & - \frac{4}{\pi a} \sin\left(\frac{ab}{2}\right) \\ & \times \sum_{n=0}^{\infty} (-1)^{n} \frac{\sin((2n+1)\beta)}{2n+1} [J_{2n}(a) - J_{2n+2}(a)]\,, \end{aligned} \tag{2.21}$$

with $a = 4\pi w b$, $b = 2|u|/u_{\mathrm{c}}$, the maximum wavefront difference $w \approx \mathrm{NA}^2 \Delta z/(2\eta)$,[11] $\beta = \arccos(|u|/u_{\mathrm{c}})$, where $u_{\mathrm{c}} = 2\mathrm{NA}/\lambda_{\mathrm{f}}$ denotes the cut-off frequency, λ_{f} the wavelength of fluorescence light, η the diffraction index, Δz the defocus amount and $J_n(x)$ the nth order Bessel function of the first kind. Since the series in Eq. (2.21) converge slowly [100], it is convenient to apply a further approximation as proposed in Ref. [101], resulting in

$$H_{\mathrm{obj}}^{\mathrm{dif}}(u, \Delta z) = \begin{cases} \dfrac{1}{\pi}(2\beta - \sin\beta)\,\mathrm{jinc}\left[\dfrac{8\pi w}{\lambda}\left(1 - \dfrac{|u|}{u_{\mathrm{c}}}\right)\dfrac{|u|}{u_{\mathrm{c}}}\right] & \text{for } u \le u_{\mathrm{c}}\,, \\ 0 & \text{for } u > u_{\mathrm{c}}\,, \end{cases} \tag{2.22}$$

[11] The maximum wavefront difference is usually geometrically derived and discussed in the image space, see Ref. [100]. Treating the microscope as a thick lens and following Refs. [99, 100], assuming the amount of defocus being small, we infer a relation for the maximum wavefront differences which is completely characterized by the parameters in the object space.

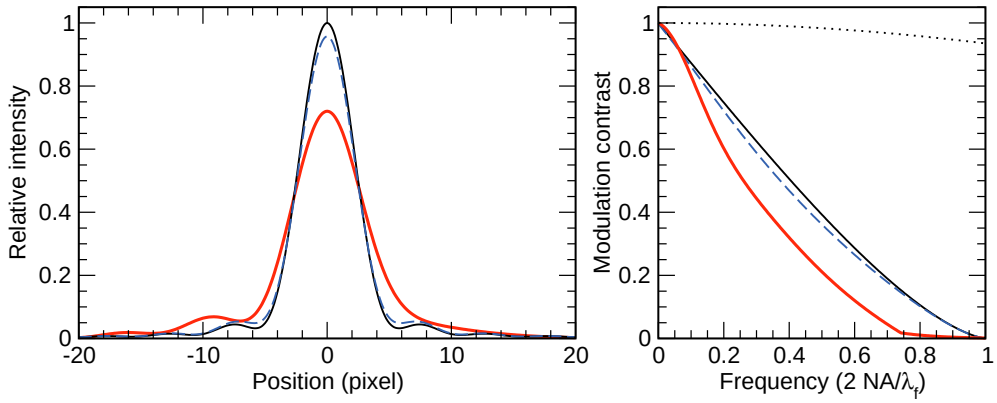

Figure 2.7.: (**a**) Theoretical, diffraction-limited line spread function (LSF) of the microscope objective without ($L^{\mathrm{dif}}_{\mathrm{obj}}(x)$, solid thin line) and with incorporating the radial motion of the atoms ($\tilde{L}^{\mathrm{dif}}_{\mathrm{obj}}(x)$, dashed thin line). The solid thick line shows the experimentally determined LSF $L(x)$ modeled from the sub-pixel resolved intensity distribution of a single atom. For comparison, all area normalized LSF are scaled by $1/L^{\mathrm{dif}}_{\mathrm{obj}}(0)$ to directly reveal the Strehl ratio from the value at zero position, see Eq. (2.19). (**b**) The corresponding modulation transfer functions (MTFs). The dotted line shows the MTF of the detector in the region set by the cut-off frequency $u_{\mathrm{c}} = 2\mathrm{NA}/\lambda_{\mathrm{f}}$ of the optical system.

where $\mathrm{jinc}(x) = 2J_1(x)/x$. This approximation has been experimentally proven [102] to yield sufficiently good results for our purpose.

In the ideal case, assuming the atoms being strongly confined in the radial direction of the one-dimensional optical lattice in the focal plane, the theoretical OTF is given by

$$H^{\mathrm{dif}}_{\mathrm{obj}}(u, \Delta z = 0) = \begin{cases} \frac{2}{\pi}(\beta - \sin\beta) & \text{for } u \leq u_{\mathrm{c}}\,, \\ 0 & \text{for } u > u_{\mathrm{c}}\,. \end{cases} \tag{2.23}$$

The corresponding LSF and MTF are shown in Fig. 2.7. However, taking the radial motion of the atoms into account by averaging Eq. (2.22) weighted with the spread distribution of the thermal wave packet in radial direction of the one-dimensional lattice, $P_{\mathrm{rad}}(z)$, the OTF of a diffraction-limited objective imaging radially oscillating atoms can be calculated by

$$\tilde{H}^{\mathrm{dif}}_{\mathrm{obj}}(u) = \int_{-\infty}^{\infty} P_{\mathrm{rad}}(z) H^{\mathrm{dif}}_{\mathrm{obj}}(u, z)\,\mathrm{d}z\,. \tag{2.24}$$

For our system, the radial motion of the atoms decreases the Strehl ratio to SR = 0.96, corresponding to a peak-valley wavefront distortion of $\lambda_{\mathrm{f}}/9$ (see Ref. [97]). The corresponding LSF and MTF, imposing the intrinsic limit of our fluorescence imaging, are shown in Fig. 2.7. Both functions reveal only small discrepancies, compared to the case of radially confined atoms: For the MTF, we deduce a maximum relative deviation of 8% at $u \approx u_{\mathrm{c}}/2$. Note that, even if the degradation of

the imaging quality due to the radial motion of the atoms is small for our setup, its influence on the Strehl ratio becomes more dominant for objectives with higher numerical apertures. This fact needs to be considered in upgrading or replacing the present microscope objective in the future.

The effect of detector sampling and magnification

To estimate the OTF of the detector, we assume that the whole rectangular pixel of the *effective* pixel width Δ, incorporating the magnification factor, responds uniformly to the incident light, neglecting diffusion and charge transfer efficiency. The OTF of the detector is than given by [98]

$$H_{\mathrm{det}}(u) = \mathrm{sinc}(\pi\Delta \cdot u)\,. \tag{2.25}$$

The corresponding MTF, $M_{\mathrm{det}}(u)$, is shown in Fig. 2.7. From $M_{\mathrm{det}}(u) \geq 0.94$ for $u \leq u_{\mathrm{c}}$ with u_{c} being the cut-off frequency of the optical system, we deduce that for the given magnification, the resolution of the imaging setup is not limited by the sampling of the detector. Moreover, the effect of the detector on the overall OTF and MTF, and thus on the SR of the imaging system is negligible. Note that, even though increasing the magnification of the imaging system does not affect the optical resolution, the sampling resolution can in principle be improved. The latter plays a decisive role in the success of numerical post-processing of the acquired images. However, there is an upper limit for improving the sampling by magnification. This limit is exceeded, if the number of incident photons per pixel is so small that the resulting signal is indistinguishable from statistical fluctuations or detection noise.

MTF of the imaging system and resolution limit

The MTF of the imaging system is calculated from the self-consistent model of the LSF of Eq. (2.13) fitted to the sub-pixel resolved, binned intensity distributions in the isoplanatic patch, see Sec. 2.3.3. In Figure 2.7, the LSF and the resulting MTF are shown together with the corresponding theoretical, diffraction-limited counterparts. The measured LSF reveals a significant asymmetry, characteristic for coma-type aberrations: Pronounced sinc^2-like features on the one side of the central peak and a smeared out tail on the other side, both indicate that the binning of the image is performed perpendicular to the plane of the aberration axis. Therefore, the imaged atoms are most likely not in line with the optical axis of the objective in the horizontal plane along the optical lattice axis. From the well-pronounced sinc^2-like features, we deduce that spherical aberrations or possible defocusing play a minor role. The MTF also reveals a strong degradation of the imaging system, providing a reduced modulation contrast almost over the whole frequency range. The resulting Strehl ratio of 0.72 corresponds to a peak-valley wavefront distortion of $(3/10)\lambda_{\mathrm{f}}$. This distortion is higher than the expected value of $\lambda_{\mathrm{f}}/4$, measured with

the share-plate interferometer [77, 78]. However, it should be noted that the share-plate measurement has been performed on a separated compact setup, allowing an easier alignment and thus avoiding coma-type aberrations.

Finally, we use the measured LSF to infer the limit of optical resolution, employing the contrast of two atoms with equal fluorescence contribution, separated by a distance d, as a characteristic quantity. The contrast is defined by $C = (I_{\max} - I_{\min})/(I_{\max} + I_{\min})$, where $I_{\max}$ denotes the maximum intensity of the binned intensity distribution and $I_{\min}$ the minimum intensity occurring in the region between the atoms. According to the Rayleigh criterion [87], the minimum distance resolved by a diffraction-limited objective is given by $d_{\min} = 0.61\lambda_{\mathrm{f}}/\mathrm{NA}$, yielding a minimum contrast of $C_{\min} \approx 19\%$. This distance corresponds to a minimum resolvable separation of four optical lattice sites. For the measured LSF, the minimum contrast is exceeded for distances larger than five lattice sites. Hence, in both cases the optical resolution is far beyond the requirements to resolve two atoms on neighboring or even next-nearest neighbor sites. Therefore, numerical post-processing is essential to overcome the resolution limit imposed by the imaging system.

2.3.5. Parametric deconvolution

To determine the positions of the atoms, we use a deconvolution method related to the spike-convolution model fitting presented in Ref. [103]. This method is restricted to a particular class of signals, including the modeled unblurred distribution of the atoms $S(x)$ in Eq. (2.6). It uses a trigonometric moment estimation to roughly estimate the parameters in Eq. (2.7). We use this estimation procedure to calculate an initial guess for a subsequently applied, iterative maximum likelihood estimation method — the Levenberg-Marquardt fitting algorithm [104, 105].

In the following, for the sake of convenience, we consider a binned intensity distribution $I[x_l]$ of a single ROI defined by the interval $J = \{x_1, \ldots, x_M\}$ which consists of an *even* number M of equally spaced pixels. The distance between neighboring pixels is given by Δ, the width of the ROI by $M\Delta$, accordingly. The number of atoms N within the ROI is determined using the counting procedure presented in Sec. 2.3.1.

We assume the LSF to be analytically known, twice continuously differentiable and have a finite support in $[-\beta, \beta]$, where $\beta = M\Delta/2$, with no hole in the corresponding Fourier transform. This assumption ensures that the Fourier coefficients of the LSF

$$\hat{v}_j = \frac{1}{2\pi} \int_{-\beta}^{\beta} L(x)\, e^{ij\pi x/\beta} \mathrm{d}x\,, \tag{2.26}$$

calculated for $j = 0, \ldots, N$, do not vanish.

The connection between the trigonometric moments and the parameters of the signal $S(x)$ in Eq. (2.6) is given by the spectral structure of the Toeplitz matrix

constructed from the Fourier coefficients of the binned intensity distribution $I[x_l]$:

$$\hat{f}_j = \frac{1}{M} \sum_{l=1}^{M} I[x_l] e^{ij\mathcal{T}(x_l)} \,, \tag{2.27}$$

where the transformation $\mathcal{T} : [x_1, x_M] \to [-\pi, \pi]$, $x \mapsto \mathcal{T}(x) = -\pi + \pi(x - x_1)/\beta$ is used. Using the Fourier coefficients from Eq. (2.26) and (2.27), we calculate $\hat{g}_0 = \hat{f}_0$, $\hat{g}_j = \hat{f}_j \hat{v}_0 / \hat{v}_j$ and $\hat{g}_{-j} = \hat{g}_j^*$ for $j = 1, \ldots, N$. It can be shown by direct calculation that $\hat{g}_j$ are the Fourier coefficients of the unknown signal $S(x)$.

We construct the Toeplitz matrix $\hat{G}_N = (\hat{g}_{m-j})_{j,m=0,\ldots,N}$, compute its smallest eigenvalue which corresponds to the (local) background baseline a_0 in Eq. (2.6) and the corresponding eigenvector $\alpha = (\alpha_0, \ldots, \alpha_N)$, see Ref. [103] and references therein. By solving the polynomial equation

$$\prod_{j=1}^{N} (z - e^{i\tau_j}) = \sum_{j=0}^{N} \alpha_j z^j = 0 \,, \tag{2.28}$$

we determine the N distinct roots on the unit cycle, which we denote as $\{e^{i\tau_j} \,|\, j = 1, \ldots, N\}$. From the latter, we directly obtain the trigonometric moment estimates of the atomic positions $\xi_j = \mathcal{T}^{-1}(\tau_j)$, using the inverse transformation $\mathcal{T}^{-1} : [-\pi, \pi] \to [x_1, x_M]$, $x \mapsto \mathcal{T}^{-1}(t) = x_1 + \beta(t + \pi)/\pi$.

After estimating the atomic positions, we determine the fluorescence contributions of each atom a_j by a *linear* least squares method based on Givens decomposition, minimizing

$$\min_{\{a_j \,|\, j=1,\ldots,N\}} \sum_{l=1}^{M} \left\{ I[x_l] - a_0 - \sum_{j=1}^{N} a_j L(x_l - \xi_j) \right\}^2 . \tag{2.29}$$

Note that at this stage, the additive noise in Eq. (2.7) is not explicitly considered, e.g. by additional weighting in Eq. (2.29).

Although the trigonometric moments estimation method is fast, it suffers from a lower accuracy compared to the commonly used iterative non-linear maximum likelihood minimization algorithms, including the Gauss-Newton [106] or the more robust Levenberg-Marquardt [104, 105] algorithm. The convergence of the latter, however, strongly depends on the initial guess, which in the ideal case has to be close to the final solution. For this reason, we combine the trigonometric moment estimation and the iterative minimization algorithm, combining the advantages of both methods. We subsequently improve the estimated parameters a_0, a_k and ξ_k using them as an initial guess in a Levenberg-Marquardt fitting algorithm, minimizing

$$\min_{\{a_0, a_j, \xi_j \,|\, j=1,\ldots,N\}} \sum_{l=1}^{M} \frac{1}{\sigma_l^2} \left\{ I[x_l] - a_0 - \sum_{j=1}^{N} a_j L(x_l - \xi_j) \right\}^2 , \tag{2.30}$$

where at this stage, we optionally consider the noise $\epsilon[x_l]$ by weighting the fitted data with $\sigma_l^2 = \mathrm{Var}(\epsilon[x_l])$.

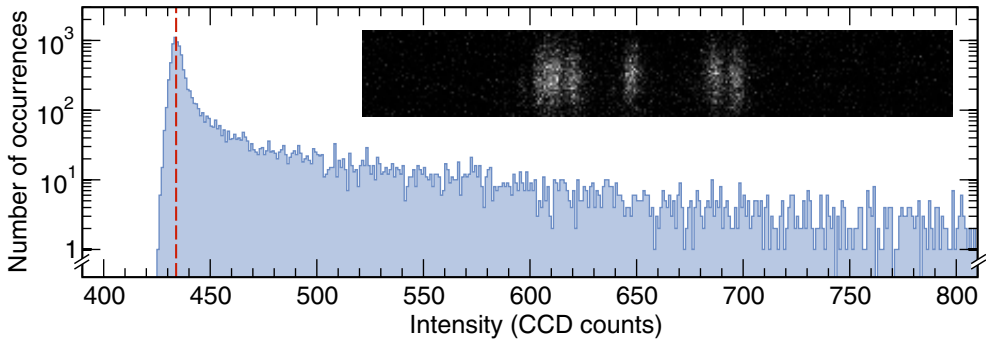

Figure 2.8.: Estimation of the digitizer offset from the intensity histogram of an acquired image (inset). The digitizer offset value corresponds to the position of the maximum value in the histogram (vertical dashed line).

2.3.6. Inferring the signal-noise relation

In general, the performance and accuracy of parameter estimation using the Levenberg-Marquardt algorithm is increased by weighting the data points according to the errors (see Eq. (2.30)), which in our case, arise from the detection noise. The noise model is well known (see Sec. 2.2.2), assigning detection noise to an originally *clean* signal. The model parameters still need to be determined to infer a signal-noise relation which enters the Levenberg-Marquardt algorithm. However, it is inherently impossible to determine a clean signal from a single noisy image. Therefore, even knowing the signal-noise relation, a small systematical error in the wighting of the data points has to be accepted.

In the following, we present a statistical method based on the analysis of several hundred of images, which allows us to estimate the noise level to a set of intensity levels of the binned intensity distributions rising above the background baseline (fluorescence signal). For signals much larger than noise, this method has been confirmed by simulations to provide a good approximation of the signal-noise relation. To cover the full signal range, we extend the noise estimation to signals falling below the background baseline, using a standard method which infers the noise from uniform intensity distributions for different mean intensity levels. Finally, we estimate the lower noise limit, imposed by the conversion noise of the readout process, from a statistical model. From a fit of the noise model of Eq. (2.4) to the set of signal and noise values, we finally infer an analytical expression of the signal-noise relation.

Estimating noise for signals above the background baseline

To infer the signal-noise relation above the background baseline, we consider a set of successively acquired images of the same atom distribution (with the typical exposure time of 1 s) of, on average, four atoms loaded into the optical lattice. We

adjust the intensity distribution $I_{\mathrm{2D}}[x_i, y_j]$ of each image for digitizer offset[12] by pixel-wise subtracting its value b_{offset}

$$\mathcal{I}_{\mathrm{2D}}[x_i, y_j] = I_{\mathrm{2D}}[x_i, y_j] - b_{\mathrm{offset}} \,. \tag{2.31}$$

The offset value is estimated from an intensity histogram of each image separately, thereby eliminating the effects of offset fluctuations over time. It corresponds to the position of the maximum value in the histogram (see Fig. 2.8), assuming that most pixels in the detection area do not accumulate any photoelectrons and the amount of dark electrons is negligible during exposure.

Let $\mathcal{I}^{(1)}_{\mathrm{2D}}[x_i, y_j]$ and $\mathcal{I}^{(2)}_{\mathrm{2D}}[x_i, y_j]$ be two offset-adjusted intensity distributions of successively acquired images of the same atom distribution. From both distributions, we calculate the pixel-wise average using

$$\bar{\mathcal{I}}_{\mathrm{2D}}[x_i, y_j] = \frac{1}{2}\left(\mathcal{I}^{(1)}_{\mathrm{2D}}[x_i, y_j] + \mathcal{I}^{(2)}_{\mathrm{2D}}[x_i, y_j]\right) \,. \tag{2.32}$$

The resulting distribution roughly approximates the clean intensity signal. Note that the accuracy of this approximation can in principle be increased by calculating the average from significantly more than two images. However, we intentionally restrict the analysis to two images for two reasons: First, due the limited storage time of the atoms in the optical lattice, the probability to acquire a high number of images of the same (stationary) atom distribution is low, especially for distributions comprising a high number of atoms. Second, we have checked by simulations that for signals much larger than noise the two-image approximation of the clean signal already provides accurate results using the statistical method described below.

The squared noise assigned to the clean signal is inferred from the squared standard deviation of both initial intensity distributions using the average

$$\begin{aligned}\sigma^2_{\mathrm{2D}}[x_i, y_j] &= \left(\mathcal{I}^{(1)}_{\mathrm{2D}}[x_i, y_j] - \bar{\mathcal{I}}_{\mathrm{2D}}[x_i, y_j]\right)^2 + \left(\mathcal{I}^{(2)}_{\mathrm{2D}}[x_i, y_j] - \bar{\mathcal{I}}_{\mathrm{2D}}[x_i, y_j]\right)^2 \\ &= \frac{1}{2}\left(\mathcal{I}^{(1)}_{\mathrm{2D}}[x_i, y_j] - \mathcal{I}^{(2)}_{\mathrm{2D}}[x_i, y_j]\right)^2 \,. \end{aligned} \tag{2.33}$$

Since we are interested in the signal-noise relation of the binned data, we calculate the clean binned intensity distribution and the corresponding squared noise

$$\bar{\mathcal{I}}[x_i] = \sum_j \bar{\mathcal{I}}_{\mathrm{2D}}[x_i, y_j] \,, \tag{2.34}$$

$$\sigma^2[x_i] = \sum_j \sigma^2_{\mathrm{2D}}[x_i, y_j] \,. \tag{2.35}$$

[12] A positive digitizer offset is used in an analog-to-digital converter to represent the average zero value of an analog signal. It prevents clipping of the negative portion of the analog signal in the conversion process, since a digitizer only has positive numbers while an analog signal can fluctuate both above and below an average value.

From the latter, we pixel-wise assign the noise to the binned signal, $\sigma[x_i] \mapsto \bar{\mathcal{I}}[x_i]$. This assignment, however, is not unique, i.e., signals of equal intensity level on different positions of the binned distribution are assigned to different noise values, which in turn, are Gaussian distributed around a mean value. The accuracy of the mean value increases with the number of estimated noise values, assigned to the same intensity level. For a binned intensity distribution with only few atoms, the number of data points of equal intensity level decreases with increasing intensity, see Fig. 2.8. Therefore, several distributions are required to cover the full intensity range, increasing the accuracy of the mean noise values. For this reason, up to 1000 images providing 500 clean intensity distributions are considered in the following analysis.

From now on, we label each clean intensity distribution, the positions of its data points and the assigned noise by an index $k \in \mathbb{N}$, namely $\bar{\mathcal{I}}_k[x_{k,i}]$ and $\sigma_k[x_{k,i}]$. We divide the intensity range into sub-intervals $U_{l\in\mathbb{N}} = [(l-1)\delta u, l\delta u)$ of a fixed width δu . For each sub-interval U_l, we trace all clean intensity distributions for intensity values lying within the sub-interval and construct a set of indices $\Omega_{k,l} = \{i|\bar{\mathcal{I}}_k[x_{k,i}] \in U_l\}$ of the corresponding data points. We calculate the mean intensity representing the sub-interval using

$$\bar{\mathcal{I}}_l = \frac{1}{N_l} \sum_k \sum_{i\in\Omega_{k,l}} \bar{\mathcal{I}}_k[x_{k,i}]\,, \tag{2.36}$$

where $N_l = \sum_k N_{k,l}$ with $N_{k,l}$ being the number of elements in the set $\Omega_{k,l}$. The corresponding mean squared noise is than given by

$$\bar{\sigma}_l^2 = \frac{1}{N_l} \sum_k \sum_{i\in\Omega_{k,l}} \sigma_l^2[x_{k,i}]\,. \tag{2.37}$$

Finally, we assign the mean noise to each intensity level of the sampled region, $\bar{\sigma}_l \mapsto \bar{\mathcal{I}}_l$, see Fig. 2.10. The sampling density of the intensity region is determined by the width of the sub-intervals δu, whereas the accuracy of the assigned mean noise value by the number of data points N_l.

Estimating noise for signals below the background baseline

The signal-noise relation below the background baseline is inferred from images with a uniform intensity distribution over the isoplanatic patch, acquired for a fixed signal intensity each. The photon signal intensity is aligned by the power of the laser beams, forming the optical molasses. The amount of dark current is controlled by the exposure time, while the internal shutter of the EMCCD camera is closed. From the binned intensity distribution $\mathcal{I}[x_i]$ of each offset-adjusted image $\mathcal{I}_{2\mathrm{D}}[x_i, y_i]$, we calculate the mean intensity signal level and its standard deviation, corresponding to the noise. To increase the accuracy of the mean value and the standard deviation, ten images acquired under identical conditions are considered for the calculation. Results are shown in Fig. 2.10.

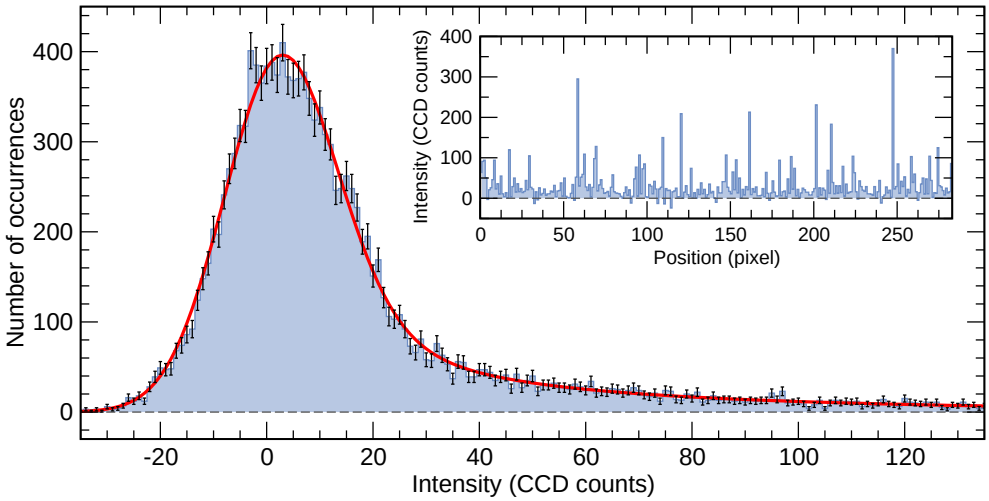

Figure 2.9.: Intensity histogram of 50 binned intensity distributions, dominated by the readout noise. In the inset, a single binned intensity distribution is shown, revealing characteristic spikes due to the electron multiplied clock-induced charges. The solid line in the histogram shows the fit of the statistical model of Eq. (2.40).

Estimating the readout noise arising from signal conversion

The readout noise arising from the charge-to-voltage and analog-to-digital conversion determines the noise level in the low-intensity limit of the image acquisition process. To infer this limit for the binned intensity distributions, we acquire a set of 50 images in darkness with the internal shutter closed and an exposure time of 50 ms each. At this exposure time and an EMCCD temperature of $-70\,^{\circ}\mathrm{C}$, the dark current is negligible. From all binned intensity distributions of offset-adjusted images, we calculate a histogram of intensities, see Fig. 2.9. The histogram reveals a characteristic shape determined by the two contributions of the readout noise (see Sec. 2.2.2): A Gaussian peak centered close to zero resulting from the noise of the conversion process,[13] followed by a long tail due to clock-induced charges generated during the frame transfer operation or the electron multiplication. To extract the contribution of the conversion process, we fit a statistical model to the histogram. The model incorporates weighted probability distributions describing the random output of each of the three involved readout stages (for details, see Ref. [107,108]):

(i) A Gaussian probability distribution $G(x)$ with a zero mean and a standard deviation $\sigma_{\mathrm{conv,bin}}$ describing the output after the conversion process.

(ii) Assuming that after the frame transfer operation, a clock-induced charge (CIC) is present at the input of the multiplication register with a probability of

[13] For an intensity histogram of a single pixel, the Gaussian distribution is centered exactly at zero. However, for the binned data the Gaussian contribution of the histogram appears to be shifted due to the convolution of the asymmetric single pixel distributions of the binned pixels.

p_{cic}, then the probability of x_{cic} electrons to be present at the output is given by [107, 108]

$$P_{\mathrm{cic}}(x_{\mathrm{cic}}) = \begin{cases} \dfrac{p_{\mathrm{cic}} \exp(-x_{\mathrm{cic}}/M)}{M}\,, & \text{if} \quad x_{\mathrm{cic}} > 0 \\ 1 - \displaystyle\int_{x>0} P_{\mathrm{cic}}(x)\mathrm{d}x\,, & \text{if} \quad x_{\mathrm{cic}} = 0\,, \end{cases} \tag{2.38}$$

where M denotes the mean gain of the electron multiplication process, see Sec. 2.2.2.

(iii) Considering a small probability $p_{\mathrm{cic}}^{\mathrm{em}}$ to generate a spurious electron at each stage of the electron multiplication register, the probability of $x_{\mathrm{cic}}^{\mathrm{em}}$ electrons being present at the output is given by [108]

$$P_{\mathrm{cic}}^{\mathrm{em}}(x_{\mathrm{cic}}^{\mathrm{em}}) = \begin{cases} \displaystyle\sum_{l=1}^{N} \frac{p_{\mathrm{cic}}^{\mathrm{em}} \exp(-x_{\mathrm{cic}}^{\mathrm{em}}/M^{(N-l)/N})}{M^{(N-l)/N}}\,, & \text{if} \quad x_{\mathrm{cic}}^{\mathrm{em}} > 0 \\ 1 - \displaystyle\int_{x>0} P_{\mathrm{cic}}^{\mathrm{em}}(x)\mathrm{d}x\,, & \text{if} \quad x_{\mathrm{cic}}^{\mathrm{em}} = 0 \end{cases} \tag{2.39}$$

with $N = 536$ multiplication stages of the register.
The probability distribution to find a given number of electrons reading a single pixel, after passing all three readout stages, is determined by the convolution of the distributions (i), (ii) and (iii). Since we are interested in the binned data, we convolve the resulting distribution K times with itself, where K denotes the number of pixel rows of the images. We fit this distribution to the histogram, minimizing

$$\min_{\{a,c,\sigma_{\mathrm{conv,bin}},p_{\mathrm{cic}},p_{\mathrm{cic}}^{\mathrm{em}}\}} \sum_n \left\{H(\mathcal{I}_n) - a(G * P_{\mathrm{cic}} * P_{\mathrm{cic}}^{\mathrm{em}})^{*K}(c\mathcal{I}_n)\right\}^2\,, \tag{2.40}$$

where the fit parameter a normalizes the histogram and c denotes the conversion factor between CCD counts and the number of electrons. From the fit, we infer a noise of the conversion process of $\sigma_{\mathrm{conv,bin}} = (10.3 \pm 1.1)$ CCD counts, whereas $p_{\mathrm{cic}} = (2.2 \pm 0.7) \times 10^{-2}$, $p_{\mathrm{cic}}^{\mathrm{em}} = (6.1 \pm 1.5) \times 10^{-4}$ and $c = (12.0 \pm 1.5)\,\mathrm{e}^-/\mathrm{CCD}$ counts. The noise of the conversion process agrees well with that determined in Ref. [108], and also $p_{\mathrm{cic}}^{\mathrm{em}} \ll p_{\mathrm{cic}}$ meets the expectation [96].

Signal-noise relation for binned intensity distributions

Joining results of signal-noise assignments for signals above and below the background baseline and including the noise level in the low-intensity limit $\sigma_{\mathrm{conv,bin}}$ allows us to fully characterize the signal-noise relation in the relevant intensity region. In Figure 2.10, results of these assignments for binned intensity distributions are shown. We observe a dominant square-root dependency of the noise on the intensity signal, apparent on the slope in the double-logarithmic plot. As expected, small deviations appear for high intensity levels reflecting the increasing influence of

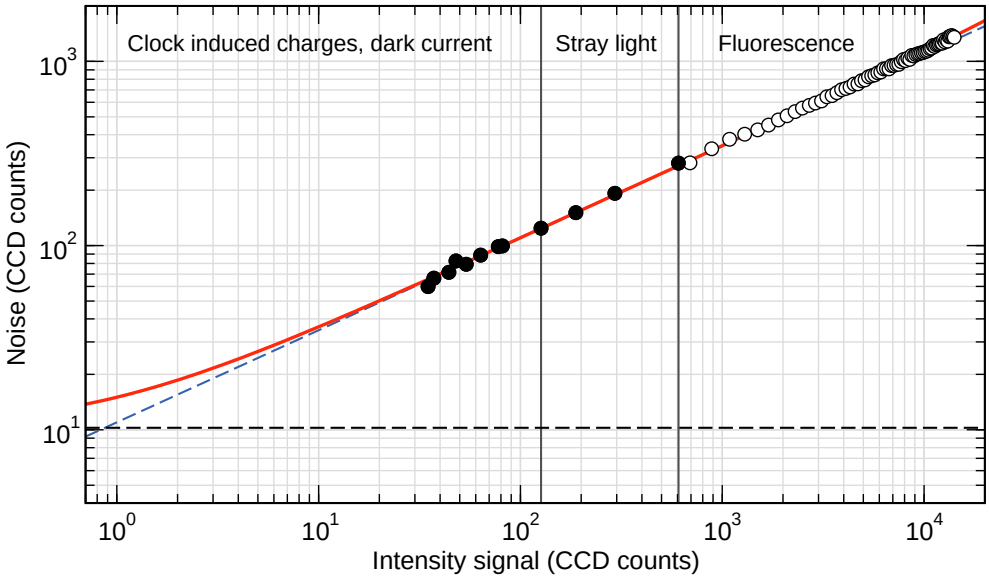

Figure 2.10.: Signal-noise relation for a binned intensity distribution, estimated from a statistical analysis of images. Open circles show results from the two-image analysis; filled circles from the calculation of the mean value and standard deviation of a uniform intensity distribution for different intensity levels. The error bars are smaller than the point size. The horizontal line indicates the lower limit of the noise, arising from the electron-to-voltage and analog-to-digital conversion. Vertical lines separate the regions labeled to the respective signal contributions. The dashed line indicates the trend, expected from a shot noise dominated image acquisition.

linear scaling noise, e.g. arising from the photo-response non-uniformity (PRNU), see Sec. 2.2.2. We stress that the signal-noise relations inferred from two different methods merge seamlessly, confirming the accuracy of the two-image approximation deduced from simulations. Following the noise model of Eq. (2.4), we fit

$$\sigma(\bar{\mathcal{I}}) = \sqrt{\sigma^2_{\mathrm{conv,bin}} + c_1^2\bar{\mathcal{I}} + c_2^2\bar{\mathcal{I}}^2} \tag{2.41}$$

to the data points of the signal-noise relation (see Fig. 2.10), obtaining $c_1 = 10.98 \pm 0.05$ and $c_2 = (3.0 \pm 0.2) \times 10^{-2}$. This result quantitatively confirms the shot noise dominance over the relevant intensity region. However, it should be noted that the linear noise contribution of the PRNU may be inherently underestimated by the two-images method, since fixed systematic effects cancel when two images are subtracted.

Finally, we construct a relation directly assigning squared errors σ_l^2 in Eq. (2.30) to each data point $I[x_l]$ with the objective of maintaining the real-time performance of the parametric deconvolution. For this purpose, computationally expensive operations, e.g. calculation of intensity histograms for each image to adjust the images

to the digitizer offset, have to be avoided. Thus, we take the background baseline a_0 of the stray light as a constant reference, which, fixing the power of laser beams forming the optical molasses, turns out to be stable over time. Therefore, once the background baseline level is determined with respect to the digitizer offset a_{const} from several preacquired images, the squared error entering the Levenberg-Marquardt fitting algorithm in Eq. (2.30) is given by

$$\begin{aligned}\sigma_l^2 &= \sigma \left(I[x_l] - a_0 + a_{\mathrm{const}}\right)^2 \\ &= \sigma_{\mathrm{conv,bin}}^2 + c_1^2 \left(I[x_l] - a_0 + a_{\mathrm{const}}\right) + c_2^2 \left(I[x_l] - a_0 + a_{\mathrm{const}}\right)^2 . \end{aligned} \tag{2.42}$$

2.3.7. Filtering of erroneous results

In some numerically challenging cases, mainly occurring for many optically unresolved atoms in a ROI, the parametric deconvolution fails to accurately determine the position of the atoms. This may happen for an inaccurate initial guess, yielding the subsequent fitting algorithm to settle on a set of parameters that minimizes Eq. (2.30) in the local sense but not in the global sense, being caught in a local minimum. A further source of errors are atoms which leave the optical lattice during the exposure time. In all these cases, the erroneous results have to be efficiently identified and excluded from further analysis to maintain a high reliability of inferring the positions of the atoms. Since manual verification of each result is time-consuming and therefore inapplicable for real-time processing, we aim on an automatic verification scheme. This scheme requires an unbiased reliability criterion based on a sensitive, easily accessible error indicator. For this, we utilize the fluorescence contributions of the atoms a_j estimated in the final stage of the parametric deconvolution, see Eq. (2.30). These parameters turn out to be sufficiently sensitive to identify most of the deconvolution errors.

In Figure 2.11, a histogram of fluorescence contributions a_j is shown, obtained from the parametric deconvolution of 20530 atoms from approximately 6000 images with up to eight atoms per ROI (the same data set as used in Sec. 2.3.1). The histogram reveals a Gaussian peak centered at $\bar{a} = (90669 \pm 42)$ CCD counts with a standard deviation of $\sigma_{\bar{a}} = (6492 \pm 51)$ CCD counts. Both values only slightly deviate from the averaged single atom fluorescence contribution $I_{\mathrm{a}} = (90934 \pm 126)$ CCD counts and the corresponding standard deviation $\sigma_1 = (6795 \pm 111)$ CCD counts, inferred from the fit of Eq. (2.9) to the histogram of I_k^{tot}, see Sec. 2.3.1. This fact indicates the proper working of the algorithm. The homogeneous background in the histogram mainly arises from fluorescence contributions of atoms leaving the optical lattice during exposure. The same applies to the contributions with $a_j > \bar{a}$, where one of two or many nearby atoms leave the trap, whereas its partial contribution is wrongly assigned to the nearby atoms by the algorithm. The noticeable rising in the histogram close to $2\bar{a}$ and the zero value corresponds to the cases of two atoms being wrongly regarded as one by the algorithm, even though neither of the involved atoms has left the trap during exposure. We stress that the interpretation of the respective histogram contributions relies on a manual investigation of the

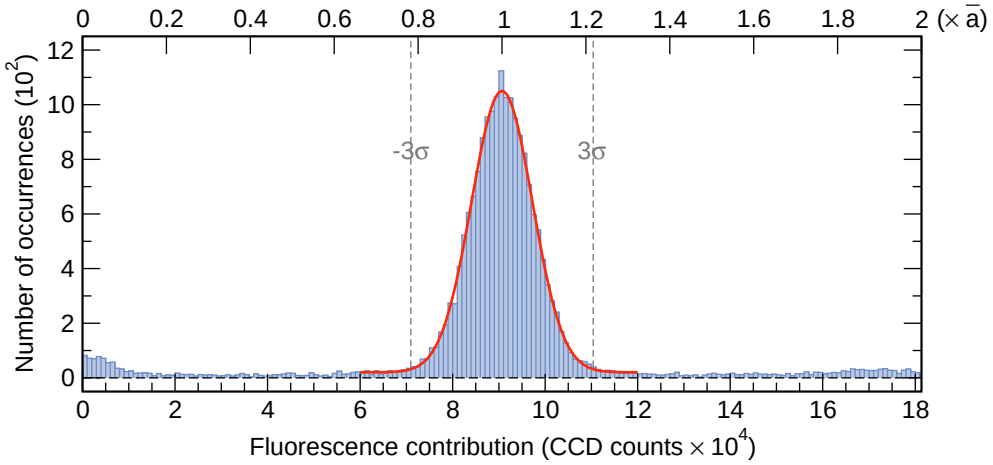

Figure 2.11.: Histogram of fluorescence contributions of a single atom a_j, calculated using the parametric deconvolution. The solid line indicates a Gaussian fit to a local region of the histogram. Vertical dashed lines indicate the borders of a typical acceptance region, corresponding to the $\pm 3\sigma$ confidence interval.

respective binned intensity distributions, carried out on random samples. Atoms leaving the trap during exposure are identified from a sequence of successive images of the same atom distribution.

Following the analysis of the histogram in Fig. 2.11, it is apparent to regard those results of the parametric deconvolution as reliable, the parameters a_j of which contribute to the Gaussian distribution centered around the average single atom fluorescence contribution $\bar{a}$. Consequently, the reliability criterion for the automatic verification can be written as

$$|a_j - \bar{a}| < \varepsilon \,, \tag{2.43}$$

where ε determines the borders of the acceptance region. Results of which parameters fail to pass this criterion are regarded as erroneous being excluded from the subsequent analysis. In addition, we exclude the total ROI containing the erroneous result, since it may affect the estimation accuracy for the nearby atoms. Note that, apart from the number of excluded results, the width of the acceptance region also affects the accuracy of determining the positions of the atoms, see Sec. 2.4.1. For typical applications, we set $\varepsilon = 3\sigma_{\bar{a}}$, providing 14% of the results failing the reliability check. Most of these result can be traced back to the numerically challenging cases with several atoms occupying nearest lattice sites. In comparison, only 5% of the atoms leave the optical lattice during the exposure time.

2.3.8. Remarks on implementation and performance

The image analysis module is written in ANSI C in LabWindows CVI (National Instruments) software development environment. It utilizes high-performance li-

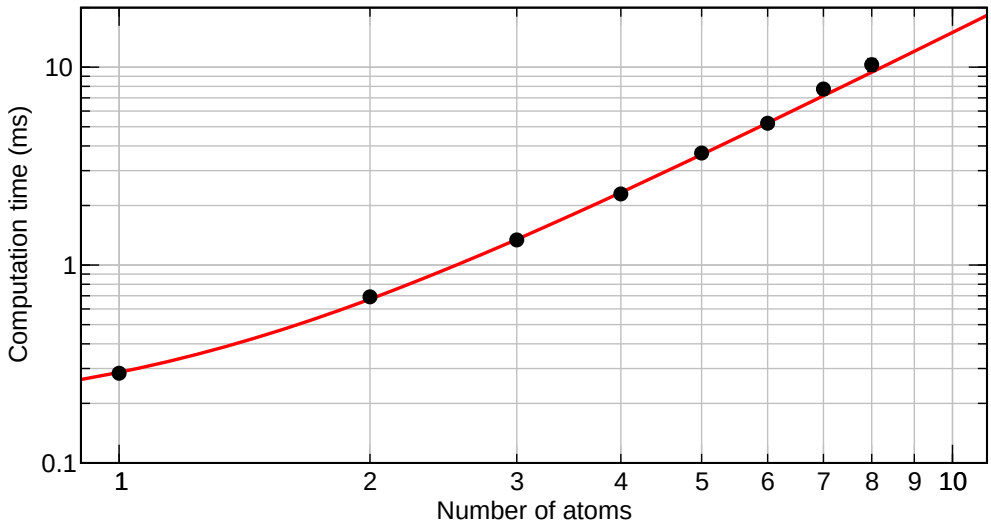

Figure 2.12.: Average computation time of the parametric deconvolution for a single ROI. The error bars are smaller than the data points. The solid line shows a fit of Eq. (2.44).

braries, e.g., the LabWindows CVI Advance Analysis Library, mainly for matrix operations, including solving of eigenvalue and eigenvector problems, and Numerical Recipes [109], providing a fast and customizable Levenberg-Marquardt fitting algorithm. The image analysis module is part of two self-developed software versions: a real-time image acquisition and image analysis software "iXacq" and a post-analysis software "Post Deconvolution" to post-analyze the acquired data from stored image files, for details see App. A.2 and A.4, respectively. Both versions are optimized for computational performance. The real-time version additionally utilizes the multi-threading and multi-core capability of the CPU (Intel Pentium D 935, 3.2 GHz), allowing to simultaneously analyze and store the acquired images while new images are acquired. By this, we avoid computational delays in sequences relying on successively acquired images, e.g. for continuous monitoring of atoms. Results for atom positions, atom numbers and atom separations are stored in separated files, including the erroneous results being marked as such for root cause analysis.

In Figure 2.12, the average computation time of the parametric deconvolution for a single ROI as a function of the number of atoms n is shown.[14] From a fit of the function

$$f(n) = t_0 + t_1 n^{\alpha}\,, \tag{2.44}$$

we infer the fit parameters $t_0 = (0.17 \pm 0.01)\,\mathrm{ms}$, $t_1 = (0.11 \pm 0.01)\,\mathrm{ms}$ and $\alpha = 2.10 \pm 0.04$. Therefore, the computation time scales approximately quadratically with the number of atoms per ROI. Incorporating the transfer time of the image

[14] The benchmark test has been performed on an Intel Pentium M processor with 1.6 GHz. Note that the lab computer (Intel Pentium D 935, 3.2 GHz) used for real-time deconvolution provides a higher performance.

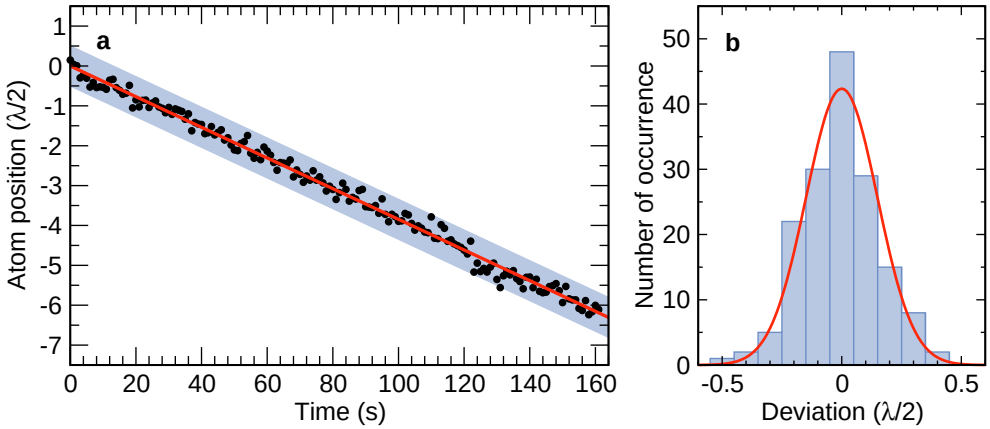

Figure 2.13.: (**a**) Position of a single atom continuously monitored with a time step of 1 s. The solid line indicates the drift of the respective lattice site; the shaded stripe, the maximum trapping region. (**b**) Histogram of deviation of the atom position from the lattice site center. The solid line shows a Gaussian fit to the histogram.

from the camera, the time for vertical binning, image segmentation, determination of atom number and storing the images and deconvolution results, we estimate an upper limit of the overall time to analyze a typical image being far below the shortest reasonable exposure time of 100 ms. Thus, the frame rate for continuous monitoring of atomic positions is limited by the exposure time, rather than by the parametric deconvolution.

2.4. Detecting atoms on neighboring lattice sites

The parametric deconvolution allows us to continuously monitor the positions of the atoms with a frame rate limited by the exposure time. The determined positions of the atoms, however, are subjected to position fluctuations and drifts of the optical lattice relative to the imaging optics, affecting the accuracy of the parametric deconvolution. Improving the accuracy by averaging the position from several successively acquired images is only reasonable, if the drift of the optical lattice is negligible during the acquisition time. Furthermore, drifts of the optical lattice strongly affect the reliability of inferring the transport distance of atoms whenever atoms are transported in the lattice, see Sec. 4.5.3.

To infer the drift of the optical lattice relative to the imaging optics and the accuracy to determine the atom position from a single image, we track the position of a single atom over a long time period from successively acquired images with 1 s exposure time each, see Fig. 2.13(a). We observe small fluctuations of the atom position around an approximately linear trend, indicating a slow drift of the optical lattice. This drift mainly originates from the thermal expansion of the

optical table. From a linear fit to the atom positions, we deduce a drift-velocity of $(16.6 \pm 0.1)\,\mathrm{nm/s}$, which is negligible for all applications presented in this work.[15]

The accuracy of determining the position from a single image with a typical exposure time of 1 s is inferred from a histogram of deviations of the atom positions from the fitted center of the lattice site. The histogram reveals a Gaussian distribution, see Fig. 2.13(b). From a fit, we infer an accuracy of $\sigma_{\mathrm{pos}} = (0.149 \pm 0.007)\lambda/2 = (65 \pm 3)\,\mathrm{nm}$ (standard deviation of the Gaussian). For comparison, the spread of the Gaussian thermal wave packet of the atoms along the trap axis is given by $\sigma_{\mathrm{th}}^{\mathrm{hor}} = 23\,\mathrm{nm}$. Note that the estimated accuracy incorporates the non-resolvable fluctuations of the optical lattice. Therefore, the numerical accuracy of the parametric deconvolution to determine the atom positions from a single image is expected to be higher.

Some applications presented in this work require the relative distance between atoms occupying different lattices sites rather than their absolute positions to be known. Compared to the accuracy of determining the absolute positions, the accuracy of determining distances is decreased ($\sigma_{\mathrm{dis}} = \sqrt{2}\sigma_{\mathrm{pos}}$). However, because the fluctuations and drifts of the optical lattice equally affect all trapped atoms, by averaging the distances from many successively acquired images of the same distribution the accuracy of determining the distances can be significantly increased [43, 110], being only limited by the storage time of the atoms. So far atoms have to be optically resolved to reliably infer the correct number of sites separating them [43,110]. In the following, we show that the parametric deconvolution presented in Sec. 2.3.5 together with a precisely determined LSF and the signal-noise relation overcome the previous restrictions.

2.4.1. Parametric deconvolution of atom clusters

We apply our numerical method to approximately 6000 images in order to both investigate its efficiency and accuracy, and to extract the distribution of atom separations. For this purpose, we repeatedly load on average four atoms into the optical lattice and successively acquire several images of the same atom distribution. From each image with N atoms passing the reliability criterion of Eq. (2.43), we determine the atom positions and calculate the corresponding $N(N-1)$ distances. Following Ref. [43], we additionally calculate the averaged distances from successively acquired images of the same atoms to reduce the statistical error. For a large number of atoms loaded in the optical lattice, the atoms are rather clustered than being well isolated from each other. This results in ROIs containing several optically inseparable atoms, see Fig. 2.14. These atom clusters constitute the most challenging cases for our numerical post-processing method.

In Figure 2.15, the histograms of determined distances from both single images and three-image averages are shown. Both histograms reveal a periodic structure,

[15] The drift of the optical lattice is usually checked prior each measurement requiring an accurate estimation of positions and the distance covered by the atoms after being transported in the lattice. From all these measurement we infer an upper limit of the drift-velocity of 20 nm/s.

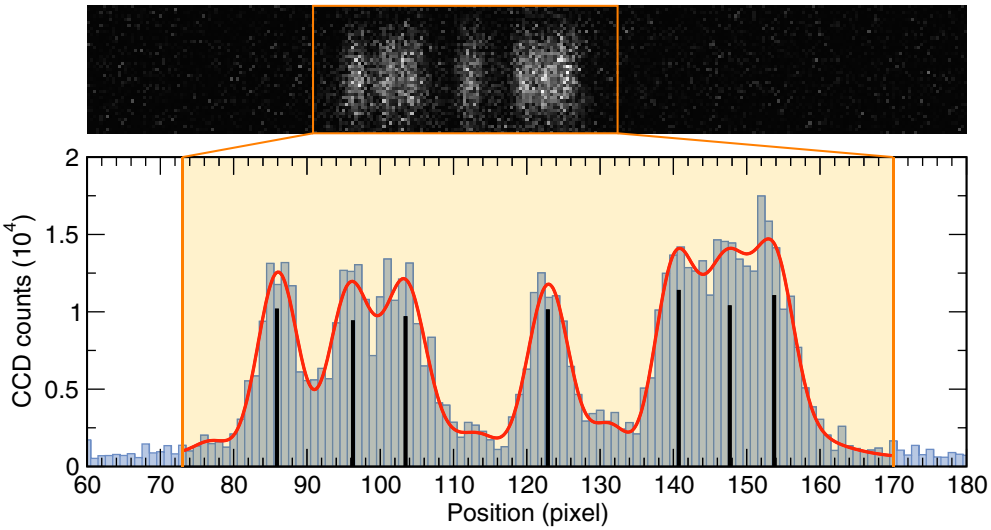

Figure 2.14.: Fluorescence image and the corresponding vertically binned intensity distribution $I[x_i]$ of an atom cluster. The shaded region indicates the ROI. The extracted positions ξ_k and the (scaled) fluorescence contributions a_k of the atoms are shown as vertical lines. The solid line shows the resulting source distribution $S(x)$ of Eq. (2.6) convolved with the LSF.

perfectly reproducing the periodicity of the optical lattice, as well as a marked decay in the number of occurrences for small separations. We stress that the lattice periodicity does not enter in any way our estimation procedure. Thus, the strict adherence to the periodicity and the well separated histogram peaks provide a striking confirmation for the high precision and reliability of our detection. For each histogram peak, we estimate the reliability F_n of inferring the correct number $n \in \mathbb{N}$ of sites separating two atoms, assuming Gaussian distributions of the measured distances around $d_n = n\lambda/2$ and fitting a sum of Gaussians centered at d_n to the histogram

$$f(x) = \sum_{n=1}^{30} h_n e^{-(x-d_n)^2/(2\sigma_n^2)}\,, \tag{2.45}$$

where σ_n estimates the accuracy of determining the distance d_n. The reliability F_n is then given by the area of the normalized Gaussian centered at d_n within $[d_n - \lambda/4, d_n - \lambda/4]$

$$F_n = \frac{1}{\sqrt{2\pi}\sigma_n} \int_{-\lambda/4}^{\lambda/4} e^{-(x-d_n)^2/(2\sigma_n^2)} \mathrm{d}x\,. \tag{2.46}$$

For site separations below the theoretical diffraction limit ($n < 5$), we obtain $F_{1\text{-}4} = 81.0\text{-}99.7\%$ ($\sigma_{1\text{-}4} = 72\text{-}123\,\mathrm{nm}$), whereas above the diffraction limit $F_{5\text{-}29} =$

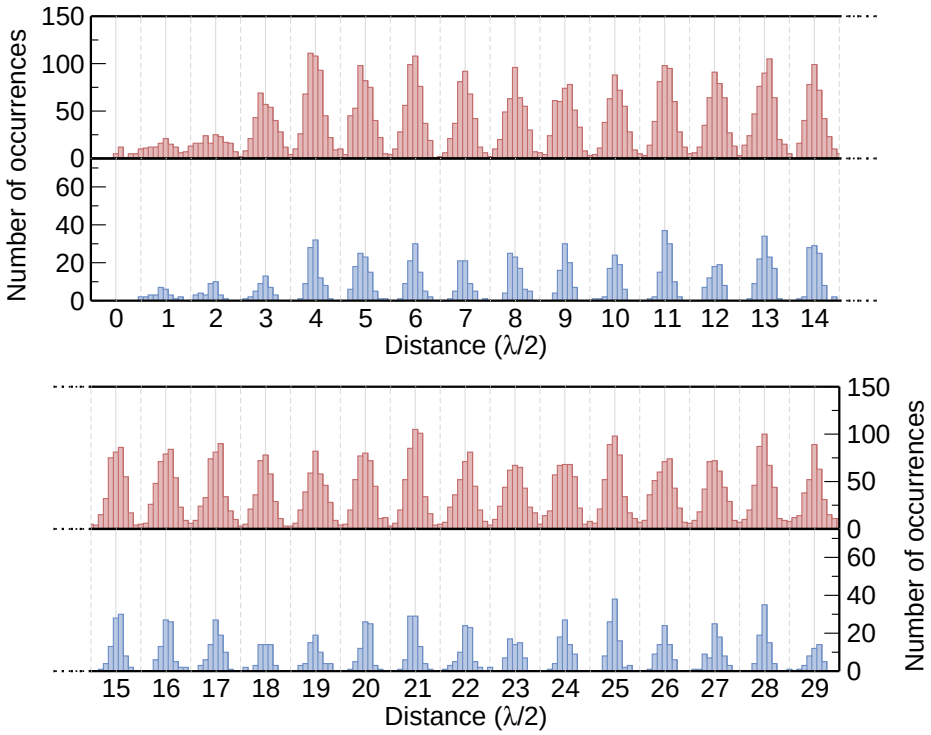

Figure 2.15.: Histogram of determined distances. The upper rows correspond to the distances obtained from a single image; the lower rows to the distances obtained from the averages over three successively acquired images of the same atoms.

98.2-99.9% ($\sigma_{5\text{-}29}$ = 67-91 nm). Reducing the statistical error by averaging the distances from three successively acquired images of the same atoms increases the reliability to $F^{(3)}_{1\text{-}4} \geq 99.98\%$, and $F^{(3)}_{5\text{-}29} \geq 99.992\%$. This allows us to investigate possible atomic interactions in the nearest-neighbor regime.

The marked decay in the number of occurrences for small separations can partially be traced back to the cases with three or more atoms occupying nearest lattice sites. These cases are challenging from a numerical point of view and cause our algorithm to provide increasingly inaccurate results, which then fail to pass the reliability criterion of Eq. (2.43). From simulations, we deduce that this does not hold for pairs of nearest neighbors separated by at least two lattice sites from other atoms.

Adjusting the acceptance region and incorporating the noise characteristics

In the following, we investigate the influence of the acceptance region and the incorporated signal-noise relation in the final stage of the parametric deconvolution on both, the accuracy of determining the distances and the reliability of inferring the correct number of sites separating two atoms for separations below and above the theoretical diffraction limit. For this, we reanalyze the previous data set for different

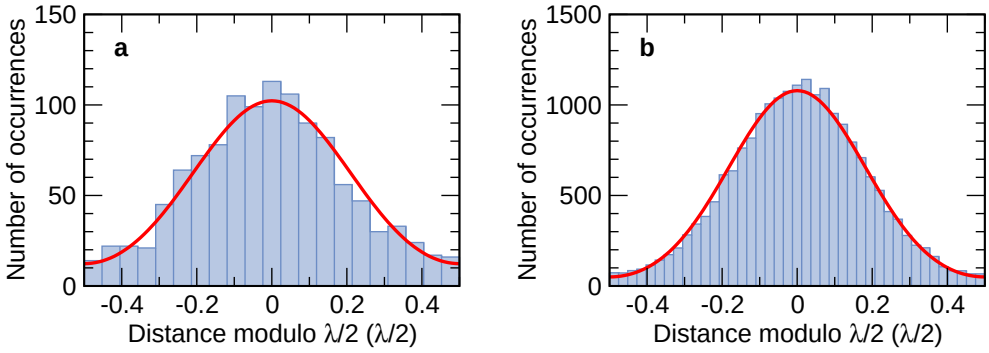

Figure 2.16.: Histogram of distances modulo $\lambda/2$ for distances (**a**) below, $d_i \in D_\varepsilon^{\mathrm{bel}}$, and (**b**) above, $d_i \in D_\varepsilon^{\mathrm{abv}}$, the theoretical diffraction limit, obtained from a single image with 1 s exposure time for a typical acceptance region border of $\varepsilon = 3\sigma_{\bar{a}}$. The solid line shows the fit of Eq. (2.47) to the histogram. The fit parameters $\sigma_{\mathrm{bel}} = (0.21\pm0.01)\lambda/2 = (91\pm4)$ nm and $\sigma_{\mathrm{abv}} = (0.182\pm0.001)\lambda/2 = (79.8\pm0.4)$ nm provide the mean accuracy of the distance measurement, respectively.

borders ε of the acceptance region (see Eq. (2.43)), with and without incorporating the signal-noise relation in the parametric deconvolution. We divide the set of distances $D_\varepsilon = \{d_i | i = 1, \ldots, M_\varepsilon\}$ calculated from single images into two subsets: $D_\varepsilon^{\mathrm{bel}} = \{d_i \in D_\varepsilon | d_i < 4.5\lambda/2\}$ and $D_\varepsilon^{\mathrm{abv}} = \{d_i \in D_\varepsilon | d_i \geq 4.5\lambda/2\}$, corresponding to atom separations below and above the theoretical diffraction limit, respectively. Utilizing the periodicity of the optical lattice, for each subset, a histogram of the distances modulo $\lambda/2$ shifted by $\lambda/4$ is calculated. Such a histogram reveals only a single peak centered at zero, see Fig. 2.16. Compared to the multi-peak histogram analysis, this procedure allows us to reduce the statistical error of inferring the accuracy and reliability, arising from an insufficient number of accepted results for small values of ε. From a fit of

$$f(x) = h\left(e^{-(x+\lambda/2)^2/(2\sigma^2)} + e^{-x/(2\sigma^2)} + e^{-(x-\lambda/2)^2/(2\sigma^2)}\right) \tag{2.47}$$

to the histogram, where the fit parameter h incorporates the heights of the three superimposed Gaussian distributions, for each subset, we deduce the mean accuracy of determined distances (σ_{bel} and σ_{abv}). The mean reliability of inferring the correct number of sites separating two atoms is calculated according to Eq. (2.46).

In Figure 2.17, the accuracy and reliability for different borders of the acceptance region are shown for distances below and above the theoretical diffraction limit, with and without incorporating the noise characteristics, respectively. In both regions, incorporating the signal-noise relation in the parametric deconvolution increases the accuracy of determining the distances by $\approx 5\%$. This increase, however, translates only in a noticeable improvement of the reliability for distances below the diffraction limit. By increasing the width of the acceptance region, both the accuracy and reliability decrease, since erroneous results increasingly enter the

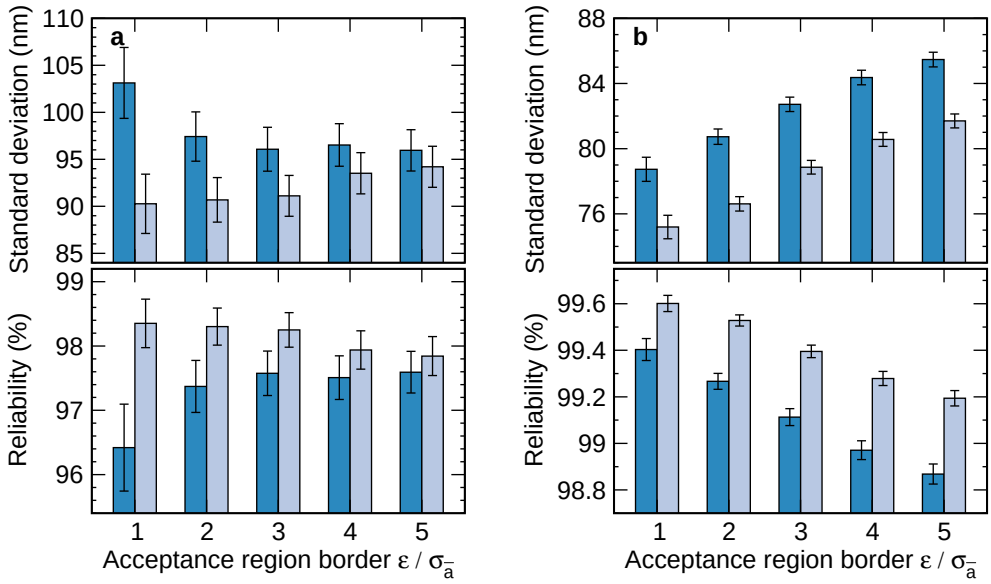

Figure 2.17.: Accuracy of determining the distances (upper graphs) and reliability of inferring the correct number of sites separating two atoms (lower graphs) for different borders ε of the acceptance region for distances below, $d_i \in D_\varepsilon^{\mathrm{bel}}$, (**a**) and above, $d_i \in D_\varepsilon^{\mathrm{abv}}$, (**b**) the theoretical diffraction limit. Lighter (darker) bars indicate the values with (without) incorporating the signal-noise relation in the Levenberg-Marquardt algorithm.

histogram of distances. Due to the Gaussian distribution of fluorescence contributions around a mean value $\bar{a}$ (see Fig. 2.11) and a negligible homogenous background arising from an insignificant number of atoms leaving the optical lattice during the exposure time, the effect of erroneous results entering the histogram of distance in Fig. 2.16 is comparably small and thus certainly underestimated. Decreasing the acceptance region border below $\varepsilon = 3\sigma_{\bar{a}}$, in contrast, increases the accuracy and reliability at the expense of the number of results passing the reliability criterion. The acquisition of N_{img} successive images of the same atom distribution provides a more efficient strategy for increasing the accuracy, reducing the statistical error by $\sqrt{N_{\mathrm{img}}}$. This strategy, however, significantly increases the duration of experimental sequences which are mainly dominated by the exposure time.

2.4.2. Calibration of the image scale

Resolving the precisely known periodicity of the optical lattice from distances between atoms occupying different lattice sites allows us to calibrate the image scale, relating the length units of CCD pixels in the detection plane to the length units in the object plane. For this purpose, we introduce a conversion factor α_{conv} defined by

$$d_{\mathrm{obj}} = \alpha_{\mathrm{conv}} d_{\mathrm{det}} \,, \tag{2.48}$$

where d_{obj} denotes the distance in the object plane (in meters) and d_{det} the corresponding distance in the detection plane (in CCD pixels). Therefore, knowing the periodicity of the optical lattice in the object plane, the corresponding periodicity in the detection plane needs only to be precisely determined to infer the conversion factor α_{conv}.

We infer the periodicity in the detection plane from a Fourier analysis of a set of distances [111], $D = \{d_{\mathrm{det},j} | j = 1, \ldots, M\}$ with $M = 4082$, calculated from averages of three successively acquired images of the same atom distribution.[16] From this set, we construct the periodic distribution function

$$f(x) = \frac{1}{M} \sum_{j=1}^{M} \delta(x - d_{\mathrm{det},j}) \,, \tag{2.49}$$

and calculate its Fourier transform

$$\hat{f}(k) = \mathrm{FT}\{f(x)\} = \frac{1}{\sqrt{2\pi}} \int_{-\infty}^{\infty} f(x) e^{2\pi i k x} \mathrm{d}x = \frac{1}{\sqrt{2\pi} M} \sum_{j=1}^{M} e^{2\pi i k d_{\mathrm{det},j}} \,. \tag{2.50}$$

The latter allows us to determine the period of $f(x)$ corresponding to the $\lambda/2$ periodicity of the atomic separations.

The real part of $\hat{f}(k)$ exhibits sharp peaks at integer multiples of the spatial frequency k_0, corresponding to the periodicity of the optical lattice, whereas its imaginary part provides zero crossings at these frequencies, see Fig. 2.18. Therefore, according to Eq. (2.48), the conversion factor α_{conv} can be calculated by

$$\alpha_{\mathrm{conv}} = k_0 \lambda / 2 \,. \tag{2.51}$$

From the Fourier transform of $f(x)$, we infer

$$\alpha_{\mathrm{conv}}^{\mathrm{Re}} = (294.65 \pm 0.02)\,\mathrm{nm/pixel} \,, \tag{2.52}$$

$$\alpha_{\mathrm{conv}}^{\mathrm{Im}} = (294.63 \pm 0.01)\,\mathrm{nm/pixel} \,, \tag{2.53}$$

where $\alpha_{\mathrm{conv}}^{\mathrm{Re}}$ denotes the conversion factor obtained from the position of the first peak in the real part of $\hat{f}(k > 0)$, $\alpha_{\mathrm{conv}}^{\mathrm{Im}}$ the conversion factor obtained from the corresponding zero crossing of the imaginary part, respectively. The statistical error, originating from the finite size of the set D is estimated similar to Ref. [111]. From the average of both conversion factors, we finally obtain

$$\alpha_{\mathrm{conv}} = (294.64 \pm 0.02)\,\mathrm{nm/pixel} \,. \tag{2.54}$$

Thus, for a pixel size of $16\,\mu$m, we deduce a magnification of 54.3.

The decay of the peak heights in the real part of $\hat{f}(k)$ with increasing integer multiple of k_0 arises from the deviations of the Dirac spikes in $f(x)$ from a perfectly

[16] We use the same set of data as for the calculation of the histogram in Fig. 2.15 of Sec. 2.4.1.

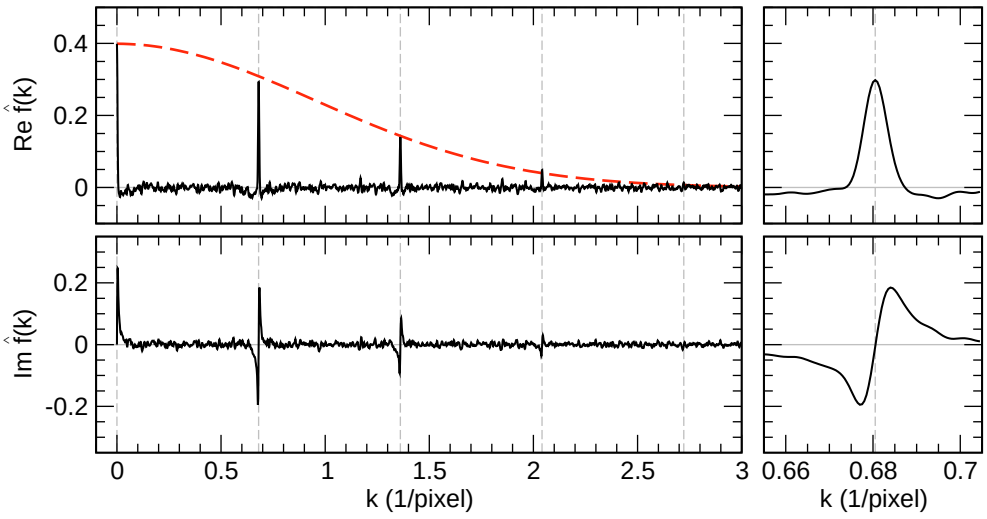

Figure 2.18.: Real and imaginary part of the Fourier transform $\hat{f}(k)$ of the periodic distribution function $f(x)$. Vertical dashed lines indicate the integer multiple of the spatial frequency k_0. The peak of the real part and the zero crossing of the imaginary part at k_0 are shown in a detail view. The dashed line shows a Gaussian envelope fitted to the peaks maxima.

periodic distribution, i.e. a Dirac comb with a spike separation of $1/k_0$. This can be intuitively explained assuming the determined distances $d_{\mathrm{ccd},j}$ being Gaussian distributed around the spikes positions of the Dirac comb with a standard deviation σ. The deviations of $d_{\mathrm{det},j}$ from the spikes of this comb can be incorporated by convolving the comb with the Gaussian distribution. According to the convolution theorem, the Fourier transform of the resulting function is a product of the Dirac comb with a spatial frequency separation of k_0 and the Gaussian function with a standard deviation of $\hat{\sigma} = 1/(2\pi\sigma)$, forming the envelope of the Dirac comb. The real part of the resulting function reasonably agrees with $\mathrm{Re}\,\hat{f}(k)$ inferred from the measurement, see Fig. 2.18. From a fit of the Gaussian envelope to the peak maxima of $\mathrm{Re}\hat{f}(k)$ at integer multiple of k_0, we deduce the (mean) accuracy of determining the separations of atoms of $\sigma = (72 \pm 1)\,\mathrm{nm}$. The corresponding (mean) reliability of $F = 99.7\%$ agrees well with the values, estimated from the histogram of distances, see Sec. 2.4.1. Small deviations are expected due to the fact that the distances in D cover only a finite interval, whereas according to the definition, the width of the interval covered by the spikes of the Dirac comb is infinite.

2.4.3. Parametric deconvolution of atom pairs

To investigate the influence of possible interaction induced effects in the physically interesting regime of neighboring atoms, and to get an unbiased insight in the statistics of atom pair separations, in the following experiment, we focus on the

distance distribution of isolated atom pairs only. For this purpose, we reduce the mean number of atoms loaded into the MOT to about two atoms using a high field gradient of 345 G/cm, which also favors short distances. From single-atom images, we infer the interaction-free position distribution, which is given by the overlap of the MOT and the one-dimensional lattice. From two-atom images, we determine the atom separations averaging over three successively acquired images of each pair of atoms.

To remove the bias of our numerical method from the statistics of atom pair separations, leading to the decay in the number of occurrences for small separations, the parametric deconvolution is extended by an additional stage. This stage aims on reanalyzing the data, whenever convergence failures of the Levenberg-Marquardt algorithm occur yielding results which fail the reliability criterion of Eq. (2.43). Most of these failures arise from an incorrect initial guess of the trigonometric moment estimation, increasingly occurring for nearby atoms. Fortunately, for only two nearby atoms in a ROI, the positions of both atoms can be easily guessed, assuming them in a small region on both sides of the center of the ROI. This assumption turns out to be sufficiently accurate for the subsequent deconvolution steps. We utilize this assumption in the additional stage: Whenever a ROI with two atoms fails the reliability check, the initial guess is automatically reestimated by the "simple guess" and reentered the Levenberg-Marquardt algorithm. The convergence of the latter is facilitated by reducing the number of parameters to be estimated. Considering the fact that nearby atoms are less affected by inhomogeneous illumination or detector sensitivity, the fluorescence contribution of both atoms can be assumed to be equal, and thus described by a single parameter. By this, we recover all results which previously failed the reliability criterion for convergence reasons. Deconvolution results for atom pairs in the optically resolvable and non-resolvable regime are shown in Fig. 2.19(a-f).

In Figure 2.20, the histograms of single-atom positions and pair separations are shown. The latter reveals a clear gap for two atoms loaded into the same lattice site, reflecting light induced atom losses. The underlying loss mechanism is known [112–114]: The atoms gain sufficient kinetic energy in an excited molecular potential to leave the optical lattice. For larger separations, starting from nearest-neighbor sites, the distance distribution follows a Gaussian shape. This shape fits well to a modeled distribution which assumes statistically independent positions of both atoms. The number of occurrences Q as a function of distance d is then given by

$$Q(d) = 2Q_0(P * P)(d) = 2Q_0 \int_{-\infty}^{\infty} P(x)P(x-d)\mathrm{d}x\,, \tag{2.55}$$

where $P(x)$ denotes the normalized fitted single-atom position distribution (Gaussian with a standard deviation of $\sigma = 9.5\lambda/2$), see Fig. 2.20(a), and Q_0 the total number of analyzed atom pairs. From this fact, we conclude that for our one-dimensional lattice, atoms in neighboring lattice sites do not affect each others' storage time, which is limited by background gas collisions. We stress that for

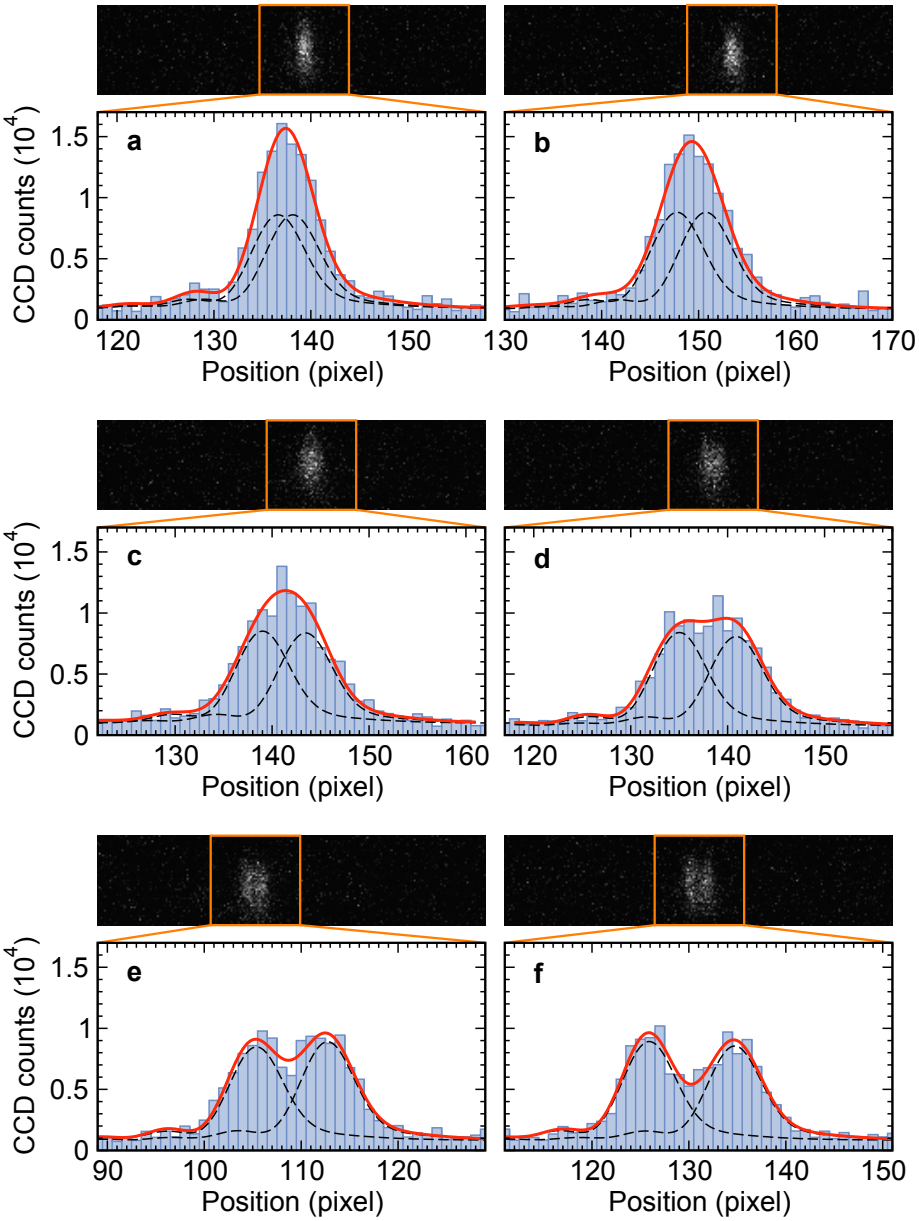

Figure 2.19.: Parametric deconvolution of atom pairs (**a**) occupying neighboring lattice sites, i.e. separated by one lattice site, (**b**) separated by two, (**c**) three, (**d**) four, (**e**) five and (**f**) six lattice sites. The dashed lines indicate the contribution of each individual atom convolved with the LSF; the solid line the respective contribution of their sum.

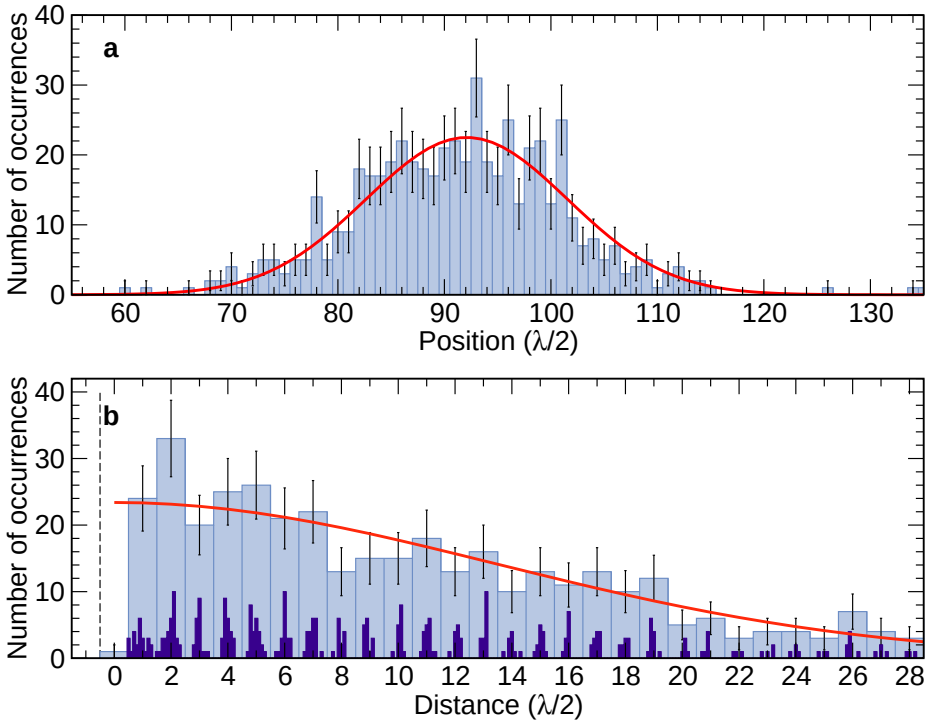

Figure 2.20.: (**a**) Histogram of absolute positions of single atoms transferred from the MOT into the one-dimensional lattice. Error bars indicate the statistical error. The solid line shows a Gaussian fit. (**b**) Histogram of distances between two transferred atoms. Solid bars correspond to the measured distances averaged over three successively acquired images; shaded bars to the distance distribution in terms of lattice sites. The solid line shows the distribution Q(d) of Eq. (2.55).

isolated atom pairs with separations below the diffraction limit, our numerical procedure provides an increased reliability of more than 95.0%, exceeding the number quoted for clusters of atoms.

2.5. Conclusion

In this chapter, I have presented the developed and adopted numerical post-processing methods which allow us to accurately and reliably determine the number, the positions and separations of individual atoms in a sparsely filled one-dimensional optical lattice at all relevant distances from fluorescence images. The imaging setup has been discussed in detail, meeting the requirements on efficient fluorescence collection, imaging quality, suppression of stray light and noise performance. The microscope objective is capable of optically resolving the atoms separated by more than five lattice sites. The parametric deconvolution overcomes this limit, reliably inferring the correct number of sites separating two atoms down to nearest neigh-

bors. This has been demonstrated by resolving the periodicity of the optical lattice down to separations of neighboring lattice sites of 433 nm.

The parametric deconvolution requires the LSF of the optical system to be analytically known. I have presented a method, providing a precise and self-consistent estimation of the LSF with sub-pixel accuracy, directly from a set of images of isolated atoms. This method has been used to determine the isoplanatic patch. Another method has been developed to directly deduce the noise performance of the detector from a set of atom images by inferring its signal-noise relation. The dominant square-root dependency of the noise on the signal in this relation reveals that our fluorescence detection is primarily shot noise limited in the relevant signal region. By incorporating the measured signal-noise relation in the parametric deconvolution, the accuracy of determining atom separations has been increased by 5%. High computational performance of the deconvolution enables to continuously monitor the positions of the atoms almost in real-time with a frame rate limited by the exposure time.

The new degree of precision in detection allows us to directly observe light-induced atom losses and to distinguish between on-site and nearest-neighbor contributions, from statistics of atom pair separations. Furthermore, it paves the way for preparation and manipulation of single atoms in confined spaces, simplifying the engineering of two atoms interactions using state-selective optical lattices, see Chap. 7.

3. Engineering internal states of neutral atoms in an optical lattice

Engineering internal states of microscopic two-level quantum systems (qubits) forms the basis of a recently growing research field of experimental quantum physics, with implications for quantum information [13,14,16], quantum cryptography [115,116], and communication [117, 118]. Cesium atoms in optical lattices form ideal two-level quantum systems, exhibiting favorable properties for storing and processing of quantum information. Their easily accessible, long living internal states make them ideally suited for robust qubit states. In the past decade, experimental methods to prepare, coherently manipulate and detect internal states of individual cesium atoms have been developed [46–48]. Further methods, well-established in related research fields, have been recently adopted [119]. In this chapter, I present the technical implementation of these methods, analyzing their performance with regard to the state-selective transport and its applications.

3.1. State preparation and detection

In general, any state of a two-level quantum system can be generated by a sequence of unitary operations on a well-defined initial state. The initial state is usually one of the two basis states spanning the Hilbert space of the qubit $\mathcal{H}_{\mathrm{qbit}} = \mathbb{C}^2$. It is selected to provide a high preparation efficiency with a minimum of technical effort. For cesium atoms, the outermost Zeeman sublevels of the hyperfine ground states, $|0\rangle \equiv |F = 4, m_{\mathrm{F}} = 4\rangle$ and $|1\rangle \equiv |F = 3, m_{\mathrm{F}} = 3\rangle$, see Fig. 3.1(a), are ideally suited for the basis states. The $|0\rangle \leftrightarrow |1\rangle$ transition frequency can be easily tuned sufficiently far from other transition frequencies by an external magnetic field which lifts the degeneracy of the Zeeman sublevels. Both basis states play a particular role in the quantum state engineering adopted in this thesis: State $|0\rangle$ is selected as the initial state, being easily and reliably prepared using optical pumping, whereas state $|1\rangle$ is used for the state-selective detection. Both, state preparation and detection, but also any coherent manipulation on the qubit states are performed on molasses cooled atoms in an adiabatically lowered optical lattice with a depth of $k_{\mathrm{B}} \times 80\,\mu\mathrm{K}$, resulting in a typical temperature of the atoms of $10\,\mu\mathrm{K}$.

3.1.1. State initialization by optical pumping

To prepare trapped cesium atoms in the initial state $|0\rangle$, the atoms are optically pumped with a σ^+-polarized laser beam, which is resonant with the $F = 4 \rightarrow F' = 4$

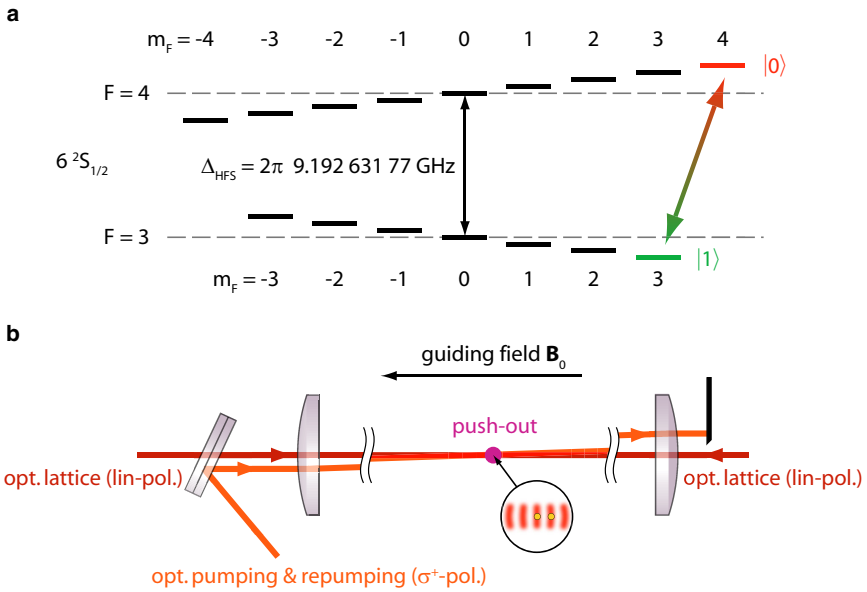

Figure 3.1.: (**a**) Zeeman splitting of magnetic sublevels in the $6^2S_{1/2}$ ground state manifold of cesium. The degeneracy of the magnetic sublevels is lifted by an external guiding field due to the linear Zeeman effect. State $|0\rangle = |F = 4, m_F = 4\rangle$ and state $|1\rangle = |F = 3, m_F = 3\rangle$ define the orthogonal basis states spanning the Hilbert space of the qubit. (**b**) Geometrical arrangement and polarizations of the laser beams used for state initialization and detection. The incident optical pumping and repumping beam is blocked after passing the trapping region.

transition. An equally polarized beam of the repumping laser, frequency stabilized on the $F = 3 \rightarrow F' = 4$ transition, is used to transfer the atoms back to the optical pumping cycle, whenever the atoms decay to the $F = 3$ ground state. Since the final state $|0\rangle$ is a dark state, scattering of photons during optical pumping cycles is reduced to a minimum. The power of the optical pumping ($P_{\mathrm{opt}} = 30\,\mathrm{nW}$) and repumping beam ($P_{\mathrm{rep}} = 7\,\mathrm{nW}$), as well as their pulse durations ($\tau_{\mathrm{opt}} = 20\,\mathrm{ms}$ and $\tau_{\mathrm{rep}} = 21\,\mathrm{ms}$), are experimentally optimized to prevent the atoms from being heated during the pumping process. The difference in pulse durations is deliberately chosen to ensure that the repumping laser is switched off long after the optical pumping laser, incorporating delays of the shutters.

As a source of the optical pumping light, we decouple a part of the unshifted MOT cooling laser, considering the fact that the $F = 4 \rightarrow F' = 3 - F' = 5$ crossover transition is detuned by only $+25\,\mathrm{MHz}$ from the required $F = 4 \rightarrow F' = 4$ transition. The small residual detuning is partly compensated by the light shift of the atomic transitions arising from the light field generating the optical lattice. For the repumping light, a part of the MOT repumping laser is decoupled.

The optical pumping and repumping beam are shined along the lattice axis, parallel to the quantization axis, see Fig. 3.1(b). The latter is defined by a magnetic

guiding field with a strength of $|B_0| = (2.95 \pm 0.02)\,\mathrm{G}$ (see Sec. 3.2.3), which counteracts depolarization of the optically pumped atoms due to uncompensated DC components and AC fluctuations of magnetic fields. To ensure polarization purity of both laser beams in the trapping region of the atoms, polarization distortions arising from optical elements in the beam path are precompensated using a combination of a polarizer, a half- and a quarter-wave plate, aligned to the maximum optical pumping efficiency.

The experimental setup of the states-selective optical lattice incorporates retardation elements affecting the polarization of the retro-reflected beam, see Sec. 4.3. To prevent the optical pumping and repumping beam from being retro-reflected and reentering the trapping region with a "wrong" polarization, both incident beams are slightly tilted with respect to the lattice axis, allowing them to be blocked after passing the trapping region. The earth magnetic field and other DC magnetic fields in this region are compensated using three orthogonal pairs of compensation coils, see Fig. 1.6(b) in Sec. 1.1.4. Perfect compensation is achieved by minimizing the width of a Zeeman spectrum [49]. Performing microwave spectroscopy on the $|0\rangle \leftrightarrow |1\rangle$ transition (see Sec. 3.2.3), the efficiency of optical pumping is measured to exceed 97%. A small loss in efficiency is attributed to the tilting angle of the optical pumping beam with respect to the quantization axis.

3.1.2. State-selective detection

The population in $F = 3$ (including the qubit basis state $|1\rangle$) is detected using a so-called "push-out" technique [49], which removes the atoms in $F = 4$ (including state $|0\rangle$) from the optical lattice while leaving those in $F = 3$ unaffected. For this, we shine a laser beam operating on the $F = 4 \rightarrow F = 5$ transition, perpendicular to the optical lattice axis, see Fig. 3.1(b). The power $P_{\mathrm{push}} = 40\,\mu\mathrm{W}$ and the pulse duration $\tau_{\mathrm{push}} = 150\,\mu\mathrm{s}$ of the push-out beam are optimized so that its radiation pressure force overcomes the radial dipole force and pushes the atoms in $F = 4$ out of the lattice within less than half a radial oscillation period. By this, we prevent off-resonant excitations to $F' = 4$, from where the atoms can spontaneously decay into the $F = 3$ ground state. For the push-out beam, we use the cooling laser beam of the MOT which is shined perpendicular to the lattice axis. It is tuned to resonance and switched using an AOM, while the retro-reflected beam and the other MOT beams are previously blocked using shutters. In contrast to Ref. [79], where the quantization axis is rotated along the push-out beam prior to the push-out to prevent spontaneously decay to $F = 3$ by employing the $(F = 4, m_{\mathrm{F}} = 4) \rightarrow (F = 5, m_{\mathrm{F}} = 5)$-transition, we intentionally oppose this strategy for two reasons: First, for our system, rotating the quantization axis by changing the direction of the guiding field does not provide any improvements in the push-out efficiency. Second, by omitting changes of the guiding field, additional delays of tens of milliseconds between state manipulation and detection are avoided. Furthermore, since there is no need for changing the guiding field within a short time interval, the stability of magnetic compensation and guiding fields generated by the

coils can be increased using low-pass filters with a high time constant ($> 20\,\mathrm{ms}$) for the respective driving currents.

The state-selective detection allows to directly infer the population of atoms in state $F = 3$ from the mean ratio of number of atoms initially loaded into the optical lattice and surviving the state-selective push-out. For M repetitions of an experimental sequence involving the push-out, the mean population in $F = 3$ is then given by

$$\widetilde{P}_{F=3} = \frac{1}{M} \sum_{k=1}^{M} \frac{N_{\mathrm{aft},k}}{N_{\mathrm{bef},k}}\,, \tag{3.1}$$

where $N_{\mathrm{bef},k}$ denotes the number of atoms determined from an initial image acquired before, and $N_{\mathrm{aft},k}$ the number of atoms in a subsequent (final) image acquired after the push-out. To infer the mean population in $F = 4$, atom losses within the time interval between each pair of acquired images have to be taken into account. Assuming these losses being state-independent, the mean population in $F = 4$ can be determined from

$$\widetilde{P}_{F=4} + \widetilde{P}_{F=3} = p_{\mathrm{sur}}(\tau_{\mathrm{img}})\,, \tag{3.2}$$

where $p_{\mathrm{sur}}(\tau_{\mathrm{img}})$ denotes the survival probability of the atoms within the time interval τ_{img} between the acquisition of each initial and final image. The survival probability can be directly measured by omitting the push-out in the sequence. We stress that populations of the atoms in states $F = 3$ and $F = 4$ should not be confused with the projections on these states, which can be defined by

$$P_{F=3} = \frac{\widetilde{P}_{F=3}}{p_{\mathrm{sur}}(\tau_{\mathrm{img}})} = \frac{\widetilde{P}_{F=3}}{\widetilde{P}_{F=3} + \widetilde{P}_{F=4}}\,, \tag{3.3a}$$

$$P_{F=4} = \frac{\widetilde{P}_{F=4}}{p_{\mathrm{sur}}(\tau_{\mathrm{img}})} = \frac{\widetilde{P}_{F=4}}{\widetilde{P}_{F=3} + \widetilde{P}_{F=4}}\,, \tag{3.3b}$$

obeying the normalization $P_{F=3} + P_{F=4} = 1$. These projections describe the probability of finding an atom in a given state if no atom loss occurs. The situation is different for measurements of population in the qubit basis states. Here, the population in state $|0\rangle$ can be directly measured by coherently inverting the basis states $|0\rangle$ and $|1\rangle$ prior to the push-out (see Sec 3.2.4), assuming negligible spin relaxations and photon scattering processes transferring the atoms into states lying outside the Hilbert space of the qubit.

The statistical accuracy of determining $\widetilde{P}_{F=3}$ from Eq. (3.1) increases with the number of atoms $N_{\mathrm{bef},k}$ initially loaded into the optical lattice and the number of repetitions M of the experimental sequence. It is also limited by the reliability of inferring the correct number of atoms in the optical lattice. For this reason, in experiments relying on atom counting in the MOT, the state-selective detection has provided only reasonably results for a small number of initially loaded atoms ($N_{\mathrm{bef},k} \approx 5$) [79]. Therefore, high numbers of repetitions have been used to sufficiently reduce the statistical error. By counting atoms directly in the optical lattice,

we overcome this restriction allowing the state-selective detection being performed on ensembles comprising higher number of initially loaded atoms ($N_{\mathrm{bef},k} \approx 30$). By this, the number of repetitions can be reduced down to $M = 5$.

The efficiency of our state-selective detection is measured according to Ref. [79]: We initialize the atoms in the ground state $F = 3$ and $F = 4$ by switching off the MOT repumping laser 1 ms before and after the cooling laser, respectively. For each of both initialized states, we determine the mean survival probability after the push-out from the ratios of the numbers of atoms, initially loaded and surviving the push-out operation, see Eq. (3.1). The mean survival probability of atoms prepared in $F = 4$ is smaller than 1%, whereas for atoms prepared in $F = 3$, it is larger than 99%, imposing a lower limit of the push-out efficiency.

3.2. Quantum state manipulation using microwave radiation

An attractive feature of a two-level quantum system (qubit) is its ability to be prepared in any desired superposition of its basis states

$$|\psi\rangle = \alpha|0\rangle + \beta|1\rangle \tag{3.4}$$

with $\alpha, \beta \in \mathbb{C}$ and $|\alpha|^2 + |\beta|^2 = 1$. This ability fundamentally distinguishes the qubit from its classical counterpart, the bit, opening up entirely new possibilities for the information science. While our preparation of qubit states is deterministic, employing coherent manipulations by driving magnetic dipole transitions between the basis states using microwave radiation, their measurement, however, is probabilistic and irreversible. It yields a collapse of the qubit states to a projection state, e.g. one of the basis states, either $|0\rangle$ or $|1\rangle$ with probability $|\alpha|^2$ and $|\beta|^2$, respectively. Since the adopted projective measurement of state $|1\rangle$ is unable to directly reveal the amplitudes α and β in Eq. (3.4), sequences of well-defined single-qubit operations prior to the projection are required to determine these amplitudes up to a global phase.

3.2.1. The Bloch sphere representation

An illustrative geometrical representation of a pure single qubit state is a vector with a tip on the surface of a so-called *Bloch sphere* — a unit sphere in $\mathbb{R}^3$. By transferring the complex amplitudes α and β into polar coordinates, the general qubit state of Eq. (3.4) can be rewritten as

$$|\psi\rangle = e^{i\gamma}\left(\cos(\theta/2)|0\rangle + e^{i\phi}\sin(\theta/2)|1\rangle\right), \tag{3.5}$$

where the polar $0 \leq \theta \leq \pi$ and azimuthal angle $0 \leq \phi \leq 2\pi$ define the position on the sphere. The tip of the *Bloch vector*, see Fig. 3.2(a), is thus specified by

$$\boldsymbol{u} \equiv (u, v, w) = (\cos\phi\sin\theta, \sin\phi\sin\theta, \cos\theta). \tag{3.6}$$

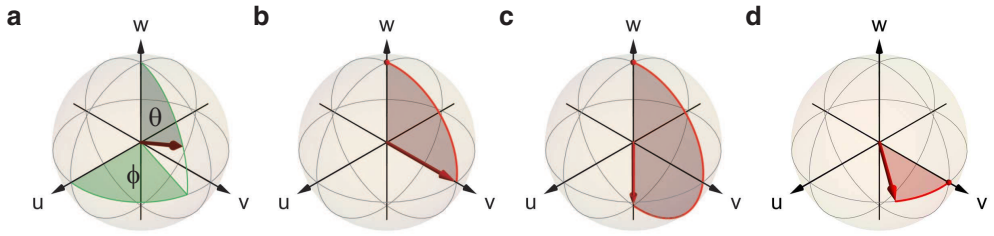

Figure 3.2.: (**a**) Bloch vector representation of a qubit state on a Bloch sphere. The Bloch vector is parameterized by the polar ϕ and azimuthal angle θ. (**b**) Evolution of the Bloch vector initialized in $\boldsymbol{u}(t_0) = (0, 0, 1)$ ($|0\rangle$) for a resonant $\pi/2$-pulse with $\phi_{\mathrm{rf}} = 0$, resulting in an equal superposition of the qubit basis states $|0\rangle$ and $|1\rangle$. Shaded regions in (**b**) and (**c**) indicate the rotation plane and the rotation angle $\theta_{\mathrm{rf}}(t)$. (**c**) A resonant π-pulse swaps the population of the two qubit basis states. (**d**) Without any driving ($\Omega_{\mathrm{R}} = 0$) the Bloch vector precesses around the w-axis. The accumulated phase $\Phi(t)$ is indicated by the shaded region.

The $+u$-, $+v$- and $+w$-axis of the Bloch sphere correspond to the qubit states $\frac{1}{\sqrt{2}}(|0\rangle + |1\rangle)$, $\frac{1}{\sqrt{2}}(|0\rangle + i|1\rangle)$ and $|0\rangle$, respectively. As long as the two-level quantum system is well isolated from its environment, different values of the global phase $0 \leq \gamma \leq 2\pi$ in Eq. (3.5) can be ignored. Being indistinguishable in a probabilistic projection measurement, they are represented by the same vector on the Bloch sphere.

The time evolution of a Bloch vector $\boldsymbol{u}(t)$ on the sphere due to interaction of magnetic dipole moment of the atom μ with an oscillating, near-resonant microwave radiation field is well approximated by the semiclassical description of the optical Bloch equations [120, 121]: Let B_{rf} be the strength, ω the frequency and ϕ_{rf} the phase of the microwave radiation field, $B_{\mathrm{rf}} \cos(\omega t + \phi_{\mathrm{rf}})$, then the Bloch equations in the reference frame rotating at the microwave frequency read [120, 121]

$$\dot{\boldsymbol{u}} = -\boldsymbol{\Omega} \times \boldsymbol{u}\,, \tag{3.7}$$

where $\boldsymbol{\Omega} \equiv (\Omega_{\mathrm{R}} \cos\phi_{\mathrm{rf}}, -\Omega_{\mathrm{R}} \sin\phi_{\mathrm{rf}}, \delta)$ denotes the torque vector, $\Omega_{\mathrm{R}} = \mu B_{\mathrm{rf}}/\hbar$ the Rabi frequency and $\delta = \omega - \omega_0$ the detuning of the microwave frequency ω from the $|0\rangle \leftrightarrow |1\rangle$ transition frequency ω_0. The u and v components of the Bloch vector can be interpreted as the in-phase and in-quadrature components with respect to the driving field, whereas the w component describes the population difference of the two atomic levels $w = +1$ and $w = -1$, corresponding to state $|0\rangle$ and $|1\rangle$, respectively.

For any microwave driven, coherent manipulation on the two-level quantum system in a well-defined state, the evolution of the Bloch vector on the sphere can be directly deduced by solving the differential equations (3.7). For instance, driving the two-level system with a monochromatic radiation of constant amplitude,

the Bloch vector initialized in $\boldsymbol{u}(t_0) = (0, 0, 1)$ (state $|0\rangle$) performs a so-called Rabi oscillation, with the time evolution of the population difference given by

$$w(t) = 1 - 2\frac{\Omega_\mathrm{R}^2}{\Omega^2}\sin^2\left(\frac{\Omega t}{2}\right), \tag{3.8}$$

where $\Omega = \sqrt{\Omega_\mathrm{R}^2 + \delta^2}$ denotes the *generalized* Rabi frequency. From Eq. (3.8), we infer that a complete population transfer is only achievable for the resonant case ($\delta = 0$), yielding $\boldsymbol{u}(t) = (\sin(\Omega_\mathrm{R}t)\sin\phi_\mathrm{rf}, \sin(\Omega_\mathrm{R}t)\cos\phi_\mathrm{rf}, \cos(\Omega_\mathrm{R}t))$. Therefore, resonant microwave pulses rotate the initial Bloch vector $\boldsymbol{u}(t_0) = (0, 0, 1)$ around the axis defined by a vector $\boldsymbol{r}(\phi_\mathrm{rf}) = (\cos\phi_\mathrm{rf}, -\sin\phi_\mathrm{rf}, 0)$ in the uv-plane, e.g. the u-axis for $\phi_\mathrm{rf} = 0$, see Fig. 3.2(b), or v-axis for $\phi_\mathrm{rf} = -\pi/2$. The same applies for an arbitrary initial Bloch vector $\boldsymbol{u}(t_0) = (u_0, v_0, w_0)$, yielding

$$\boldsymbol{u}(t) = \boldsymbol{\Theta}(t, \phi_\mathrm{rf})\boldsymbol{u}(t_0) \tag{3.9}$$

with the rotation matrix

$$\boldsymbol{\Theta}(t, \phi_\mathrm{rf}) = \begin{pmatrix} r_u^2 + (1 - r_v^2)\cos(\Omega_\mathrm{R}t) & r_u r_v(1 - \cos(\Omega_\mathrm{R}t)) & -r_v\sin(\Omega_\mathrm{R}t) \\ r_u r_v(1 - \cos(\Omega_\mathrm{R}t)) & r_v^2 + (1 - r_v^2)\cos(\Omega_\mathrm{R}t) & r_u\sin(\Omega_\mathrm{R}t) \\ r_v\sin(\Omega_\mathrm{R}t) & -r_u\sin(\Omega_\mathrm{R}t) & \cos(\Omega_\mathrm{R}t) \end{pmatrix}, \tag{3.10}$$

where $r_u = \cos(\phi_\mathrm{rf})$ and $r_v = -\sin(\phi_\mathrm{rf})$ are the two non-zero components of the vector $\boldsymbol{r}(\phi_\mathrm{rf}) = (r_u, r_v, 0)$ defining the rotation axis. The rotation angle corresponds to the integral of the Rabi frequency over the pulse duration t

$$\theta_\mathrm{rf}(t) = \int_0^t \Omega_\mathrm{R}(t')\mathrm{d}t', \tag{3.11}$$

where the time-dependency of $\Omega_\mathrm{R}(t')$ incorporates possible modulation of the Rabi frequency during the pulse, e.g. by modulating the strength of the microwave radiation. Therefore, any transformation of the Bloch vector can be carried out by a sequence of rotations on the Bloch sphere implemented by resonant pulses with controlled duration and phase.

It is often convenient to characterize the effect of a pulse by the area enclosed by the integral of Eq. (3.11). Two types of pulses commonly used throughout this thesis are the resonant ($\theta_\mathrm{rf}(t) = \pi/2$)-pulse and the ($\theta_\mathrm{rf}(t) = \pi$)-pulse. A resonant $\pi/2$-pulse rotates the Bloch vector initialized in one of the two qubit basis states $|0\rangle$ and $|1\rangle$ into the uv-plane, creating an equal superposition of these states, see Fig. 3.2(b). It is commonly used in the Ramsey spectroscopy to measure coherence properties of a two-level quantum system, see Sec. 3.3.2. A resonant π-pulse swaps the population of the qubit basis states, see Fig. 3.2(c). It is an inherent part of the state-selective transport (see Sec. 4.5) as well as any spin-echo sequence, being usually used as a rephasing pulse, see Sec. 3.3.3.

Operation	Symbol	Dirac representation	Matrix representation
$\pi/2$-pulse ($\phi_{\mathrm{rf}}=0$, $\delta=0$)	$\hat{U}_{\pi/2}$	$\|0\rangle \to \frac{1}{\sqrt{2}}\left(\|0\rangle + i\|1\rangle\right)$ $\|1\rangle \to \frac{i}{\sqrt{2}}\left(\|0\rangle - i\|1\rangle\right)$	$\frac{1}{\sqrt{2}}\begin{pmatrix}1 & i\\ i & 1\end{pmatrix}$
$\pi/2$-pulse ($\phi_{\mathrm{rf}}\in\mathbb{R}$, $\delta=0$)	$\hat{U}_{\pi/2,\phi_{\mathrm{rf}}}$	$\|0\rangle \to \frac{1}{\sqrt{2}}\left(\|0\rangle + ie^{-i\phi_{\mathrm{rf}}}\|1\rangle\right)$ $\|1\rangle \to \frac{ie^{i\phi_{\mathrm{rf}}}}{\sqrt{2}}\left(\|0\rangle - ie^{-i\phi_{\mathrm{rf}}}\|1\rangle\right)$	$\frac{1}{\sqrt{2}}\begin{pmatrix}1 & ie^{i\phi_{\mathrm{rf}}}\\ ie^{-i\phi_{\mathrm{rf}}} & 1\end{pmatrix}$
π-pulse ($\phi_{\mathrm{rf}}=0$, $\delta=0$)	$\hat{U}_{\pi}$	$\|0\rangle \to i\|1\rangle$ $\|1\rangle \to i\|0\rangle$	$\begin{pmatrix}0 & i\\ i & 0\end{pmatrix}$
$3\pi/2$-pulse ($\phi_{\mathrm{rf}}=0$, $\delta=0$)	$\hat{U}_{3\pi/2}$	$\|0\rangle \to \frac{-1}{\sqrt{2}}\left(\|0\rangle - i\|1\rangle\right)$ $\|1\rangle \to \frac{i}{\sqrt{2}}\left(\|0\rangle + i\|1\rangle\right)$	$\frac{1}{\sqrt{2}}\begin{pmatrix}-1 & i\\ i & -1\end{pmatrix}$
$3\pi/2$-pulse ($\phi_{\mathrm{rf}}\in\mathbb{R}$, $\delta=0$)	$\hat{U}_{3\pi/2,\phi_{\mathrm{rf}}}$	$\|0\rangle \to \frac{-1}{\sqrt{2}}\left(\|0\rangle - ie^{-i\phi_{\mathrm{rf}}}\|1\rangle\right)$ $\|1\rangle \to \frac{ie^{i\phi_{\mathrm{rf}}}}{\sqrt{2}}\left(\|0\rangle + ie^{-i\phi_{\mathrm{rf}}}\|1\rangle\right)$	$\frac{1}{\sqrt{2}}\begin{pmatrix}-1 & ie^{i\phi_{\mathrm{rf}}}\\ ie^{-i\phi_{\mathrm{rf}}} & -1\end{pmatrix}$
free evolution ($\Omega_{\mathrm{R}}=0$, $\delta\in\mathbb{R}$)	$\hat{Q}_{\Phi(t)}$	$\|0\rangle \to e^{i\Phi(t)/2}\|0\rangle$ $\|1\rangle \to e^{-i\Phi(t)/2}\|1\rangle$	$\begin{pmatrix}e^{i\Phi(t)/2} & 0\\ 0 & e^{-i\Phi(t)/2}\end{pmatrix}$

Table 3.1.: Dirac and matrix representation of the most common qubit operations.

Without any driving ($\Omega_{\mathrm{R}}=0$, $\mathbf{\Omega}=(0,0,\delta)$) the Bloch vector precesses around the w-axis with the angular frequency determined by δ, see Fig. 3.2(d). The accumulated phase during this free evolution is given by

$$\Phi(t) = \int_0^t \delta(t')\mathrm{d}t' \,. \tag{3.12}$$

In some parts of this thesis, the Dirac notation rather than the Bloch vector representation is used. The time evolution of the quantum state of the two-level system driven with monochromatic radiation resonant to the $|0\rangle \leftrightarrow |1\rangle$ transition is then expressed by a unitary operator. Its matrix representation reads

$$\hat{U}_{\theta_{\mathrm{rf}}(t),\phi_{\mathrm{rf}}} \equiv \exp\left(i\frac{\theta_{\mathrm{rf}}(t)}{2}\boldsymbol{r}(\phi_{\mathrm{rf}})\hat{\boldsymbol{\sigma}}\right) = \cos\left(\frac{\theta_{\mathrm{rf}}(t)}{2}\right)\hat{\mathbb{1}} + i\sin\left(\frac{\theta_{\mathrm{rf}}(t)}{2}\right)\boldsymbol{r}(\phi_{\mathrm{rf}})\hat{\boldsymbol{\sigma}}\,, \tag{3.13}$$

where the basis is defined by $|0\rangle \equiv (1,0)$ and $|1\rangle \equiv (0,1)$, respectively, and $\hat{\boldsymbol{\sigma}} = (\hat{\sigma}_u, \hat{\sigma}_v, \hat{\sigma}_w)$ denotes the Pauli "vector" with the Pauli matrices

$$\hat{\sigma}_u \equiv \hat{\sigma}_1 = \begin{pmatrix}0 & 1\\ 1 & 0\end{pmatrix}\,,\ \hat{\sigma}_v \equiv \hat{\sigma}_2 = \begin{pmatrix}0 & -i\\ i & 0\end{pmatrix} \text{ and } \hat{\sigma}_w \equiv \hat{\sigma}_3 = \begin{pmatrix}1 & 0\\ 0 & -1\end{pmatrix}\,. \tag{3.14}$$

The Dirac and matrix representation of the most common qubit operations employed in this thesis are listed in Tab. 3.1.

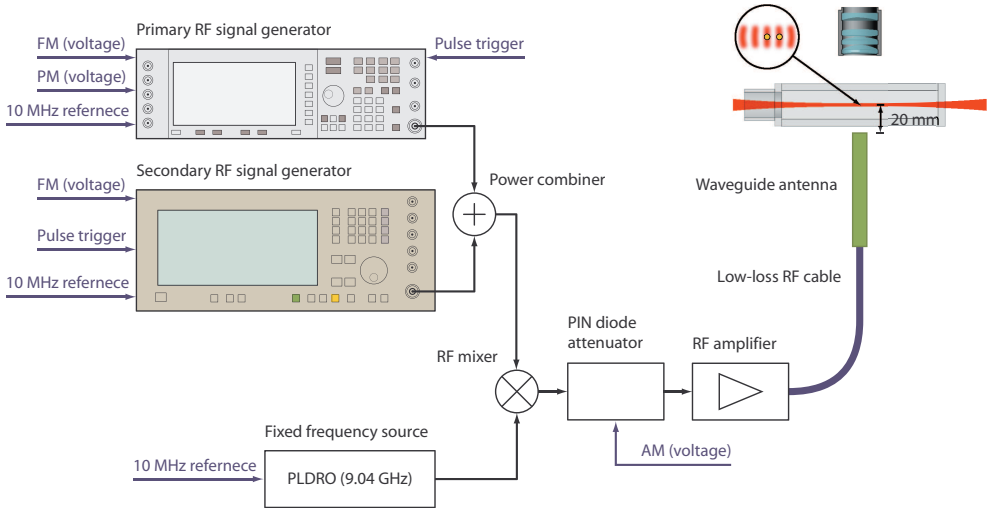

Figure 3.3.: Microwave setup for coherent manipulation of the qubit states of individual atoms. Both RF signal generators and the fixed frequency source are frequency stabilized to a 10 MHz rubidium frequency standard. Frequency (FM) and phase modulation (PM) of the generators are voltage controlled using arbitrary waveform generators or computer-controlled analog output devices. An analog PIN diode attenuator is used for amplitude modulation (AM).

3.2.2. Experimental setup

To generate microwave pulses, a cost efficient solution is used: The RF signal of a fixed frequency source is mixed with the signal of one of the two narrow-band vector signal generators — a *primary* generator with a frequency range of 250 kHz . . . 3.2 GHz and a *secondary* generator with 300 kHz . . . 3.3 GHz. Since most experiments presented in this thesis require either frequency modulation (FM), including stepwise frequency sweeps, or phase modulation (PM), in most cases, only one, namely the primary signal generator is used. The situation is different for experiments employing fast multiple pulse sequences, e.g. controlled collisions of two individual atoms (see Chap. 7), whereof one part of pulses is frequency modulated while another part is phase modulated. Due to the limited dwell time of tens of milliseconds required for changing the modulation mode, both modulations cannot be simultaneously controlled by a single generator. For these experiments both signal generators are sequentially used in combination: one for FM pulses, the other for PM pulses. In the following, a brief overview of the individual components of the microwave setup is given and schematically shown in Fig. 3.3.

Primary RF signal generator The primary vector signal generator (Agilent E4432B ESG-D, 250 kHz . . . 3 GHz) permits frequency and phase modulation employing either the internal modulation source, a 40 MHz arbitrary waveform generator featuring 14 bit resolution, or external modulation sources using two

external analog input channels. The I-Q-modulation option of the generator has not been used so far. Both, frequency and phase modulation can be also operated in a stepped sweep or a list mode with a minimum dwell time of 2 ms and a maximum frequency and phase deviation of 0.1%. The generator permits externally triggered pulse operation with rising and falling times of 150 ns, providing a typical output power of +13 to −136 dBm in the relevant frequency range of 250 kHz . . . 1 GHz. The pulse triggers are generated either by an arbitrary waveform generator (e.g. Agilent 33250A) for timing-critical applications or the computer control system, see Sec. 1.3. We operate the signal generator with an output power of 14.1 dBm, adjusted for optimum performance with all subsequent, serially connected RF components. The generator is frequency stabilized to a rubidium frequency standard — a low phase noise, 10 MHz rubidium-disciplined crystal oscillator (Stanford Research Systems, PRS10).

For practical reasons, in most experiments involving timing-critical sequences, we prefer to modulate the frequency and phase of the pulses using an external arbitrary waveform generator (e.g. Agilent 33250A) rather than internal modulation source. This strategy simplifies the monitoring, adjusting and synchronizing of pulse timings to other computer-controlled components of the experimental setup.

Secondary RF signal generator The secondary vector signal generator (Rohde & Schwarz SMIQ03B, 300 kHz . . . 3.3 GHz) is frequency stabilized to the same rubidium frequency standard. It permits comparable properties to the primary one. This generator is only used in experiments involving controlled collisions of two individual atoms, generating fast pulse trains with variable frequency. Its optimum output power is set at 12.1 dBm.

Power combiner We use a zero-degree resistive (50 Ω) power combiner (Mini-Circuits ZFRSC-123-S+) with a frequency range of DC to 12 GHz to combine the RF signals of both signal generators into a single output. The resistive component prevents reflections of the incident RF signals back to the respective sources due to mismatched impedances, which otherwise would cause distortions of the RF signal.

Fixed frequency source As a fixed frequency source, we use a *phase-locked dielectric resonator oscillator* (PLDRO, MITEQ PLDRO-10-09040-3-15P) with a frequency of 9.04 GHz. The PLDRO is frequency stabilized to a rubidium frequency standard. The measured single sideband phase noise of the PLDRO at a frequency offset of 1 kHz from the carrier is lower than −105 dBc/Hz [122].

RF mixer The output signal of the power combiner is mixed with the RF signal of the fixed frequency source using a single sideband upconverter (MITEQ SSM0812LC2CDC). The latter generates an upper sideband with the summed frequency of both signals at the inputs while suppressing the carrier and the

lower sideband by 30 dB and 35 dB, respectively. A measured output spectrum is shown in Ref. [122].

Analog PIN diode attenuator To modulate the amplitude of the RF signals, e.g. for generating Gaussian-shaped pulses (see Sec. 3.4.4), we use a PIN[1] diode attenuator (MITEQ MPAT-08001200-60-10) with a rising time of 150 ns and a maximum attenuation of 63 dB. The dependency of the attenuation on the control voltage ($U = 0 \ldots 10\,\mathrm{V}$) is non-linear. For pulse shaping, we comprise this nonlinearity by a previously measured calibration curve. From a fit to the measured calibration curve, we deduce that the signal output amplitude of the PIN attenuator scales with $A_{\mathrm{out}} = C(U/V)A_{\mathrm{inp}}$, where A_{inp} denotes the signal amplitude at input and $C_{\mathrm{amp}}(U/V) = a(U/V)^{-b}$ the scaling function with $a = 0.191 \pm 0.003$ and $b = -2.57 \pm 0.03$. Even though both RF signal generators permit amplitude modulation using an external analog input channel, the properties of the upconverter significantly change with its input level. For this reason, both signal generators are operated at a fixed optimum output power, while amplitude modulation is performed on the mixed RF signal.

RF amplifier and antenna The amplifier (MITEQ AMF-6B-08500950-40-41P-TTL) amplifies the RF signal by 50 dB up to a maximum output power of 41 dBm (12.5 W) at a noise figure of 2.3 dB. It is mounted on a water-cooled plate for heat dissipation, which in contrast to an air-cooling solution, prevents from heating of the surrounding optical elements. The output signal of the amplifier is guided by a low-loss (0.52 dB/m) RF cable (Spectrum Elektrotechnik 300-1300-11-11) with a length of 1.3 m to a waveguide-to-coax adapter (FLANN 15094-SF40). This adapter is flanged to a terminator with an open end (FLANN 15040) forming a microwave waveguide antenna. Its rectangular cross-section is small enough to fit between the MOT coils, allowing to put the end of the waveguide antenna close to the UHV glass cell, 2 cm away from the trapping region of the atoms. Following Reference [47], the inner walls of the waveguide antenna have been sharpened at the output to reduce reflections. The position and orientation of the antenna has been iteratively optimized to maximize the intensity I_{rf} of the microwave radiation in the trapping region of the atoms. In each iteration the Rabi frequency $\Omega_{\mathrm{R}} \propto \sqrt{I_{\mathrm{rf}}}$ has been measured (see Sec. 3.2.3), resulting in a maximum Rabi frequency of $\Omega_{\mathrm{R}} = 2\pi \times (60 \pm 1)\,\mathrm{kHz}$.

3.2.3. Microwave spectroscopy

Coherent manipulation of qubit states using a sequence of resonant microwave pulses requires the $|0\rangle \leftrightarrow |1\rangle$ transition frequency to be precisely known. This frequency is shifted with respect to the hyperfine transition frequency Δ_{HFS} mainly due to the linear Zeeman effect of the guiding field, see Fig. 3.1. The quadratic

[1] PIN: Positive-Intrinsic-Negative.

Zeeman effect and the differential light shifts of states $|0\rangle$ and $|1\rangle$, induced by the light field generating the optical lattice, contribute lesser, but still measurably to the total shift. Each shift contribution depends on a variety of experimental parameters, which are not only affected by the everyday alignment but also by technical imperfections of the experimental setup. Most of these imperfections are fluctuations on short time scales (noise) or long-term drifts decreasing the reproducibility of repeatable sequences required in probabilistic measurements. The Zeeman shifts, for instance, depend on the spatial homogeneity of magnetic fields in the trapping region of the atoms and their stability over time. The light shifts, in turn, are affected by power and frequency stability of the laser generating the optical lattice, but also by the purity of polarization and geometrical alignment of the counter-propagating beams. The effects of these imperfections on the total shift have been investigated in detail on a comparable experiment [49, 79]. Theoretical estimations concerning our experiment can be found in Ref. [78].

In addition, there are contributions which indirectly affect the transition frequency via one of the two shift types. The temperature of the atoms, for instance, determines the energy distribution of the atoms and thus the spread of the atomic wave function of each atom in its trapping potential of the optical lattice. Due to the lattice geometry, a large spread of the wave function, especially in the less confined radial direction, yields a broadening of the energy levels defining the qubit basis states. Thus, performing repeatable measurements on an atomic ensemble, the $|0\rangle \leftrightarrow |1\rangle$ transition line is effectively broadened. Let $p(\delta)$ be a normalized detuning distribution describing the broadening of the transition frequency, then the measured microwave spectrum can be mathematically expressed as a convolution of the ideal, Fourier-limited spectrum $P(\delta)$ with the detuning distribution

$$\bar{P}(\delta) = \int_{-\infty}^{\infty} p(\delta')P(\delta - \delta')\,\mathrm{d}\delta' \,. \tag{3.15}$$

From Eq. (3.15), two characteristic properties of the measured spectrum can be deduced: First, since $p(\delta)$ is a normalized distribution with a finite support, the widths of the peaks in the measured spectrum $\bar{P}(\delta)$ are increased compared to the ideal spectrum, while their heights are decreased. Second, assuming the ideal spectrum to be locally symmetric around a peak at a resonance frequency, this symmetry is not maintained for the measured spectrum whenever an asymmetric distribution $p(\delta)$ is involved. Asymmetric distributions are mostly attributed to temperature effects described by the Boltzmann distribution, see Sec. 3.3.2.

The dependency of the $|0\rangle \leftrightarrow |1\rangle$ transition frequency on various experimental parameters affected by long-term drifts or changes in the everyday alignment, requires a simple measurement technique to calibrate this frequency immediately prior to the sequences involving qubit operations. The microwave spectroscopy is ideally suited for this purpose. On the one hand, it allows to easily determine the transition frequency with a high precision. On the other hand, from the shape of the microwave spectrum, experimental imperfection affecting the Zeeman shifts and the light shifts

entering the spectrum by a characteristic distribution $p(\delta)$ (see Eq. (3.15)) can be inferred. The most critical parameters of our experimental setup, including the polarization purity of the light field generating the optical lattice and the temperature of the trapped atoms affected by the efficiency of the optical molasses, can be directly probed by the atoms themselves. This property is utilized in the everyday alignment, whereby the Fourier limited spectrum serves as a reference. Note that even though the microwave spectrum reveals experimental imperfections, in general, their sources cannot be directly distinguished from a single spectrum alone.

Experimental sequence

To record a microwave spectrum, we stepwise sweep the microwave frequency $\omega_i = \omega_1 + (i-1)\delta\omega$ $(i = 1, \ldots, K)$ within a frequency region of interest $I = [\omega_1, \omega_K]$ including the $|0\rangle \leftrightarrow |1\rangle$ transition frequency in its center. For this, we use the frequency modulation of the (primary) RF signal generator in a triggered, stepped sweep mode. The number of steps K defines the step size $\delta\omega = (\omega_K - \omega_1)/K$ and thus, the sampling resolution of the recorded spectrum. The sequence to record a microwave spectrum is computer-controlled, comprising the following steps:

(A) The atoms are initially loaded into the MOT and subsequently transferred into the optical lattice with an initial depth of $k_\mathrm{B} \times 0.4\,\mathrm{mK}$, by switching off the magnetic field gradient. The strength of the field gradient, the loading and transfer time are chosen in such a way that on average 30 atoms remain in the optical lattice after the transfer. The molasses parameters, including the power ($60\,\mu$W per beam) and detuning of the cooling laser (25 MHz red-detuned with respect to the $F = 4 \rightarrow F' = 5$ transition), are adjusted for image acquisition, providing maximum fluorescence signal while avoiding heating of the atoms. The number of atoms initially loaded into the lattice $N_{\mathrm{bef},k}(\omega_i)$ is determined from a fluorescence image with an exposure time of 100 or 200 ms, see Sec. 2.3.1. After the image acquisition, molasses cooling is continued for another 10 ms with parameters adjusted for optimum cooling performance.[2] Finally, the cooling lasers are switched off. The optical lattice is adiabatically lowered to a depth of $k_\mathrm{B} \times 80\,\mu$K within 50 ms, while the guiding field is switched on.

(B) The atoms are initialized into the qubit basis state $|0\rangle$ using optical pumping, see Sec. 3.1.1

(C) For a predefined microwave power, controlled using the PIN diode attenuator, we apply a rectangular microwave pulse with the frequency ω_i and a duration meeting the π-pulse condition for resonant driving. The π-pulse condition is

[2] The molasses parameters for optimum cooling performance are adjusted in a preliminary measurement, by measuring the temperature of the atoms (see Ref. [65]) while the power and detuning of the cooling laser are successively scanned.

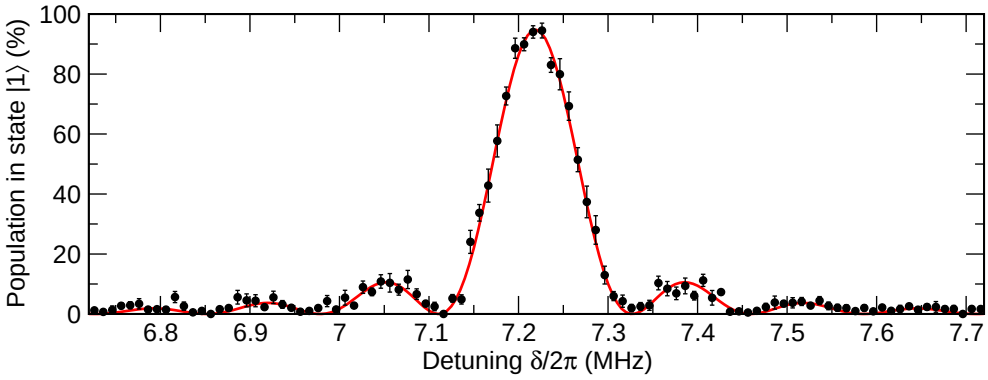

Figure 3.4.: Fourier limited microwave spectrum of a rectangular π-pulse with a duration of $8\,\mu$s, showing the population in state $|1\rangle$ as a function of detuning from the unshifted resonance frequency Δ_{HFS}. The solid line shows a fit of Eq. (3.16) to the data points.

found by iteratively recording microwave spectra and Rabi oscillations, see below.

(D) A subsequent application of the push-out removes the atoms in $F = 4$, including those in state $|0\rangle$ from the lattice (see Sec. 3.1.2), while atoms in state $|1\rangle$ remain unaffected.

(E) We switch off the guiding field, rise the depth of the optical lattice back to its initial value, switch on the optical molasses with parameters adjusted for image acquisition and acquire a final image, from which the number of remaining atoms $N_{\mathrm{aft},k}(\omega_i)$ is determined. The atoms are finally heated out off the lattice using the optical molasses, while lowering its depth to a minimum.

The internal sequence loop (A-E) is repeated M times and subsequently repeated with the next frequency ω_i until the border of the frequency region of interest is reached. From the numbers of atoms, $N_{\mathrm{bef},k}(\omega_i)$ and $N_{\mathrm{aft},k}(\omega_i)$, we calculate the population of atoms transferred to state $|1\rangle$ using Eq. (3.1), yielding a sampled microwave spectrum $\widetilde{P}_{|1\rangle}(\omega_i)$.

In Figure 3.4, a Fourier limited microwave spectrum of a rectangular microwave π-pulse with a duration of $8\,\mu$s is shown, plotted as a function of frequency detuning relative to the unshifted resonance frequency $\delta = \omega - \Delta_{\mathrm{HFS}}$. The spectrum is recorded with $M = 10$ repetitions and a sampling distance of $\delta\omega/2\pi = 10\,\mathrm{kHz}$. From the fit of a function based on Eq. (3.8)

$$\widetilde{P}_{|1\rangle}(\delta) = \widetilde{P}_{\max} \cdot \frac{1}{2}\left(1 + w(t)\right) = \widetilde{P}_{\max} \cdot \frac{\Omega_{\mathrm{R}}^2}{\Omega^2} \sin^2\left(\frac{\Omega t}{2}\right) \tag{3.16}$$

with $\Omega = \sqrt{\Omega_{\mathrm{R}}^2 + (\delta - \delta_0)^2}$ to the measured data, we infer a maximum population transfer of $\widetilde{P}_{\max} = (95 \pm 1)\%$, a Rabi-frequency of $\Omega_{\mathrm{R}} = 2\pi \times (60 \pm 1)\,\mathrm{kHz}$ and a

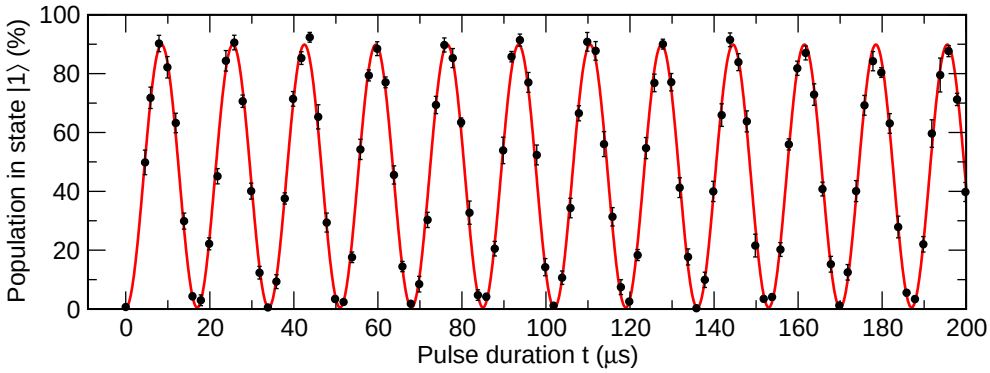

Figure 3.5.: Rabi oscillation between the qubit basis states $|0\rangle$ and $|1\rangle$. The solid line shows the fit of Eq. (3.17) to the data points.

shift of the peak position of $\delta_0 = 2\pi \times (7.2189 \pm 0.0006)\,\mathrm{MHz}$. The inferred pulse duration of $t = (8.06 \pm 0.04)\,\mu\mathrm{s}$ agrees well with the preset value. Note that the maximum population transfer $\widetilde{P}_{\mathrm{max}}$ is affected by the survival probability of the atoms within the time interval between the acquisition of each initial and final image, with a typical value of 98% for the used sequence. The remaining decrease of $\widetilde{P}_{\mathrm{max}}$ can be attributed to the limited optical pumping efficiency, since atoms in $|F = 4, m_{\mathrm{F}} \neq 4\rangle$ are far off-resonant due to the Zeeman shift in the presence of the guiding field and thus not affected by the microwave pulses. Dampings due to spin relaxations (see Sec. 3.3) are negligible for the short pulse duration.

From the peak position δ_0, the strength of the magnetic guiding field B_0 in the trapping region of the atoms can be directly inferred, considering the fact that the linear Zeeman effect provides the most dominant shift contribution, whereas contributions of quadratic Zeeman shift and differential light shifts are two orders of magnitude smaller. From $\delta_0/2\pi = (3g_3 - 4g_4)\mu_{\mathrm{B}}B_0/h$, where $g_4 \approx 1/4$ and $g_3 \approx -1/4$ denote the Landé factors, μ_{B} the Bohr magneton and h the Plank constant, we infer a strength of $|B_0| = (2.95 \pm 0.02)\,\mathrm{G}$.

Rabi oscillation

The measurement of Rabi oscillations provides a simple and accurate method to determine the Rabi frequency required to adjust the pulse duration of any resonant rectangular pulse $\theta_{\mathrm{rf}}(t) = \Omega_{\mathrm{R}}t$, see Eq. (3.11). For this, a similar sequence as for recording a microwave spectrum is used, whereas instead of the microwave frequency the pulse duration t is swept, while the microwave frequency is fixed to the measured $|0\rangle \leftrightarrow |1\rangle$ transition frequency, see above. In Figure 3.5, a measured Rabi oscillation with a sampling resolution of $2\,\mu\mathrm{s}$ is exemplarily shown. Note that the microwave power used in this measurement is slightly different from that of the recorded spectrum. Therefore, the measured spectrum and the Rabi oscillations should be regarded independently. From the fit of a function based on Eq. (3.8)

($\delta = 0$)

$$\widetilde{P}_{|1\rangle}(t) = \widetilde{P}_{\min} + \frac{\widetilde{P}_{\max} - \widetilde{P}_{\min}}{2}\left(1 - \cos\left(\Omega_R t\right)\right) \tag{3.17}$$

to the measured data, we obtain $\widetilde{P}_{\min} = (0.5 \pm 0.1)\%$, $\widetilde{P}_{\max} = (89.9 \pm 0.4)\%$ and $\Omega_{\mathrm{R}} = 2\pi \times (58.82 \pm 0.01)\,\mathrm{kHz}$. The deviation of $\widetilde{P}_{\min}$ from the zero value is attributed to the limited push-out efficiency, whereas a smaller value of $\widetilde{P}_{\max}$ compared to that of the recorded spectrum, mainly results from a reduced survival probability due to a larger time interval between the acquisition of each initial and final image. To restrict the effect of survival probability only to the maximum population transfer, removing its bias from possible decay of the Rabi oscillation with increasing time,[3] the time interval between the images is kept fixed, being defined by the maximum pulse duration in the sweep. By this, all measured data points are affected by the same survival probability value. From $\widetilde{P}_{\min}$ and $\widetilde{P}_{\max}$, we finally infer a fringe contrast of

$$C = \frac{\widetilde{P}_{\max} - \widetilde{P}_{\min}}{\widetilde{P}_{\min} + \widetilde{P}_{\max}} = (98.9 \pm 0.2)\%\,, \tag{3.18}$$

determining the reliability of coherent state manipulations.

3.2.4. Quantum state tomography

The methods presented so far revealed only a part of the information encoded into a quantum two-level system, namely the projection of the quantum state onto the basis state $|1\rangle$. In some cases, the complete quantum state $|\psi\rangle$, characterized by the complex amplitudes α and β in Eq. (3.4) or the polar and azimuthal angles ϕ and θ in Eq. (3.5), needs to be known. The *quantum state tomography* aims to determine this state up to a global phase through a series of projection measurements in different basis states. Since each projection measurement disturbs the quantum state, making it useless for further measurements, quantum state tomography must be carried out in stages on a number of identical copies of this state. In each stage a distinct aspect of the unknown state is revealed. The number of copies, generated by repeating an experimental sequence or performing measurements on ensembles of qubits, determines the accuracy of the extracted quantum state. Throughout this thesis, we focus on the state tomography of a single qubit. A more general review, including systems of many qubits in entangled states, can be found in Ref. [123,124] and references therein.

So far, we have considered a single qubit in a pure state $|\psi\rangle$, represented by Eqs. (3.4) and (3.5). However, measurements on ensembles of qubit states may comprise ensembles of different pure states. In that case, the overall state is called mixed. A *mixed* state is described by a probabilistically weighted incoherent sum

[3] For the recorded Rabi oscillation shown in Fig. 3.5 the decay in the oscillation amplitude due to spin relaxation is negligible and thus not considered in the fit function of Eq. (3.17).

of pure states, represented by a density matrix operator

$$\hat{\rho} = \sum_i p_i |\xi_i\rangle\langle\xi_i| \,, \tag{3.19}$$

where p_i denotes the probabilistic weights ($\sum_i p_i = 1$) and $|\xi_i\rangle$ the corresponding pure states. For an ensemble of isolated qubits, the matrix of this operator can be uniquely represented by only three parameters, S_1, S_2 and S_3 [125]:

$$\hat{\rho} = \frac{1}{2}\left(\hat{\mathbb{1}} + \sum_{i=1}^{3} S_i \hat{\sigma}_i\right) , \tag{3.20}$$

with the Pauli matrices $\hat{\sigma}_i$ defined in Eq. (3.14) and the parameters $S_i \in \mathbb{R}$ given by

$$S_i = \mathrm{Tr}\left\{\hat{\sigma}_i \hat{\rho}\right\} . \tag{3.21}$$

For a pure state, these parameters obey $\sum_i S_i^2 = 1$, whereas for a mixed state, it is $\sum_i S_i^2 < 1$. For $\sum_i S_i^2 = 0$ the density operator describes a completely mixed state. Each parameter S_i corresponds to the outcome of a specific pair of projective measurements on orthogonal basis states

$$S_1 = P_{\frac{1}{\sqrt{2}}(|0\rangle+|1\rangle)} - P_{\frac{1}{\sqrt{2}}(|0\rangle-|1\rangle)} \,, \tag{3.22a}$$

$$S_2 = P_{\frac{1}{\sqrt{2}}(|0\rangle+i|1\rangle)} - P_{\frac{1}{\sqrt{2}}(|0\rangle-i|1\rangle)} \,, \tag{3.22b}$$

$$S_3 = P_{|0\rangle} - P_{|1\rangle} \,, \tag{3.22c}$$

where $P_{|\xi\rangle}$ denotes the projection of $\hat{\rho}$ on state $|\xi\rangle$, i.e. the probability to measure state $|\xi\rangle$, given by [125]

$$\begin{aligned} P_{|\xi\rangle} &= \langle\xi|\hat{\rho}|\xi\rangle \\ &= \mathrm{Tr}\left\{|\xi\rangle\langle\xi|\hat{\rho}\right\} \end{aligned} \tag{3.23}$$

with

$$P_{|\xi\rangle} + P_{|\xi_\perp\rangle} = 1 \tag{3.24}$$

and $|\xi_\perp\rangle$ being the orthogonal complement of the basis state $|\xi\rangle$ obeying $\langle\xi|\xi_\perp\rangle = 0$, e.g. $|0_\perp\rangle = |1\rangle$, etc. By combining Eqs. (3.24) and (3.22), it appears that three projective measurements in the basis states $\frac{1}{\sqrt{2}}(|0\rangle + |1\rangle)$, $\frac{1}{\sqrt{2}}(|0\rangle + i|1\rangle)$ and $|0\rangle$ completely characterize the unknown quantum state $\hat{\rho}$. This result is evident considering the fact that the above basis states correspond to u-, v- and w axis of the Bloch sphere uniquely defining a point in $\mathbb{R}^3$, see Sec. 3.2.1. The parameters S_i, in turn, are directly related to the components of the Bloch vector, $\boldsymbol{u} = (u, v, w) = (S_1, S_2, S_3)$, extending the Bloch sphere representation to the mixed states: For pure quantum states, the tip of the Bloch vector lies on the surface of the Bloch sphere ($|\boldsymbol{u}| = 1$), whereas for mixed states it lies inside the sphere ($|\boldsymbol{u}| < 1$). A Bloch vector with

$|\boldsymbol{u}| = 0$ represents a completely mixed state, accordingly. The degree of "quantumness" of the system is commonly characterized by the polarization of the state

$$\Pi = \sqrt{S_1^2 + S_2^2 + S_3^2}\,, \tag{3.25}$$

specifying the length of the Bloch vector.

To perform quantum state tomography on a single qubit employing the state-selective detection presented in Sec. 3.1.2, some additional considerations have to be taken into account: First, due to atom losses in the optical lattice, either the population of the complement basis state $|\xi_\perp\rangle$ or the survival probability of the atoms $p_{\mathrm{sur}}(\tau_{\mathrm{img}})$ has to be additionally measured to determine the projection on the basis state $|\xi\rangle$, see Eq. (3.3). We prefer the former approach, even if twice as many population measurements are required. The surplus information content can be supportively used for consistency checks and error analysis, allowing to infer the reliability of determining the unknown quantum state. Second, since our state-selective detection enables only measurements of the population in state $|1\rangle$, proper microwave pulses have to be applied just before the detection to transform the remaining five states of interest onto the detectible state. A resonant $\pi/2$-pulse with $\phi_{\mathrm{rf}} = \pi/2$, for instance, transforms the basis state $\frac{1}{\sqrt{2}}(|0\rangle + |1\rangle)$, which is associated with the $+u$-axis of the Bloch Sphere, onto the detectible state $|1\rangle$ — the $-w$-axis of the Bloch sphere, see Sec. 3.2.1. The same can be attained for the basis state $\frac{1}{\sqrt{2}}(|0\rangle + i|1\rangle)$ ($+v$-axis) up to a global phase, applying a resonant $\pi/2$-pulse with $\phi_{\mathrm{rf}} = 0$ prior to the state-selective push-out. Finally, considering the fact that two orthogonal basis states can be transformed into each other by driving a resonant π-pulse, this pulse has to be applied prior to the push-out to measure the population in state $|0\rangle$. Accordingly, the populations of complement states to those above can be determined, by extending the respective pulses from $\pi/2$ to $3\pi/2$-pulses, i.e. a $3\pi/2$-pulse with $\phi_{\mathrm{rf}} = \pi/2$ for the population in state $\frac{1}{\sqrt{2}}(|0\rangle - |1\rangle)$ ($-u$-axis) and a $3\pi/2$-pulse with $\phi_{\mathrm{rf}} = 0$ for $\frac{1}{\sqrt{2}}(|0\rangle - i|1\rangle)$ ($-v$-axis). We summarize the above considerations, by mathematically expressing our implementation of the state tomography on a state $\hat{\rho}$ as follows:

$$S_1 = -1 + 2P_{\frac{1}{\sqrt{2}}(|0\rangle+|1\rangle)}[\hat{\rho}] = \frac{\widetilde{P}_{|1\rangle}[\mathcal{U}_{\pi/2,\pi/2}\hat{\rho}] - \widetilde{P}_{|1\rangle}[\mathcal{U}_{3\pi/2,\pi/2}\hat{\rho}]}{\widetilde{P}_{|1\rangle}[\mathcal{U}_{\pi/2,\pi/2}\hat{\rho}] + \widetilde{P}_{|1\rangle}[\mathcal{U}_{3\pi/2,\pi/2}\hat{\rho}]}\,, \tag{3.26a}$$

$$S_2 = -1 + 2P_{\frac{1}{\sqrt{2}}(|0\rangle+i|1\rangle)}[\hat{\rho}] = \frac{\widetilde{P}_{|1\rangle}[\mathcal{U}_{\pi/2}\hat{\rho}] - \widetilde{P}_{|1\rangle}[\mathcal{U}_{3\pi/2}\hat{\rho}]}{\widetilde{P}_{|1\rangle}[\mathcal{U}_{\pi/2}\hat{\rho}] + \widetilde{P}_{|1\rangle}[\mathcal{U}_{3\pi/2}\hat{\rho}]}\,, \tag{3.26b}$$

$$S_3 = -1 + 2P_{|0\rangle}[\hat{\rho}] = \frac{\widetilde{P}_{|1\rangle}[\mathcal{U}_{\pi}\hat{\rho}] - \widetilde{P}_{|1\rangle}[\hat{\rho}]}{\widetilde{P}_{|1\rangle}[\mathcal{U}_{\pi}\hat{\rho}] + \widetilde{P}_{|1\rangle}[\hat{\rho}]}\,, \tag{3.26c}$$

where brackets are used to distinguish the projection and population measurements on different density matrix operators and

$$\mathcal{U}\hat{\rho} \equiv \hat{U}\hat{\rho}\hat{U}^\dagger\,. \tag{3.27}$$

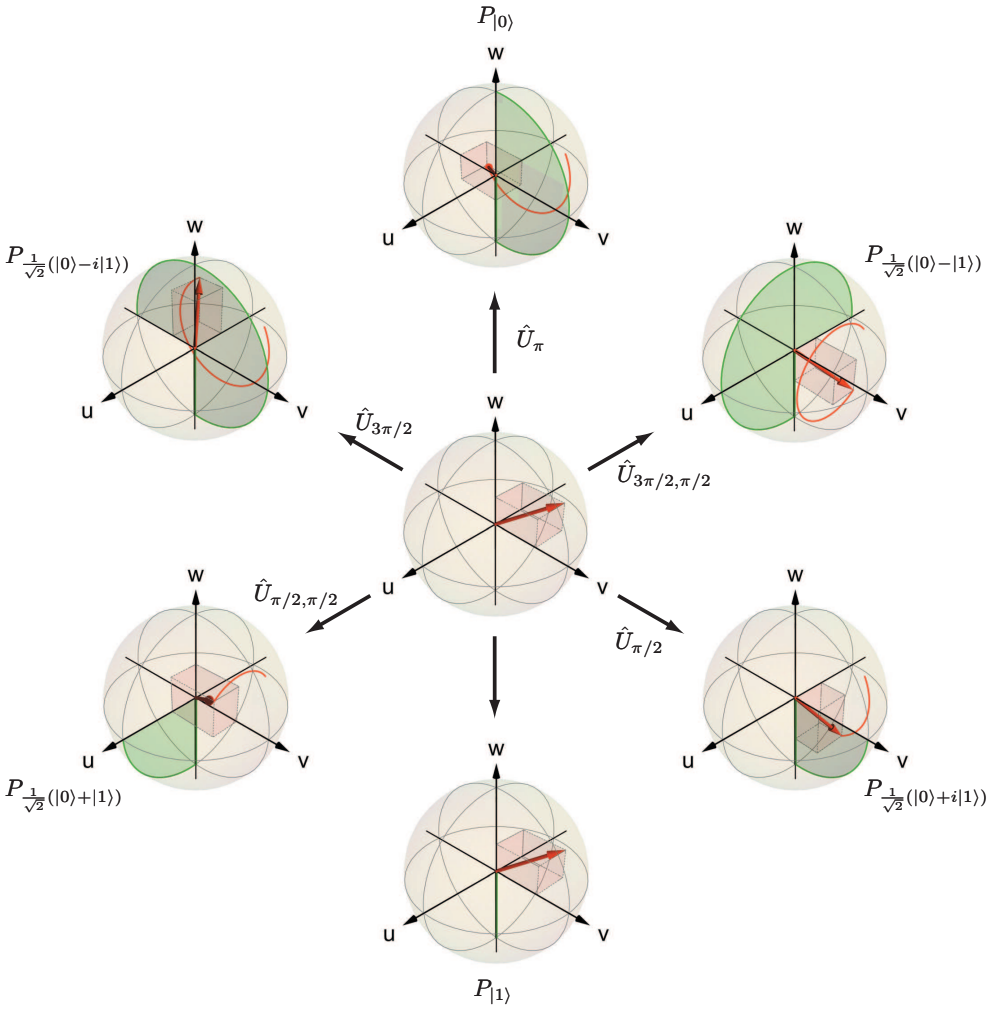

Figure 3.6.: Implementation of quantum state tomography for a state-selective detection restricted to only one directly detectible basis state $|1\rangle$. The unknown mixed state $\hat{\rho}$ is represented by a Bloch vector, the components of which are illustrated by a cuboid. Resonant microwave pulses with different phases transform (rotate) the remaining non-detectible basis states, $\frac{1}{\sqrt{2}}(|0\rangle + |1\rangle)$ ($+u$-axis), $\frac{1}{\sqrt{2}}(|0\rangle - |1\rangle)$ ($-u$-axis), $\frac{1}{\sqrt{2}}(|0\rangle + i|1\rangle)$ ($+v$-axis), $\frac{1}{\sqrt{2}}(|0\rangle - i|1\rangle)$ ($-v$-axis) and $|0\rangle$ ($+w$-axis) onto the detectible state $|1\rangle$ ($-w$-axis). A subsequent measurement of the population in state $|1\rangle$ after each transformation reveals a different aspect (component contribution) of the Bloch vector. The required unitary operations, performing rotations on the Bloch sphere are visualized by red trajectories for the Bloch vector, whereas (green) shaded areas indicate the rotation angle and the rotation plane for each transformed basis state (axis).

The respective unitary operators are defined in Tab. 3.1. Their Bloch sphere representations are show in Fig. 3.6.

Remarks on tomography errors

In practice, reconstruction of the density matrix from a series of independent measurements can never be performed exactly, especially if the measurements themselves contain statistical or systematical errors imposed by technical imperfections. In that case, independent projection measurements may even be contradictious, yielding unphysical parameters S_i which violates the relation $\sum_i S_i^2 \leq 1$. State tomography errors can be divided into three categories: errors in the projected basis, statistical errors and errors related to the stability of the experimental setup. Errors in the projection basis mostly arise from inaccurate microwave pulses, be it due to pulse amplitude, frequency or phase errors. These errors can be easily identified in preliminary measurements, e.g. using the microwave spectroscopy. Furthermore, since the influence of these errors on the reconstructed density matrix is predictable, they can be easily modeled and incorporated in commonly used maximum likelihood algorithms [123, 126] to constrainedly estimate the unknown state. The same applies for statistical errors, which can be easily reduced by generating a sufficiently large number of copies of the unknown state. In our experiment, errors related to the stability of the experimental setup are the most dominant errors, being attributed to technical limitations. These errors, however, are difficult to characterize. They arise from drifts of experimental parameters over time, affecting the time evolution of the unknown qubit state and the microwave operations over the course of tomography, either in creation of copies of the unknown state or its detection. Because a measurement of each basis state population takes approximately between 10-30 minutes, yielding total durations of 1-3 hours for a complete tomography, small changes in the experimental parameters are unavoidable. Since the time evolution of experimental parameters is not exactly known, it is nearly impossible to incorporate these errors in a numerical model which aims to constrain the reconstruction of the unknown state.

3.3. Coherence properties

Suppose there is a perfectly isolated two-level quantum system, the time evolution of which is unitary and thus reversible. Then, quantum information encoded in its state would be preserved forever. Although such an ideal system would be highly desirable, there is no perfectly isolated system in reality. A certain coupling of the qubit to its environment is always present. As a consequence, the two-level quantum system suffers decoherence — an irreversible evolution of an initially encoded pure state to a completely mixed state, manifesting itself in a loss of phase relation between two orthogonal basis states of the qubit. The characteristic timescale, on which this phase relation is preserved to a certain degree, is denoted as coherence time. The coherence time imposes a fundamental limit for most applications in

quantum information science. For this reason, it is important to precisely determine this quantity, identify the underlying decoherence mechanisms, and finally, infer to which extent the requirements imposed by the application are fulfilled. Ramsey spectroscopy [127, 128] has established itself for this purpose, becoming a standard technique which provides a direct insight into coherence properties of various quantum systems. In the following, we use this technique to investigate coherence properties of our system.

3.3.1. Classification of decoherence effects

Measurements of a quantum state employ statistically large samples of its copies, revealing only ensemble averages of microscopic polarizations. In this context, decoherence (or dephasing) of a quantum state manifest itself in a decay of the measured *macroscopic* polarizations. Although dephasing of a quantum system can be caused by a variety of effects, all of them can be classified into two main categories: *homogenous* and *inhomogeneous* dephasing effects. Homogeneous dephasing affects each qubit of the measured ensemble in the same way, whereas in case of inhomogeneous dephasing, the phase of each qubit evolves differently. In the context of quantum state engineering, however, the most significant difference between both dephasing types concerns the reversibility: While inhomogeneous dephasing can be reversed by spin-echo techniques (see Sec. 3.3.3), homogeneous dephasing is irreversible and rarely avoidable, imposing a limit on some of the experimental results presented in this thesis.

Optical Bloch equations with damping

So far, we have considered only the *coherent* evolution of a quantum two-level system interacting with an external microwave field, resulting in a reversible dynamics of its quantum state. This dynamics is adequately described by the optical Bloch equations (3.7), from which unitary operators, representing coherent manipulations on the quantum state can be directly inferred. In real situations, however, this system can irreversibly relax and dephase to a steady state. These relaxations can be phenomenologically included by extending the optical Bloch equations to ensembles of identical qubits, incorporating decay rates of population inversion $\langle w \rangle$ and coherence, $\langle u \rangle$ and $\langle v \rangle$, respectively. The resulting optical Bloch equations with damping are then given by [120, 121]

$$\langle \dot{u} \rangle = \delta \langle v \rangle - \Omega_{\mathrm{rf}} \sin(\phi_{\mathrm{rf}}) \langle w \rangle - \frac{\langle u \rangle}{T_2}\,, \tag{3.28a}$$

$$\langle \dot{v} \rangle = -\delta \langle u \rangle - \Omega_{\mathrm{rf}} \cos(\phi_{\mathrm{rf}}) \langle w \rangle - \frac{\langle v \rangle}{T_2}\,, \tag{3.28b}$$

$$\langle \dot{w} \rangle = \Omega_{\mathrm{rf}} \sin(\phi_{\mathrm{rf}}) \langle u \rangle - \Omega_{\mathrm{rf}} \cos(\phi_{\mathrm{rf}}) \langle v \rangle - \frac{\langle w \rangle - w_{\mathrm{st}}}{T_1}\,, \tag{3.28c}$$

where $\langle \ldots \rangle$ denotes ensemble average, T_1 the longitudinal relaxation time describing the decay of population $\langle w \rangle$ to a stationary value w_{st},[4] and T_2 the total transverse relaxation time, also referred to as the total dephasing time. This dephasing time, in turn, incorporates contributions of the polarization decay time T_2', and the reversible inhomogeneous dephasing time T_2^* by the following relation

$$\frac{1}{T_2} = \frac{1}{T_2'} + \frac{1}{T_2^*} \,. \tag{3.29}$$

Once these characteristic time constants are known, the evolution of the quantum state into a mixed state is predictable on all relevant time scales.

In our experiment, the longitudinal relaxation time T_1 is mainly affected by scattering of photons from the light field of the optical lattice, coupling the two hyperfine ground states via a two-photon Raman transition. It is of the order of 100 ms and thus considerably larger than the time interval in which preparation, manipulation and detection of quantum states is performed. Therefore, longitudinal relaxation plays only a minor role in experimental results presented in this thesis.

The polarization decay, characterized by the decay time T_2', arises from fluctuations of experimental parameters during the time interval of generating and detecting copies of a quantum state. These fluctuations are attributed to technical imperfections affecting the differential light shift and the Zeeman shift, and thus the $|0\rangle \leftrightarrow |1\rangle$ transition frequency of the atoms in the trapping region. Possible sources include intensity fluctuations of the light field generating the optical lattice, either due to laser power or beam pointing instabilities, but also retardation elements used for the implementation of state-selective lattice potentials. In particular, the electro-optical modulator (see Sec. 4.3) degrades the polarization purity of the light field, introducing an additional vulnerability to fluctuations of temperature and driving voltage of the modulator. Magnetic fields fluctuations are mostly attributed to driving currents of the coils, but also to stray fields from electronic devices in the lab.

The inhomogeneous dephasing time T_2^* is affected by inhomogeneous effects which assign each atom its own individual resonance frequency, resulting in macroscopic polarization damping of the ensemble. In our case, this dephasing is dominated by the finite temperature of the trapped atoms, yielding a thermal distribution of atomic motion in potential wells of the lattice, which translates into a distribution of differential light shift, see Sec. 3.3.2. This dominance and the relevant characteristic decay times can be directly deduced from the evolution of the macroscopic polarization and the phase of the qubits, measured using the Ramsey and spin-echo spectroscopy.

3.3.2. Ramsey spectroscopy

Ramsey spectroscopy is a standard technique to investigate coherence properties of a two-level quantum system, providing a direct insight into the underlying dephasing

[4] Note that atom losses in the optical lattice are not included in this decay time constants.

mechanisms. There are different variants of Ramsey sequences, including a time scan only, a combined frequency-time scan and a combined phase-time scan. Each of the them reveals a different aspect of the quantum system. While time evolution of its macroscopic polarization can be equally inferred from all three variants of Ramsey sequences, a combined frequency-time scan is particularly suited for high-precision frequency measurements, whereas a combined phase-time scan provides a direct insight into time evolution of the macroscopic phase. This so-called Ramsey phase spectroscopy is preferred throughout this thesis.

The experimental sequence of the Ramsey phase spectroscopy is similar to that of the microwave spectroscopy, see Sec. 3.2.3, except for step (C) and the scanned parameter. Instead, two resonant $\pi/2$-pulses separated by a preset time interval τ, the so-called *Ramsey time*, are applied, whereby the phase ϕ_{rf} of the final pulse is stepwise scanned. To understand the shape of the resulting Ramsey spectrum, in the following, we consider a single atom initially prepared in state $|0\rangle$. The first resonant $\pi/2$-pulse, represented by the unitary operator $\hat{U}_{\pi/2}$ (see Tab. 3.1), generates an equal superposition of the basis states $|0\rangle$ and $|1\rangle$

$$\hat{U}_{\pi/2}|0\rangle = \frac{1}{\sqrt{2}}\left(|0\rangle + i|1\rangle\right) , \tag{3.30}$$

rotating the initial Bloch vector $\boldsymbol{u}_0 = (0,0,1)$ to $\boldsymbol{u} = (0,1,0)$ in the uv-plane of the Bloch sphere. During the Ramsey time τ, the Bloch vector precesses in the uv-plane, accumulating a phase $\Phi_{\mathrm{a}}(\tau)$, see Fig. 3.7. The corresponding quantum state reads

$$\hat{Q}_{\Phi_{\mathrm{a}}(\tau)}\frac{1}{\sqrt{2}}\left(|0\rangle + i|1\rangle\right) = \frac{1}{\sqrt{2}}\left(e^{i\Phi_{\mathrm{a}}(\tau)/2}|0\rangle + ie^{-i\Phi_{\mathrm{a}}(\tau)/2}|1\rangle\right) . \tag{3.31}$$

The accumulated phase is finally probed using a second $\pi/2$-pulse with a preset Ramsey phase ϕ_{rf}. This pulse transforms the components of the Bloch vector from the uv-Plane onto a perpendicular plane containing the projection axis — the w-axis

$$\begin{aligned}&\hat{U}_{\pi/2,\phi_{\mathrm{rf}}}\frac{1}{\sqrt{2}}\left(e^{i\Phi_{\mathrm{a}}(\tau)/2}|0\rangle + ie^{-i\Phi_{\mathrm{a}}(\tau)/2}|1\rangle\right)\\ &= -ie^{i\phi_{\mathrm{rf}}/2}\sin\left(\frac{1}{2}\left[\phi_{\mathrm{rf}} - \Phi_{\mathrm{a}}(\tau)\right]\right)|0\rangle + ie^{-i\phi_{\mathrm{rf}}/2}\cos\left(\frac{1}{2}\left[\phi_{\mathrm{rf}} - \Phi_{\mathrm{a}}(\tau)\right]\right)|1\rangle .\end{aligned} \tag{3.32}$$

A subsequent projection of the resulting state onto the detectible basis state $|1\rangle$

$$P_{\mathrm{a},|1\rangle}(\phi_{\mathrm{rf}},\tau) = \left|\langle 1|\hat{U}_{\pi/2,\phi_{\mathrm{rf}}}\hat{Q}_{\Phi_{\mathrm{a}}(\tau)}\hat{U}_{\pi/2}|0\rangle\right|^2 = \frac{1}{2}\left\{1 + \cos[\phi_{\mathrm{rf}} - \Phi_{\mathrm{a}}(\tau)]\right\} \tag{3.33}$$

yields a cosinusoidal pattern for the scanned phase — the so-called *Ramsey fringe*.

The transition from a single atom to an ensemble of atoms is performed by ensemble averaging over all single-atom projection contributions. Note that, due to inhomogeneous dephasing, the accumulated phase of each atom can be different.

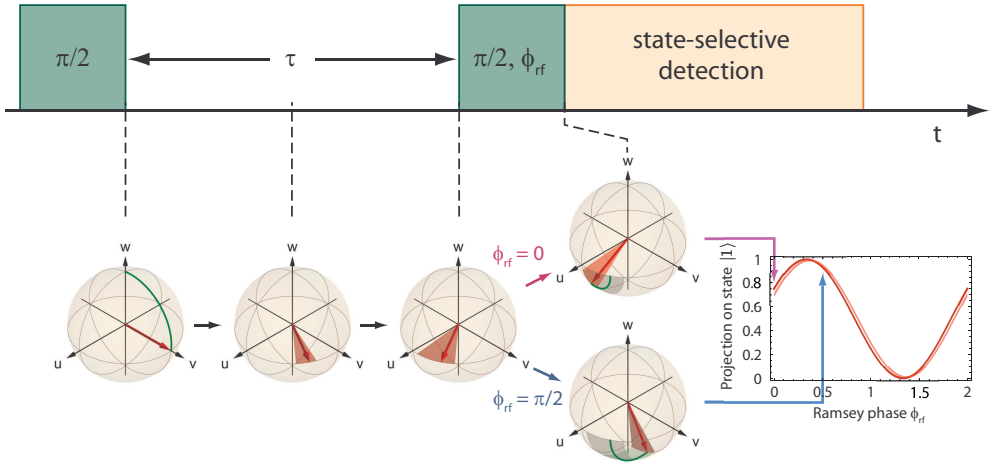

Figure 3.7.: Sequence of a Ramsey phase spectroscopy in Bloch sphere representation for an ensemble of qubits: The first $\pi/2$-pulse rotates the initial Bloch vectors in the uv-plane. A green trajectory shows the pulse driven evolution of a single Bloch vector of the ensemble. During the Ramsey time τ, each Bloch vector precesses in the uv-plane, e.g. due to a detuning between microwave radiation field and the $|0\rangle \leftrightarrow |1\rangle$ transition frequency. Dephasing is indicated by a shaded area. A final $\pi/2$-pulse with a preset phase ϕ_{rf} with respect to that of the first pulse (here $\phi_{\mathrm{rf}} = 0$ and $\phi_{\mathrm{rf}} = \pi/2$) maps the accumulated phases onto the projection axis (w-axis), resulting in a cosinusoidal Ramsey fringe.

The resulting population in state $|1\rangle$ as a function of Ramsey phase yields again a cosinusoidal Ramsey fringe

$$\begin{aligned}\widetilde{P}_{|1\rangle}(\phi_{\mathrm{rf}}, \tau) &= p_{\mathrm{sur}}(\tau_{\mathrm{img}}) \langle P_{\mathrm{a},|1\rangle}(\phi_{\mathrm{rf}}, \tau) \rangle \\ &= \frac{p_{\mathrm{sur}}(\tau_{\mathrm{img}})}{2} \left\{1 + C(\tau) \cos[\phi_{\mathrm{rf}} - \Phi(\tau)]\right\} \end{aligned} \tag{3.34}$$

with a modified Ramsey contrast $C(\tau)$, the accumulated *macroscopic* phase $\Phi(\tau)$ and the survival probability of the atoms in lattice $p_{\mathrm{sur}}(\tau_{\mathrm{img}})$, see Sec. 3.1.2.

To investigate the time evolution of the Ramsey contrast and the accumulated phase, Ramsey fringes are recorded for different values of Ramsey times using $\pi/2$-pulses with a typical pulse duration of $4\,\mu$s. The atomic ensembles contain on average 30 atoms. The Ramsey phase is typically scanned in an interval of $[0, 4\pi]$ using 25 equidistant steps. To reduce statistical errors, for each phase value of the scan interval, five repetitions of the Ramsey sequence are performed. Two recorded Ramsey fringes are exemplarily shown in Fig. 3.8(a,b).

From a fit of Eq. (3.34) to each of the recorded Ramsey fringes with the fit parameters $C(\tau)$, $\Phi(\tau)$ and $p_{\mathrm{sur}}(\tau_{\mathrm{img}})$, the Ramsey contrasts and the accumulated phases for different Ramsey times τ are inferred. The resulting time evolutions of both quantities are shown in Fig. 3.8(c,d).

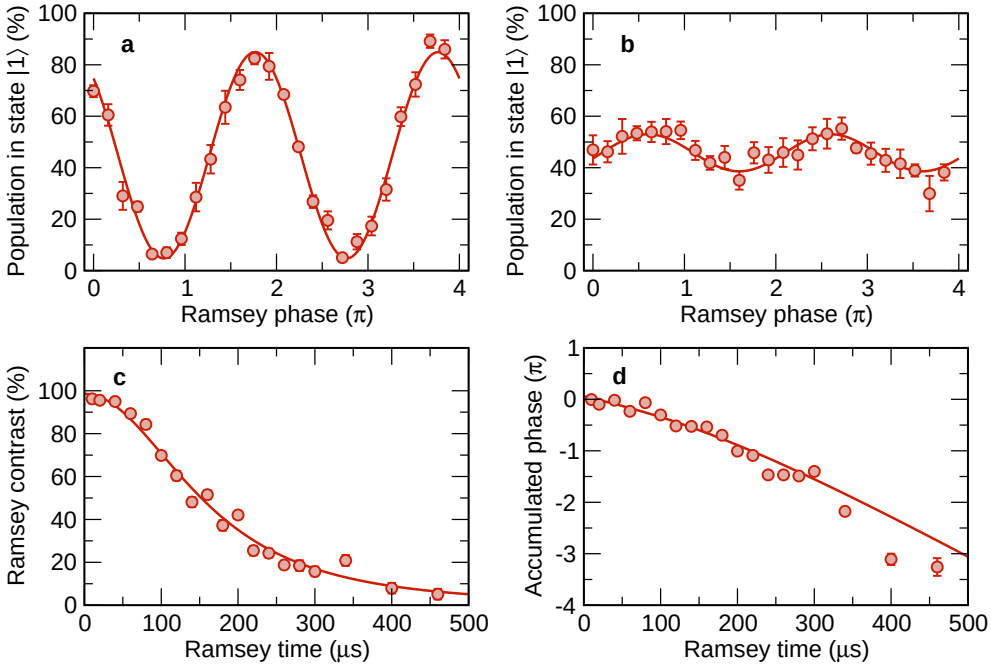

Figure 3.8.: Experimentally measured Ramsey fringes for a Ramsey time of (**a**) $\tau = 60\,\mu$s and (**b**) $\tau = 300\,\mu$s. The solid line shows a fit of Eq. (3.34) from which the Ramsey contrast (**c**) and the accumulated macroscopic phase (**d**) is inferred. Both quantities are plotted as a function of Ramsey time (**c**,**d**). Solid lines in (**c**) and (**d**) show a fit of Eq. (3.42) and Eq. (3.40), respectively, both inferred from a semiclassical model describing inhomogeneous broadening of the $|0\rangle \leftrightarrow |1\rangle$ transition frequency due to energy-dependent light shift. The inferred phase is a modulo 2π quantity. Therefore, for fitting purposes, an offset of 2π is subtracted from the data points for Ramsey times of $\tau > 300\,\mu$s. Results of both fits are listed in Tab. 3.2.

Inhomogeneous dephasing

To interpret the experimental results, we derive an analytical expression for the evolution of Ramsey contrast and the accumulated macroscopic phase in time. The derivation is based on a semiclassical approach, which has been proven to reasonably agree with quantum mechanical density matrix calculation to within one percent [66]. In this approach, the quantized motion of atoms trapped in potential wells of an optical lattice is neglected, whereas the evolution of the phase during the time interval between both $\pi/2$-pulses is only characterized by the average differential light shift.

Consider the inhomogeneous broadening of the $|0\rangle \leftrightarrow |1\rangle$ transition frequency being only caused by the energy-dependent light shift $\delta_{ls}(E)$ of each individual atom. Then, by describing the energy distribution of the trapped atoms by a three-

dimensional Boltzmann distribution with the probability density [65]

$$p_{\mathrm{B}}(E) = \frac{E^2}{2(k_{\mathrm{B}}T)^3} \exp\left(-\frac{E}{k_{\mathrm{B}}T}\right) , \tag{3.35}$$

the distribution of the differential light shifts of the trapped atoms reads [66]:

$$p_{\mathrm{ls}}(\delta_{\mathrm{ls}}) = \frac{\beta^3}{2}(\delta_{\mathrm{ls}} - \delta_{\mathrm{ls},0})^2 \exp\left[-\beta\left(\delta_{\mathrm{ls}} - \delta_{\mathrm{ls},0}\right)\right] \quad \text{with} \quad \beta = \frac{2U_0}{k_{\mathrm{B}}T\delta_{\mathrm{ls},0}} , \tag{3.36}$$

where T denotes the temperature of the atoms, $\delta_{\mathrm{ls},0} = \delta_{\mathrm{ls}}(E=0)$ the maximum differential light shift at the bottom of the potential well and U_0 the lattice depth. Note that this equation is only valid in the harmonic approximation of the trapping potential ($k_{\mathrm{B}}T \ll U_0$).

From a weighted average of all single-atom contributions of Eq. (3.33), the projection onto the detectible basis state $|1\rangle$ can be directly deduced. Assuming that the accumulated phase of each atom evolves linearly in time

$$\Phi_{\mathrm{a}}(\tau) = (\delta_{\mathrm{rf}} + \delta_{\mathrm{ls}})\,\tau + \Phi_{\mathrm{rf},0} , \tag{3.37}$$

where δ_{rf} incorporates possible frequency detuning of both $\pi/2$-pulses from the $|0\rangle \leftrightarrow |1\rangle$ transition frequency and $\Phi_{\mathrm{rf},0}$ a constant phase accumulated during these pulses, the resulting projection reads

$$P_{|1\rangle}(\phi_{\mathrm{rf}}, \tau) = \int_{\delta_{\mathrm{ls},0}}^{\infty} p_{\mathrm{ls}}(\delta'_{\mathrm{ls}}) \cdot \frac{1}{2}\left\{1 + \cos\left[\phi_{\mathrm{rf}} - \left(\delta_{\mathrm{rf}} + \delta'_{\mathrm{ls}}\right)\tau - \Phi_{\mathrm{rf},0}\right]\right\} \mathrm{d}\delta'_{\mathrm{ls}} \tag{3.38a}$$

$$= \frac{1}{2}\left\{1 + C(\tau)\cos[\phi_{\mathrm{rf}} - \Phi(\tau)]\right\} \tag{3.38b}$$

with the Ramsey fringe contrast

$$C(\tau) = \left(1 + \frac{\tau^2}{\beta^2}\right)^{-3/2} , \tag{3.39}$$

determining the polarization of the quantum state, and the phase of the Ramsey fringe, given by

$$\Phi(\tau) = 3\arctan\left(\frac{\tau}{\beta}\right) + \phi_{\mathrm{rf}} \cdot \tau + \Phi_{\mathrm{rf},0} . \tag{3.40}$$

The arctan term in Eq. (3.40) arises from the asymmetry of the differential light shift distribution of Eq. (3.36). Note that the upper integration limit in Eq. (3.38a) has been intentionally set to infinity instead of the maximum physically reasonable value of $\delta_{\mathrm{ls},0}/2$ to guarantee an analytic solution of the integral.
Despite the non-exponential decay of the Ramsey contrast, the inhomogeneous dephasing time T_2^* can be defined as the $1/e$-time of the contrast

$$C(T_2^*) \equiv C(0)e^{-1} \quad \Rightarrow \quad T_2^* = \beta\sqrt{e^{2/3} - 1} . \tag{3.41}$$

Fit parameters		results
Ramsey contrast at $\tau = 0$	$C_{\max}$	$(99 \pm 1)\%$
microwave detuning	$\delta_{\mathrm{rf}}/2\pi$	$-(4.25 \pm 0.04)\,\mathrm{kHz}$
phase offset	$\Phi_{\mathrm{rf},0}$	0.19 ± 0.02
inhomogeneous dephasing time:		
from the Ramsey contrast	T_2^*	$(196 \pm 3)\,\mu\mathrm{s}$
from the accumulated phase	T_2^*	$(199 \pm 7)\,\mu\mathrm{s}$

Table 3.2.: Results from a fit of Eqs. (3.42) and (3.40) to the Ramsey contrast and the accumulated phase shown in Fig. 3.8(c) and 3.8(d).

Therefore, by incorporating Eq. (3.36), the inhomogeneous dephasing time is proportional to the inverse of the temperature of the atoms.

To fit the data in Fig. 3.8(c), we extend Eq. (3.39) by an additional fit parameter $C_{\max}$ which takes the deviation of the contrast from its ideal value into account, arising from the microwave pulses themselves. This deviation has been already observed in the measured Rabi oscillations, see Eq. (3.18) in Sec. 3.2.3. The extended fit function thus reads

$$\widetilde{C}(\tau) = C_{\max} \cdot C(\tau)\,. \tag{3.42}$$

The fit results are listed in Tab. 3.2, together with results from the fit of Eq. (3.40) to the accumulated phase, see Fig. 3.8(d).

The inhomogeneous dephasing times T_2^*, independently inferred from the Ramsey contrast and the accumulated macroscopic phase, demonstrate a good conformity. The same applies to the maximum contrast $C_{\max}$ at $\tau = 0$, which agrees well with the value from the measured Rabi oscillations, see Sec. 3.2.3. The unintentional detuning of $\delta_{\mathrm{rf}}/2\pi \approx 4\,\mathrm{kHz}$, revealed by the fit, is most likely attributed to drifts of the $|0\rangle \leftrightarrow |1\rangle$ transition frequency over time. Note that Ramsey spectroscopy is particularly sensible to such drifts, since they directly translate into the Ramsey contrast and the accumulated phase. Knowing the temperature for the preset lattice depth [129], from Eq. (3.36), we infer a maximum differential light shift of $\delta_{\mathrm{ls},0}/2\pi = (13 \pm 2)\,\mathrm{kHz}$. This value, however, is significantly larger than the theoretically expected value of 4 kHz [78], assuming a perfectly linear polarized light field generating the optical lattice, and thus, taking only the scalar component of the differential light shift into account. The discrepancy from the measured value most likely arises from polarization distortions of the light field due to circular polarized components, introduced by the retardation elements of the experimental setup. In particular, we expect most polarization distortions arising from the electro-optical modulator. For magnetically sensitive qubit states ($m_{\mathrm{F}} \neq 0$), circular components in the light field affect the overall differential light shift by its vectorial or tensorial components [47]. This pertains in particular to the outer Zeeman levels, used as qubit states in our experiment.

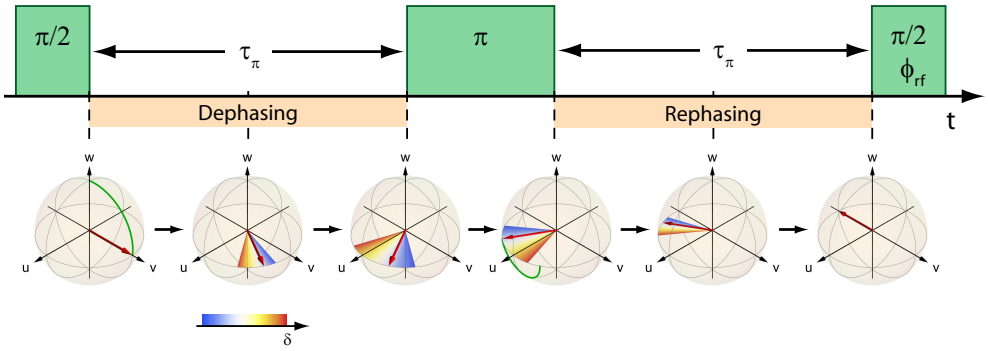

Figure 3.9.: Spin-echo sequence in Bloch sphere representation. A π-pulse between the two Ramsey $\pi/2$-pulses rephases the dephasing Bloch vectors which are represented by a shaded region. A colors gradient is used to visualize different detunings form the atomic resonance frequency; green trajectories indicate the pulse driven evolution of a single Bloch vector.

3.3.3. Spin-echo spectroscopy

Inhomogeneous dephasing can be reversed by a so-called spin-echo sequence, which was invented by E. Hahn in 1950 for nuclear magnetic resonance [130] and successively applied to experiments with neutral atoms in optical lattices [46, 131] just a few years ago. This sequence extends the Ramsey sequence by a further π-pulse applied between the two $\pi/2$-pulses, which aims to rephase the dephased ensemble, see Fig. 3.9. We use the spin-echo sequence to infer the homogeneous transverse dephasing time T_2' of the atoms trapped in the optical lattice.

To derive the shape of the expected Ramsey fringes of a spin-echo sequence, in analogy to Sec. 3.3.2, we consider the projection of the quantum state of a single atom on the basis state $|1\rangle$. After the completion of the spin-echo sequence, it is given by

$$\begin{aligned} P_{\mathrm{a},|1\rangle}(\phi_{\mathrm{rf}}, 2\tau_\pi) &= \left| \langle 1 | \hat{U}_{\pi/2,\phi_{\mathrm{rf}}} \hat{Q}_{\Phi_{\mathrm{a},2}(\tau_\pi)} \hat{U}_\pi \hat{Q}_{\Phi_{\mathrm{a},1}(\tau_\pi)} \hat{U}_{\pi/2} | 0 \rangle \right|^2 \\ &= \frac{1}{2} \left\{ 1 + \cos[\phi_{\mathrm{rf}} - \Delta\Phi_{\mathrm{a}}(\tau_\pi) + \pi] \right\} , \end{aligned} \tag{3.43}$$

where $2\tau_\pi$ denotes the spin-echo time with τ_π the time between each $\pi/2$-pulse and the rephasing π-pulse, $\Delta\Phi_{\mathrm{a}}(\tau_\pi) = \Phi_{\mathrm{a},2}(\tau_\pi) - \Phi_{\mathrm{a},1}(\tau_\pi)$ the difference between the accumulated phases during the time interval between the first $\pi/2$-pulse and the π-pulse $\Phi_{\mathrm{a},1}(\tau_\pi) = \int_0^{\tau_\pi} \delta_{\mathrm{a}}(t)\mathrm{d}t$, and the time interval between the π-pulse and the final $\pi/2$-pulse $\Phi_{\mathrm{a},2}(\tau_\pi) = \int_{\tau_\pi}^{2\tau_\pi} \delta_{\mathrm{a}}(t)\mathrm{d}t$, respectively. Again, the transition from a single atom to an ensemble of atoms is performed by averaging over all single-atom projection contributions, yielding

$$P_{|1\rangle}(\phi_{\mathrm{rf}}, 2\tau_\pi) = \frac{1}{2} \left\{ 1 + C(2\tau_\pi) \cos[\phi_{\mathrm{rf}} - \Delta\Phi(\tau_\pi) + \pi] \right\} . \tag{3.44}$$

In the ideal case, assuming that the individual resonance frequency of each atom of the ensemble does not change during the sequence, i.e. $\delta_\mathrm{a}(t) = \mathrm{const}$ ($\Delta\Phi_\mathrm{a}(\tau_\pi) = 0$), complete rephasing occurs at the spin-echo time, resulting in a fully polarized quantum state with a spin-echo contrast of $C(2\tau_\pi) = 100\%$. However, due to fluctuations of experimental parameters affecting the $|0\rangle \leftrightarrow |1\rangle$ transition frequency, the difference between the accumulated phases is $\Delta\Phi_\mathrm{a}(\tau_\pi) \neq 0$, being different from one sequence repetition to another. In this case, the rephasing is incomplete.

In the following, we assume that all atoms experience identical fluctuations of the $|0\rangle \leftrightarrow |1\rangle$ transition frequency, regardless of their energy in the optical lattice, i.e. a homogeneous dephasing mechanism. We express the difference between the accumulated phase by an average detuning difference $\Delta\delta$ (averaged over τ_π)

$$\Delta\Phi_\mathrm{a}(\tau_\pi) = \Delta\delta \cdot \tau_\pi \,, \tag{3.45}$$

assuming its probability distribution to be Gaussian [46]

$$p(\Delta\delta, \tau_\pi) = \frac{1}{\sqrt{2\pi}\sigma_{\Delta\delta}(\tau_\pi)} \exp\left[-\frac{(\Delta\delta)^2}{2\sigma^2_{\Delta\delta}(\tau_\pi)}\right] \tag{3.46}$$

with mean $\overline{\Delta\delta} = 0$ and variance $\sigma^2_{\Delta\delta}(\tau_\pi)$. From a weighted ensemble average of all single-atom contributions of Eq. (3.33), we obtain

$$\begin{aligned} P_{|1\rangle}(\phi_\mathrm{rf}, 2\tau_\pi) &= \int_{-\infty}^{\infty} p(\Delta\delta, \tau_\pi) \cdot \frac{1}{2}\left\{1 + \cos[\phi_\mathrm{rf} - \Delta\delta \cdot \tau_\pi + \pi]\right\} \\ &= \frac{1}{2}\left\{1 + C(2\tau_\pi)\cos[\phi_\mathrm{rf} + \pi]\right\} \end{aligned} \tag{3.47}$$

with the spin-echo contrast

$$C(2\tau_\pi) = \exp\left(-\frac{1}{2}\tau_\pi^2 \sigma^2_{\Delta\delta}(\tau_\pi)\right) . \tag{3.48}$$

Analogous to the inhomogeneous dephasing time T_2^*, we define the homogeneous dephasing time T_2' as the $1/e$-time of the spin-echo contrast

$$C(2\tau_\pi = T_2') \equiv C(0)e^{-1} \quad \Rightarrow \quad T_2' = \frac{\sqrt{2}}{\sigma_{\Delta\delta}(\tau_\pi)} \,. \tag{3.49}$$

To determine the homogeneous dephasing time, we perform Ramsey phase spectroscopy, employing the spin-echo sequence for different values of spin-echo time. For this, we use the same experimental parameters as in the previous section. From a fit of

$$\widetilde{P}_{|1\rangle}(\phi_\mathrm{rf}, 2\tau_\pi) = \frac{p_\mathrm{sur}(\tau_\mathrm{img})}{2}\left\{1 + C(2\tau_\pi)\cos[\phi_\mathrm{rf} + \pi + \delta\Phi(2\tau_\pi)]\right\} \tag{3.50}$$

to each recorded spectrum, we infer the spin-echo contrast $C(2\tau_\pi)$ and the deviation from the expected macroscopic phase $\delta\Phi(2\tau_\pi)$. This phase reveals how well the

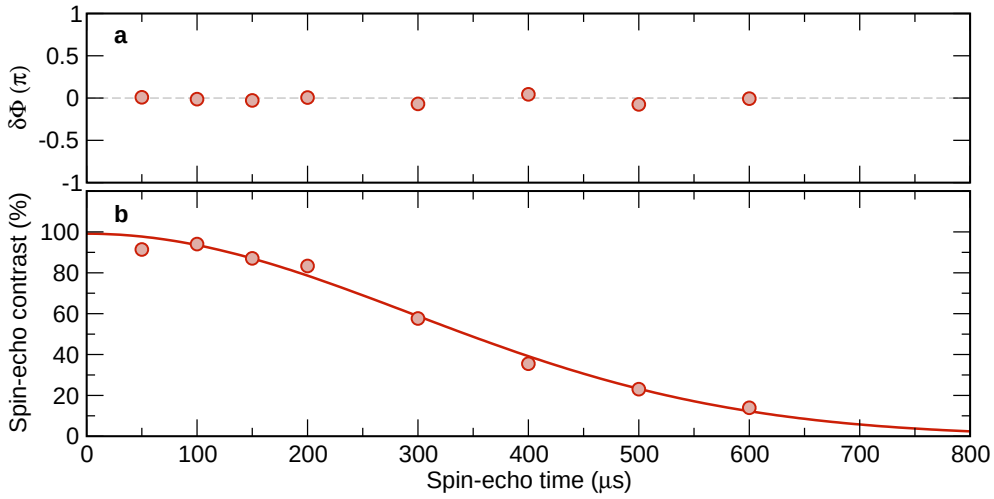

Figure 3.10.: Spin-echo contrast (**b**) and deviation of the macroscopic phase $\delta\Phi$ (**a**) as a function of spin-echo time $2\tau_\pi$. The solid line in (**b**) shows a fit of Eq. (3.51), from which a homogeneous dephasing time T_2' is inferred.

assumption $\overline{\Delta\delta} = 0$ in Eq. (3.46) is fulfilled. The fit parameter $p_{\mathrm{sur}}(\tau_{\mathrm{img}})$ denotes the survival probability of the atoms in the optical lattice.

In Figure 3.10, the resulting spin-echo contrast and the deviation of the macroscopic phase are shown as a function of spin-echo time. The deviation of the macroscopic phase from the zero value is negligible (see Fig. 3.10(a)), indicating that the mean value of the average detuning difference is zero. Furthermore, it reveals that inhomogeneous dephasing effects employing asymmetric detuning distributions (see Sec. 3.3.2) are completely reversed. The same applies to the phase evolution due to unintentional detuning of the microwave frequency from the $|0\rangle \leftrightarrow |1\rangle$ transition frequency. From a fit of

$$\widetilde{C}(2\tau_\pi) = C_{\mathrm{max}} \cdot C(2\tau_\pi) \tag{3.51}$$

to the inferred data, we obtain $C_{\mathrm{max}} = (99 \pm 1)\%$ and $\sigma_{\Delta\delta}(\tau_\pi)/2\pi = (542 \pm 10)\,\mathrm{Hz}$, yielding an irreversible dephasing time of

$$T_2' = (415 \pm 8)\,\mu\mathrm{s}\,. \tag{3.52}$$

In the next section, we will show that this value does not impose the upper limit for most experimental results presented in this thesis. The irreversible dephasing time can in principle be elongated by means of a multiple spin-echo sequence.

3.3.4. Carr-Purcell sequence

A spin-echo sequence can only recover from fluctuations that are effectively constant over the time interval τ_π. Fluctuations on a time scale shorter than τ_π are in general

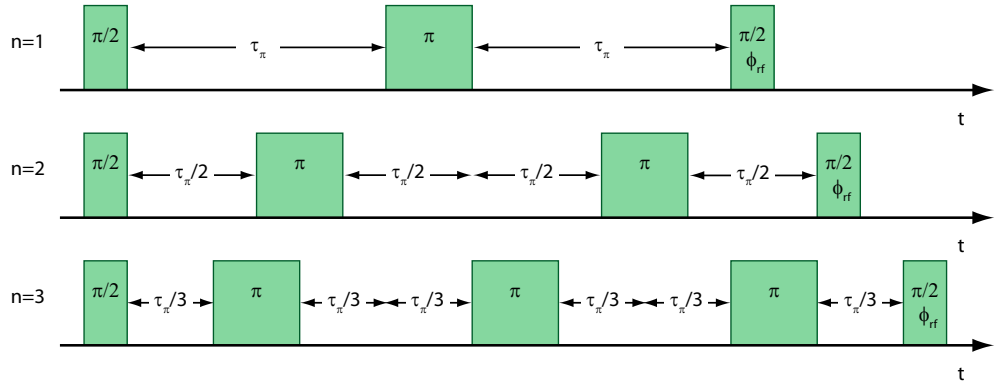

Figure 3.11.: Carr-Purcell sequence. The Carr-Purcell or multiple spin-echo sequence comprises n successively repeated spin-echos. The time interval separating the $\pi/2$- and the π-pulse is given by $\tilde{\tau}_\pi = \tau_\pi/n$, whereas two π-pulses are separated by the spin-echo time $2\tilde{\tau}_\pi$, respectively.

not removed by a single rephasing pulse. However, if the rephasing sequence is repeated more frequently and the time scales of dominant fluctuations are longer than τ_π, the homogeneous dephasing time T_2' can be in principle elongated. This is the idea behind the so-called Carr-Purcell (CP) sequence [132] — a sequence of multiple rephasing pulses:

$$\hat{\mathcal{S}}_{\mathrm{CP}} = \hat{U}_{\pi/2,\phi_{\mathrm{rf}}} \left[\prod_{i=1}^{n} \hat{Q}_{\Phi_{\mathrm{a},2i}(\tilde{\tau}_\pi)} \hat{U}_\pi \hat{Q}_{\Phi_{\mathrm{a},2i-1}(\tilde{\tau}_\pi)} \right] \hat{U}_{\pi/2} \quad \text{with} \quad \tilde{\tau}_\pi = \tau_\pi/n\,. \tag{3.53}$$

The Carr-Purcell sequence comprises multiple successively repeated spin-echos, being also referred to as multiple spin-echo sequence, see Fig. 3.11. It aims to completely rephase the atomic ensemble, by effectively reducing the difference of the accumulated phases $\Delta\Phi_{\mathrm{a},i} = \Phi_{\mathrm{a},2i}(\tilde{\tau}_\pi) - \Phi_{\mathrm{a},2i-1}(\tilde{\tau}_\pi)$. In the limit of $n \to \infty$ ($\Delta\Phi_{\mathrm{a},i} \to 0$), the multiple-echo sequence approaches a driven Rabi oscillation. Consequently, in the ideal case, the homogeneous dephasing time tends towards its upper limit imposed by the spin relaxation time T_1.

The Carr-Purcell sequence can be also seen as a high-pass filter acting on the spectrum of fluctuations affecting a two-level quantum system. The roll-off frequency of this filter $1/\tilde{\tau}_\pi$ determines the elongation performance of the homogeneous dephasing time. Since multiple π-pulses are an essential part of the state-selective transport (see Sec. 4.5), the Carr-Purcell sequence is already part and parcel of most experiments presented in this thesis. In these experiments, the transport time of $\tau_{\mathrm{trans}} \approx 20\,\mu$s set the lower limit for the time interval between the $\pi/2$-pulse and the subsequent π-pulse ($\tilde{\tau}_\pi \geq \tau_{\mathrm{trans}}$), and thus the upper limit for elongation of the homogeneous dephasing time.

To determine the elongated homogeneous dephasing time, we repeat the Ramsey phase spectroscopy, applying the multiple spin-echo sequence for different values of

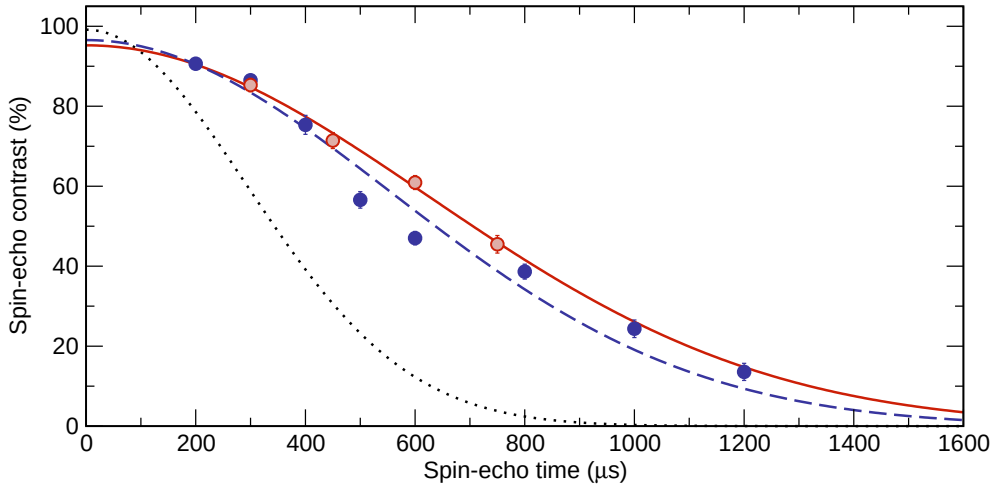

Figure 3.12.: Measured contras of a multiple spin-echo sequence with n echo repetitions as a function of spin-echo time $2n\tilde{\tau}_\pi$. Filled circles show data for $n = 2$, open circles for $n = 3$. Dashed (solid) line shows a fit of Eq. (3.56) to the data for $n = 2$ ($n = 3$) echo repetitions. From the fit results the elongated homogeneous dephasing times are inferred, see Tab. 3.3. For comparison, the dotted line indicates the fitted curve of a single-echo sequence ($n = 1$), as obtained from Fig. 3.10.

n and different spin-echo times. For this, we use the same experimental parameters as in the previous sections. Similar to previous sections, it can be shown that Ramsey fringes, measured after completing a multiple spin-echo sequence can be expressed by

$$\widetilde{P}_{|1\rangle}(\phi_{\mathrm{rf}}, 2n\tilde{\tau}_\pi) = \frac{p_{\mathrm{sur}}(\tau_{\mathrm{img}})}{2}\left\{1 + C(2n\tilde{\tau}_\pi)\cos[\phi_{\mathrm{rf}} + o(n)\pi + n\cdot\delta\Phi(2\tilde{\tau}_\pi)]\right\} \tag{3.54}$$

with

$$o(n) = \begin{cases} 0\,, & \text{for } n \text{ even} \\ 1\,, & \text{for } n \text{ odd}\,. \end{cases} \tag{3.55}$$

Analogous to Sec. 3.3.3, we denote $2n\tilde{\tau}_\pi$ as the (multiple) spin-echo time.

The deviation of the accumulated phase (negligible, and thus not shown) and the (multiple) spin-echo contrast are inferred by fitting Eq. (3.54) to the measured data. The resulting spin-echo contrast, plotted as a function of spin-echo time, is shown in Fig. 3.12. Similar to Sec. 3.3.3, we determine the elongated homogeneous dephasing time $\widetilde{T}_2'$ from a fit of

$$\widetilde{C}(2n\tilde{\tau}_\pi) = C_{\max}\exp\left(-\frac{1}{2}n^2\tilde{\tau}_\pi^2\sigma_{\Delta\delta}^2(\tilde{\tau}_\pi)\right) \tag{3.56}$$

to the spin-echo contrast, using

$$C(2n\tilde{\tau}_\pi = \widetilde{T}_2') \equiv C(0)e^{-1} \quad \Rightarrow \quad \widetilde{T}_2' = \frac{\sqrt{2}}{\sigma_{\Delta\delta}(\tilde{\tau}_\pi)}\,. \tag{3.57}$$

Number of spin echos		$n = 1$	$n = 2$	$n = 3$
Fit parameters				
Maximum contrast	$C_{\max}$	$(99 \pm 1)\%$	$(97 \pm 1)\%$	$(95 \pm 2)\%$
Fluctuation amplitude	$\frac{\sigma_{\Delta\delta}(\tilde{\tau}_\pi)}{2\pi}$	$(542 \pm 10)\,\mathrm{Hz}$	$(287 \pm 5)\,\mathrm{Hz}$	$(256 \pm 9)\,\mathrm{Hz}$
Homogeneous dephasing time	$\widetilde{T}_2'$	$(415 \pm 1)\,\mu\mathrm{s}$	$(787 \pm 2)\,\mu\mathrm{s}$	$(879 \pm 5)\,\mu\mathrm{s}$

Table 3.3.: Results inferred from a fit of Eq. (3.56) to the data shown in Fig. 3.11.

Results for $n = 1$, 2 and 3 are listed in Tab. 3.3.

The fit results in Tab. 3.3 confirm the expected elongation of the homogeneous dephasing time by the Carr-Purcell sequence. However, significant elongation can be only observed by comparing the results of a single-echo sequence $n = 1$ and the Carr-Purcell sequence with $n = 2$. Further increase of n provides only marginal elongations, i.e. the fitted curve for $n = 3$ reasonably fits to the data of $n = 2$ except of two data points, which may also be attributed to sudden changes of experimental parameters during the measurement. Pulse trains with pulse separation limited by the transport time $\tilde{\tau}_\pi \approx \tau_{\mathrm{trans}}$ provide similar results. From this fact, we conclude that dominant fluctuations, mostly contributing to homogeneous dephasing, are settled in the high-frequency region above $1/\tau_{\mathrm{trans}} \approx 50\,\mathrm{kHz}$. The origin of these fluctuations has not yet been identified. Further investigation are therefore needed in the future.

The evolution of the fit parameter $C_{\max}$ with increasing pulse number partially reveals the main shortcoming of the Carr-Purcell sequence: Fixed errors in pulse frequency, amplitude or duration may accumulate throughout the sequence causing progressive departure of the freely precessing Bloch vectors from the equatorial plane and thus yielding a decay in the contrast of the echo train. This shortcoming becomes more relevant in applications of the state-selective transport (see Sec. 4.5), in which larger numbers of π-pulses are employed. While errors in pulse frequency can be suppressed by broadband composite pulses (see Sec. 3.5), fixed errors in pulse amplitude and length can be compensated by an extended version of the Carr-Purcell sequence, also known as the Carr-Purcell-Meiboom-Gill or CPMG sequence [133]. In the CPMG sequence the rephasing pulses are shifted by $\phi_{\mathrm{rf}} = \pi/2$ with respect to the initial $\pi/2$-pulse:

$$\hat{\mathcal{S}}_{\mathrm{CPMG}} = \hat{U}_{\pi/2,\phi_{\mathrm{rf}}} \left[\prod_{i=1}^{n} \hat{Q}_{\Phi_{\mathrm{a},2i}(\tilde{\tau}_\pi)} \hat{U}_{\pi,\pi/2} \hat{Q}_{\Phi_{\mathrm{a},2i-1}(\tilde{\tau}_\pi)} \right] \hat{U}_{\pi/2}\,. \tag{3.58}$$

By this, pulse errors are compensated on even-numbered echoes and are thus not cumulative [21]. In our experiment, the CPMG sequence provides no considerable improvement over the Carr-Purcell sequence, most likely due to the fact that the

dominant pulse errors are not fixed. Instead, they unpredictably drift over time.

Analysis of dephasing mechanisms

Following Ref. [66], we aim to identify the dominant mechanisms responsible for the observed homogeneous dephasing. For this, we compare the magnitude of the inferred fluctuation amplitude from Tab. 3.3 to the amplitudes estimated from measured fluctuations of experimental parameters. Details on the estimations can be found in Refs. [66, 78].

Magnetic field fluctuations Fluctuations of magnetic fields directly translate into fluctuations of the $|0\rangle \leftrightarrow |1\rangle$ transition frequency due to the linear Zeeman effect. They can be primarily attributed to the driving current of the coils, which generate the magnetic guiding field. The power supply (Toellner TOE 8733-1) provides a relative current stability of $I_{\mathrm{rms}}/I_0 = 3 \times 10^{-6}$ on the relevant timescales,[5] resulting in a fluctuation amplitude of $\sigma_{\Delta\delta}(\tilde{\tau}_\pi)/2\pi = 222\,\mathrm{Hz}$. The frequency spectrum of these fluctuations, however, is expected to settle in the low-frequency region $< 1\,\mathrm{kHz}$, particularly due to a low-pass filter employed in the circuit which suppresses the high-frequency components. For this reason, we expect that fluctuations of the guiding field affect marginally the homogeneous dephasing time whenever Carr-Purcell sequences with $\tilde{\tau}_\pi = \tau_{\mathrm{trans}} \approx 20\,\mu\mathrm{s}$ are employed. Note that this does not apply for magnetic field fluctuations caused by electronic devices in the vicinity of the trapped atoms. The magnitude and frequency spectrum of these fluctuations has yet to be investigated.

Beam pointing instability Pointing instability of the beams generating the optical lattice yields a variation of the trap depth. The latter in turn affects the differential light shift and thus the resonance frequency of the atoms. To roughly estimate the pointing stability in the trapping region, we record position fluctuations of the atoms perpendicular to the lattice axis using fluorescence imaging, yielding fluctuations with a relative deviation of 5% of the beam waist. This results in a fluctuation amplitude of $\sigma_{\Delta\delta}(\tilde{\tau}_\pi)/2\pi = 16\,\mathrm{Hz}$.

Intensity fluctuations Similarly to beam pointing instability, intensity fluctuations of the laser generating the optical lattice contribute to homogeneous dephasing. The relative intensity fluctuations are of the order of 2%, yielding a fluctuation amplitude of $\sigma_{\Delta\delta}(\tilde{\tau}_\pi)/2\pi = 260\,\mathrm{Hz}$. Thus, from all estimated fluctuation amplitudes, it is closest to that inferred from the multiple spin-echo measurement. Therefore, for our experimental setup, intensity fluctuations of the laser provide the most dominant contribution to homogeneous dephasing. Further investigations, including a frequency spectrum of the fluctuations

[5] Thermal fluctuations of the power supply on a time scale of several hours are not considered, since they do not affect the homogeneous dephasing time.

will be needed to estimate their impact on the elongation of the homogeneous dephasing time.

Other dephasing mechanisms Other dephasing mechanisms, including elastic collisions and heating [66] have been estimated to be several orders of magnitude weaker than the dominating dephasing effects discussed above. They play a negligibly role on the time scale of the measured homogeneous dephasing time.

3.4. Position-dependent quantum state manipulation

So far, we performed coherent quantum state manipulation on atomic ensembles, i.e. simultaneously on all atoms randomly distributed over sites of a one-dimensional optical lattice. In that case, each individual atom is equally manipulated, irrespective of its position in the lattice. Recent applications in quantum information science, however, place much higher demands with regard to controlled positioning of atoms and their selective coherent manipulation with single-site resolution. In the last decade, significant progress has been made in controlling positions and generating regular patterns of atoms. Various approaches ranging from optical tweezers [134], optical conveyor belts [89], and magnetic micro-traps [135] have been successfully applied for this purpose. Coherent manipulation of individual atoms has been demonstrated rather for atoms occupying distant sites ($2.5\,\mu$m) of a lattice in the optical wavelength domain [47], or for atoms on neighboring sites of a lattice with a period of $5.3\,\mu$m [85]. Single-site resolution in optical wavelength domain has not yet been achieved. Recently, single-site addressability in a two-dimensional optical lattice with 600 nm lattice spacing has been demonstrated, by removing atoms from selected sites using a focused electron beam [45]. By employing this technique, predefined patterns of atoms have been generated. Although this type of addressing is not coherent, it impressively demonstrates that preparation of atom patterns and single-site addressability are mutually compatible.

In this section, we pick up the ideas of nuclear magnetic resonance (NMR) techniques. We employ a magnetic field gradient to manipulate quantum states of individual atoms by tuning the frequency of the microwave radiation to the respective Zeeman-shifted atomic resonance frequency. Our modified configuration of anti-Helmholtz coils enables us to coherently manipulate individual atoms with almost single-site resolution. We utilize this ability to prepare regular strings of atoms with predefined distances. These strings are used as a starting point for the realization of controlled two-atom collisions discussed in Chap. 7.

3.4.1. Position-dependent Zeeman shift

In our experiment, position-selective manipulation of atoms is performed in a quadrupole magnetic field $\boldsymbol{B}_{\mathrm{quad}}(\boldsymbol{r}, I)$. The field originates from two coils in anti-Helmholtz configuration, where the symmetry axis of the coils coincides with the optical lattice axis (z-axis), see Sec. 1.1.4. At the center of the trapping region,

the axial field gradient along the z-axis is thus twice as large as the gradient in the xy-plane. Including the homogeneous guiding field $\boldsymbol{B}_0$ along the lattice axis, the total magnetic field in the trapping region reads:

$$\boldsymbol{B}(\boldsymbol{r}, I) = \begin{pmatrix} B_x \\ B_y \\ B_z \end{pmatrix} = \boldsymbol{B}_0 + \boldsymbol{B}_{\mathrm{quad}}(\boldsymbol{r}, I) = \begin{pmatrix} 0 \\ 0 \\ B_0 \end{pmatrix} + B'(I) \begin{pmatrix} -x/2 \\ -y/2 \\ z \end{pmatrix}, \tag{3.59}$$

where $B'(I)$ denotes the magnitude of the gradient field along the symmetry axis for a preset coil current I. Due to the linear Zeeman effect, the $|0\rangle \leftrightarrow |1\rangle$ transition frequency depends linearly on the modulus of $\boldsymbol{B}(\boldsymbol{r}, I)$, yielding

$$\begin{aligned} \omega_0(\boldsymbol{r}, I) &= \Delta_{\mathrm{HFS}} + \gamma |\boldsymbol{B}(\boldsymbol{r}, I)| \\ &\approx \Delta_{\mathrm{HFS}} + \gamma \left(B_0 + B'(I) z + \frac{B'(I)^2}{8 B_0} \rho^2 \right) \\ &= \Delta_{\mathrm{HFS}} + \delta_0 + \omega'(I) z + \frac{\omega'(I)^2}{8 \delta_0} \rho^2 , \end{aligned} \tag{3.60}$$

where $\gamma = (3g_3 - 4g_4)\mu_B/\hbar \approx 2\pi \times 2.5\,\mathrm{MHz/G}$ is the gyromagnetic ratio, $\delta_0 = \gamma B_0$ denotes the contribution of the guiding field (see Sec. 3.2.3), $\omega'(I) = \gamma B'(I)$ the position-dependent shift and $\rho = \sqrt{x^2 + y^2}$ the radial distance from the symmetry axis of the coils. Finally, $|\boldsymbol{B}(\boldsymbol{r}, I)|$ has been approximated to second order in ρ, valid for $(B_0 + B'(I)z)^2 \gg B'(I)^2 \rho^2/4$. Note that, due to misalignment, the optical lattice axis can be radially offset by a small amount ρ_0 relative to the axis of symmetry. While linear dependency of $\omega_0(\boldsymbol{r}, I)$ on the axial position z is still maintained, this offset imposes a dominant obstacle to single-site addressability, see Sec. 3.4.4.

The resonance frequency of an atom as a function of its position along the lattice axis is inferred from a calibration measurement, in which atoms themselves are used as a probe [47]. This measurement can be regarded as microwave spectroscopy in position space. The corresponding sequence is therefore similar to that of recording a microwave spectrum (see Sec. 3.2.3), except that the frequency is not swept but preset to a fixed value ω_0 and the field gradient $\boldsymbol{B}_{\mathrm{quad}}(\boldsymbol{r})$ is additionally switched on and off together with a guiding field. By this, frequency dependency of the microwave spectrum is mapped onto position space, whereas its amplitude is simultaneously probed and directly inferred from acquired images in each step of the sequence.

3.4.2. Microwave spectroscopy in position space

Recording a microwave spectrum in position space requires a large cloud of atoms ($N_{\mathrm{bef}} \gg 50$) homogeneously distributed over the lattice sites rather than a countable ensemble. For this, the MOT and the optical lattice are overlapped during a time interval of 500 ms.[6] Due to light-induced collisions, atoms occupying the same

[6] The time interval strongly depends on the amount of cesium atoms in the background gas, which can be roughly regulated by the flow from the cesium reservoir.

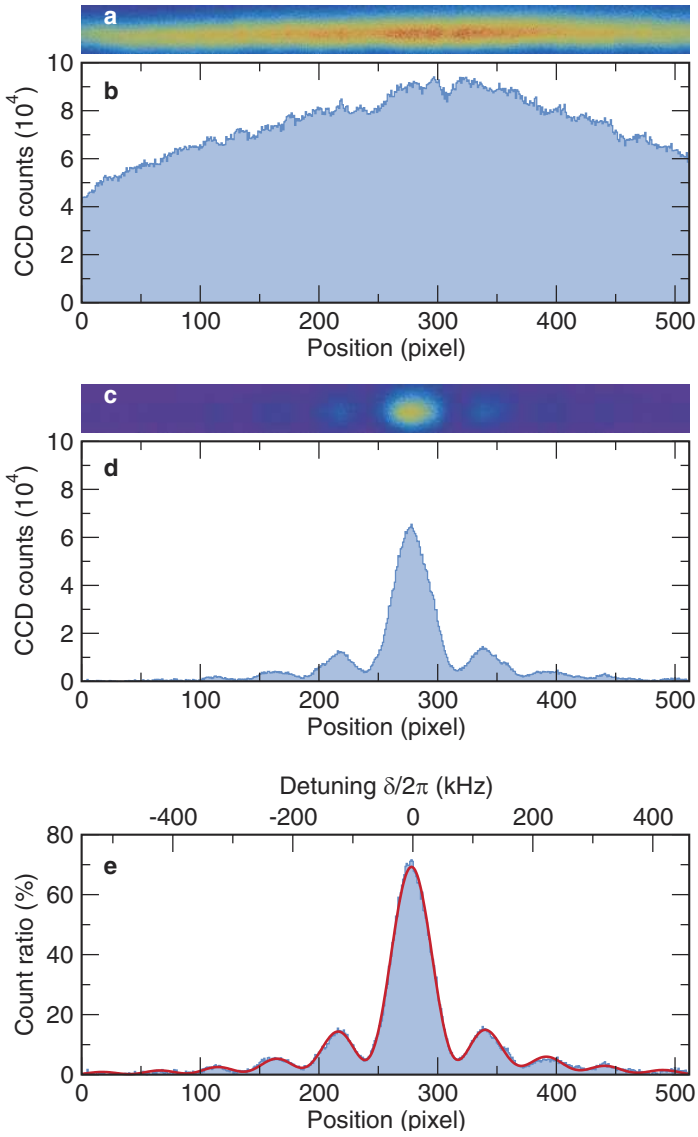

Figure 3.13.: Microwave spectroscopy in position space. (**a**) Intensity distribution of an atomic cloud loaded into the optical lattice, as inferred from an average of 50 initial images; (**b**) the corresponding digitizer offset and background corrected binned intensity distribution. (**c**) Averaged intensity distribution of atoms remaining in the lattice after application of a rectangular π-pulse with a pulse duration of 10 μs and the state-selective push-out. The corresponding binned distribution (**d**) reveals regions in which atoms in state $|1\rangle$ can be found. By dividing the distribution of (**d**) by the initial distribution (**b**) the normalized intensity distribution is inferred (**e**), revealing a microwave-spectrum in position space. The count ratio is directly related to the population transfer in state $|1\rangle$. A solid line shows a fit of the expected spectrum convolved with the LSF of the imaging system. The frequency scale is inferred from a calibration measurement.

lattice sites are removed, subsequently recaptured by the MOT and reloaded into the lattice [67], resulting in a broad distribution of atoms over almost the entire detection region, see Fig. 3.13(a). After initializing the atoms in state $|0\rangle$, applying a π-pulse with a preset frequency ω_0 and the state-selective push-out, only those atoms remain in the lattice, for which the $|0\rangle \leftrightarrow |1\rangle$ transition frequency has been tuned resonant to the microwave frequency by the position-dependent Zeeman shift. The region comprising these atoms is revealed by a subsequently acquired (final) image, see Fig. 3.13(c).

To increase the signal-to-noise ratio, the above sequence is repeated up to $M = 50$ times. Then, we calculate the average of binned intensity distributions of all initial (Fig. 3.13(b)) and all final images (Fig. 3.13(d)), respectively, all of them digitizer offset and background baseline corrected, see Sec. 2.3.6. Dividing the averaged final distributions by the averaged initial distribution yields a distribution which corresponds to a convolution of a Fourier-limited spectrum with the LSF of the imaging setup (Fig. 3.13(e)). From a fit of the expected spectrum shape to the resulting distribution, the axial position z of the atom region corresponding to the preset microwave frequency $\omega_0(\boldsymbol{r}, I)$ in Eq. (3.60) is inferred.

In Figure 3.13(e), a microwave spectrum in position space of a rectangular π-pulse with a duration of $10\,\mu$s is shown. From a fit of Eq. (3.16) comprising the calibration discussed below, an approximation of the stray light background[7] and a convolution with the LSF of the imaging setup, we infer a Rabi frequency of $\Omega_{\mathrm{rf}} = 2\pi \times (57 \pm 1)\,\mathrm{kHz}$ and a pulse duration of $t = (10.6 \pm 0.3)\,\mu$s. The pulse duration agrees reasonably well with the preset value. Even though the spectrum amplitude $P_{\max} = (77 \pm 5)\%$ is significantly reduced, the frequency-dependent amplitude modulations are accurately reflected.

Microwave spectroscopy in position space is therefore a useful tool, which immediately and quickly reveals information encoded in the frequency domain with a high resolution, controlled by the strength of the field gradient. This method is much faster than a usual scan in frequency across the resonance in a homogeneous field to map out the full spectrum. The time to obtain a spectrum with a compatible signal-to-noise ration is reduced from approximately 3 h for the homogeneous field method to $12 \ldots 20\,\mathrm{s}$ for the gradient method. Furthermore, using microwave pulses with a narrow-band spectrum, it allows us to monitor the evolution of the transition frequency arising from changes of experimental parameters from shot to shot. The "shot rate" is mainly limited by the time interval required to switch the coils and acquire the images. We stress that the shape of the microwave spectrum in position space is broadened due to the optical imaging when the features in frequency space become smaller than the optical diffraction limit. A further broadening may exist due to a radial offset of the lattice axis with respect to the symmetry axis of the coils, see Sec. 3.4.4. This effect, however, becomes only significant for narrow-band

[7] In this measurement, the density of cesium atoms in the UHV cell was increased, resulting in an increase of stray light, which disturbs the uniformity of the background base line. We have incorporated this fact in the fit by modeling the background by a Gaussian function.

pulses with a high spectral selectivity

3.4.3. Calibration of the frequency shift

To calibrate the position-dependent frequency shift due to the magnetic field gradient, we employ a microwave spectroscopy in position space for different values of microwave frequencies and gradient strengths (coil currents), each time determining the central position of the remaining atoms. To simplify the subsequent analysis, we use Gaussian-shaped π-pulses (see below) with a typical pulse $1/\sqrt{e}$ half-width of $\sigma_t = 15\,\mu$s rather than rectangular π-pulses. The frequency spectrum of the former comprises a nearly Gaussian shape,[8] which provides a better selectivity and is easier to fit. Since for calibration purposes, the amplitude of the spectrum in position space is irrelevant, we usually skip the acquisition of initial images to reduce the duration of the calibration measurements. This, however, can only be done in detection regions, in which the initial atom distribution is assumed to be nearly homogeneous.

The resulting calibration curves are shown in Fig. 3.14(a). They reveal a linear position-dependency on the preset microwave frequency, irrespective of the coil current. From the fitted slopes of all measured curves, we deduce the frequency shift dependency on the coil current I, see Fig. 3.14(b). This dependency is confirmed to be also linear. A fit of its slope yields a frequency shift of

$$\frac{\omega'(I)}{2\pi I} = (197 \pm 1)\frac{\mathrm{Hz}}{\mathrm{pixel\,A}} = (291 \pm 2)\frac{\mathrm{Hz}}{(\lambda/2)\,\mathrm{A}} = (671 \pm 3)\frac{\mathrm{Hz}}{\mu\mathrm{m\,A}}\,, \tag{3.61}$$

where for unit conversion, we have employed the calibration of the image scale, see Sec. 2.4.2. This frequency shift corresponds to a strength of magnetic field gradient along the lattice axis of $B'(I)/I = -(274 \pm 1)\,\mu\mathrm{G}/\mu\mathrm{m\,A}$, which agrees reasonably well with the value measured with a Hall-probe, see Sec. 1.1.4.

In the ideal case, i.e. for a perfect coincidence of the optical lattice axis with the symmetry axis of the coils, the calibration curves for different coil currents should intersect at a common point at a frequency of $\Delta_{\mathrm{HFS}} + \delta_0$, which corresponds to the resonance frequency of the atoms in absence of the magnetic field gradient. This, however, does not apply for the measured data due to a radial offset of the optical lattice axis relative to the symmetry axis of the coils. To estimate this offset, we determine the positions of the atoms at the frequency $\Delta_{\mathrm{HFS}} + \delta_0$ from the fitted curves, see Fig. 3.14(c). By this, Eq. (3.60) may be reduced to

$$0 = \omega'(I)(z - z_0) + \frac{\omega'(I)^2}{8\delta_0}\rho^2 \quad \Rightarrow \quad z = z_0 - \frac{\omega'(I)}{8\delta_0}\rho^2\,, \tag{3.62}$$

where z_0 has been introduced to incorporate an axial offset of the zero position of the detection region from the center of the quadrupole field. Knowing the guiding

[8] The Gaussian shape of the spectrum only applies in the ideal case of a perfectly isolated two-level quantum system with $T_1, T_2 \to \infty$. Nevertheless, for calibration purposes, this shape provides a sufficiently good approximation to the measured spectrum.

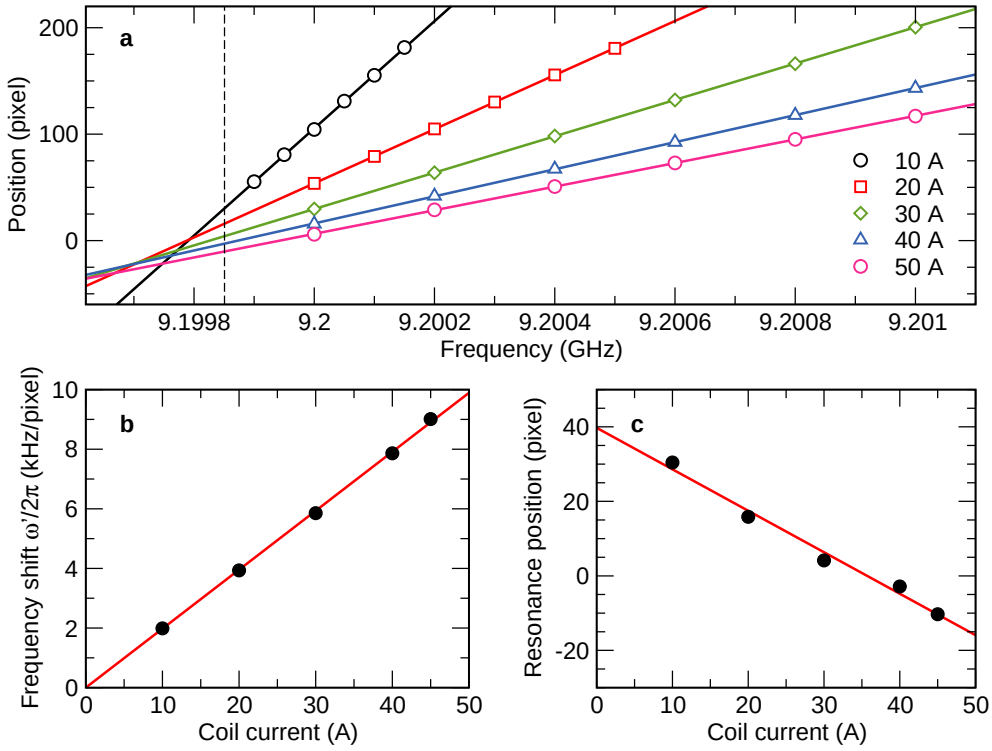

Figure 3.14.: Calibration of the $|0\rangle \leftrightarrow |1\rangle$ transition frequencies in the presence of a magnetic field gradient. (**a**) Central position of atoms for different microwave frequencies and coil currents $I = \{10, 20, 30, 40, 45\}$ A. Error bars are smaller than the size of the data points. From the slopes of the fitted linear curves (solid lines), the respective frequency shifts $\omega'(I)$ are inferred and plotted as a function of I in (**b**). A linear fit to the data yields the frequency-current dependency of Eq. (3.61). (**c**) Estimation of the radial offset of the lattice axis relative to the symmetry axis of the coils: The central positions of the atoms for different values of I, are inferred from $\omega_0(\boldsymbol{r}, I) = \Delta_{\mathrm{HFS}} + \delta_0$ (indicated by the dashed line in (**a**)) and plotted in (**c**). A solid line in (**c**) shows a fit of Eq. (3.62), yielding a radial offset of $\rho_0 = (168 \pm 6)\,\mu$m.

field contribution δ_0 from a recorded microwave spectrum (see Sec. 3.2.3) and the frequency shift $\omega'(I)$ from the calibration measurement, we finally infer a radial offset of $\rho_0 = (168 \pm 6)\,\mu$m from a fit of Eq. (3.62). It should be noted that the radial offset value may vary from one to day another, but also within a measurement due to thermal expansion of the coils or radial drifts of the optical lattice.

3.4.4. Preparation of predefined patterns of atoms

Microwave spectroscopy in position space employs a simple concept: In presence of a magnetic field gradient, only those lattice sites remain occupied after the state-selective push-out, at which atoms have been shifted resonant to the microwave π-

pulse. In the following, we will show that the same concept can be used to prepare arbitrary patterns of atoms, i.e. initial atom distributions with atoms occupying predefined lattice sites. By this, rearranging of atoms, as proposed in Refs. [89,111], becomes redundant, while the preparation precision is strongly increased.

The experimental sequence to generate a predefined pattern structure is similar to that of recording a microwave spectrum in position space. The only difference is the number of applied π-pulses. Instead of a single π-pulse, a pulse train of N successively applied π-pulses with different frequencies ω_i is used. By incorporating the periodicity of the optical lattice using

$$\frac{|\omega_i - \omega_j|}{\omega'(I)\lambda/2} \in \mathbb{N} \quad \text{with} \quad i,j = 1,\ldots,N\,,\; i \neq j\,, \tag{3.63}$$

these frequencies define the pattern structure. To ensure high selectivity in the position-dependent population transfer, the maximum available strength of the magnetic field gradient is used, providing a frequency shift of up to $\omega'(I = 45\,\mathrm{A}) \approx 2\pi \times 13\,\mathrm{kHz}/(\lambda/2)$. Furthermore, Gaussian π-pulses with a $1/\sqrt{e}$ spectral half-width down to $\sigma_\omega/2\pi = 6\,\mathrm{kHz}$ are employed rather than rectangular π-pulses in order to suppress side lobes. For the maximum available frequency shift, these pulses are in principle capable of manipulating individual atoms with almost single-site resolution. To increase the selectivity in the preparation of the pattern structures, we optionally use several iterations of state initialization, application of π-pulses and the state-selective push-out, see below.

Before proceeding with technical details and limitations, we first demonstrate the versatility of our method. In Figure 3.15, two exemplarily generated patterns are shown: A string of eight almost equidistant atoms (Fig. 3.15(a,b)), for instance, is ideally suited for a quantum register [47]. Such a register has previously been implemented using atoms randomly distributed over the lattice sites, in which case the position of each atom needed to be determined and fed back to the microwave source prior to quantum state manipulation on the atoms. For a predefined string of atoms, this feedback is not required, since the frequency of each individual atom of the string is defined by the preparation sequence itself.

So far, strings of atoms have been realized by rearranging randomly distributed atoms using two crossed movable one-dimensional lattices [111]. This method turned out to be technically demanding, not to mention the lower limit for the minimum achievable atom separation imposed by the waist of the crossed lattice beams. At this point, the advantage of our method becomes apparent: It allows us to prepare strings of atoms separated by only two (Fig. 3.15(c,d)) or four (see Chap. 7) lattice sites. These small separations are essential for an efficient implementation of controlled two-atom collisions using the state-selective transport, see Chap. 7. Despite of all advantages, the method presented in this thesis also has some major drawbacks, which will be discussed below.

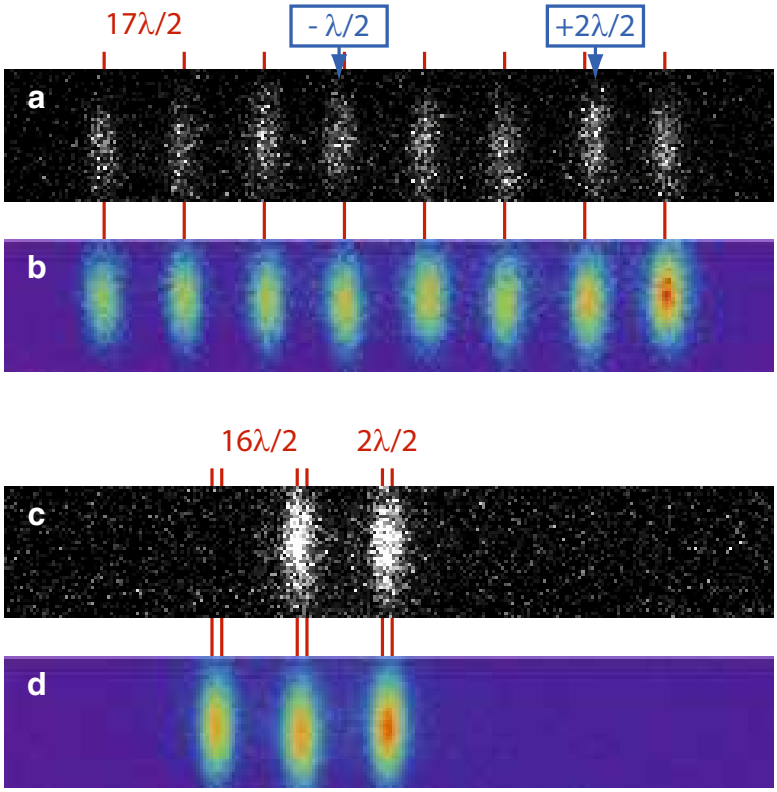

Figure 3.15.: Strings of atoms in an optical lattice: Greyscale images show a single image acquired after application of the patterning sequence (**a**) for a predefined string of equidistant atoms with separations of $17\lambda/2$ and (**c**) for a predefined string of three atom pairs of next-nearest neighbors. Corresponding averages over 50 acquired images are shown as the false color images, (**b**) and (**d**), respectively. Atoms deviating from predefined positions are indicated by an arrow, the deviation by a boxed value. Missing atoms in (**c**) are mostly attributed to the limited preparation efficiency (see text).

Limit of the initial atom distribution

Efficient preparation of patterned structures by removing the undesired atoms requires that predefined lattice sites are initially occupied by a single atom. For this reason, initial atom distributions with ideally unity filling factor (i.e. one atom per lattice site) in the region of interest are highly desirable. Such distributions, however, have not yet been achieved for optical lattices loaded from a MOT due to light-induced inelastic two-body collisions [58, 136] during the transfer process. In presence of the near-resonant molasses light, two atoms are expelled from a commonly occupied lattice site. Part of the inelastic collisions, however, lead to losses of one atom only, see e.g. Chap. 7. These one-atom losses are attributed to so-called radiative escape, which has been investigated and observed in Ref. [63].

Suppose that two-atom losses dominate the loss process at commonly occupied

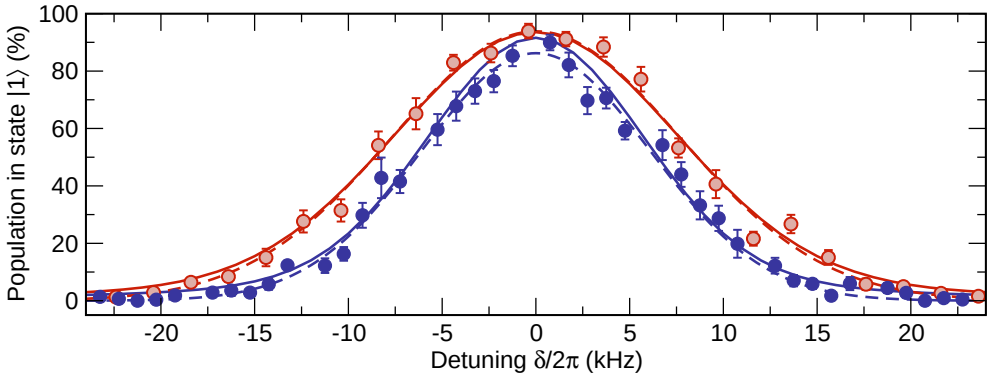

Figure 3.16.: Microwave spectra of two commonly used Gaussian π-pulses with a $1/\sqrt{e}$ pulse half-width of $\sigma_t = 15\,\mu$s (open dots) and $\sigma_t = 20\,\mu$s (filled dots) and a pulse duration of $t = 150\,\mu$s. Solid lines show theoretical spectra as obtained from the optical Bloch equations with damping, employing the measured relaxation times T_1 and T_2. Dashed lines show a Gaussian fit to the measured data.

lattice sites. The resulting steady-state distribution of atoms in the lattice will show either only one or no atoms, resulting in a filling factor of about 0.5, yielding a probability of finding an atom at one selected lattice site of $p_\mathrm{a} \approx 50\%$. This probability imposes an upper limit for the efficiency of generating the entire pattern structure: for a pattern of N atoms, the probability that all desired lattice sites are initially populated is given by $p_\mathrm{ini} = p_\mathrm{a}^N$, yielding $p_\mathrm{ini} \approx 0.4\%$ for a string of eight atoms, whereas for a single atom pair, $p_\mathrm{ini} \approx 25\%$. Since our atom detection is restricted to sparsely filled lattices (see Sec. 2.3.1), a detailed investigation of the loading process with high atom densities could not be performed so far. Further investigations aiming at the increase of the filling factor are required in the future.

Selectivity of microwave pulses

For an atom at a predefined lattice site, the selective microwave operation, a π-pulse for instance, should fulfill two conditions. First, it should operate on the selected atom with high fidelity. The selectivity of this π-pulse, in turn, specified by its spectral width and its shape in the frequency domain, determines to what extent neighboring atoms are affected by this pulse and whether neighboring atoms are completely removed from the lattice or remain trapped with a certain probability. For efficient preparation of pattern structures, this probability should ideally be zero. Therefore, we use microwave π-pulses with a Gaussian envelope resulting in a Rabi frequency of

$$\Omega_\mathrm{R}(t') = \Omega_\mathrm{max} \exp\left[-\frac{(t' - t/2)^2}{2\sigma_t^2}\right], \quad \text{for} \quad 0 \le t' \le t\,, \tag{3.64}$$

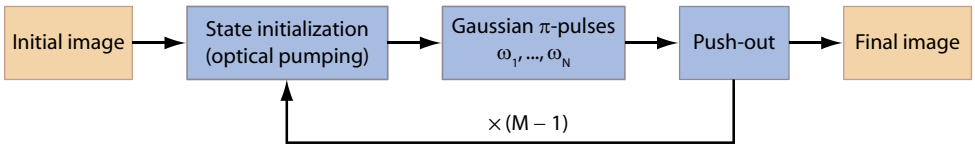

Figure 3.17.: Sequence for preparation of pattern structures involving multiple application of the inner sequence core of state transfer and push-out (blue shaded blocks).

where the maximum amplitude $\Omega_{\max}$ is adjusted to fulfill the π-condition, $\pi = \int_0^t \Omega_{\mathrm{R}}(t')\mathrm{d}t'$, for a preset pulse duration t and the $1/\sqrt{e}$ pulse half-width σ_t. Experimentally, the modulation of the amplitude is voltage controlled using the PIN diode attenuator, see Sec. 3.2.2. The advantage of Gaussian pulses over rectangular pulses is their exponential decay from the carrier frequency and the missing sinc-like contributions in the frequency spectrum.

In Figure 3.16, frequency spectra of two Gaussian π-pulses with a $1/\sqrt{e}$ pulse half-width of $\sigma_t = 15\,\mu$s and $\sigma_t = 20\,\mu$s, and a pulse duration of $t = 150\,\mu$s are shown, both plotted as a function of frequency detuning relative to the atomic resonance. Since the envelope of both spectra is well approximated by a Gaussian, we infer the maximum population transfer and the $1/\sqrt{e}$ spectral half-width σ_ω from a Gaussian fit, yielding

$$\widetilde{P}_{\max} = (94 \pm 1)\%\,, \quad \sigma_\omega/2\pi = (7.51 \pm 0.06)\,\mathrm{kHz} \qquad \text{for} \quad \sigma_t = 15\,\mu\mathrm{s}\,, \tag{3.65a}$$

$$\widetilde{P}_{\max} = (84 \pm 1)\%\,, \quad \sigma_\omega/2\pi = (6.4 \pm 0.1)\,\mathrm{kHz} \qquad \text{for} \quad \sigma_t = 20\,\mu\mathrm{s}\,. \tag{3.65b}$$

For $\sigma_t = 15\,\mu$s, the spectrum agrees reasonably well with the numerical solution of the optical Bloch equations with damping (see Eq. (3.28)) in which the measured relaxation times T_1 and T_2 have been employed. The same applies for the $1/\sqrt{e}$ spectral half-width of both spectra. For $\sigma_t = 20\,\mu$s, however, the measured maximum population transfer slightly deviates from the theoretical expectation. This deviation becomes even more dominant for larger $1/\sqrt{e}$ pulse half-widths. By recalculating the dephasing time T_2 directly from the measured spectrum using the optical Bloch equation with damping, we obtain $T_2 = 100\,\mu$s for $\sigma_t = 20\,\mu$s. This value significantly deviates from that inferred from the Ramsey measurement by 51%. Furthermore, the recalculated dephasing time is not compatible with the measured spectrum for $\sigma_t = 15\,\mu$s. Since both spectra have been reproduced several times, sudden changes of experimental parameters can be excluded from a possible explanation. It remains to conclude that for selective pulses the optical Bloch equation cannot entirely explain the measured data.

The decreasing in the maximum population transfer for $\sigma_t > 15\,\mu$s suggests that the selectivity of the Gaussian pulse cannot be infinitely improved by increasing the pulse half-width σ_t. For this reason, we employ a simple technique, which at least for generation of pattern structures presented in this section, effectively improves the selectivity performance of the Gaussian π-pulses. The underlying idea is to

utilize the probabilistic and destructive nature of our state-selective push-out.

Suppose that a single application of the microwave spectroscopy sequence with a Gaussian π-pulse provides a spectrum given by

$$\widetilde{P}_{|1\rangle}(\delta) = \widetilde{P}_{\max} \exp\left(-\frac{\delta^2}{2\sigma_\omega^2}\right) . \tag{3.66}$$

Then, by repeatedly applying the inner sequence core comprising state initialization, application of the π-pulse and the push-out by a total of M times (see Fig. 3.17), we expect again a Gaussian-shaped spectrum

$$\widetilde{P}^M_{|1\rangle}(\delta) = \left[\widetilde{P}_{\max} \exp\left(-\frac{\delta^2}{2\sigma_\omega^2}\right)\right]^M = (\widetilde{P}_{\max})^M \exp\left(-\frac{\delta^2}{2(\sigma_\omega/\sqrt{M})^2}\right) , \tag{3.67}$$

with a $1/\sqrt{e}$ spectral half-width $\sigma_\omega^{\mathrm{res}}(M) = \sigma_\omega/\sqrt{M}$, however, with a rescaled maximum population transfer $\widetilde{P}^{\mathrm{res}}_{\max}(M) = (\widetilde{P}_{\max})^M$.

In Figure 3.18, the scaling behavior of both quantities is exemplarily shown for a Gaussian pulse with $\sigma_t = 20\,\mu$s, where the spectra have been taken in the frequency domain rather than by position-dependent spectroscopy. The scaling is perfectly reproduced by the measured data, for both quantities inferred from a fit. The same applies for the microwave spectroscopy in position space. Considering the measured data of Eqs. (3.65) and the scaling behavior, the following conclusion can be drawn: For efficient generation of pattern structures it is rather preferable to repeat the inner sequence core with a π-pulse of $\sigma_t = 15\,\mu$s by a total of two or three times rather than a single application of the sequence with a pulse of $\sigma_t = 20\,\mu$s. The former scheme results in

$$\widetilde{P}^{\mathrm{res}}_{\max}(2) = (88 \pm 2)\% , \quad \sigma_\omega^{\mathrm{res}}(2) = (5.31 \pm 0.03)\,\mathrm{kHz} , \tag{3.68a}$$

$$\widetilde{P}^{\mathrm{res}}_{\max}(3) = (83 \pm 3)\% , \quad \sigma_\omega^{\mathrm{res}}(3) = (4.34 \pm 0.03)\,\mathrm{kHz} , \tag{3.68b}$$

providing a higher selectivity and comparable maximum population transfer compared to the latter scheme, see Eq. (3.65).

To investigate the efficiency, resolution and possible imperfections of our patterning method, we generate a pattern of three pairs of next-nearest neighbors, see Fig. 3.15(c,d). Each atom pair is separated by 16 lattice sites from another, to reliably determine the distances of the atoms using the parametric deconvolution, see Sec. 2.4.1. The internal sequence core employs a pulse train of six subsequent applied Gaussian π-pulses with $\sigma_t = 20\,\mu$s,[9] $t = 150\,\mu$s, $\{\omega_1, \ldots \omega_6\} = \delta_0 + \omega'(45\,\mathrm{A}) \times \{-19, -17, -1, 1, 17, 19\}\lambda/2$ and a pulse separation time of $t_{\text{p-p}} = 200\,\mu$s. This pulse separation time ensures accurate settling of the voltage controlled frequencies from the list.[10] The inner sequence core is repeated by a total of $M = 2$ times. Consequently, we expect a maximum population transfer of $\widetilde{P}^{\mathrm{res}}_{\max}(2) = (71 \pm 2)\%$ at

[9] Despite of a maximum population transfer of only $\widetilde{P}_{\max} = (84 \pm 1)\%$, this pulse provides a reasonable $1/\sqrt{e}$ spectral half-width to reduce unwanted population transfer of adjacent atoms.

[10] Since the pulse separation time is of the order of the T_2 dephasing time, the population transfer of the atoms at lattice sites affected by more than one pulse of the pulse train adds up incoherently.

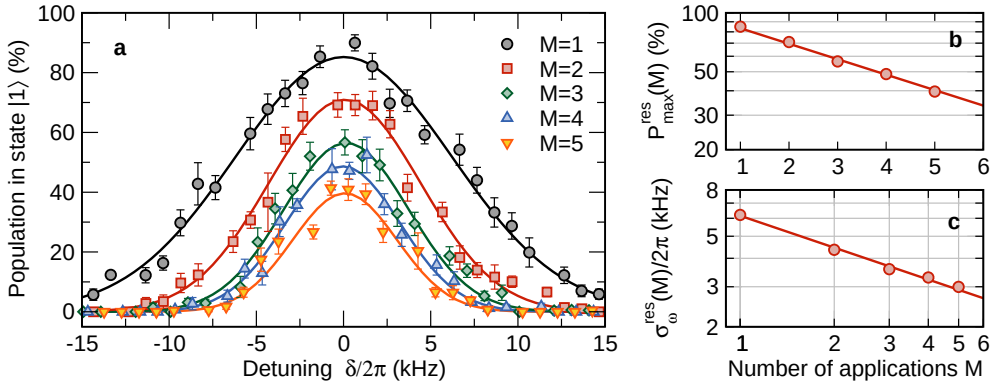

Figure 3.18.: (**a**) Microwave spectra for different numbers of applications M of the inner sequence core. Solid lines show Gaussian fits, from which (**b**) the dependency of the inferred maximum transfer efficiency $\widetilde{P}^{\mathrm{res}}_{\mathrm{max}}(M)$ (logarithmic plot) and (**c**) the $1\sqrt{e}$ spectral half-width $\sigma^{\mathrm{res}}_{\omega}(M)$ (double-logarithmic plot) on the number of applications is inferred. Both dependencies perfectly agree with the expected trend.

the predefined sites and a $1/\sqrt{e}$ spectral half-width of $\sigma^{\mathrm{res}}_{\omega}(2)/2\pi = (4.5 \pm 0.1)\,\mathrm{kHz}$. The latter corresponds to a $1/\sqrt{e}$ half-width in position space of

$$\sigma^{\mathrm{res}}_{z,\mathrm{exp}}(2) = (0.34 \pm 0.01)\lambda/2\,, \tag{3.69}$$

specifying the selectivity region for a single atom.

The entire patterning sequence is repeatedly recorded 500 times. From fluorescence images of the atoms, each acquired with an exposure time of 800 ms,[11] the positions and the distances of the atoms are determined. For a survival probability of a single atom of $p_{\mathrm{sur}} = (95 \pm 1)\%$ and an assumed filling factor of $p_{\mathrm{ini}} = 50\%$, the number of pairs correctly prepared with the predefined distance is expected to be

$$N_{\mathrm{exp}} = 3K(p_{\mathrm{ini}})^2(p_{\mathrm{sur}})^2(\widetilde{P}^{\mathrm{res}}_{\mathrm{max}}(2))^2 = 171 \pm 10\,. \tag{3.70}$$

In Figure 3.19 a histogram of measured distances between atoms forming the pairs is shown. It reveals a Gaussian-shaped distribution centered at the predefined separation of two lattice sites. From the histogram, we infer $N_{\mathrm{meas}} = 40 \pm 6$ correctly prepared pairs and a $1/\sqrt{e}$ half-width of the distances of $\sigma^{\mathrm{res}}_{\mathrm{dist}}(2) = (0.85 \pm 0.08)\lambda/2$ from a Gaussian fit. The corresponding selectivity region of a single atom is thus specified by

$$\sigma^{\mathrm{res}}_{z,\mathrm{meas}}(2) = \sigma^{\mathrm{res}}_{\mathrm{dist}}(2)/\sqrt{2} = (0.60 \pm 0.06)\lambda/2\,. \tag{3.71}$$

Both, the number of correctly prepared pairs and the $1/\sqrt{e}$ half-width of the selectivity region deviates from the expected values of Eqs. (3.69) and (3.70). These

[11] Even though the exposure time is shorter than that used in Sec. 2.4.1, the fluorescence signal of the atoms is comparable. Therefore, we expect the same reliability of inferring the correct number of sites separating two atoms as for an exposure time of 1 s

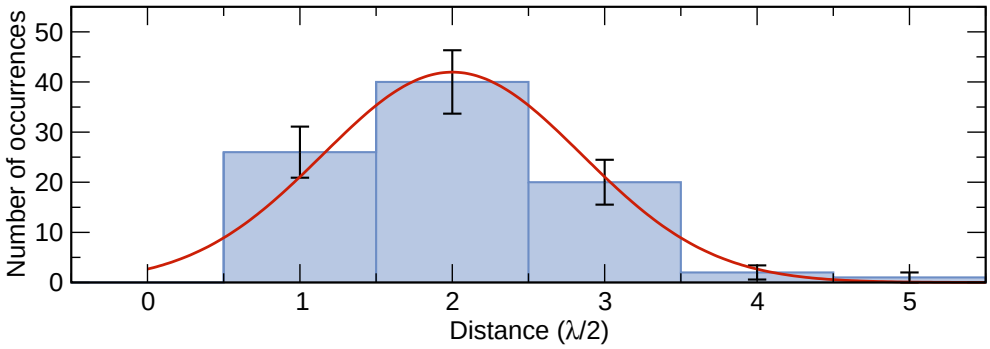

Figure 3.19.: Histogram of distances between two atoms forming the atom pairs shown in Fig. 3.15(c,d). A solid line shows a Gaussian fit to the histogram, from which the $1/\sqrt{e}$ half-width of the distances and the selectivity region of a single atom is inferred, see Eq. (3.69).

deviations can be attributed to the axial drift of the optical lattice and the radial offset of the lattice axis relative to the symmetry axis of the coils, see below. Nevertheless, the method has proved itself highly useful for the generation of predefined patterns.

Effect of axial drift of the optical lattice

In Section 2.4, the axial drift of the optical lattice with respect to the microscope objective has been investigated. Due to position-dependent frequency shift in the field gradient, an axial drift of the lattice also affects the $1/\sqrt{e}$ half-width of the selectivity region. Because the total measurement time, i.e. the time for measuring a full data set including up to 500 individual experimental sequences, is much longer than the time interval in which the lattice axially drifts over a distance of $\lambda/2$, the effect of this drift on the spectrum in position space can be described by a convolution equation

$$\widetilde{P}_{|1\rangle,\mathrm{drift}}(z) = \int_{-\infty}^{\infty} R(z')\widetilde{P}_{|1\rangle}(z-z')\mathrm{d}z' \,, \quad \text{with } R(z') = \begin{cases} 2/\lambda & \text{for } |z'| \leq \lambda/4 \,, \\ 0 & \text{else,} \end{cases} \tag{3.72}$$

where the rectangular function $R(z')$ comprises the periodicity of the optical lattice, including the fact that only drifts modulo $\lambda/2$ are distinguishable and relevant. By inverting the convolution equation, we infer a "drift-free" $1/\sqrt{e}$ half-width of the selectivity region of

$$\sigma^{\mathrm{res}}_{z,\mathrm{df}}(2) = (0.52 \pm 0.07)\lambda/2 \,. \tag{3.73}$$

This value explains part of the deviation between measurement and expectation mentioned above.

Effect of a radial offset of the lattice axis

In the following, we investigate the effect of a radial offset of the lattice axis with respect to the symmetry axis of the coils on the maximum population transfer and the selectivity region of a Gaussian π-pulse with $\sigma_\omega/2\pi = 6.4\,\mathrm{kHz}$ — the same pulse as used for the preparation of the string of atom pairs. All experimental parameters entering the calculations, including frequency shifts due to the guiding field δ_0 and the gradient field $\omega'(I = 45\,\mathrm{A})$, the temperature T, and the axial and radial trapping frequencies Ω_{ax} and Ω_{rad} of the atoms, are based on the typical values of the patterning sequence employed above. Experimental imperfections arising not from the field gradient itself are incorporated in the shape of the measured spectrum and its $1/\sqrt{e}$ spectral half-width σ_ω. For simplicity, we set the origin of the coordinate axes x', y' and z' to the spatial center of the lattice site in which the $|0\rangle \leftrightarrow |1\rangle$ transition frequency is shifted resonant to the pulse frequency by the field gradient. For this coordinate system, the spatial detuning in the presence of a radially offset field gradient is given by

$$\delta(\boldsymbol{r}', \boldsymbol{r}_0) = \omega_0(\boldsymbol{r}' - \boldsymbol{r}_0, I) - \omega_0(-\boldsymbol{r}_0, I) \tag{3.74}$$

with $\boldsymbol{r}' = (\rho' \cos\varphi', \rho' \sin\varphi', z')$, the offset vector $\boldsymbol{r}_0 = (\rho_0 \cos\varphi_0, \rho_0 \sin\varphi_0, z_0)$ and $\omega_0(\boldsymbol{r}, I)$ from Eq. (3.60).

In Figure 3.20, calculated regions addressed by the pulse (addressing regions) for which $|\delta(\boldsymbol{r}', \boldsymbol{r}_0)| \leq \sigma_\omega$ and $|\delta(\boldsymbol{r}', \boldsymbol{r}_0)| \leq 2\sigma_\omega$ in the presence of the field gradient are shown for different values of radial offset ρ_0. Atoms located in these regions experience a minimum population transfer of $\widetilde{P}_{\mathrm{min}} \geq 0.6\widetilde{P}_{\mathrm{max}}$ and $\widetilde{P}_{\mathrm{min}} \geq 0.13\widetilde{P}_{\mathrm{max}}$, respectively, whenever the Gaussian π-pulse is applied. Because of the quadratic dependence of $\delta(\boldsymbol{r}', \boldsymbol{r}_0)$ on the radial component, see Eqs. (3.74) and (3.60), the addressing regions are extending over neighboring lattice sites for increasing values of ρ_0. This yields a decrease of the spatial selectivity of the Gaussian π-pulses. Furthermore, we observe a decreasing intersection of the Gaussian thermal wave packet of a trapped atom and the addressing region. This leads to a decreased effective population transfer at desired lattice sites.

We quantify both observations by calculating the expected position-dependent spectra, i.e. the population transfer as function of axial displacement z' from the resonance position $\boldsymbol{r}' = \boldsymbol{0}$ for different radial offsets. For this, we average the population transfer specified by the spectrum of the Gaussian π-pulse (see Eq. (3.66)) over all position-dependent detunings, weighted with the axial and radial probability density of an atom in the trapping potential of the lattice. The latter read

$$p_{\mathrm{ax}}(z') = \frac{1}{\sqrt{2\pi}\vartheta_{\mathrm{ax}}} \exp\left(-\frac{z'^2}{2\vartheta_{\mathrm{ax}}^2}\right), \quad \text{with} \quad \vartheta_{\mathrm{ax}} = \sqrt{\frac{k_{\mathrm{B}}T}{m\Omega_{\mathrm{ax}}^2}} \tag{3.75}$$

and

$$p_{\mathrm{rad}}(\rho', \varphi') = \frac{\rho'}{2\pi\vartheta_{\mathrm{rad}}^2} \exp\left(-\frac{\rho'^2}{2\vartheta_{\mathrm{rad}}^2}\right), \quad \text{with} \quad \vartheta_{\mathrm{rad}} = \sqrt{\frac{k_{\mathrm{B}}T}{m\Omega_{\mathrm{rad}}^2}}, \tag{3.76}$$

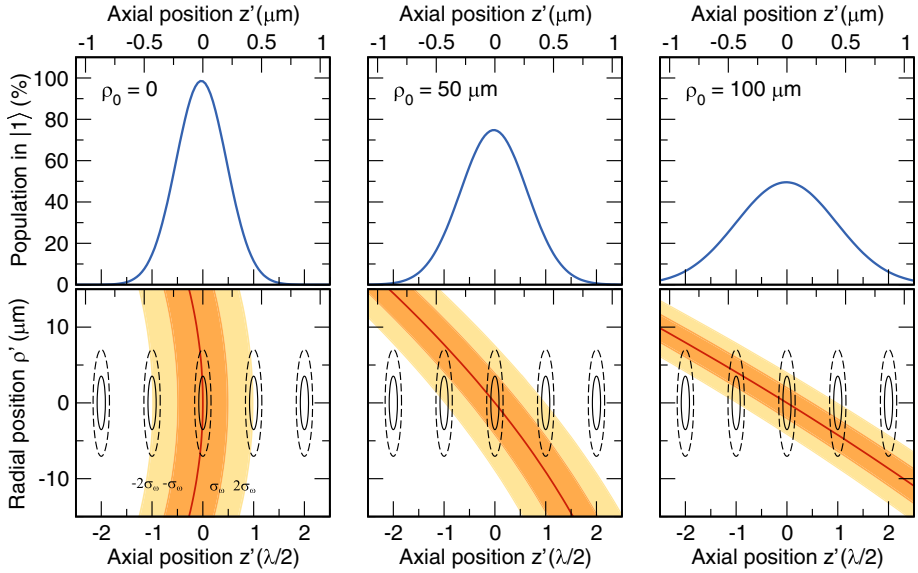

Figure 3.20.: Addressing regions, defined by $|\delta(\boldsymbol{r}', \boldsymbol{r}_0)| \leq \sigma_\omega$ and $|\delta(\boldsymbol{r}', \boldsymbol{r}_0)| \leq 2\sigma_\omega$ in the presence of the field gradient for different values of radial offsets ρ_0 (lower contour plots). The displayed plane is the common plane of the lattice axis and the symmetry axis of the coils. The horizontal axes are along the lattice axis. Ellipses indicate the $1/\sqrt{e}$ (solid lines) and $1/e^2$ (dashed lines) spread of the Gaussian thermal wave packets of atoms trapped in the potential wells (sites) of the optical lattice. Upper graphs show the corresponding effective spectra in position space, i.e. the population transfer as a function of axial displacement z' from the resonance position $\boldsymbol{r}' = \boldsymbol{0}$, as obtained from Eq. (3.77) for a Gaussian π-pulse with $\sigma_\omega/2\pi = 6.4\,\mathrm{kHz}$ and $\widetilde{P}_{\max} = 100\%$.

where ϑ_{ax} and ϑ_{rad} denote the axial $1/\sqrt{e}$ half-width, and $1/\sqrt{e}$ radius of the Gaussian thermal wave packet of the trapped atom, respectively. The position-dependent population transfer is then given by

$$\bar{P}_{|1\rangle}(z', \rho_0) = \int_{-\infty}^{\infty} \int_{0}^{2\pi} \int_{0}^{\infty} p_{\mathrm{ax}}(\zeta') p_{\mathrm{rad}}(\rho', \varphi') \widetilde{P}_{|1\rangle}(\delta(\boldsymbol{r}' - \zeta' \boldsymbol{e}_{z'}, \boldsymbol{r}_0))\, \mathrm{d}\rho'\, \mathrm{d}\varphi'\, \mathrm{d}\zeta' \,, \quad (3.77)$$

yielding again an approximately Gaussian-shaped spectrum in position space, see Fig. 3.20, from which the *effective* maximum population transfer $\bar{P}_{\max}$ and the *effective* $1/\sqrt{e}$ half-width in position space $\bar{\sigma}_z$ can be inferred. The dependency of both quantities on the radial offset of the lattice axis is shown in Fig. 3.21 for an ideal Gaussian π-pulse with $\widetilde{P}_{\max} = 100\%$ and $\sigma_\omega/2\pi = 6.4\,\mathrm{kHz}$. It confirms the expected behavior graphically inferred from the intersection of the thermal wave packets with the addressing regions. According to this calculation, the measured drift-free selectivity region for $M = 1$, specified by $\sigma^{\mathrm{res}}_{z,\mathrm{df}}(1) = \sqrt{2}\sigma^{\mathrm{res}}_{z,\mathrm{df}}(2)$ (see Eq. (3.73)), corresponds to a radial offset of $\rho_0 = (64 \pm 14)\,\mu\mathrm{m}$, which is of the order of magnitude of the value inferred from the calibration curves, see Sec. 3.4.3. The

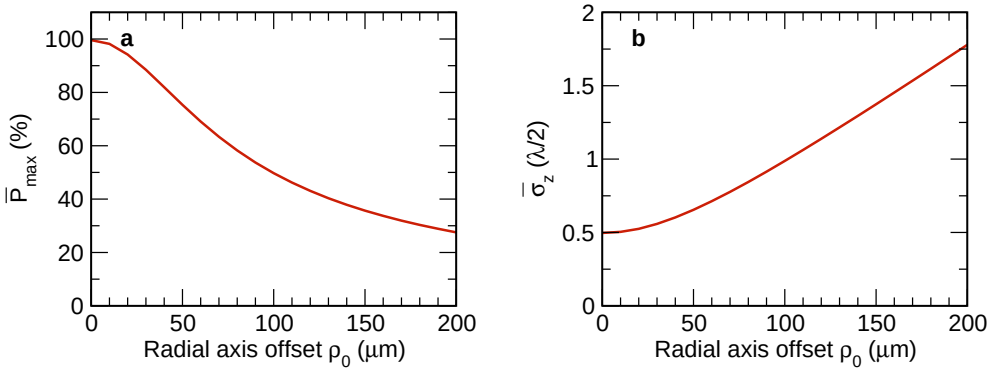

Figure 3.21.: (**a**) Dependency of the effective maximum population transfer $\bar{P}_{\max}$, and (**b**) the $1/\sqrt{e}$ half-width in position space $\bar{\sigma}_z$ on the radial offset of the lattice axis with respect to the symmetry axis of the coils. The data points of the curves have been determined from the numerical evaluation of Eq. (3.77).

deviation can be attributed to the thermal expansion of the coils and the entire holding construction, resulting in a drift of the coils axis from one day to another. Note that the calibration curves have been measured on another day. The inferred radial offset ρ_0 yields a maximum population transfer of $\bar{P}_{\max} = (58 \pm 8)\%$, and thus, an expected number of correctly prepared atom pairs of

$$\bar{N}_{\text{exp}} = 3K(p_{\text{ini}})^2(p_{\text{sur}})^2(\bar{P}^{\text{res}}_{\max}(2))^2 = 39 \pm 14\,. \tag{3.78}$$

This value agrees reasonably well with the measured value N_{meas} deduced from the histogram in Fig. 3.19.

The above investigation has shown that the radial offset of the lattice axis with respect to the symmetry axis of the coils significantly affects the selectivity performance and the position-dependent population transfer of the Gaussian π-pulses. By this, it also affects the resolution and the efficiency of generating predefined atom strings. In the future, methods aiming a precise and reliable alignment of overlap of both axis prior to an experimental sequence need to be developed.

Selectivity limit of the Gaussian π-pulse

Due to atomic motion in potential wells of an optical lattice, in the presence of a magnetic field gradient, atoms inherently experience transition frequency broadening over the course of the experimental sequence. This motion, which has been incorporated by the spread of the Gaussian thermal wave packet in our calculations, imposes a limit on the selectivity of the Gaussian π-pulses. To estimate this limit for our experimental setup, we assume a perfectly aligned setup ($\rho_0 = 0$) and calculate the effective spectra in position space for Gaussian π-pulses with $\widetilde{P}_{\max} = 100\%$ and different values of σ_ω using Eq. (3.77). Analogous to the previous section, from each resulting spectrum, we infer the effective parameters $\bar{P}_{\max}$ and $\bar{\sigma}_z$. Furthermore, we

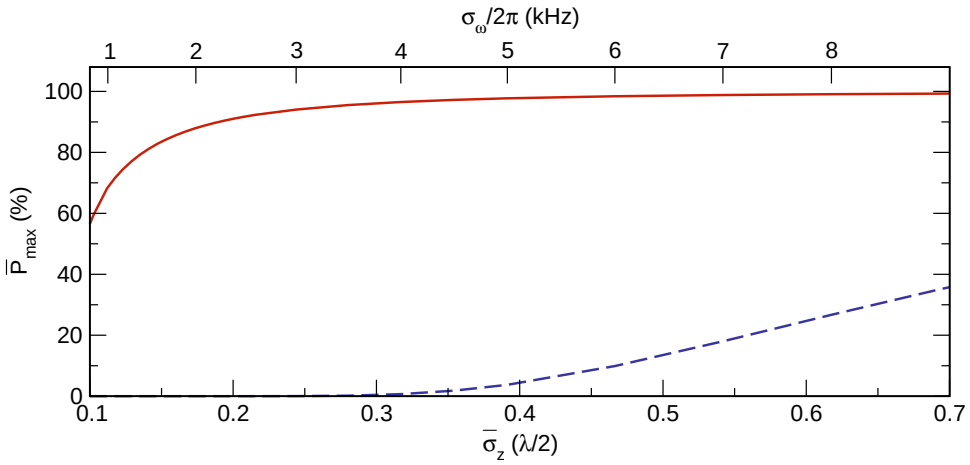

Figure 3.22.: Selectivity performance of a Gaussian π-pulse with $\widetilde{P}_{\max} = 100\%$ for a perfectly aligned system $\rho_0 = 0$ and different values of $1/\sqrt{e}$ spectral half-width σ_ω and the $1/\sqrt{e}$ half-width of the axial selectivity region in position space $\bar{\sigma}_z$. Solid line shows the effective maximum population transfer $\bar{P}_{\max}$ of an atom on a lattice site, shifted resonant to the π-pulse; dashed line, the population transfer of an atom on the neighboring site.

calculate the population transfer of an atom occupying a neighboring lattice site. A plot of these parameters is shown in Fig. 3.22. It reveals a decay of $\bar{P}_{\max}$ with decreasing σ_ω and $\bar{\sigma}_z$ which is mainly attributed to the axial spread of the thermal wave packet of the atoms. This axial spread exceeds the addressing region below a certain spectral pulse width. In case of $\rho_0 = 0$, the radial spread plays only a marginal role. For increasing σ_ω and $\bar{\sigma}_z$, in turn, the population transfer on the neighboring lattice sites increases.

Suppose we demand an effective maximum population transfer of $\bar{P}_{\max} = 95\%$ for an atom on a site which is shifted resonant to the pulse frequency. The lower selectivity limit is then specified by $\bar{\sigma}_z = 0.27\lambda/2$, yielding a population transfer of $\leq 0.1\%$ for atoms on neighboring lattice sites. From this, we conclude that single-site addressability is in principle possible with the current setup, however, only for a perfect overlap of the lattice axis and the symmetry axis of the coils. Otherwise, due to the radial offset, the radial spread of thermal wave packet of the atoms dominates the degradation of the addressability resolution. This effect can in principle be reduced by a stronger radial confinement of the one-dimensional optical lattice.

3.5. Composite pulses

Previously, we demonstrated quantum state manipulation either in the absence of, or the presence of a magnetic field gradient, each of which has its own benefits. While the former allows to equally manipulate all atoms of an ensemble by a single

pulse, the latter is used for selective manipulation. For some applications, both benefits are required simultaneously. The state-selectively transport of two atoms in opposite directions (see Chap. 7), for instance, requires both atoms to be initially prepared in orthogonal qubit basis states. The atoms are then stepwise moved from site to site, whereas in each step, their qubit states have to be flipped by a π-pulse. However, since the switching and decay time of the field gradient is of the order of the T_1 relaxation time, after selective state preparation, the state-selective transport has to be performed in the field gradient. Hence, the atomic resonance frequency changes during the transport. While for distant atoms this problem could be in principle solved by stepwise readjusting the pulse frequencies for each transported atom, the situation becomes more difficult for adjacent atoms. There, a π-pulse adjusted for one atom may unintentionally affect another adjacent atom. This situation, however, cannot be avoided in the implementation of controlled two-atoms collisions where two atoms are prepared at adjacent sites and transported towards a common lattice site.

Instead, another strategy is followed in this thesis: We employ an efficient state inversion in a wide frequency range of interest using a broadband composite pulse. For atoms occupying lattice sites at which the frequency shift lies within the pulse bandwidth, this composite pulse provides a similar inversion efficiency as a regular π-pulse in absence of the field gradient. So far, adiabatic passages have been used for this purpose [48,79], providing a broadband inversion within milliseconds. However, our experimental sequences require efficient inversions within tens of microseconds.

Composite pulses comprise a small number of contiguous, or near-contiguous pulses with different phases. They emulate the effect of a single pulse, providing additional compensatory mechanism which renders them less sensitive to experimental imperfections. By concatenation of several pulses, operations being more accurate than just for a single pulse can be achieved. Furthermore, systematic errors and other unwanted systematic effects can be selectively canceled. A general overview of composite pulses can be found in Refs. [21,137] and references therein. In this thesis, we restrict ourselves to a specific class of contiguous composite pulses, the so-called broadband composite pulses.

First, we briefly introduce a common pulse notation: A composite pulse sequence is typically written in chronological order from left to right. The pulse type and phase of each pulse of the sequence is characterized by degrees rather than radian units. A single π-pulse with $\phi_{\mathrm{rf}} = \pi/2$ ($\hat{U}_{\pi,\pi/2}$, see Tab. 3.1), for instance, is written as a 180_{90}-pulse. A 90_0180_{90}-pulse describes a composite pulse comprising a $\pi/2$-pulse with $\phi_{\mathrm{rf}} = 0$ subsequently followed by a π-pulse with $\phi_{\mathrm{rf}} = \pi/2$, accordingly. It corresponds to the operator $\hat{C} = \hat{U}_{\pi,\pi/2}\hat{U}_{\pi/2}$. Throughout this thesis, we will use the degree notation whenever sequences of composite pulses are involved. Otherwise, the standard radian notation will be used.

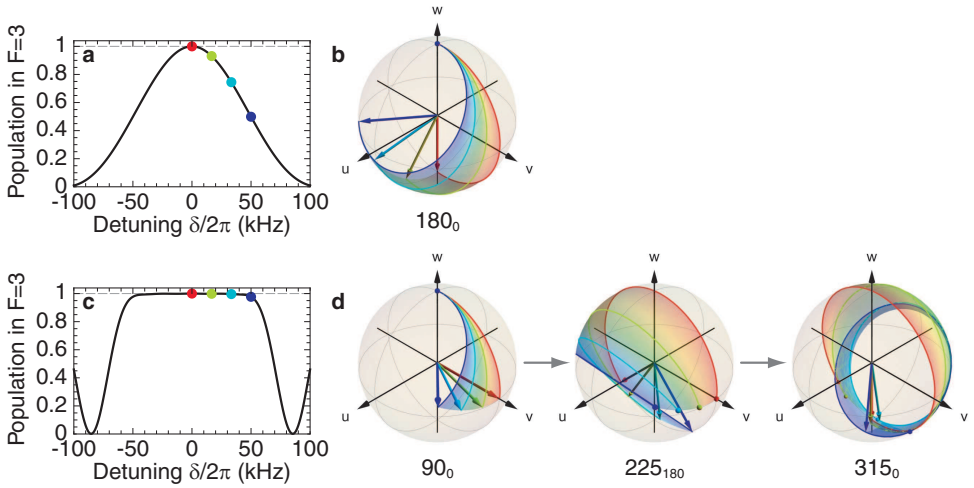

Figure 3.23.: Inversion performance of a single rectangular 180_0-(π-)pulse and a broadband $90_0225_{180}315_0$-(composite-)pulse of equal Rabi frequency. (**a**) Theoretical spectrum of the rectangular 180_0-pulse of $8\,\mu$s duration. (**b**) Dynamics of the Bloch vectors (colored arrows with trajectories) on the Bloch sphere, during MW operations for different frequency detuning. The colors of the Bloch vectors, correspond to a detuning of $\delta/2\pi = \{0, 1/3, 2/3, 1\} \times 50\,\text{kHz}$, indicated by the colored dots in the theoretical spectrum. (**c**) Theoretical spectrum of the $90_0225_{180}315_0$-(composite-)pulse of $28\,\mu$s duration. The respective Bloch vector dynamics (**d**) is decomposed into the individual pulses of the sequence.

The $90_0225_{180}315_0$-pulse

From all researched and experimentally tested broadband pulses, the $90_0225_{180}315_0$-pulse [138] provides the best performance in our experiment, concerning the bandwidth, inversion efficiency and the pulse duration. It is compatible with the constraints imposed by the coherence time and the applications presented in this thesis. The $90_0225_{180}315_0$-pulse comprises three pulses with lengths and phases adjusted in such a way, that Bloch vectors initialized in $\boldsymbol{u}_0 = (0, 0, 1)$ ($|0\rangle$) are perfectly refocused near $\boldsymbol{u}(t) = (0, 0, -1)$ ($|1\rangle$) for a wide range of frequency detuning, see Fig. 3.23. Furthermore, this pulse sequence provides similar compensation performance for pulse amplitude errors to that of a regular 180_0-(π)-pulse of equal Rabi-frequency almost over the entire relevant bandwidth, see Fig. 3.24(c). Due to a total pulse duration of $t = 28\,\mu\text{s} \ll T_2$, the $90_0225_{180}315_0$-pulse is only marginally affected by dephasing mechanisms of our experiment.

In Figure 3.24(a), a recorded microwave spectrum of the $90_0225_{180}315_0$-pulse is shown, together with the spectrum of the 180_0-pulse. It perfectly fits to the simulated spectrum, obtained by solving the optical Bloch equations with damping, employing the measured relaxation times T_1 and T_2. The spectrum reveals the expected uniform top-hat shape with a population transfer exceeding 90% over a

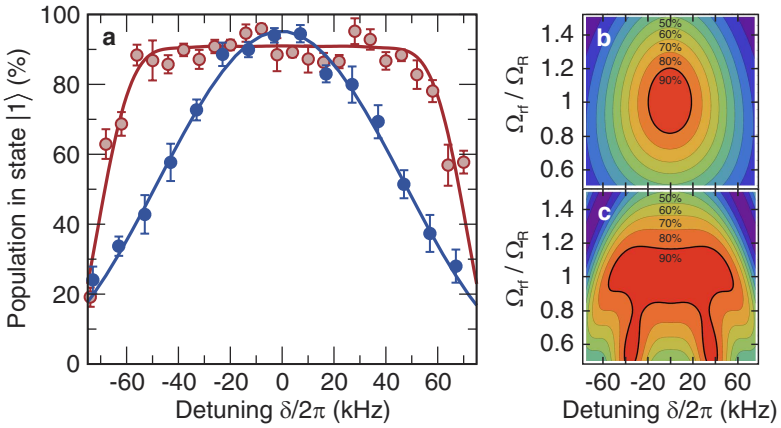

Figure 3.24.: (**a**) Measured inversion performance of a single rectangular 180_0-pulse with a pulse duration of $8\,\mu$s (filled dots) and a broadband $90_0225_{180}315_0$-pulse of equal Rabi frequency (open dots). Solid lines shows the amplitude fitted solutions of the optical Bloch equations with damping, employing the measured relaxation times T_1 and T_2. (**b**) Calculated inversion performance of a 180_0-pulse and (**c**) a $90_0225_{180}315_0$-pulse in the presence of amplitude errors, expressed as the relative deviation of the rf-Amplitude Ω_{rf} from the Rabi frequency Ω_{R}.

frequency range of $\Delta\omega/2\pi = (92 \pm 2)\,\mathrm{kHz}$ — the bandwidth of the composite pulse. Consequently, in the presence of a maximum available magnetic field gradient yielding a position-dependent frequency shift of $\omega'(I = 45\,\mathrm{A}) \approx 13\,\mathrm{kHz}$, this pulse can efficiently transfer the population of the atoms in a region comprising seven lattice sites. In the absence of field gradients, this pulse is ideally suited to compensate pulse frequency errors. Considering the fact that experiments on two-atom collisions are usually performed on atoms which are initially separated by four lattice sites, this region is sufficiently large.

3.6. Conclusion

In this chapter, I have presented the experimental implementation of methods to initialize, coherently manipulate, detect and completely characterize the internal quantum state of a two-level quantum system formed by cesium atoms trapped in an optical lattice. The required experimental setup, the performance and limitations of each adopted method have been disused in detail. Using Ramsey and (multiple) spin-echo spectroscopy, the contributions to the total coherence time of our quantum system have been measured. Furthermore, dominant decoherence mechanisms of our setup have been inferred. Polarization distortions of the light field of the optical lattice introduced by retardation elements of the experimental setup significantly affect the differential light shift. For the given lattice geometry and temperature of the atoms, this differential light shift and its fluctuations, provide the most

dominant source of decoherence.

Besides collective manipulation on atomic ensembles, selective manipulation of individual atoms employing a position-dependent frequency shift in the presence of a magnetic field gradient has been successfully adopted and demonstrated. Our modified configuration of anti-Helmholtz coils enables us to coherently manipulate individual atoms close to single-site resolution. This ability was utilized to prepare regular patterns of atoms with predefined distances. The preparation efficiency and strategies to effectively increase the selectivity of the involved pulse trains have been discussed in detail. Deviations in selectivity and preparation performance from theoretical expectations have been attributed to the axial drift of the optical lattice and particularly to the radial offset of the lattice axis relative to the symmetry axis of the coils.

Finally, we employed a broadband composite pulse to perform efficient quantum state inversion in a field gradient in a region comprising several lattice sites. All methods and strategies discussed in this chapter, together with the inferred knowledge on their limitations and technical imperfections will be employed in the investigation of the state selective-transport and its applications, presented in the following chapters.

4. State-selective transport of neutral atoms

Apart from selective manipulation of individual qubits, the most interesting applications of quantum engineering and quantum information science require a controlled interaction between qubits, or a coupling of qubits to an additional, well-controlled degree of freedom. Controlled interactions between atoms in adjacent lattice sites can be either realized by photon transfer in a high-fines cavity [31–33], Rydberg blockade interactions [34–36] or just by bringing two atoms into contact [37]. For the latter approach, state-selective transport in optical lattices have been proposed which allows to transport atoms from one lattice site to another, whereby the transport direction of each atom is determined by its encoded qubit state. Such transport can be used to realize fundamental quantum gates [16, 53, 55] or create large-scale entanglement [37, 54].

In the last decade, state-selective transport of large ensembles of Rubidium atoms in a Mott insulating state [38, 39] has been realized [40], impressively demonstrating controlled and coherent delocalization of an atomic wave function over a defined number of lattice sites. Using this technique, large-scale entanglement has been achieved [41], albeit a quantitative measurement for the size of the entangled many-body state has been not feasible so far. The question whether such coherent transport can be adopted to a thermal ensemble of atoms and to which extent coherence properties are then maintained, remained unanswered so far. Inspired by its versatility and results for large atomic ensembles, new ideas emerged which aim to adopt the state-selective transport to smaller systems comprising few atoms only. In contrast to large ensembles, such systems allow full control over each individual atom. By this, unbiased insights into details of two atom interactions are anticipated.

Multipath quantum interference of a delocalized single-particle wave function recently receives more and more attention in the context of so-called quantum walks [4], which provide an alternative approach for universal quantum computing [5, 6]. Recently, realization of quantum walks using coherent state-selective transport of neutral atoms in optical lattices has been proposed [50]. However, it is initially unclear whether a thermal ensemble of atoms is eligible for this purpose.

In this chapter, the basic concepts and properties of the state-selective transport of single atoms in a one-dimensional optical lattice are discussed. I present the experimental realization and results, from which the transport efficiency is initially inferred. Coherence properties of the state-selective transport of thermal atoms and results of some of its applications, including a single atom interferometer, a quan-

tum walk in position space and controlled collisions between two individual atoms, employing the new degree of precision in detection and selective manipulations of atoms, are separately presented and investigated in subsequent chapters.

4.1. State-selective potentials

The state-selective transport extends the concept of dipole potentials, in which atoms are state-selectively trapped. We briefly introduce this concept initially assuming that atoms are prepared in one of the qubit basis states, either $|0\rangle$ or $|1\rangle$, before focusing on the more interesting cases of superpositions of basis states. The latter play a decisive role in analysis of coherence properties of the transport and realization of a single atom interferometer and a quantum walk.

To illustrate the basic concept of state-selective potentials, for the sake of simplicity, we first restrict the discussion to the fine structure representation of qubit basis states, initially ignoring the hyperfine structure of cesium atoms. In this representation, the qubit basis states $|0\rangle$ and $|1\rangle$ are replaced by their fine structure counterparts, $|0'\rangle \equiv |J = 1/2, m_J = +1/2\rangle$ and $|1'\rangle \equiv |J = 1/2, m_J = -1/2\rangle$. In presence of a light field, light shifts of the respective energy levels are assumed to be dominated by contributions of the first excited states, i.e. those of the $6^2P_{1/2}$ and $6^2P_{3/2}$ manifold, see Fig. 4.1. Their transition frequencies with respect to the ground state correspond to the D_1 and D_2 line of cesium.

Consider a linearly polarized light field, decomposed in the basis of σ^+ and σ^- polarization, and detuned between the D_1 and D_2 line. On the one hand, the light field is red-detuned with respect to the $J = 1/2 \rightarrow J' = 3/2$ transition, forming an attractive dipole potential. Regarding the $J = 1/2 \rightarrow J' = 1/2$ transition, on the other hand, the light field is blue-detuned, yielding a repulsive contribution to the potential. By detuning the light field near to the middle of the D_1 and D_2 line, both, the attractive and the repulsive contributions from the $m'_J = \pm 1/2$ transitions cancel. The uncompensated attractive contributions from the outermost states of the $6^2P_{3/2}$ manifold ($|J' = 3/2, m'_J = \pm 3/2\rangle$) form the state-selective potentials, in which atoms in different fine structure ground states are separately trapped. Therefore, atoms in state $|0'\rangle$ are trapped in a potential generated by σ^+ polarized component of the light field, whereas atoms in state $|1'\rangle$ only experience a potential from the σ^- polarized component.

Incorporating the hyperfine structure

A more accurate description requires the nuclear spin of cesium $I = 7/2$ and the resulting hyperfine structure to be taken into account. For this, we exploit the fact that states of the hyperfine structure can be decomposed into the fine structure basis using the following relation

$$|I, J, F, m_F\rangle = \sum_{m_I, m_J} \langle I, m_I, J, m_J | I, J, F, m_F\rangle |I, m_I\rangle \otimes |J, m_J\rangle \,, \tag{4.1}$$

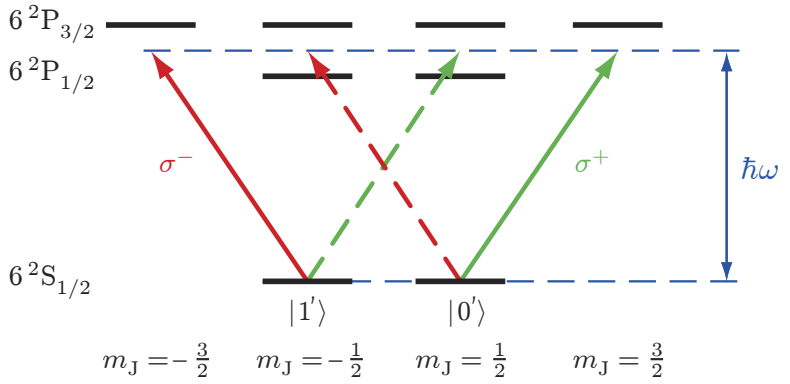

Figure 4.1.: Zeeman sublevels in the fine structure of the ground and the first excited states of cesium. Possible transitions for σ^+ and σ^- polarized light are indicated by red and green arrows, respectively. For a characteristic frequency ω of the light field, detuned near the middle of the D_1 and D_2 transition, both light shift contributions from the $m'_\mathrm{J} = \pm 1/2$ transitions (dashed arrows) to the trapping potential cancel.

where the matrix elements $\langle I, m_\mathrm{I}, J, m_\mathrm{J} | I, J, F, m_\mathrm{F}\rangle$ correspond to the Clebsch-Gordan coefficients [139] of the basis transformation $|I, J, F, m_\mathrm{F}\rangle \rightarrow |I, m_\mathrm{I}\rangle \otimes |J, m_\mathrm{J}\rangle$. For the qubit basis state employed in this thesis, we thus obtain

$$|0\rangle = |I = 7/2, m_\mathrm{J} = 7/2\rangle \otimes |0'\rangle\,, \tag{4.2a}$$

$$|1\rangle = \sqrt{\frac{7}{8}}|I = 7/2, m_\mathrm{J} = 7/2\rangle \otimes |1'\rangle - \sqrt{\frac{1}{8}}|I = 7/2, m_\mathrm{J} = 5/2\rangle \otimes |0'\rangle\,. \tag{4.2b}$$

Therefore, state $|0\rangle$ couples perfectly to the fine structure state $|0'\rangle$, whereas state $|1\rangle$ has an overlap with both fine structure states, state $|1'\rangle$ and $|0'\rangle$, at a ratio of $\sqrt{7}$ to 1. For the proper detuning of the light field (see above), atoms in state $|0\rangle$ are still only affected by the σ^+ polarized component of the light field. Atoms in state $|1\rangle$, however, see a mixture of σ^+ and σ^- polarized light, whereas the coupling to the σ^- component prevails. This mixture is unavoidable, yielding secondary effects which significantly affect the properties of the state-selective transport, see Sec. 4.2.

Characteristic wavelength

Following the illustrative explanation, the proper detuning of the light field, also referred to as the characteristic wavelength λ, is constrained by the condition that atoms in qubit state $|0\rangle$ are only affected by the σ^+ polarized component of the light field. In other words, the dipole potential for the σ^- polarized component has to vanish:

$$U_{|0\rangle}(q = -1, \lambda_{|0\rangle}, \boldsymbol{r}) = 0\,. \tag{4.3}$$

Assuming that only the first excited states $6^2\mathrm{P}_{1/2}$ and $6^2\mathrm{P}_{3/2}$ significantly contribute to the light shifts of the $6^2\mathrm{S}_{1/2}$ ground states, the dipole potential is given

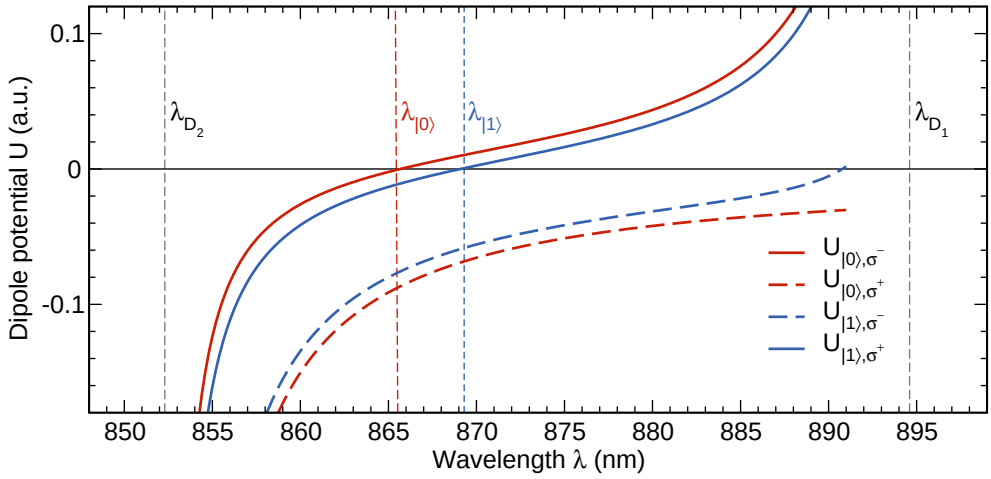

Figure 4.2.: Wavelength dependency of dipole potential contributions of the σ^+ and σ^- polarized light field in the relevant region Λ, calculated for both qubit basis states, $|0\rangle$ and $|1\rangle$, using Eq. (4.4). Zero-crossings of $U_{|0\rangle,\sigma^-} \equiv U_{|0\rangle}(-1,\lambda,\boldsymbol{r})$ and $U_{|1\rangle,\sigma^+} \equiv U_{|1\rangle}(+1,\lambda,\boldsymbol{r})$ specify the characteristic wavelengths $\lambda_{|0\rangle}$ and $\lambda_{|1\rangle}$, respectively.

by [78]

$$U_{|F,m_\mathrm{F}\rangle}(q,\lambda,\boldsymbol{r}) = \frac{3e^2}{2m_\mathrm{e}c\varepsilon_0} I_q(\boldsymbol{r})(2F+1) \times \sum_{J',F',m'_\mathrm{F}} \frac{(2F'+1)f_{1/2,J'}}{|\omega_{J',F'}|(2\pi c/\lambda - \omega_{J',F'})} \begin{pmatrix} F & 1 & F' \\ m_\mathrm{F} & q & -m'_\mathrm{F} \end{pmatrix}^2 \begin{Bmatrix} J' & 1/2 & 1 \\ F & F' & 7/2 \end{Bmatrix}^2 . \quad (4.4)$$

Here q characterizes the polarization of the light field ($q = 0, \pm 1$ for linearly, circularly $\sigma^\pm$), $I_q(\boldsymbol{r})$ denotes its intensity, $\omega_{J'F'}$ the transition frequencies between the ground states and the manifold of the first excited states and $f_{1/2,J'}$ the corresponding oscillator strengths, both taken from Ref. [140]. Brackets $(\ldots)$ and $\{\ldots\}$ denote the Wigner $3j$- and $6j$-symbols, respectively. By solving Eq. (4.3), we obtain a characteristic wavelength of

$$\lambda_{|0\rangle} = 865.9\,\mathrm{nm}\,. \quad (4.5)$$

Analogous to Eq. (4.3), a similar condition for atoms in state $|1\rangle$ and the σ^- polarized light can be established, yielding a characteristic wavelength of $\lambda_{|1\rangle} = 869.3\,\mathrm{nm}$. At this wavelength, coupling of state $|1\rangle$ to both polarization components is effectively counteracted, resulting in an opposite situation: While atoms in state $|1\rangle$ are now affected only by the σ^- component of the light field, atoms in state $|0\rangle$ are coupled to both circular components.

In Figure 4.2, the dependency of potential contributions for both circularly polarized components and qubit basis states on the wavelength in the relevant region $\lambda \in \Lambda = [\lambda_{\mathrm{D}_2}, \lambda_{\mathrm{D}_1}]$ between the D_2 ($\lambda_{\mathrm{D}_2} = 894.6\,\mathrm{nm}$) and D_1 ($\lambda_{\mathrm{D}_1} = 852.3\,\mathrm{nm}$) lines

is shown. Zero-crossings of these contributions specify the characteristic wavelengths $\lambda_{|0\rangle}$ and $\lambda_{|1\rangle}$, respectively. Since $U_{|0\rangle}(q=-1,\lambda,\boldsymbol{r}) \neq U_{|1\rangle}(q=+1,\lambda,\boldsymbol{r})$ for $\lambda \in \Lambda$, there is no characteristic wavelength at which both qubit basis states couple solely to a different circular component. Note that, in principle, each wavelength in Λ is suitable for the realization of state-selective potentials. Differences with regard to the state-selective transport arise merely from different couplings of qubit basis states to the undesired polarization component. For technical reasons, we prefer the characteristic wavelength $\lambda \equiv \lambda_{|0\rangle}$. Possible benefits of other wavelengths are discussed in Ref. [78].

4.2. Moving atoms in state-selective potentials

Employing the idea of state-selective potentials, a state-selective transport can be achieved by a light field comprising orthogonally circularly polarized standing waves, each forming an optical lattice, which can be spatially shifted with respect to each other in a controlled manner. This can be realized by two counterpropagating linearly polarized laser beams in a lin-θ-lin configuration with a continuously varied polarization angle θ of one of the beams. Let

$$\boldsymbol{E}_{\mathrm{inc}}(\boldsymbol{r},t) = A(\boldsymbol{r})\cos(\omega t - f(\boldsymbol{r}))\cdot\boldsymbol{e}_{\theta=0}\,, \tag{4.6a}$$

$$\boldsymbol{E}_{\mathrm{ret}}(\boldsymbol{r},t) = A(\boldsymbol{r})\cos(\omega t + f(\boldsymbol{r}))\cdot\boldsymbol{e}_{\theta} \tag{4.6b}$$

be the electric fields of two counterpropagating identical Gaussian beams, an incident and a returning beam with an amplitude $A(\boldsymbol{r})$ and a phase $f(\boldsymbol{r})$, both introduced in Sec. 1.2.2. By decomposing the linear polarization vector $\boldsymbol{e}_\theta$ in a circular basis

$$\boldsymbol{e}_\theta = \begin{pmatrix}\cos\theta\\ \sin\theta\end{pmatrix} = \frac{1}{\sqrt{2}}\left(e^{-i\theta}\boldsymbol{e}_{\sigma^+} + e^{i\theta}\boldsymbol{e}_{\sigma^-}\right), \quad \text{with} \quad \boldsymbol{e}_{\sigma^\pm} = \frac{1}{\sqrt{2}}\begin{pmatrix}1\\ \pm i\end{pmatrix}, \tag{4.7}$$

the resulting total field can be written as

$$\boldsymbol{E}(\boldsymbol{r},t) = \boldsymbol{E}_{\mathrm{inc}}(\boldsymbol{r},t) + \boldsymbol{E}_{\mathrm{ret}}(\boldsymbol{r},t) = \boldsymbol{E}_{\sigma^+}(\boldsymbol{r},t) + \boldsymbol{E}_{\sigma^-}(\boldsymbol{r},t) \tag{4.8}$$

with the circularly polarized field components

$$\boldsymbol{E}_{\sigma^\pm}(\boldsymbol{r},t) = \sqrt{2}A(\boldsymbol{r})\cos(f(\boldsymbol{r}) \mp \theta/2)\cdot \mathrm{Re}\left\{e^{i(\omega t \mp \theta/2)}\boldsymbol{e}_{\sigma^\pm}\right\}. \tag{4.9}$$

The intensity of the resulting light field,

$$I(\boldsymbol{r}) = c\varepsilon_0\langle\boldsymbol{E}^2(\boldsymbol{r},t)\rangle = c\varepsilon_0\left[\langle\boldsymbol{E}^2_{\sigma^+}(\boldsymbol{r},t)\rangle + \langle\boldsymbol{E}^2_{\sigma^-}(\boldsymbol{r},t)\rangle\right] = I_{\sigma^+}(\boldsymbol{r}) + I_{\sigma^-}(\boldsymbol{r})\,, \tag{4.10}$$

can similarly be decomposed into circularly polarized components with

$$I_{\sigma^\pm}(\boldsymbol{r}) = A^2(\boldsymbol{r})\cos^2(f(\boldsymbol{r}) \mp \theta/2) \equiv I_{q=\pm1}(\boldsymbol{r})\,, \tag{4.11}$$

where we used the fact that mixed contributions $\langle \boldsymbol{E}_{\sigma^\pm}(\boldsymbol{r},t)\boldsymbol{E}_{\sigma^\mp}(\boldsymbol{r},t)\rangle$ vanish in the time-average, denoted as $\langle \ldots \rangle$. These intensity components form two orthogonally circularly polarized standing waves. By varying the angle θ, each of them is shifted in opposite direction by a distance of $z_\pm = \mp(\lambda/2\pi)(\theta/2)$, resulting in a total displacement of $\delta z = |z_+ - z_-| = (\lambda/2)(\theta/\pi)$ with respect to each other. According to Eq. (4.4), the shift of the standing waves directly translates into a displacement of the respective dipole potential components $U_{|j\rangle}(\pm 1, \lambda, \boldsymbol{r})$ for $j = \{0, 1\}$. Considering the fact that atoms in one of both qubit basis states are trapped in only one, the prevailing potential component, we finally have realized a state-selective transport.

Effect of undesired polarization components

The general effective trapping potential of atoms in state $|j\rangle$, including those cases, in which atoms are affected by both circularly polarized components of the light field, is given by

$$U_{\mathrm{dip},|j\rangle}(\boldsymbol{r},\theta) \equiv U_{|j\rangle,\sigma^+}\cos^2\left(f(\boldsymbol{r}) - \theta/2\right) + U_{|j\rangle,\sigma^-}\cos^2\left(f(\boldsymbol{r}) + \theta/2\right)\,, \tag{4.12}$$

where $U_{|j\rangle,\sigma^\pm}$ denotes the depth of the respective potential component $U_{|j\rangle}(\pm 1, \lambda, \boldsymbol{r})$, see Eq. (4.4). It can be rewritten as

$$U_{\mathrm{dip},|j\rangle}(\boldsymbol{r},\theta) = V_{|j\rangle}(\theta) + W_{|j\rangle}(\theta)\cos^2\left(f(\boldsymbol{r}) + \vartheta_{|j\rangle}(\theta)\right) \tag{4.13}$$

with an effective phase

$$\vartheta_{|j\rangle}(\theta) = \begin{cases} 0 & \text{if} \quad \theta = \pi n \quad (n \in \mathbb{Z})\,, \\ \frac{1}{2}\arctan\left[\frac{U_{|j\rangle,\sigma^+} + U_{|j\rangle,\sigma^-}}{U_{|j\rangle,\sigma^+} - U_{|j\rangle,\sigma^-}}\tan\left(\theta - \frac{\pi}{2}\right)\right] - \frac{\pi}{4} & \text{else}\,, \end{cases} \tag{4.14}$$

an effective contrast

$$W_{|j\rangle}(\theta) = \left(U_{|j\rangle,\sigma^+} + U_{|j\rangle,\sigma^-}\right) \times \begin{cases} 1 & \text{if} \quad \theta = (2n+1)\frac{\pi}{2} \quad (n \in \mathbb{Z}) \\ \frac{\cos\theta}{\cos\left(2\vartheta_{|j\rangle}(\theta)\right)} & \text{else}\,, \end{cases} \tag{4.15}$$

and an effective offset

$$V_{|j\rangle}(\theta) = \frac{1}{2}\left(U_{|j\rangle,\sigma^+} + U_{|j\rangle,\sigma^-} - W_{|j\rangle}(\theta)\right)\,. \tag{4.16}$$

From Eq. (4.13), two characteristic properties of a trapping potential comprising both circularly polarized contributions ($U_{|j\rangle,\sigma^+}, U_{|j\rangle,\sigma^-} \neq 0$) can be deduced: First, in contrast to the purely circular polarized components, the shift of the effective potential depends non-linearly on the polarization rotation angle θ, see Eq. (4.14). This fact has to be taken into account, whenever customized profiles for polarization rotation to optimize the transport velocity and the acceleration have to be employed. Second, according to Eqs. (4.15) and (4.16), the effective potential depth

$$U_{0,|j\rangle}(\theta) \equiv V_{|j\rangle}(\theta) + W_{|j\rangle}(\theta) \tag{4.17}$$

and the effective potential contrast $W_{|j\rangle}(\theta)$ change during the shift, affecting all related parameters, e.g. the axial and radial trapping frequencies of atoms in the optical lattice, see Fig. 4.5(b) in Sec. 4.4. By this, excitations of atoms into higher vibrational states may occur, e.g. when trapping potentials become shallow during the shift. Avoiding these excitations is of particular importance for applications of the state-selective transport, especially for those employing interference phenomena and those imposing high demands on coherence properties, see e.g. Chap. 5 and Chap. 6. Note that changes of the trapping potential also affect the evolution of qubit phase during the transport, see Sec. 5.1.

For the characteristic wavelength employed in this thesis, the depths of the dipole potential components obey $U_{|0\rangle,\sigma^+}/U_{|0\rangle,\sigma^-} \approx \infty$ and $U_{|1\rangle,\sigma^+}/U_{|1\rangle,\sigma^-} \approx 1/7$. Therefore, ideally only atoms in basis state $|1\rangle$ experience changes of the trapping potential during the state-selective transport.

4.3. Experimental setup

The tilt angle θ between polarization vectors of the incident and returning beam is dynamically adjusted through an electro-optical modulator (EOM) and additional polarization optics, similar to Ref. [40]. The respective setup is schematically show in Fig. 4.3. Details on optical components and their performance can be found in Ref. [68]. The polarization control setup comprises a quarter-wave plate and an EOM, the principal axes of which are parallel and perpendicular to the polarization vector of the incident, linearly polarized beam respectively, whereas the axes of the half-wave plate in between are tilted by 22.5°. Note that instead of using a half-wave plate, the EOM could be just rolled around the beam axis by 45°. However, for practical reasons, it is much easier to precisely rotate a half-wave plate rather than to roll the EOM. Both custom-made zero-order[1] wave plates are housed in mounts with high-precision, backlash-free micrometer drive for ultra-fine rotational adjustment. The EOM (Conoptics 350-80BK) is mounted on a self-developed holder which permits precise adjustment of translational, yaw and pitch degrees of freedom using micrometer actuators.

In a preparatory step, all retardation components of the polarization control setup are successively aligned to the minimum extinction ratio using two high-quality polarizers, which may be temporality placed between the respective components. This also applies for the polarization of the incident laser beam, the purity of which is affected by distortion from the glass cell and the vacuum window. We precompensate these distortions using a combination of a half-wave and a quarter-wave plate, see Fig. 1.7 in Sec. 1.2.3. The remaining components are then aligned to the polarization of the incident beam, which defines the reference system (x-axis in Fig. 4.3). Fine-alignment of retardation components (mainly the EOM) is finally performed by probing the polarization purity in the trapping region of atoms using microwave spectroscopy, see Sec. 4.5.

[1] Specified for (867 ± 0.3) nm

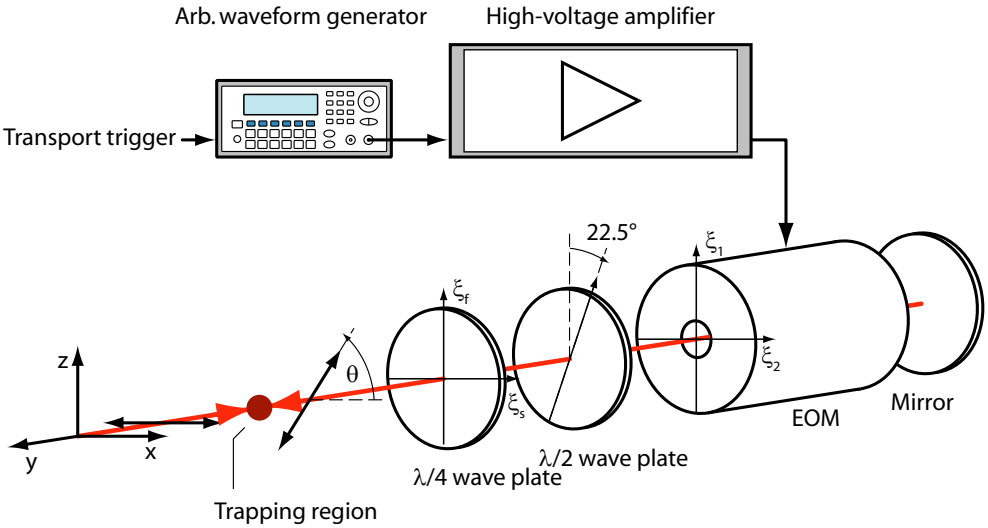

Figure 4.3.: Polarization control setup to dynamically adjust the tilt angle θ between polarization vectors of the incident and returning beam using an electro-optical modulator (EOM). The principle axes of the quarter-wave plate are labeled by ξ_f and ξ_s (fast and slow axis), those of the EOM as ξ_1 and ξ_2. They are parallel and perpendicular to the polarization vector of the incident, linearly polarized beam respectively. A half-wave plate in between is used to rotate the initial polarization vector exactly between both principal axes of the EOM.

Once the polarization control setup is aligned, the incident beam passes the trapping region and the quarter-wave plate unaffected. The following half-wave plate rotates its polarization by 45°, i.e. exactly between both principal axes of the EOM, so that intensities of light field components along both principal axis are identical. The EOM introduces a phase shift between its axes, depending on the voltage $\mathcal{V}$ applied. After retro-reflecting the incident beam, it repasses through the EOM effectively doubling its voltage controlled phase shift. Finally, passing the quarter-wave plate once again, the polarization vector of the returning beam is tilted by an angle $\theta = \pi\mathcal{V}/\mathcal{V}_{\lambda/2}$ with respect to the initial polarization (see Fig. 4.3), where $\mathcal{V}_{\lambda/2}$ denotes the half-wave voltage of the EOM ($\mathcal{V}_{\lambda/2} \approx 452\,\mathrm{V}$ at $\lambda = 865.9\,\mathrm{nm}$).

The EOM is driven by a high-voltage amplifier (Conoptics 302RM) which has a specified bandwidth of 250 kHz. It provides a rise time of 1 μs and an output voltage of $\mathcal{V}_\mathrm{max} = 750\,\mathrm{V_{p\text{-}p}}$, limiting the range of possible tilt angles to approximately 1.7π. For timing-critical applications requiring a high-degree of precision, driving ramps of the amplifier are voltage-controlled by an external arbitrary wave form generator (Agilent 33250A) which in turn is triggered by a computer.

In a certain time interval, the polarization control setup can be regarded as linear and time-invariant.[2] Therefore, analogous to the imaging system, its dynamic

[2]Note that both properties are well preserved within a time interval of only 100 ms. On longer

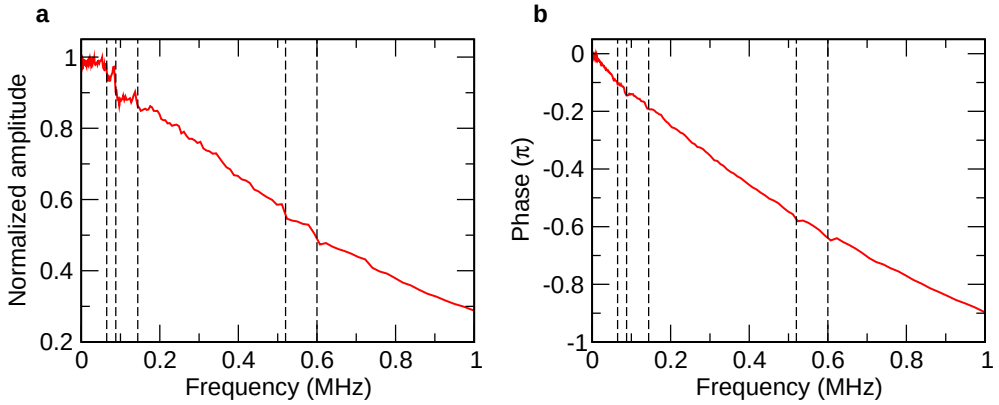

Figure 4.4.: Normalized spectral amplitude (**a**) and phase (**b**) of the transfer function, recorded in a frequency range of 1 MHz. Dashed vertical lines at frequencies of $\nu = \{65, 88, 144, 520, 600\}$ kHz indicate positions of noticeable resonances which are mostly attributed to piezoelectric resonances of the EOM crystals.

performance can be characterized by the respective transfer function. We have optically measured and recorded the transfer function in the frequency domain, employing a system of polarization components, a high bandwidth photodiode and a network analyzer (Hewlett-Packard 3589A). The latter provides a normalized[3] spectral amplitude $A(\nu)$ and phase $\phi(\nu)$, from which the transfer function can be directly inferred

$$O(\nu) = A(\nu)e^{i\phi(\nu)} \,. \tag{4.18}$$

Both characteristic quantities are also referred to as amplitude and phase response of a driven system. Details on the measurement and the respective experimental setup can be found in Ref. [122].

In Figure 4.4, the normalized spectral amplitude and phase of the transfer function of our setup is shown. From the former, we infer a -3 dB bandwidth of 370 kHz which exceeds the manufacturer's specification of 250 kHz. Both, the spectral amplitude and phase reveal noticeable resonances at $\nu = \{65, 88, 144, 520, 600\}$ kHZ which are mostly attributed to piezoelectric resonances of the EOM crystals. In our special clamped version of the EOM (BK option), these piezoelectric resonances are significantly suppressed compared to EOMs, previously employed in our setup, see Ref. [122]. Therefore, no particular attention in choice of driving ramps for transport sequences is required.

timescales, problems in holding high voltages, which results in drifts of the tilt angle θ occur, see also Ref. [68]. These technical problems have been not solved so far. Strategies to partly overcome them in applications requiring a precise dynamical polarization control are discussed in Sec. 4.5.

[3]The spectral amplitude is normalized to its DC value, i.e. $A(\nu) = \tilde{A}(\nu)/\tilde{A}(\nu \to 0)$, where $\tilde{A}(\nu)$ denotes the amplitude as inferred from the network analyzer.

Knowing the transfer function, the polarization dynamics for a preset driving ramp, feed into the input of the amplifier, can be directly inferred. This allows us, among others, to estimate and predict the effect of the limited bandwidth on relevant experimental parameters, see e.g. Sec. 4.4. It turns out that excitations between motional states of the atoms during the state-selective transport limit the choice of reasonable driving ramps and ramp times rather than the bandwidth of our polarization control setup. Optimum driving ramps which provide both, short ramp times and marginal excitations are almost perfectly followed by the optical response of our setup, whereas solely the retardation and settling time need to be taken into account for synchronizing microwave pulses applied between the transport operation in the sequences, see Sec. 4.5. Consequently, at least for all driving ramps employed in this thesis, no precompensation of the driving signal considering the transfer function of our polarization control setup is required.[4]

4.4. Excitation of motional states in moving potentials

Employing quantum interference of atomic wave functions in applications of the state-selective transport requires the preservation of both, the motional states of atoms and coherence of their internal states. At first glance, these requirements appear to be contradictory: On the one hand, atoms have to be shifted adiabatically to preserve their vibrational state. On the other hand, shifting of state-selective lattices should be fast enough so that the entire sequence will finish within the coherence time. Note that throughout this thesis we consider the internal qubit state as being unaffected by changes of vibrational states, hence vibrational contributions to the atomic wave function can be investigated separately.

To determine a parameter region, which complies the above requirements and incorporates the specifics of our experimental setup, we calculate the probability to excite an atom into higher vibrational states using first-order perturbation theory [141]. In this calculation, we assume the atoms being trapped in a harmonic potential, regarding them as harmonic oscillators with decoupled axial and radial dynamics. Since lattice potentials are shifted only along the lattice axis (i.e. in axial direction), it suffices to restrict attention just to the axial dynamics. Radial dynamics is regarded as unaffected by the lattice shift. By this, the entire problem is reduced to that of a one-dimensional (1D) harmonic oscillator.

The eigenenergies E_n and eigenfunctions $\psi_n(z)$ of the time-independent Schrödinger equation of a 1D harmonic oscillator, $\mathcal{H}\psi_n(z) = E_n\psi_n(z)$, are given by [139]

[4] Note that the self-developed software "WaveGen" which is used to control the arbitrary waveform generator (see Sec. A.3), provides a build-in feature to precompensate the generated driving ramp.

$$E_n = \hbar\omega_{\mathrm{ax}}\left(n+\frac{1}{2}\right)\,, \tag{4.19a}$$

$$\psi_n(z) = \frac{1}{\sqrt{2^n n!}}\left(\frac{1}{\pi a^2}\right)^{1/4}\exp\left(-\frac{z^2}{2a^2}\right)H_n\left(\frac{z}{a}\right)\,. \tag{4.19b}$$

They characterize the motional component of a trapped atom, being in the nth axial vibrational state ($n \in \mathbb{N}$), where $H_n(x)$ denotes the Hermite polynomials of nth order and $a = \sqrt{\hbar/m_{\mathrm{Cs}}\omega_{\mathrm{ax}}}$ the harmonic oscillator length. Let $s(t)$ be a shift function with $s(0) = 0$ and $s(\tau_{\mathrm{trans}}) = 1$, which parameterizes the axial shift of the trapping potential during a transport time τ_{trans}, providing a total shift distance of $\lambda/4$, and thus, a displacement of the state-selective potentials by one lattice site with respect to each other. Then, the time-dependent wave functions read

$$\psi_n(z,t) = \psi_n(z \pm \tfrac{\lambda}{4}s(t))\,, \tag{4.20}$$

where the sign specifies the direction of the shift. These functions remain solutions of the time-independent Schrödinger equation.

In first-order perturbation theory, the probability to directly[5] excite an atom from an initial vibrational state n to a final state n' by shifting the optical lattice is given by [139]

$$p_{n\to n'}(t) = |c_{nn'}(t)|^2 \tag{4.21}$$

with the amplitude coefficient

$$c_{nn'}(t) = -\int_0^t \widetilde{\mathcal{H}}_{nn'}(t')\exp\left(\frac{i}{\hbar}\int_0^{t'} E_{n'}(t'') - E_n(t'')\,\mathrm{d}t''\right)\,\mathrm{d}t' \tag{4.22}$$

and the interaction matrix element

$$\widetilde{\mathcal{H}}_{nn'}(t) = \int_{-\infty}^{\infty}\psi_{n'}(z,t)\frac{\mathrm{d}}{\mathrm{d}t}\psi_n(z,t)\,\mathrm{d}z\,. \tag{4.23}$$

The latter comprises the interaction Hamiltonian of the shift, $\widetilde{\mathcal{H}}(t) = \frac{\mathrm{d}}{\mathrm{d}t}$, whereas possible changes of axial trapping frequency during the shift are taken into account by replacing ω_{ax} in Eq. (4.19) by a time-dependent function. Note that the perturbatively derived excitation probability of Eq. (4.21) remain only valid, provided that $p_{n\to n'}(t) \ll 1$. Two properties of the derived excitation probability should be emphasized at this point: First, the probability to excite an atom from a vibrational state n to the nearest higher state $(n+1)$ scales as

$$p_{n\to n+1}(t) = (n+1)p_{0\to 1}(t)\,. \tag{4.24}$$

[5] Here, the contributions of excitations via several intermediate vibrational states are assumed to be negligible.

This relation provides an insight into relevant excitation properties of thermal atoms just by analyzing their properties in the vibrational ground state, see below. Second, the excitation probability is symmetric with respect to the excitation direction

$$p_{n\to n+1}(t) = p_{n+1\to n}(t)\,. \tag{4.25}$$

Therefore, excitations and deexcitations between neighboring vibrational states occur with equal probability, increasing the chance that atoms remain in the initial state after the lattice shift. Both properties are particularly useful to infer the effect of potential shift on thermal atoms by approximating the time evolution of the thermal distribution of vibrational states. Let $\varrho_n(t_0)$ be an initial distribution of vibrational states, specifying the probability to initially find an atom in a vibrational state n. Then, restricting only to transitions between neighboring vibrational states, the thermal distribution after a transport time t reads

$$\begin{aligned}\varrho_n(t_0+t) = \varrho_n(t_0) &+ p_{n+1\to n}(t)\varrho_{n+1}(t_0) + p_{n-1\to n}(t)\varrho_{n-1}(t_0)\\ &- p_{n\to n+1}(t)\varrho_n(t_0) - p_{n\to n-1}(t)\varrho_n(t_0)\,.\end{aligned} \tag{4.26}$$

Using Eqs. (4.24) and (4.25), this expression can be simplified to

$$\begin{aligned}\varrho_n(t_0+t) = \varrho_n(t_0)&\\ &+ p_{0\to 1}(t)\left[(n+1)\varrho_{n+1}(t_0) + n\varrho_{n-1}(t_0) - (2n+1)\varrho_n(t_0)\right]\,.\end{aligned} \tag{4.27}$$

Thus, the evolution of a thermal distribution can be approximately inferred from the excitation probability of an atom in the ground state.

4.4.1. State-dependent shift dynamics

We first discuss the properties of state-selective potentials resulting from a driving voltage function $\mathcal{V}(t)$ with $\mathcal{V}(0) = 0$ and $\mathcal{V}(\tau_{\lambda/2}) = \mathcal{V}_{\lambda/2}$ fed to the polarization control setup, see Sec. 4.3. For an ideal setup with infinite bandwidth and no signal retardation, the driving voltage directly translates into a tilt angle between the polarizations of the two counterpropagating beams, yielding $\theta(t) = \pi\mathcal{V}(t)/\mathcal{V}_{\lambda/2}$ and $\tau_{\mathrm{trans}} = \tau_{\lambda/2}$. The shift functions which parameterize shifts of the state-selective potentials $U_{\mathrm{dip},|j\rangle}(\boldsymbol{r}, \theta(t))$ ($j = \{0, 1\}$), see Eq. (4.13), then read

$$s_{|j\rangle}(t) = \frac{2}{\pi}\vartheta_{|j\rangle}(\theta(t))\,. \tag{4.28}$$

The axial trapping frequencies depend on the potential contrast which may change during the potential shift. They are thus given by

$$\omega_{\mathrm{ax},|j\rangle}(t) = 2\pi\sqrt{\frac{2|W_{|j\rangle}(\theta(t))|}{m_{\mathrm{Cs}}\lambda^2}}\,. \tag{4.29}$$

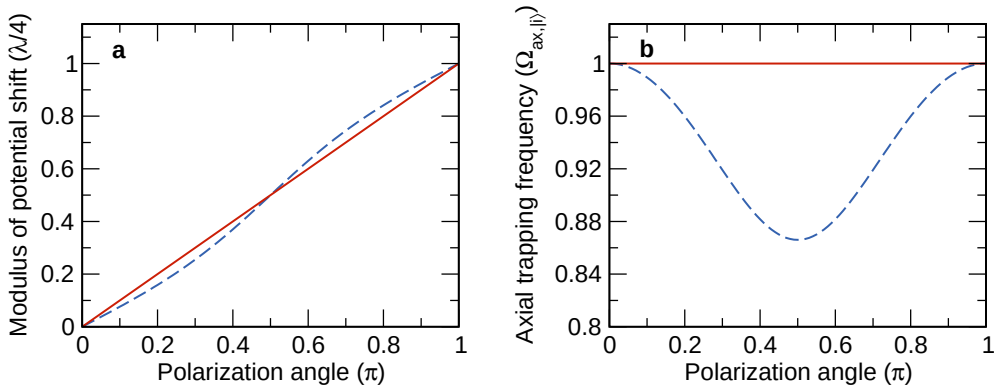

Figure 4.5.: (**a**) Parametric plot of the modulus of potential shift and (**b**) axial trapping frequency for atoms in qubit basis states $|0\rangle$ (solid lines) and $|1\rangle$ (dashed lines), as inferred from Eqs. (4.30) and (4.31).

For the characteristic wavelength $\lambda = \lambda_{|0\rangle}$, we finally obtain

$$s_{|0\rangle}(t) = \frac{1}{\pi}\theta(t)\,, \tag{4.30a}$$

$$s_{|1\rangle}(t) = \begin{cases} 0\,, & \text{if} \quad t = 0\,, \\ \frac{1}{2} + \frac{1}{\pi}\arctan\left[\frac{4}{3}\tan\left(\theta(t) - \frac{\pi}{2}\right)\right]\,, & \text{if} \quad 0 < t < \tau_{\lambda/2}\,, \\ 1\,, & \text{if} \quad t = \tau_{\lambda/2}\,, \end{cases} \tag{4.30b}$$

and

$$\omega_{\mathrm{ax},|0\rangle}(t) = \Omega_{\mathrm{ax},|0\rangle} = \mathrm{const}\,, \tag{4.31a}$$

$$\omega_{\mathrm{ax},|1\rangle}(t) = \Omega_{\mathrm{ax},|1\rangle}\left[1 - \tfrac{7}{16}\sin^2\theta(t)\right]^{1/4}\,, \tag{4.31b}$$

where $\Omega_{\mathrm{ax},|j\rangle} = 2\pi\sqrt{2|U_{0,|j\rangle}|/m_{\mathrm{Cs}}\lambda^2}$ denote the trapping frequencies of the unshifted potentials, i.e. for $\theta(t) = 0$.

In Figure 4.5, parametric plots of potential shifts and axial trapping frequencies are shown for both qubit basis states $|0\rangle$ and $|1\rangle$, as inferred from Eqs. (4.30) and (4.31). For atoms in state $|0\rangle$, the trapping frequency is constant during the state-selective transport and the potential shift is directly proportional to the tilt angle $\theta(t)$. The situation is different for atoms in state $|1\rangle$ which experience a light shift from both circular polarization components. There, the axial trapping frequency temporarily decreases to a minimum value of $\Omega_{\mathrm{ax},|1\rangle}\sqrt{3}/2$ at $\theta(t) = \pi/2$ while increasing the tilt angle from 0 to π, see Fig. 4.5(b). The nonlinear dependency of the potential shift on the tilt angle, on the other hand, yields the modulus of the potential shift to run behind the linear shift for $0 \leq \theta(t) < \pi/2$, be equal at $\theta(t) = \pi/2$ and run ahead for $\pi/2 < \theta(t) \leq \pi$, see Fig. 4.5(a). Since both parameters, $s_{|j\rangle}(t)$ and $\omega_{\mathrm{ax},|j\rangle}(t)$ enter Eq. (4.21), their state-dependent properties result in a state-dependent excitation probability of shifted atoms.

4.4.2. Excitations for linear and cosinusoidal driving ramps

To estimate the effect of state-dependent shift dynamics on the excitation probability of shifted atoms, for the sake of simplicity, we assume the atoms being initially in the vibrational ground state ($n = 0$). The interaction element in Eq. (4.23), describing the excitation to the nearest vibrational state ($n' = 1$) is then given by

$$\widetilde{\mathcal{H}}_{01,|j\rangle}(t) = \frac{\lambda}{4\sqrt{2}} \sqrt{\frac{m_{\mathrm{Cs}} \omega_{\mathrm{ax},|j\rangle}(t)}{\hbar}} \dot{s}_{|j\rangle}(t)\,, \tag{4.32}$$

whereas for the next-nearest vibrational state ($n' = 2$), we obtain

$$\widetilde{\mathcal{H}}_{02,|j\rangle}(t) = -\frac{1}{2\sqrt{2}} \frac{\dot{\omega}_{\mathrm{ax},|j\rangle}(t)}{\omega_{\mathrm{ax},|j\rangle}(t)}\,. \tag{4.33}$$

Therefore, direct excitations to the next-nearest vibrational state only occur if the trapping frequency changes during the lattice shift.

All mathematical expressions derived so far are valid for a general driving voltage function $\mathcal{V}(t)$ constrained by $\mathcal{V}(0) = 0$ and $\mathcal{V}(\tau_{\lambda/2}) = \mathcal{V}_{\lambda/2}$. From here on, we focus our analysis on two special cases: a linear and a cosinusoidal driving ramp, parameterized by

$$\mathcal{V}_{\mathrm{lin}}(t) = \mathcal{V}_{\lambda/2} \cdot \frac{t}{\tau_{\lambda/2}} \tag{4.34}$$

and

$$\mathcal{V}_{\cos}(t) = \frac{\mathcal{V}_{\lambda/2}}{2} \left[1 - \cos\left(\pi \cdot \frac{t}{\tau_{\lambda/2}}\right)\right]\,, \tag{4.35}$$

respectively. These functions can be regarded as borderline cases of a family of driving functions with point symmetry at $\mathcal{V}(\tau_{\lambda/2}/2) = \mathcal{V}_{\lambda/2}/2$. The linear ramp provides a discontinuous velocity at the beginning and the end of the shift, yielding there a sudden acceleration of the trapped atoms. The cosinusoidal ramp, in turn, permits a continuous evolution of velocity over the entire shift. For both functions, analytic expressions for the excitation probability as a function of ramp time can be deduced, at least for qubit state $|0\rangle$. Therefore, they are ideally suited to analyze the characteristic properties of motional excitation during potential shifts, including its dependency on experimental parameters.

For atoms in qubit basis state $|0\rangle$, the respective probabilities to excite an atom from the axial ground state to the nearest vibrational state are given by

$$p^{\mathrm{lin}}_{0\to1,|0\rangle}(\tau_{\lambda/2}) = \frac{m_{\mathrm{Cs}}\lambda^2}{8\hbar\Omega_{\mathrm{ax},|0\rangle}} \cdot \frac{\sin^2(\Omega_{\mathrm{ax},|0\rangle}\tau_{\lambda/2}/2)}{\tau^2_{\lambda/2}}\,, \tag{4.36a}$$

$$p^{\cos}_{0\to1,|0\rangle}(\tau_{\lambda/2}) = \frac{m_{\mathrm{Cs}}\pi^4\lambda^2\Omega_{\mathrm{ax},|0\rangle}}{32\hbar} \cdot \frac{\cos^2(\Omega_{\mathrm{ax},|0\rangle}\tau_{\lambda/2}/2)}{(\pi^2 - \tau^2_{\lambda/2}\Omega^2_{\mathrm{ax},|0\rangle})^2}\,. \tag{4.36b}$$

Their dependency on the ramp time $\tau_{\lambda/2}$ is shown in Fig. 4.6 for a characteristic wavelength $\lambda = \lambda_{|0\rangle}$ and a typical axial trapping frequency of $\Omega_{\mathrm{ax},|0\rangle} = 2\pi \times 115\,\mathrm{kHz}$.

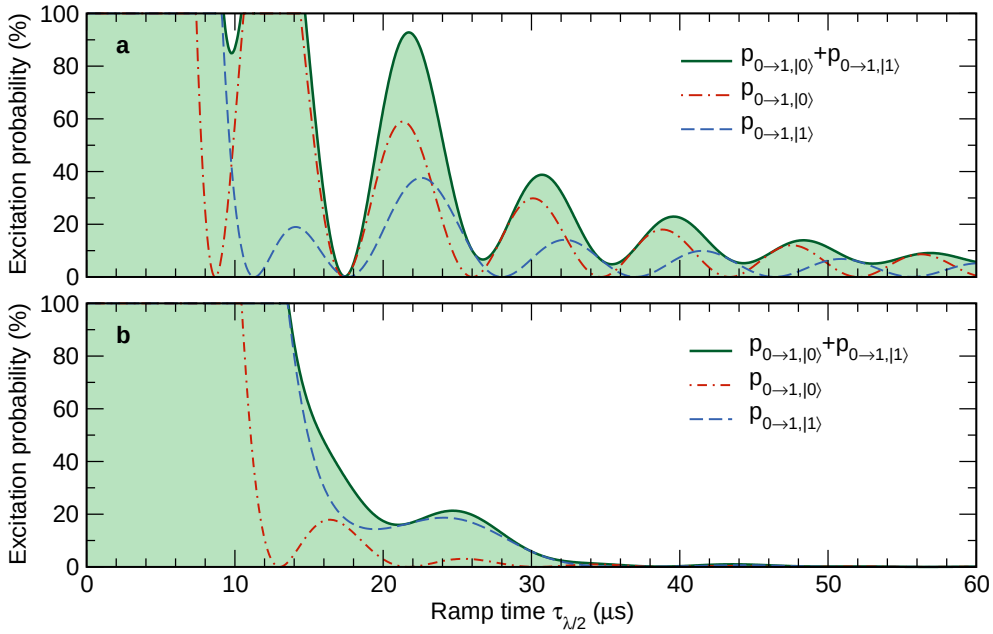

Figure 4.6.: Probability to excite an atom from the axial ground state to the nearest vibrational state for both qubit basis states $|0\rangle$ and $|1\rangle$ as a function of ramp time: (**a**) for a linear ramp (Eq. (4.34)) and (**b**) for a cosinusoidal driving ramp (Eq. (4.35)). For state $|0\rangle$, analytic expressions can be derived (see Eq. (4.36)), whereas for state $|1\rangle$ the excitation probabilities are calculated numerically. Baseline filled graphs show the sum of both excitation contributions $p_{0\to1,|0\rangle}(\tau_{\lambda/2}) + p_{0\to1,|1\rangle}(\tau_{\lambda/2})$, describing the excitation probability of an atom being once transported in both state-selective potentials.

Both excitation probabilities reveal a sinusoidal modulation with a quadratic (linear ramp) and biquadratic decay (cosinusoidal ramp) with increasing $\tau_{\lambda/2}$, providing zero-crossings at

$$\tau_{\lambda/2}^{\mathrm{lin}} = 2\pi l/\Omega_{\mathrm{ax},|0\rangle} \tag{4.37}$$

and

$$\tau_{\lambda/2}^{\cos} = (2\pi l + \pi)/\Omega_{\mathrm{ax},|0\rangle} \tag{4.38}$$

with $l \in \mathbb{N}_{>0}$,[6] respectively. Considering these zero-crossings and the decay of the envelopes in Eqs. (4.36), we conclude that increasing axial trapping frequencies allows for reducing the ramp times. This strategy, however, turns out to be inapplicable, since the currently only way to increase the axial trapping frequencies requires the lattice depth to be increased. The latter in turn, enhances the differential light shift which, in our case, has been identified as the dominant source of decoherence, see Sec. 3.3. Consequently, increasing trapping frequencies just by changing the lattice depth would finally result in a decrease of coherence times.

[6] Note that $p^{\cos}_{0\to1,|0\rangle}(\tau_{\lambda/2}) = m_{\mathrm{Cs}}\pi^2\lambda^2\Omega_{\mathrm{ax},|0\rangle}/512\hbar \neq 0$ for $\tau_{\lambda/2} \to \pi/\Omega_{\mathrm{ax},|0\rangle}$.

On the basis of both borderline cases a relevant property applying also for the intermediate functions becomes apparent: By increasing the "smoothness" of lattice acceleration at the beginning ($t = 0$) and the end of the shift ($t = \tau_{\lambda/2}$) and thus reducing the discontinuity of velocity at these points, the zero-crossings of the excitation probabilities shift to higher ramp times. At the same time, the decay of the envelope of the probability function becomes stronger, the more the driving ramps approach a differentiable function. Both properties have been systematically investigated in Ref. [122,142], using hyperbolic tangent ramps with tunable velocity discontinuities.

The biquadratic decay of cosinusoidal and related ramps makes them robust to fluctuations of experimental parameters affecting the axial trapping frequency, e.g. intensity fluctuation and beam pointing instabilities of laser beams generating the optical lattice. For sufficiently large ramp times, the excitation probability becomes marginal, irrespective of whether the ramp time meets the zero-crossing condition or not, see Fig. 4.6(b). The situation is different for the linear ramp, where deviations from the zero-crossing condition results in a significant increase of excitation probability within a large interval of ramp times, see Fig. 4.6(a). Nevertheless, regarding only the zero-crossing condition, a linear ramp may allow for shorter transport times.

So far, the excitation properties of atoms in state $|0\rangle$ have been discussed. The situation becomes more complicated for atoms in state $|1\rangle$ for which the lattice shift nonlinearly depends on the tilt angle $\theta(t)$ and the trapping frequency changes during the shift. In that case, excitation probabilities have to be calculated numerically. In Figure 4.6, results of these calculations are shown. For the linear driving ramp, we again observe a modulation of the excitation probability with a decaying envelope for increasing ramp time. Due to a temporarily decrease of the trapping frequency during the potential shift (see Eq. (4.31)), the initial zero-crossings are smeared out to almost periodic minima, some of which are more or less shifted to higher ramp times. The stronger decay of the envelope arises from reduced discontinuity of velocity ($\propto \dot{s}(t)$) at the beginning and the end of the potential shift. The same applies for the cosinusoidal ramp, whereby in this case, the smearing-out of zero-crossings and the shift of the minima is even more pronounced, while no significant improvement of the decay is observed. From this, we conclude that regarding shorter transport times, the linear ramp with ramp times at the first minima in the excitation probability seems more appropriate than a cosinusoidal ramp. For the excitation probabilities to the next-nearest vibrational state, in the relevant ramp time interval, we obtain

$$p^{\mathrm{lin}}_{0\to 2,|1\rangle}(\tau_{\lambda/2}) < 0.7\%\,, \tag{4.39}$$

$$p^{\cos}_{0\to 2,|1\rangle}(\tau_{\lambda/2}) < 0.6\%\,. \tag{4.40}$$

Therefore, these excitations are negligible.

Transporting atoms in both qubit basis states $|0\rangle$ and $|1\rangle$ requires a driving ramp and a ramp time for which both excitation probabilities $p_{0\to 1,|0\rangle}(\tau_{\lambda/2})$ and

$p_{0\to1,|1\rangle}(\tau_{\lambda/2})$ are negligible. The same applies for atoms which have to be shifted over long distances by stepwise flipping their internal qubit-state. These atoms are equally often shifted in both state-selective potentials, see Sec. 4.5. Therefore, a reasonable figure of merit should be defined as the sum of probabilities $p_{0\to1,|0\rangle}(\tau_{\lambda/2}) + p_{0\to1,|1\rangle}(\tau_{\lambda/2})$, rather than the individual components, see Fig. 4.6.[7] For the linear ramp, we observe then a single pronounced minimum with negligible excitation at a ramp time of $\tau^{\mathrm{lin}}_{\lambda/2} \approx 18\,\mu$s within the relevant time interval, whereas for the cosinusoidal ramp, comparable low excitation probabilities only appear above $\tau^{\cos}_{\lambda/2} \geq 34\,\mu$s. For the intermediate driving functions, we expect this optimum ramp time to be in between of these borderline cases. Being interested in shortest transport times, we therefore prefer the linear driving ramp for the state-selective transport.

4.4.3. Effect of limited bandwidth

For an ideal setup with infinite bandwidth and no signal retardation, the linear driving ramp with a ramp time of $\tau^{\mathrm{lin}}_{\lambda/2} \approx 18\,\mu$s has been shown to provide the shortest transport time with negligible excitation for both state-selective potentials. The EOM and its amplifier, however, have a finite bandwidth. This finite bandwidth smoothes the edges of the linear voltage ramp resulting in both, a smearing-out of minima in the calculated excitation probability and their shift towards larger ramp times, see above. Furthermore, due to retardation in the response of the driving signal, the transport time is larger than the preset ramp time ($\tau_{\lambda/2} < \tau_{\mathrm{trans}}$). Therefore, to check whether the linear ramp with a ramp time of $\tau^{\mathrm{lin}}_{\lambda/2} \approx 18\,\mu$s still provides a reasonable choice, technical limitations have to be taken into account in the calculation. For this, we assume the response of polarization rotation on a driving input voltage $\mathcal{V}(t)$ to be linear and time-invariant. In that case, the response is completely characterized by the transfer function $O(t)$ of the polarization control system. The tilt angle can be thus deduced from the following convolution relation

$$\tilde{\theta}(t) = \frac{\pi}{\mathcal{V}_{\lambda/2}}(O * \mathcal{V})(t) = \frac{\pi}{\mathcal{V}_{\lambda/2}} \int_{-\infty}^{+\infty} O(t-t')\mathcal{V}(t')\,\mathrm{d}t' \,. \tag{4.41}$$

Since we have measured the transfer function in frequency domain, employing the convolution theorem, we obtain

$$\tilde{\theta}(t) = \frac{\pi}{\mathcal{V}_{\lambda/2}} \mathrm{FT}^{-1}\left\{\mathrm{FT}\{\mathcal{V}(t)\} \cdot A(\nu)e^{i\phi(\nu)}\right\} , \tag{4.42}$$

[7] Note that time delay between two lattice shifts may significantly contribute to the excitation probability. This effect is not included just by the sum of probabilities. Instead, it requires an analysis of the entire transport sequence, see Sec. 5.1. Nevertheless, the characteristic properties, including the position of excitation minima are sufficiently captured by the sum of the respective probability contributions.

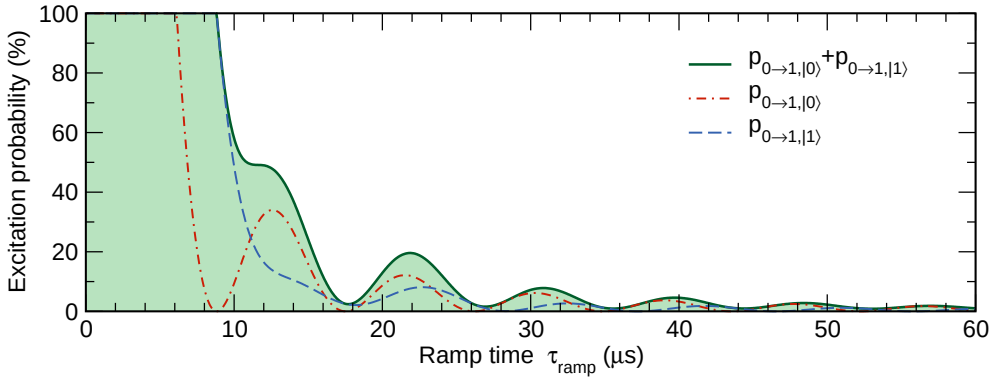

Figure 4.7.: Excitation probability of atoms in qubit states $|0\rangle$ and $|1\rangle$ from axial ground state to the nearest vibrational state for a linear driving ramp, driven by a polarization control system with limited bandwidth, see Sec. 4.3. Baseline filled graphs show the sum of both probability contributions, $p_{0\to1,|0\rangle}(\tau_{\lambda/2}) + p_{0\to1,|1\rangle}(\tau_{\lambda/2})$, describing the excitation probability of an atom being once transported in both state-selective potentials.

where $A(\nu)$ and $\phi(\nu)$ denote the spectral amplitude and phase of the transfer function, see Sec. 4.3. By this, we finally obtain the response of the rotation angle on the driving signal comprising the most dominant technical limitations.

We numerically calculate the excitation probability for a linear driving ramp using $\tilde{\theta}(t)$ instead of $\theta(t)$, whereby the integration limits in the amplitude coefficient of Eq. (4.22) are extended to the effective transport time $\tau_{\mathrm{trans}} > \tau_{\lambda/2}$. The latter comprises the retardation of the driving signal and possible fading of oscillations of the signal response. Results of this calculation are shown in Fig. 4.7. The excitation probability contributions $p_{0\to1,|j\rangle}(\tau_{\lambda/2})$ reveal the expected behavior resulting from smoothing of the edges of the linear ramp: A smearing-out of zero-crossings forming excitation minima, shifts of these minima to higher ramp times and a stronger decay of the envelope of excitation probability. Nevertheless, a pronounced minimum in the sum of both contributions at $\tau_{\lambda/2} \approx 18\,\mu$s is still maintained, yielding an excitation probability below 2.5%. We will utilize this minimum for coherent state-selective transport, whereas the optimum ramp time will be experimentally determined prior to each measurement using Ramsey type sequences, see Sec. 5.1.

Remarks on thermal atoms

Even though the excitation properties have been investigated on atoms in the axial vibrational ground state, according to Eq. (4.24), the characteristic properties including positions of excitation minima and decay of the envelope of excitation probability also apply for atoms in higher vibrational states. The former holds true for thermal atoms characterized by a thermal distribution, the change during the transport of which scales with the excitation probability of atoms in vibrational ground state, see Eq. (4.27). It should be noted that for the typical temperature

of atoms in the optical lattice, the atoms populate the axial vibrational states with a mean quantum number of $\bar{n} = 1.2$. Therefore, the harmonic approximation employed in the derivation of the excitation probabilities is well justified, whereas effects due to the anharmonicity of potentials are expected to be negligible.

4.5. Transporting atoms over several lattice sites

The state-selective transport of atoms over distances of several lattice sites forms the most basic and relevant module of key applications presented in this thesis. Unfortunately, its properties are very sensitive to experimental parameters. Therefore, particular care and effort regarding alignment, amount of preparatory measurements and consistency checks are required. For this, several procedures have been developed which guarantee a high degree of reliability and reproducibility. At first, for simplicity, we abstract the state-selective transport and its relevant properties in a Dirac representation.

4.5.1. Dirac representation of state-selective transport

Consider a single atom initialized either in qubit basis state $|0\rangle$ or $|1\rangle$ being trapped in a state-selective potential. At a tilt angle of $\theta = 0$, sites of both state-selective lattices generated by orthogonally circularly polarized components of the light field, spatially overlap, see Sec. 4.2. Such overlap configuration is required for fluorescence imaging (see Sec. 2.3) to determine the number or positions of the atoms. It is also essential for coherent manipulation of the atoms' internal states, minimizing frequency broadening of the $|0\rangle \leftrightarrow |1\rangle$ transition and degradation of the manipulation efficiency arising from vectorial and tensorial contributions to the differential light shift. Note that for a perfect overlap, the σ^+ and σ^- components of the light field add up to a purely linearly polarized optical lattice, in which both contributions to the differential light shift vanish. When increasing the tilt angle up to $\theta = \pi$, both state-selective lattices are shifted into opposite directions by a distance of $\lambda/4$ along the common lattice axis, resulting in a relative displacement of one lattice site ($\lambda/2$). Consequently, the sites of both lattices overlap again, however, spatially offset by a distance $\lambda/4$ from the original position, see Fig. 4.8(c). This process of re-overlapping periodically continues for $\theta = l\pi$ ($l \in \mathbb{N}$), whereby only for odd l an effective offset by $\lambda/4$ occurs.

Technically, the tilt angle between the polarization of the incident and retro-reflected beam cannot be infinitely increased. Our polarization control setup, allows for lattice shifts between only two neighboring overlap configurations, the $\theta = 0$ ($\mathcal{V} = 0$) and $\theta = \pi$ ($\mathcal{V} = \mathcal{V}_{\lambda/2}$) configuration (see Sec. 4.3), initially restricting the transport distance to $\lambda/4$. Furthermore, due to technical problems, only the $\mathcal{V} = 0$ configuration permits a long-term stability required for fluorescence imaging. In general, fast ramping of the driving voltage from $\mathcal{V} = 0$ to $\mathcal{V} = \mathcal{V}_{\lambda/2}$ results in systematical polarization drift. This drift already appears after $\approx 100\,\mathrm{ms}$, while holding the half-wave voltage of the EOM over several seconds. It disappears when

the voltage is driven back to the initial value, here $\mathcal{V} = 0$.[8] This technical problem has extensive consequences for our experimental sequences: First, holding the $\theta = \pi$ configuration over time intervals above 100 ms has to be avoided. Second, fluorescence imaging with exposure times exceeding the drift-free holding time has to be performed in the $\theta = 0$ configuration, which from now on is referred to as *stable* configuration. Since all sequences employing the state-selective transport comprise acquisitions of initial and final images, the transport part has to start and finish in a stable configuration. Otherwise, due to drifts of the state-selective potentials atom loss would increasingly occur during irradiation of atoms by optical molasses. Finally, considering the fact that only overlap configurations are useful for subsequent operations, we define a single *transport step* as a discrete operation shifting the atom by a distance of $\lambda/4$, i.e. from one overlap configuration to another.

Characterizing the resulting discreetness of atom positions by an integer number k ($k\lambda/4$) and neglecting transitions between different motional states during the transport,[9] shifts between both possible overlap configurations can be defined by the operators

$$\hat{S}_{\uparrow} : \begin{cases} |0,k\rangle & \rightarrow & e^{i\varphi_{|0\rangle,\mathbf{n}}}|0,k+1\rangle \\ |1,k\rangle & \rightarrow & e^{i\varphi_{|1\rangle,\mathbf{n}}}|1,k-1\rangle \end{cases} \tag{4.43}$$

and

$$\hat{S}_{\downarrow} : \begin{cases} |0,k\rangle & \rightarrow & e^{i\varphi_{|0\rangle,\mathbf{n}}}|0,k-1\rangle \\ |1,n\rangle & \rightarrow & e^{i\varphi_{|1\rangle,\mathbf{n}}}|1,k+1\rangle \end{cases} , \tag{4.44}$$

where the qubit Hilbert space $\mathcal{H}_{\mathrm{qbit}}$ has been extended by the Hilbert space of positions $\mathcal{H}_{\mathrm{pos}} = l_2(\mathbb{Z})$, i.e. $\mathcal{H}_{\mathrm{ext}} \equiv \mathcal{H}_{\mathrm{qbit}} \otimes \mathcal{H}_{\mathrm{pos}}$, and a short-hand notation of the product states $|j,k\rangle \equiv |j\rangle \otimes |k\rangle \in \mathcal{H}_{\mathrm{ext}}$ ($j = \{0,1\}$) has been introduced. Arrows in the subscript of $\hat{S}$ indicate the trend of the driving ramp, e.g. "$\uparrow$" for $0 \rightarrow \mathcal{V}_{\lambda/2}$ and "$\downarrow$" for $\mathcal{V}_{\lambda/2} \rightarrow 0$, respectively, and $\varphi_{|j\rangle,\mathbf{n}}$ the state-dependent accumulated qubit phase during the transport time τ_{trans}. The multiple index vector $\mathbf{n} \equiv (n,m,m')$ comprises the quantum numbers which specify the axial (n) and both radial components (m and m') of the vibrational states. Since both qubit basis states are shifted in different potentials, each of them undergoes a different shift dynamics, see Sec. 4.2. Therefore, in general, it is $\varphi_{|0\rangle,\mathbf{n}} \neq \varphi_{|1\rangle,\mathbf{n}}$. Furthermore, a uniform environment has been assumed, i.e. the accumulated phase does not depend on the position of the atom in the lattice. Note that accumulation of phase is only relevant for atoms prepared in superpositions of the basis states. Otherwise, it only contributes to the global phase of the qubit, being indistinguishable by projection

[8] This technical problem occurs for all tested EOMs and could not be solved so far, neither by ourselves nor by the manufacturer of the EOMs.

[9] To incorporate possible excitations between axial vibrational states in this description the Hilbert space has to be extended by additional subspace of possible vibrational states and a set of excitation operators introduced. However, since the magnitude of the excitations is expected to be negligible, we avoid its explicit consideration throughout this thesis. Instead, possible effects of these excitations are effectively treated as decoherence.

measurements. In this representation, a single transport step is defined by the application of the operator $\hat{S}_\uparrow$ or $\hat{S}_\downarrow$.

Using the Dirac representation, it becomes evident how to overcome the initial restrictions regarding the limited transport distance: By alternating application of the shift operators $\hat{S}_\uparrow$ and $\hat{S}_\downarrow$ with π-pulses in between

$$\hat{T}_{2K} \equiv \left(\hat{U}_\pi \hat{S}_\downarrow \hat{U}_\pi \hat{S}_\uparrow\right)^K, \tag{4.45}$$

atoms initialized in one of the qubit basis states can be state-selectively transported over a distance of $K \in \mathbb{N}$ lattice sites ($K\lambda/2$)

$$\hat{T}_{2K} : \begin{cases} |0,k\rangle & \rightarrow & (-1)^K e^{iK(\varphi_{|0\rangle,\mathbf{n}}+\varphi_{|1\rangle,\mathbf{n}})}|0,k+2K\rangle \\ |1,k\rangle & \rightarrow & (-1)^K e^{iK(\varphi_{|0\rangle,\mathbf{n}}+\varphi_{|1\rangle,\mathbf{n}})}|0,k-2K\rangle \end{cases}, \tag{4.46}$$

whereby the roles of $|0\rangle$ and $|1\rangle$ are exchanged after each transport step. We stress that, per definition, the transport operator $\hat{T}_{2K}$ intentionally comprises an even number of transport steps so that a transport sequence ends up in a stable overlap configuration.

In Figure 4.8, a typical sequence of a state-selective transport over several lattice sites is schematically shown. Regarding experimental parameters, it is similar to that of recording a microwave spectrum, see Sec. 3.2.3, whereas steps (C) and (D) are modified or replaced by the multiple shift and resonant π-pulse operations, see Fig, 4.8(a). Furthermore, we only load on average eight atoms into the optical lattice, which are widely spread so that their position can be reliably inferred. For the latter, typical exposure times of 0.5-1 s are employed. The optimum ramp time $\tau_{\lambda/2}$ for a preset ramp function (linear or cosinusoidal) is inferred from a Ramsey type measurement aiming to minimize excitations between motional states and thus maintaining maximum coherence, see Sec. 5.1. π-pulses typically start immediately after the shift operations and vice versa, see Fig. 4.8(b), which are specified by the transport time $\tau_{\text{trans}} = \tau_{\lambda/2} + \delta t$. The latter comprises an experimentally inferred settling time δt which ensures settling of the tilt angle for both overlap configurations $\theta = 0$ and $\theta = \pi$, taking the limited bandwidth and temporal retardations of the polarization control setup into account.

4.5.2. Adjusting settling time and half-wave voltage

The geometrical alignment of the EOM, the settling time δt and the half-wave voltage $\mathcal{V}_{\lambda/2}$ are fine-aligned by iteratively probing the purity of linear polarization in the trapping region of atoms using microwave spectroscopy, see Sec. 3.2.3. For this, we initially align the EOM at $\theta = 0$ ($\mathcal{V} = 0$) to the minimum extinction ratio. In the subsequent, iterative fine-alignment procedure, we minimize the broadening of the microwave spectrum, which arises from the vectorial and tensorial contributions to the total differential light shift. A decrease of the width of the $|0\rangle \leftrightarrow |1\rangle$ transition peak in the spectrum down to its Fourier limit indicates a reduction of

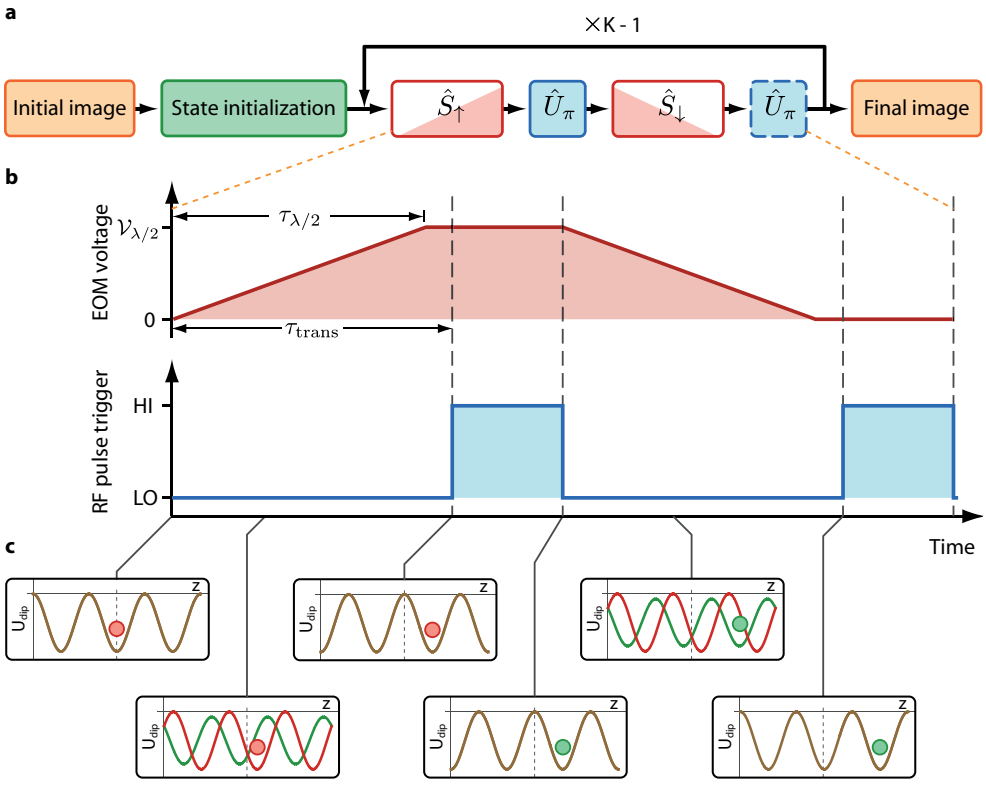

Figure 4.8.: (**a**) Schematic sequence of a state-selective transport of atoms over K lattice sites. Alternating application of the shift operators $\hat{S}_\uparrow$ and $\hat{S}_\downarrow$ with π-pulses $\hat{U}_\pi$ in between, overcomes the restrictions of transport distances initially imposed by the polarization control setup. The subsequently applied operations within the loop define the transport operator $\hat{T}_{2K}$, see Eq. (4.46). In some applications, the last π-pulse (dashed box) is omitted in the sequence. (**b**) Time sequence of experimental parameters implementing the transport operator $\hat{T}_{2K}$, here for a linear driving ramp; (**c**) the resulting evolution of state-selective dipole potentials $U_{\text{dip},|0\rangle}$ (red) and $U_{\text{dip},|1\rangle}$ (green). A π-pulse exchanges the roles of $|0\rangle$ and $|1\rangle$, i.e an atom in state $|0\rangle$ initially trapped in $U_{\text{dip},|0\rangle}$, continues the transport in $U_{\text{dip},|1\rangle}$. At $\theta = \{0, \pi\}$ both potentials overlap.

polarization impurity and thus a perfect overlap of both orthogonally circularly polarized components of the light field in the trapping region. This fine-alignment procedure, however, has a substantial disadvantage: Recording microwave spectra for each alignment iteration makes this method extremely time-consuming.

To infer the half-wave voltage $\mathcal{V}_{\lambda/2}$ and the settling time δt to a preset driving ramp and its ramp time $\tau_{\lambda/2}$, a similar procedure with a modified sequence is employed. In this sequence, state initialization by optical pumping is followed by ramping the driving voltage to a level, which is expected to yield a $\theta = \pi$ configuration. After a preset time delay $\tilde{t}$, we apply a rectangular π-pulse the frequency of which is scanned. We ramp the driving voltage back to $\mathcal{V} = 0$ and apply the

state-selective push-out. By this, we effectively record a microwave spectrum in the $\theta = \pi$ configuration. Both, the time delay and the voltage level are successively scanned until the recorded microwave spectrum approaches again its Fourier limit. The settling time and the half-wave voltage are then given $\delta t = \min \tilde{t}|_{\theta=\pi}$ and $\mathcal{V}_{\lambda/2} = \mathcal{V}|_{\theta=\pi}$, respectively. Fine-tuning of the preset ramp time will be discussed in Sec. 5.1.

4.5.3. Analyzing transport data

From initial $x_{\mathrm{bef},j}$ and final positions $x_{\mathrm{aft},j}$ of atoms, which are determined from fluorescence images before and after the state-selective transport, the distances covered by the atoms $\Delta x_j = x_{\mathrm{aft},j} - x_{\mathrm{bef},j}$ can be directly inferred. Unless stated otherwise, we label the initial position of each atom as zero and refer the final position of the atom relative to its initial position. In this convention, the position of an atom after the transport is equivalent to the transport distance.

To reduce the statistical error in the subsequent analysis, instead of working with a single atom and high numbers of sequence repetitions, we prefer to initially load on average eight atoms in the optical lattice. Unless predefined atom patterns are generated (see Sec. 3.4.4), the atoms are usually randomly distributed over the lattice sites. In that case, some atoms have to be discarded from the analysis of transport distances. Due to experimental imperfections, e.g. possible errors of π-pulses, the transport direction of each individual atoms can change from one step to another. In the worst case, such change may occur after each transport step. Under certain conditions, regarding the initial separations of atoms and the number of transport steps, paths of atoms cannot be uniquely inferred from the initial and final image. This may happen if possible paths of nearby atoms can cross during the transport. A further uniqueness issue arises, if drifts of the optical lattice in the time period between the acquisition of initial and final images are not significantly smaller than the lattice periodicity. In that case, it is unclear whether atoms changed their positions due to state-selective transport or the drift of the optical lattice.

Two statements of general validity help us to overcome the uniqueness issues:

1. Implementation of the state-selective transport presented in this thesis prohibits the atoms from being transported over distances which exceed a maximum value defined by the number of transport steps $2K$

$$|\Delta x_j| \leq K\lambda/2\,. \tag{4.47}$$

2. Starting and ending in the same overlap configuration ($\theta = 0$), the covered distances of atoms after the state-selective transport should perfectly reproduce the periodicity of the optical lattice. Otherwise, significant drifts of the lattice during the period between the acquisition of both images occurred.

Following the first statement, it is evident that after a transport sequence comprising $2K$ transport steps, transport distances of only those atoms can be uniquely

inferred, which are initially separated by at least $2K+1$ lattice sites from neighboring atoms, i.e.

$$|x_{\mathrm{bef},j} - x_{\mathrm{bef},j'}| \geq (2K+1)\lambda/2\,, \quad \text{with} \quad j \neq j'\,. \tag{4.48}$$

Atoms which do not fulfill this condition are therefore discarded from the analysis of the transport data. We also discard those atoms which leave the optical lattice during the transport. The latter can be identified just by being missing in the final image within the expected transport region $|x_{\mathrm{bef},j}| \leq K\lambda/2$. Following the second statement, which we refer to as reliability criterion, we discard the entire data set whenever a histogram of transport distances does not perfectly reproduce the periodicity of the optical lattice. Employing both conditions, we finally are able to reliably and uniquely infer the transport distances from pairs of fluorescence images.

The transport analysis module is part of the self-developed post-analysis software "Post Deconvolution" (see App. A.4) which enables to automatically analyze huge data sets comprising several thousands images.

4.6. Transport efficiency

To investigate the efficiency of our state-selective transport over distances of several lattice sites, we load on average eight atoms into the optical lattice, determine their initial positions by fluorescence imaging (exposure time of 1 s) and prepare them in the qubit basis state $|0\rangle$ using optical pumping. Since the roles of states $|0\rangle$ and $|1\rangle$ are successively changed during such a transport sequence, it suffices to investigate the transport properties on atoms in only one of these basis states. For this, we subsequently apply the transport sequence defined by $\hat{\mathcal{T}}_{2K}$ for $K = \{1, 2, \ldots, 11\}$. Each transport sequence comprises an even number of transport steps ($2K$). For each transport step, we initially use a cosinusoidal driving ramp (see Eq. (4.35)) with a ramp time of $\tau_{\lambda/2} = 30\,\mu$s and a transport time of $\tau_{\mathrm{trans}} = 32\,\mu$s, the properties of which are robust to drifts of experimental parameters and geometrical misalignment. For π-pulses, rectangular pulses with a pulse duration of $8\,\mu$s are employed. Alternatively, we use broadband composite pulses ($90_0 225_{180} 315_0$-pulses, see Sec. 3.5) with a pulse duration of $24\,\mu$s to exclude possible effects of pulse frequency detuning from the investigation of transport efficiency, see below. After transporting the atoms, we infer their final positions relative to the initial ones using fluorescence imaging. These relative positions correspond to the transport distances.

In Figure 4.9, probability histograms of relative positions for different number of transport steps K and widths of bins are shown. Each histogram has been normalized to the total number of analyzed atoms (500-1000) yielding a discrete probability distribution. Finely sampled histograms with a bin width of $\lambda/20$ reveal Gaussian peaks centered at integer multiple of $\lambda/2$, similar to that of Fig. 2.15 in Sec. 2.4.1. These peaks clearly reproduce the periodicity of the optical lattice. The

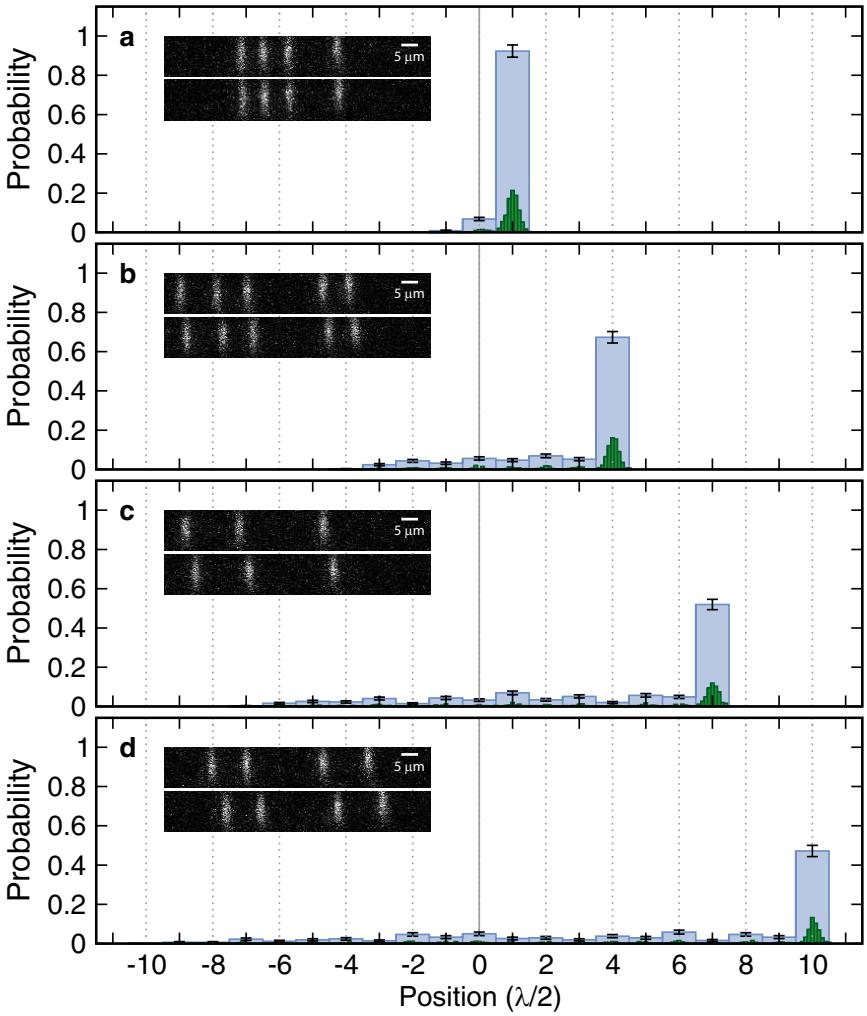

Figure 4.9.: Probability histograms of relative positions of atoms initialized in state $|0\rangle$ after a state-selective transport comprising $2K$ transport steps for (**a**) $K = 1$, (**b**) $K = 4$, (**c**) $K = 7$ and (**d**) $K = 10$. Finely sampled histograms (dark shaded) with a bin width of $\lambda/20$ reveal the periodicity of the optical lattice, as required for passing the reliability criterion, whereas roughly sampled histograms (light shaded) with a bin width of $\lambda/2$ indicate the relative position of the atoms in terms of lattice sites. Insets show initial (upper) and final (lower) fluorescence images of efficiently transported atoms.

recorded data sets thus pass the reliability criterion, see above. Roughly sampled histograms with a bin width of $\lambda/2$ reveal the probability P_k to find an atom, initially starting from zero position, at a relative position of $k\lambda/4$ after the transport sequence. Here, k is an even number, since only even numbers of transport steps are employed in our sequences. Formally, the probability P_k is expressed as the

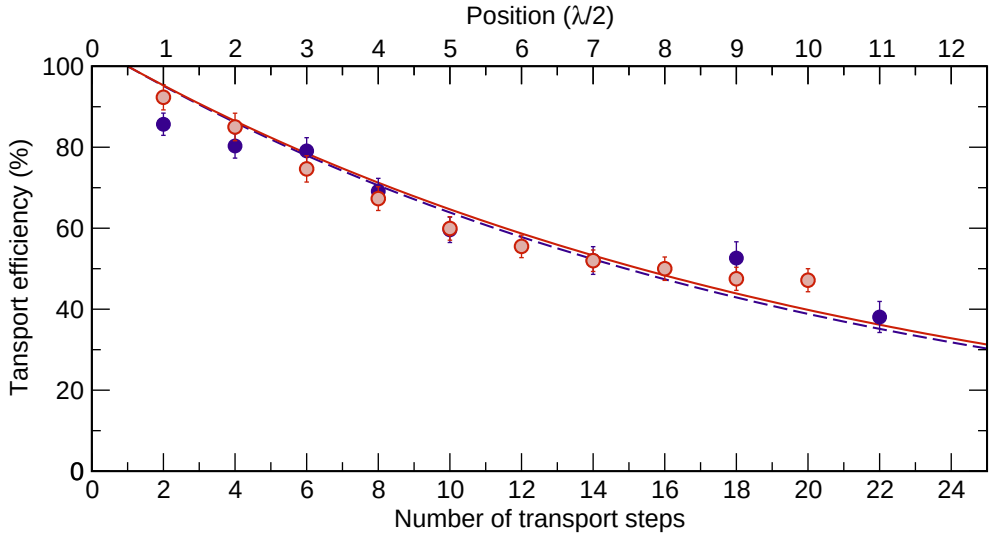

Figure 4.10.: Transport efficiency P_{2K} as a function of number of transport steps K for a cosinusoidal driving ramp with $\tau_{\lambda/2} = 30\,\mu$s and $\tau_{\mathrm{trans}} = 32\,\mu$s, using rectangular $180_0(\pi)$-pulses with a pulse duration of $8\,\mu$s (open dots) and $90_0225_{180}315_0$-pulses of equal Rabi frequency (filled dots), see Sec. 3.5. Solid (dashed) line shows a fit of the model function of Eq. (4.52) to the data obtained using 180_0-pulse ($90_0225_{180}315_0$-pulse) in the transport sequence.

expectation value $P_k \equiv \langle\Psi|\hat{P}_k|\Psi\rangle$ of the projection operator

$$\hat{P}_k = |0,k\rangle\langle k,0| + |1,k\rangle\langle k,1| \tag{4.49}$$

in the product state $|\Psi\rangle \equiv \hat{T}_{2K}|0,0\rangle$. In the ideal case, starting from state $|0,0\rangle$ and applying $2K$ transport steps, we expect only a single peak in each histogram at a relative position of $K\lambda/2$ with a probability of $P_{2K} = 100\%$. We indeed observe dominant peaks at the expected positions, however, with a reduced probability P_{2K} which, unless otherwise stated, we refer to as the efficiency of the transport for $2K$ transport steps. Note that this definition does not include any statement about coherence properties of the transport. It solely reveals the aspect of successful displacement of atoms from one lattice site to another. The efficiency of the *coherent* transport of atoms over several lattice sites will be discussed in Sec. 5.2.2.

The transport efficiency stepwise decreases with the number of transport steps, see Fig. 4.10. It therefore indicates a progressive accumulation of errors during the sequence. Some atoms most likely change their internal state and thus their transport direction either once or multiple times during the sequence, resulting in a distribution of their relative positions within the transport region and thus reducing the transport efficiency. In the following, we will list and discuss possible processes affecting the efficiency of the state-selective transport. Since tunneling of atoms is extremely improbable during shifts of the state-selective lattices, we assume the

$m_\mathrm{F} =$	-4	-3	-2	-1	0	1	2	3	4
$F = 4$	0	1/7	1/3	3/5	1	5/3	3	7	∞
$F = 3$		7	3	5/3	1	3/5	1/3	1/7	

Table 4.1.: Ratio of depths of the dipole potential components $U_{\sigma^+}/U_{\sigma^-}$ for a characteristic wavelength of $\lambda = 865.9\,\mathrm{nm}$ and different magnetic sublevels in the $6^2\mathrm{S}_{1/2}$ ground state manifold of cesium.

shift operations $\hat{S}_\uparrow$ and $\hat{S}_\downarrow$ to be fully efficient. The only remaining sources of imperfections can thus be attributed to the internal and the motional states of atoms. Note that not all effects can be uniquely inferred from the probability histograms alone.

4.6.1. Effect of state initialization errors and photon scattering

Errors in state initialization by optical pumping at the beginning of the transport sequence or scattering of photons from the light field of the optical lattice during the sequence may transfer the atoms into states outside the qubit Hilbert space, i.e. $|F = 4, m_\mathrm{F} \neq 4\rangle$ or $|F = 3, m_\mathrm{F} \neq 3\rangle$. Except for $m_\mathrm{F} = 0$, at our characteristic wavelength of $\lambda = 865.9\,\mathrm{nm}$, atoms in these states effectively still experience a state-selective potential, due to an unequal ratio of depths of the dipole potential components U_{σ^+} and U_{σ^-}, see Tab. 4.1. These ratios, however, lead to a lower effective potential contrast for $\theta = \pi/2$, which at least for atoms in states $|m_\mathrm{F}| < 3$ result in atom losses during the transport. Furthermore, once atoms have left the qubit Hilbert space, their frequencies of possible microwave transitions are far detuned from the preset pulse frequency which is defined by the $|0\rangle \leftrightarrow |1\rangle$ transition frequency. These atoms are then no longer affected by microwave operations of the transport sequence. Thus, for an even number of transport steps, they are transported forth and back to the lattice site at which they left the qubit Hilbert space for the first time. For these atoms the state-selective transport effectively results in a standstill.

In our experiment, scattering of photons from the light field of the optical lattice is negligible on the time scale of typical transport sequences. Because of the high efficiency of our optical pumping ($> 97\%$, see Sec. 3.1.1), errors in state initialization at the beginning of the transport sequence are also unlikely. This fact can be partially inferred form the histograms in Fig. 4.9: A vanishing probability to find an atom at a relative position of $-K\lambda/2$, indicates that the number of atoms initially prepared in state $|1\rangle$ is negligible. The same applies for the number of the atoms initialized in states outside the qubit Hilbert space, since there is no pronounced peak at the zero position in the histogram, which should occur if a non-marginal number of atoms effectively stand still from the beginning. Consequently, errors in state initialization and photon scattering processes play a marginal role for our implementation of state-selective transport.

4.6.2. Effect of microwave pulse errors

First, we consider coherent microwave operations in the transport sequence with an error in π-pulse condition and phase, parameterized by $\varepsilon \in \mathbb{R}$ and $\delta \in \mathbb{R}$, respectively. Employing both errors we cover a wide range of possible technical problems of the microwave setup, including systematical drifts of Rabi frequency from one pulse to another. The microwave frequency is assumed to be resonant to the $|0\rangle \leftrightarrow |1\rangle$ transition frequency.

To incorporate these errors in our transport sequence, we replace the ideal π-pulse operators $\hat{U}_\pi$ in Eq. (4.46) by their *biased* counterparts $\hat{U}_{\pi+\varepsilon_{j,\uparrow},\delta_{j,\uparrow}}$ and $\hat{U}_{\pi+\varepsilon_{j,\downarrow},\delta_{j,\downarrow}}$,[10] where the arrows in the subscript of ε and δ distinguish between pulses applied in the $\theta = 0$ ($\downarrow$) and $\theta = \pi$ ($\uparrow$) configuration, respectively. The index j incorporates changes of pulse errors from one pulse to another, e.g. due to systematical drifts of experimental parameters over time, which are assumed to be reproducible for each sequence repetition. By this, the transport operator finally reads

$$\hat{T}_{2K}^{\mathrm{err}} \equiv \prod_{j=1}^{K} \left(\hat{U}_{\pi+\varepsilon_{j,\downarrow},\delta_{j,\downarrow}} \hat{S}_\downarrow \hat{U}_{\pi+\varepsilon_{j,\uparrow},\delta_{j,\uparrow}} \hat{S}_\uparrow \right) . \tag{4.50}$$

The probability to find an atom initially prepared in state $|0\rangle$ at a relative position $K\lambda/2$ after $2K$ transport steps is then given by

$$P_{2K}^{\mathrm{err}} = \left(\prod_{j=1}^{K} \cos^2(\varepsilon_{j,\uparrow}/2) \right) \left(\prod_{j=1}^{K-1} \cos^2(\varepsilon_{j,\downarrow}/2) \right) , \tag{4.51}$$

accordingly. Therefore, the transport efficiency neither depends on the accumulated phase during the transport nor on phase errors of the microwave operations, as long as these operations are coherent.[11] Consequently, dephasing during the shift operations is irrelevant whenever atoms have just to be transported to a predefined lattice site. The situation is different for errors in π-condition. According to Eq. (4.51), these errors progressively accumulate with the number of transport steps.

The experimental setup is usually aligned so that for both overlap configurations, $\theta = 0$ and $\theta = \pi$, the microwave spectra are almost identical, including the amplitudes, positions and shapes of the resonance peak. Thus, neglecting drifts of experimental parameters which may affect the microwave operations from one pulse to another, we can assume that $\varepsilon_{j,\uparrow} = \varepsilon_{j,\downarrow} =: \bar{\varepsilon}$. Then, Eq. (4.51) simplifies to

$$P_{2K}^{\mathrm{err}} = \left[\cos^2(\bar{\varepsilon}/2)\right]^{2K-1} = \left(\bar{P}_{|1\rangle}\right)^{2K-1} , \tag{4.52}$$

[10] For definition of these operators see Eq. (3.13) in Sec. 3.2.1.

[11] Note, that this does not apply for $P_{2K'}^{\mathrm{err}}$ with $-(K-1) < K' < K$, where quantum interference of delocalized matter wave components with themself may occur and thus strongly affect the probability to find an atom on the sites $K'\lambda/2$. This effect will be discussed in Chap. 6.

where we characterize the pulse error by the mean efficiency of the pulse to transfer state $|0\rangle$ into $|1\rangle$, given by $\bar{P}_{|1\rangle} = |\langle 1|\hat{U}_{\pi+\bar{\varepsilon}}|0\rangle|^2 = \cos^2(\bar{\varepsilon}/2)$. In this representation, it becomes evident that from the transport efficiency P_{2K} alone, it is impossible to distinguish errors of coherent pulses from pulses, the transfer efficiency of which is reduced by detuning of the microwave frequency from the $|0\rangle \leftrightarrow |1\rangle$ transition frequency or just decoherence during microwave operations. The same holds for the general expression of Eq. (4.51). To distinguish between resonant and detuned, or coherent and incoherent operations the probabilities $P^{\mathrm{err}}_{2K'}$ with $-(K-1) < K' < K$ have to be additionally taken into account. However, since the characteristic features in the histograms of Fig. 4.9 are partially smaller than statistical errors, the recorded histograms are not suitable for a deep analysis aiming these distinctions.

Irrespective of the distinction of errors, the mean transfer efficiency of microwave pulses can be directly inferred from a fit of Eq. (4.52) to the transport efficiency in Fig. 4.10, yielding

$$\bar{P}_{|1\rangle} = (95.3 \pm 0.2)\% \,. \tag{4.53}$$

Deviations of the data points from the fitted curve can be partially attributed to systematical drifts of polarization over time, resulting in changes of pulse efficiency from one pulse to another. These drifts cannot be uniquely inferred from the transport efficiency alone, since the number of employed pulses exceeds the number of data points. Drifting of polarization has been independently confirmed by monitoring the polarization (or more precisely, its projection behind a polarizer) of the retro-reflected beam after passing the trapping region of the atoms.

In comparison, for a "static" optical lattice, a pulse efficiency of $(98.9 \pm 0.2)\%$ has been deduced, see Sec. 3.2.3. The mean transfer efficiency of the π-pulses in the transport sequence is only marginally worser. However, because of successive nature of our state-selective transport and its characteristic accumulation of errors, the impact of reduced transfer efficiency is enhanced. For this reason, whenever possible, transport of atoms over larger distances should be avoided.

To exclude effects of frequency detuning (frequency errors) of the π-pulses from the transport efficiency, instead of rectangular 180_0-pulses, we employ broadband composite pulses in the transport sequence. For population transfers between both qubit basis states, the $90_0 225_{180} 315_0$-pulse has been proven to be sufficiently robust against frequency detuning, see Sec. 3.5. The resulting transport efficiency as a function of transport steps is shown in Fig. 4.10. It agrees reasonably well with that of the 180_0-pulses, providing a similar decay for increasing number of transport steps. From a fit of Eq. (4.52) to the transport efficiency, we obtain

$$\bar{P}_{|1\rangle,\mathrm{CP}} = (95.1 \pm 0.2)\% \,, \tag{4.54}$$

which agrees reasonably well with the value of the regular pulse, see Eq. (4.53). From this, we conclude that the characteristic decay cannot be attributed to detuning of the microwave pulses, be it due to improper preset frequency or drifts of the $|0\rangle \leftrightarrow |1\rangle$ transition frequency. Note that the $|0\rangle \leftrightarrow |1\rangle$ transition frequency is usually checked at the beginning and the end of a transport measurement using

microwave spectroscopy. In case of significant frequency drifts, the entire data set is usually discarded.

4.6.3. Effect of decoherence

Spin-relaxation during the entire transport sequence and dephasing during microwave operations are two more effects which may significantly reduce the transport efficiency. The former is characterized by the longitudinal relaxation time T_1, which has been measured to be of the same order as for sequences without a transport (100 ms). In this measurement, we prepare atoms in state $|0\rangle$ or $|1\rangle$ and perform a typical transport, whereby π-pulses are removed from the sequence, and thus effects of pulse errors as well. Atoms are then only transported forth and back to the initial lattice site. Finally, we determine the population in state $|1\rangle$ using the state-selective push-out, deduce the decay of the initial population and infer its characteristic time constant T_1.

The measurement of the total dephasing time T_2 which only affects the pulse operations during the transport sequence turns out to be non-trivial, since the effect of dephasing during the lattice shifts cannot be excluded by using typical Ramsey and spin-echo sequences. We therefore estimate the T_2 time by solving the optical Bloch equation with damping (see Eq. (3.28)), for π-pulses employed in the transport sequence with a mean transfer efficiency of Eq. (4.53), yielding $T_2 = 41\,\mu$s. Despite the reservations with regard to the precision of this approach, this dephasing time is considerably shorter compared to that inferred from the "static" configuration, see Sec. 3.3. However, it should be taken into account that the microwave pulses are applied in a dynamic configuration, in which settling to a configuration with constant polarization is hardly expected. Fluctuations of polarization which in turn directly translate into fluctuations of differential light-shifts, certainly lead to broadening of the transition frequency and dephasing, see Sec. 3.2.3 and Sec. 3.3. Employing optimum control techniques [143] might help to counteract or compensate technical imperfections of our system, either by particular pulse-shaping or active polarization control, and thus, improve the pulse efficiency in the future.

4.7. Conclusion

In this chapter, I have presented basic concepts and properties of the state-selective transport of single atoms in a 1D optical lattice. Employing the idea of state-selective potentials, I have demonstrated that such transport can be realized for cesium atoms as well, using two counterpropagating linearly polarized laser beams at a characteristic wavelength in a lin-θ-lin configuration with a continuously varied tilt angle θ. The resulting light field comprises orthogonally circularly polarized standing waves, each forming an optical lattice which traps atoms in one of the qubit basis states $|0\rangle$ or $|1\rangle$, respectively. By varying the tilt angle, these lattices

are spatially shifted with respect to each other. The polarization control setup for dynamically adjusting this angle has been discussed in detail.

I have investigated the state-dependent shift dynamics for a characteristic wavelength of $\lambda_{|0\rangle} = 865.9\,\mathrm{nm}$, incorporating effects of undesired polarization components on the respective potentials and related trap parameters. By deriving their analytical expressions, a basis for quantitative analysis of transport properties for this and subsequent chapters has been worked out. Based on this, excitations between axial motional states of the atoms in moving potentials have been estimated using first-order perturbation theory for both, linear and cosinusoidal driving ramps. It turns out that the former permit the shortest ramp and transport times of approximately $20\,\mu\mathrm{s}$, irrespective of whether the limited bandwidth of our polarization control setup is taken into account or not. A Dirac representation of shift operators has been introduced to simplify the description and discussion of the state-selective transport and its applications.

Finally, experimental results of state-selective transport of atoms over several lattice sites have been presented, alternately applying shift operations and π-pulses. Apart from a precise geometrical alignment of the polarization control setup, such transport sequences require well-adjusted settling times and the half-wave voltage of the EOM. For this, iterative procedures have been employed, which rely on probing the purity of linear polarization directly in the trapping region of atoms using microwave spectroscopy. Furthermore, uniqueness issues in analyzing transport data and strategies to overcome them have been discussed in detail.

The investigation of the state-selective transport has been initially focused on the transport efficiency, i.e. the reliability of shifting atoms from one lattice site to another. Our results show that the transport efficiency stepwise decreases with the number of transport steps, revealing a progressive accumulation of errors during the sequence. These errors arise from a finite transfer efficiency of microwave π-pulses in dynamic configuration with a mean value of $(95.3 \pm 0.2)\%$. By replacing the standard pulses with broadband composite pulses in the transport sequence, I have demonstrated that this value cannot be attributed to improper preset frequency or drifts of the $|0\rangle \leftrightarrow |1\rangle$ transition frequency. Instead, it rather results from fluctuations of polarization or its improper settling which directly translate into fluctuations of differential light-shifts, yielding broadening of the transition frequency and thus dephasing during microwave pulses.

5. Coherent state-selective transport — A single atom interferometer

So far, we have focused on the state-selective transport of atoms prepared either in qubit basis state $|0\rangle$ or $|1\rangle$, moving them as a whole from one lattice site to another. The most interesting question regarding a generic feature of qubits, however, still remains unanswered: What happens if an atom is initially prepared in a superposition of these states? According to Eq. (4.46), for $2K$ transport steps, we expect the matter wave of this atom to be split and coherently delocalized over two lattice sites, separated by a distance of $2K\lambda/2$

$$\hat{T}_{2K}\frac{1}{\sqrt{2}}\left(|0,0\rangle + i|1,0\rangle\right) = \frac{e^{i\gamma}}{\sqrt{2}}\left(|0,2K\rangle + i|1,-2K\rangle\right) ,$$

whereby the global phase $\gamma = K(\varphi_{|0\rangle,\mathbf{n}} + \varphi_{|1\rangle,\mathbf{n}} + \pi)$ can be neglected as usual. Such coherent splitting and delocalization of matter waves have been demonstrated for large ensembles of Rubidium atoms in a Mott insulating state over distances of up to seven lattice sites [40]. We will show that under certain circumstances, this works for thermal atoms as well.

By coherently merging and recombining both matter wave components on the initial lattice site and measuring the difference between their accumulated phase, a two-arm single atom interferometer can be realized. Since their first realization in the early 1990's, atom interferometers have evoked increased interest, especially in recent years [144–146]. In contrast to photons in light interferometers, atoms exhibit strong interactions with their environment, providing a remarkable sensitivity to external fields, including electric fields [147], magnetic field gradients [148] and gravity [149, 150]. These properties make them ideally suited for high-precision measurement devices [150–152]. A recent survey of atom interferometer designs and their applications can be found in Ref. [153] and references therein.

In this thesis, we primarily use single atom interferometer sequences to investigate coherence properties of the state-selective transport. These sequences allow us to precisely adjust experimental parameters for a coherent transport with marginal excitations between vibrational states. We show that by counteracting inhomogeneous dephasing from the state-selective transport itself using spin-echo techniques, coherent delocalization of atoms over distances of up to ten lattice sites is possible even for thermal atoms. This allows us for instance to probe spatial inhomogeneities of external fields in the trapping region. A quantum walk [3, 4], as an advanced application of multiple path quantum interference is finally presented in the subsequent chapter.

5.1. Coherence properties of state-selective transport

Analogous to the analysis of coherence properties of qubits in a static optical lattice (see Sec. 3.3), Ramsey and spin-echo phase spectroscopy can be also used to investigate these properties for the state-selective transport. For this purpose, the respective sequences have to be extended by shift operations. Furthermore, dephasing mechanisms arising from different shift dynamics of state-selective potentials have to be incorporated into current dephasing models. Ideally, possible excitations between vibrational states have to be taken into account. Here, we circumvent a complex quantum mechanical description of excitation processes by restricting our investigations to a case, in which experimental parameters are adjusted for negligible excitations between vibrational states.

5.1.1. Dephasing of thermal atoms

Consider a single atom being axially in a vibrational state n and radially in states m and m'. At first, we assume that these states are preserved during the entire sequence. By this, we can build on the previous Dirac representation, remaining in the usual Hilbert space $\mathcal{H}_{\text{ext}}$, see Sec. 4.5. We assign the initial position of an atom to the lattice site zero. Then, an appropriate Ramsey sequence, which emulates the dynamics of a transport over several lattice sites comprises the following steps:

(A) The atom is initialized in the qubit basis state $|0\rangle$, i.e. a total initial state $|0\rangle \otimes |k = 0\rangle = |0, 0\rangle$. A subsequently applied $\pi/2$-pulse generates an equal superposition of $|0, 0\rangle$ and $|1, 0\rangle$.

(B) The driving voltage of the EOM is (linearly) ramped to $\mathcal{V} = \mathcal{V}_{\lambda/2}$ within a preset ramp time $\tau_{\lambda/2}$. During the transport time $\tau_{\text{trans}} = \tau_{\lambda/2} + \delta t$, the atomic matter wave is split and delocalized over two neighboring lattice sites, see Fig. 5.1.

(C) Instead of a π-pulse subsequently applied in a typical transport sequence (see Sec. 4.5), the atom is kept delocalized over a time period of the corresponding pulse duration τ.

(D) The driving voltage is then ramped back to its initial value ($\mathcal{V} = 0$), merging both delocalized matter wave components on the initial lattice site.

(E) Finally, a $\pi/2$-pulse with a preset Ramsey phase ϕ_{rf} recombines both matter wave components, removes the which-way information and probes the accumulated phase difference between them.

This Ramsey sequence provides therefore one of the simplest implementations of a Michelson type, single atom interferometer.

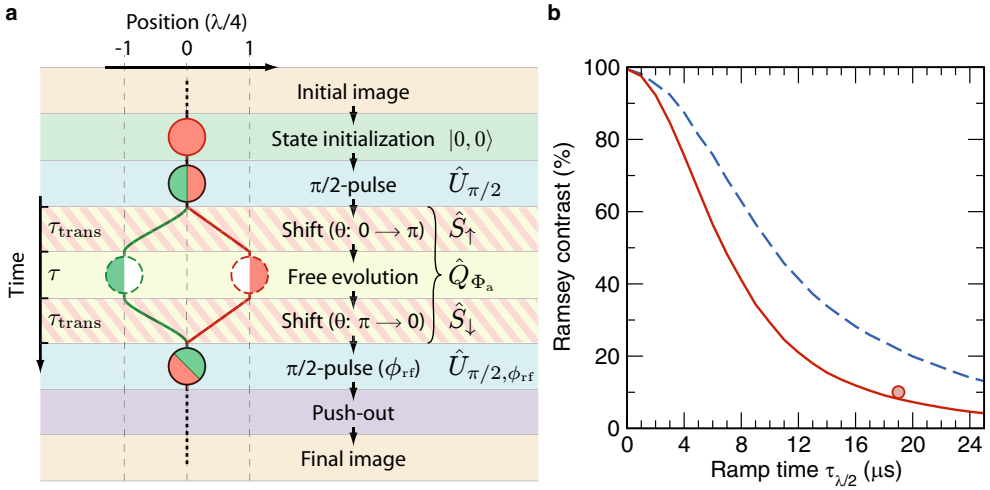

Figure 5.1.: (**a**) Ramsey sequence comprising splitting and delocalization of atomic matter waves over two neighboring lattice sites. Solid circles indicate the atom, dashed circles, its state-dependent matter wave components. Colors indicate the qubit states $|0\rangle$ (red) and $|1\rangle$ (green), semicircles their contributions to the superposition state $\frac{1}{\sqrt{2}}(|0,0\rangle + i|1,0\rangle)$. Colored paths indicate the displacement of state-selective potentials $U_{\sigma^+,|0\rangle}$ and $U_{\sigma^-,|1\rangle}$, respectively. A sequence of operations is listed on the right, including the respective operators. (**b**) Calculated Ramsey contrast as a function of ramp time $\tau_{\lambda/2}$ for a linear driving ramp (solid line) as inferred from Eq. (5.3). The single dot shows the measured Ramsey contrast in a region, in which excitations between vibrational states are negligible. The dashed line shows the calculated Ramsey contrast for an atom in the axially cooled to the vibrational ground state.

Analogous to Eq. (3.33), the contribution of a single atom to the Ramsey fringe of an atomic ensemble can be calculated by

$$\begin{aligned} P_{\mathrm{a},|1\rangle,\mathbf{n}}(\phi_{\mathrm{rf}},\tau_{\lambda/2}) &= \left|\langle 0,1|\hat{U}_{\pi/2,\phi_{\mathrm{rf}}}\hat{S}_{\downarrow}\hat{Q}_{\Phi_{\mathrm{a}}(\tau_{\pi/2})}\hat{S}_{\uparrow}\hat{U}_{\pi/2}|0,0\rangle\right|^2 \\ &= \frac{1}{2}\left\{1+\cos[\phi_{\mathrm{rf}}-2(\varphi_{|0\rangle,\mathbf{n}}-\varphi_{|1\rangle,\mathbf{n}})-\Phi_{\mathrm{a}}(\tau_{\pi/2})]\right\}, \end{aligned} \tag{5.1}$$

where $\tau_{\pi/2} = 2\tau_{\mathrm{trans}} + \tau = 2\tau_{\lambda/2} + 2\delta t + \tau$ denotes the Ramsey time, i.e. the time period between both $\pi/2$-pulses and $\mathbf{n} = (n, m, m')$. Incorporating the energy-dependent light shift by a weighted ensemble average, see Eq. (3.38a), we again obtain

$$P_{|1\rangle,\mathbf{n}}(\phi_{\mathrm{rf}},\tau_{\lambda/2}) = \frac{1}{2}\left\{1+C(\tau_{\pi/2})\cos[\phi_{\mathrm{rf}}-2(\varphi_{|0\rangle,\mathbf{n}}-\varphi_{|1\rangle,\mathbf{n}})-\Phi(\tau_{\pi/2})]\right\} \tag{5.2}$$

with the transport-independent contribution to the fringe contrast $C(\tau_{\pi/2})$ and the phase contribution $\Phi(\tau_{\pi/2})$ defined in Eqs. (3.39) and (3.40), respectively. In the absence of vibronic excitations, the Ramsey fringe of thermal atoms can be

estimated from a weighted sum of all their initial vibrational states

$$P_{|1\rangle}(\phi_{\mathrm{rf}},\tau_{\lambda/2}) = \sum_{n=0}^{\infty} \varrho_{\mathrm{ax}}^{(n)} \sum_{m,m'=0}^{\infty} \varrho_{\mathrm{rad}}^{(m,m')} P_{|1\rangle,\mathbf{n}}(\phi_{\mathrm{rf}},\tau_{\lambda/2})\,, \tag{5.3}$$

with the axial and radial occupation probabilities [154]

$$\varrho_{\mathrm{ax}}^{(n)} = \frac{\bar{n}_{\mathrm{ax}}^{n}}{(1+\bar{n}_{\mathrm{ax}})^{n+1}}\,, \tag{5.4a}$$

$$\varrho_{\mathrm{rad}}^{(m,m')} = \frac{\bar{m}_{\mathrm{rad}}^{m+m'}}{(1+\bar{m}_{\mathrm{rad}})^{m+m'+2}}\,, \tag{5.4b}$$

where $\bar{n}_{\mathrm{ax}}$ and $\bar{m}_{\mathrm{rad}}$ denote the average axial and radial occupation number, respectively. Thus, the resulting Ramsey fringe possesses again a cosinusoidal shape

$$P_{|1\rangle}(\phi_{\mathrm{rf}},\tau_{\lambda/2}) = \frac{1}{2}\left\{1 + C_{\mathrm{vib}}(\tau_{\lambda/2}) C(\tau_{\pi/2}) \cos[\phi_{\mathrm{rf}} - 2\widetilde{\varphi}(\tau_{\lambda/2}) - \Phi(\tau_{\pi/2})]\right\} \tag{5.5}$$

with an additional contrast contribution $C_{\mathrm{vib}}(\tau_{\lambda/2})$ and a phase $\widetilde{\varphi}(\tau_{\lambda/2})$, both resulting from the weighted sum of vibrational states. In the ideal case, for $\varphi_{|0\rangle,\mathbf{n}} = \varphi_{|1\rangle,\mathbf{n}}$, it is $C_{\mathrm{vib}}(\tau_{\lambda/2}) = 1$ and $\widetilde{\varphi}(\tau_{\lambda/2}) = 0$. The Ramsey fringe is then unaffected by the state-selective transport. However, due to different shift dynamics of the state-selective potentials, it is $\varphi_{|0\rangle,\mathbf{n}} \neq \varphi_{|1\rangle,\mathbf{n}}$ and $\varphi_{|0\rangle,\mathbf{n}} - \varphi_{|1\rangle,\mathbf{n}} \neq \varphi_{|0\rangle,\mathbf{n}'} - \varphi_{|1\rangle,\mathbf{n}'}$ for $\mathbf{n} \neq \mathbf{n}'$, see below. Consequently, for thermal atoms our implementation of state-selective transport introduces an additional inhomogeneous dephasing, yielding $C_{\mathrm{vib}}(\tau_{\lambda/2}) < 1$ and thus a decrease of the total Ramsey contrast.

To estimate $C_{\mathrm{vib}}(\tau_{\lambda/2})$ for typical experimental parameters, we model the phase evolution of each wave packet during the state-selective shift. For typical average occupation numbers $\bar{n}_{\mathrm{ax}} = 1.2$ and $\bar{m}_{\mathrm{rad}} = 200$, the trapping potentials of the optical lattice can be regarded as harmonic and the axial and radial motional dynamics as decoupled. For a single transport step in a spatially homogeneous environment, the accumulated phase difference between both delocalized matter wave components is then given by

$$\varphi_{|0\rangle,\mathbf{n}} - \varphi_{|1\rangle,\mathbf{n}} = \frac{1}{\hbar} \int_{0}^{\tau_{\mathrm{trans}}} \left[\left(\mathcal{U}_{|0\rangle,\mathbf{n}}(t) - \mathcal{U}_{|0\rangle,\mathbf{n}}(0)\right) - \left(\mathcal{U}_{|1\rangle,\mathbf{n}}(t) - \mathcal{U}_{|1\rangle,\mathbf{n}}(0)\right)\right] \mathrm{d}t \tag{5.6}$$

with the state-dependent energy contributions ($j = \{0,1\}$)

$$\begin{aligned}\mathcal{U}_{|j\rangle,\mathbf{n}}(t) = {} & U_{0,|j\rangle}(\theta(t)) + \delta_{j,0}\hbar\omega_0 \\ & + \hbar\omega_{\mathrm{ax},|j\rangle}(t)\left(n+\tfrac{1}{2}\right) + \hbar\omega_{\mathrm{rad},|j\rangle}(t)\left(m+m'+1\right)\,,\end{aligned} \tag{5.7}$$

where $\delta_{j,0}$ denotes the Kronecker delta, ω_0 the $|0\rangle \leftrightarrow |1\rangle$ transition frequency, $U_{0,|j\rangle}(t)$ and $\omega_{\mathrm{ax},|j\rangle}(t)$ the state-selective dipole potentials and their axial trapping frequen-

cies, defined in Eqs. (4.17) and (4.31), respectively, and

$$\omega_{\mathrm{rad},|0\rangle}(t) = \Omega_{\mathrm{rad},|0\rangle} = \mathrm{const}\,, \tag{5.8a}$$

$$\omega_{\mathrm{rad},|1\rangle}(t) = \Omega_{\mathrm{rad},|1\rangle}\sqrt{\tfrac{1}{2} + \tfrac{1}{2}\sqrt{1 - \tfrac{7}{16}\sin^2\theta(t)}} \tag{5.8b}$$

the corresponding radial trapping frequencies.[1] By incorporating these relations in Eq. (5.3), the Ramsey contrast for an ensemble of thermal atoms can be directly calculated, whereas the sums over the vibrational quantum numbers in Eq. (5.3) are truncated at $n = 10$ and $m, m' = 1000$, taking into account that the remaining contributions to the sums are negligible ($\sum_{n=11}^{\infty} \varrho_{\mathrm{ax}}^{(n)} \approx 10^{-3}$ and $\sum_{m,m'=1001}^{\infty} \varrho_{\mathrm{rad}}^{(m,m')} \approx 10^{-5}$). At this point, the origin of inhomogeneous dephasing during the transport becomes evident: It is the state-dependent evolution of potential depths and trapping frequencies during the shift. Therefore, it would be valuable to remove the state-dependency of these parameters by employing those hyperfine Zeeman states as qubit basis states, for which couplings to undesired polarization components are identical while maintaining the selectivity of both potentials. In principle, this can be achieved for states $|\widetilde{0}\rangle \equiv |F = 4, m_{\mathrm{F}} = 3\rangle$ and $|\widetilde{1}\rangle \equiv |F = 3, m_{\mathrm{F}} = 3\rangle$ at a characteristic wavelength of $\widetilde{\lambda} = 869.4\,\mathrm{nm}$. Technical modifications and further investigations concerning the suitability of these states are required in the future.

In Figure 5.1(b), the estimated Ramsey contrast as a function of ramp time $\tau_{\lambda/2}$ for a linear driving ramp is shown. For simplicity, imperfections arising from the polarization control setup have not been considered in the calculation. The transport-independent contribution to the contrast, $C(\tau_{\pi/2})$, is calculated from Eq. (3.39) for a dephasing time T_2^*, as inferred from a regular (transport-free) Ramsey sequence, see Tab. 3.2 in Sec. 3.3.2. Since our dephasing model a priori excludes excitations between vibrational states, the calculated contrast can be only verified for ramp times, for which this condition is met. Unfortunately, due to technical limitations this can be only ensured for $\tau_{\lambda/2} \approx 19\,\mu\mathrm{s}$, see Sec. 4.4 and discussion below.

The measured Ramsey contrast agrees reasonably well with the calculated value, albeit it is expected to be underestimated by the harmonic approximation. Our dephasing model seems therefore to sufficiently capture the dominant inhomogeneous dephasing mechanisms of the state-selective transport. Unlike the static case, we abstain from defining a custom inhomogeneous dephasing time for each sequence employing the state-selective transport. Apart from the sequence itself, this dephasing time would depend on the driving ramp and the ramp time, which both affect the probability of excitations between vibrational states, see Sec. 4.4. These excitations provide additional *homogeneous* dephasing, which is indistinguishable from a Ramsey phase spectroscopy alone. Instead, we will rather use the measured or estimated Ramsey contrast to quantify dephasing for a given driving ramp and its ramp time. Since the Ramsey contrast is equivalent to the polarization of a quan-

[1] Note that the contribution of $|0\rangle \leftrightarrow |1\rangle$ transition frequency ω_0 is just noted for completeness. As a constant term, it has no influence on the accumulated phase since it cancels out in Eq. (5.6).

tum state, see Eq. (3.25), it is ideally suited to characterize coherence properties of a qubit.

As an alternative approach to choosing different hyperfine Zeeman states as qubit basis states, cooling of atoms to the motional ground state could be used to eliminate the modeled inhomogeneous dephasing. Recently, one-dimensional sideband cooling of atoms to the axial vibrational ground state has been successfully implemented in our experimental setup [68,129]. According to our dephasing model, such cooling would significantly improve the Ramsey contrast, see Fig. 5.1(b), even if the average radial occupation number $\bar{m}_{\mathrm{rad}}$ cannot be currently reduced. Therefore, by incorporating sideband cooling into the experimental sequences presented in this thesis, some improvements in performance of the interferometer are expected in the future.

Finally, since our dephasing model predicts a low Ramsey contrast in the ramp time regions of interest, we finally conclude that the above Ramsey sequence is not suitable to experimentally infer optimum ramp times with high reliability. Instead, analogous to qubits in a static optical lattice, spin-echo techniques have to be employed to reverse inhomogeneous dephasing and thus extract homogeneous dephasing contributions of the transport which mainly arise from excitations between vibrational states.

5.1.2. Detecting vibrational excitations

Similar to inhomogeneous dephasing of qubits in a static optical lattice, inhomogeneous dephasing which arises from the state-selective transport of thermal atoms can be in principle reversed by extending the Ramsey sequence by a rephasing π-pulse. The resulting spin-echo sequence, which comprises delocalization of a matter wave over two neighboring lattice sites, is schematically shown in Fig. 5.2. After splitting, delocalizing and merging the atomic matter wave (steps (B-D)), a rephasing π-pulse is used to exchange the roles of states $|0,0\rangle$ and $|1,0\rangle$. Consequently, by repeating all three sequence steps once again, in total, both matter wave components will ideally accumulate identical phases before being recombined by the final $\pi/2$-pulse. The latter again removes the which-way information, providing just another implementation of a single atom interferometer.

The resulting single atom contribution to the Ramsey fringe recorded for an atomic ensemble is given by

$$\begin{aligned} P_{\mathrm{a},|1\rangle,\mathbf{n}}(\phi_{\mathrm{rf}},\tau_{\lambda/2}) &= \left|\langle 0,1|\hat{U}_{\pi/2,\phi_{\mathrm{rf}}}\hat{S}_{\downarrow,2}\hat{Q}_{\Phi_{\mathrm{a},2}(\tau_\pi)}\hat{S}_{\uparrow,2}\hat{U}_{\pi}\hat{S}_{\downarrow,1}\hat{Q}_{\Phi_{\mathrm{a},1}(\tau_\pi)}\hat{S}_{\uparrow,1}\hat{U}_{\pi/2}|0,0\rangle\right|^2 \\ &= \frac{1}{2}\left\{1+\cos[\phi_{\mathrm{rf}}-2(\Delta\varphi_{|0\rangle,\mathbf{n}}-\Delta\varphi_{|1\rangle,\mathbf{n}})-\Delta\Phi_{\mathrm{a}}(\tau_\pi)+\pi]\right\}, \quad (5.9) \end{aligned}$$

with $\Delta\varphi_{|j\rangle,\mathbf{n}} = \varphi_{|j\rangle,\mathbf{n},2} - \varphi_{|j\rangle,\mathbf{n},1}$ and $\Delta\Phi_{\mathrm{a}}(\tau_\pi) = \Phi_{\mathrm{a},2}(\tau_\pi) - \Phi_{\mathrm{a},1}(\tau_\pi)$, see Sec. 3.3.3.[2] The additional indices "1" and "2" are introduced to distinguish between operations and phase contributions before and after the rephasing pulse, respectively. In the

[2]We stress that for the derivation of this relation ideal pulses are assumed.

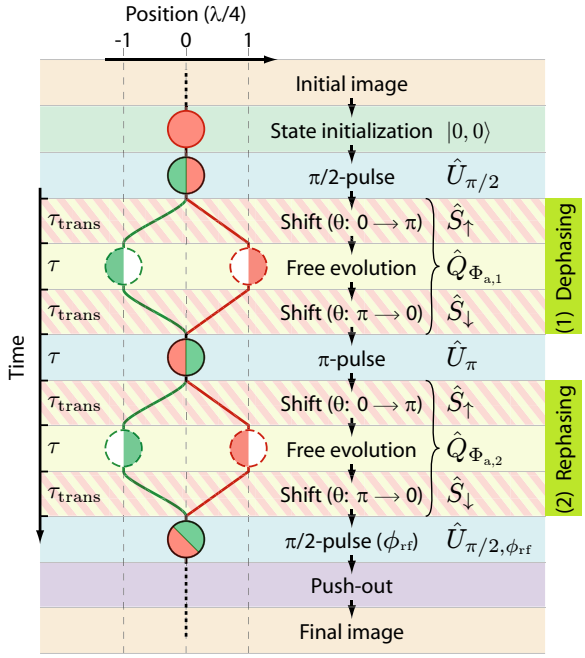

Figure 5.2.: Spin-echo sequence comprising splitting and delocalization of an atomic matter wave over two neighboring lattice sites, used to determine the optimum ramp time $\tau_{\lambda/2} = \tau_{\mathrm{trans}} - \delta t$. Symbols, paths and colors are identical to those in Fig. 5.1. A sequence of operations is listed on the right, including the respective operators.

ideal case, i.e. in absence of drifts of polarization and excitations between vibrational states, each transport step can be regarded as identical, yielding $\Delta\varphi_{|j\rangle,\mathbf{n}} = 0$. In that particular case, shift-induced inhomogeneous dephasing becomes completely rephased and the contrast unaffected by the transport. Deviations from the ideal case manifest themselves as a decrease of the spin-echo contrast. Because drifts of polarization are negligible on the time scale of typical transport sequences, excitations between vibrational states remain the only dominant source of such decrease. The spin-echo contrast provides therefore an indirect insight into excitation processes of thermal atoms. It can thus be used to determine the optimum ramp time at which such excitations are suppressed. In the following, we will qualitatively discuss the effect of excitations between vibrational states on the spin-echo contrast, distinguishing two dominant cases:

(I) Only one of the matter wave components changes its vibrational state before being recombined: Since vibrational components of the matter wave form an orthonormal system, interference terms which contribute to the spin-echo contrast vanish or at least are reduced.[3] In both cases the spin-echo contrast is expected to decrease.

[3]Note that excitations between vibrational states can indeed be coherent, generating superposi-

(II) Both recombined matter wave components change their vibrational state: If both components are in different vibrational states before being recombined by the $\pi/2$-pulse, the same applies as for case (I). Otherwise, the spin-echo contrast remains only unaffected for $\Delta\varphi_{|0\rangle,\mathbf{n}} - \Delta\varphi_{|1\rangle,\mathbf{n}} = 0$. According to our dephasing model, this can only apply if both, $\Delta\varphi_{|0\rangle,\mathbf{n}} = 0$ and $\Delta\varphi_{|1\rangle,\mathbf{n}} = 0$ holds. Fulfilling both relations, however, is only possible, if both matter wave components are temporarily excited to the same intermediate vibrational state before the rephasing pulse is applied, and subsequently deexcited to the initial state before being recombined. In the interesting region of low excitation probabilities, according to Eqs. (4.24) and (4.25) such excitation can never be entirely reversed. Thus, even in that case a decrease of spin-echo contrast should occur.

Following the qualitative discussion, we conclude that the above spin-echo sequence is in principle sensitive to both, axial and radial excitations between vibrational states of thermal atoms, while being unbiased by any reversible dephasing. We therefore employ this sequence to determine the optimum ramp time for the preferred linear driving ramp, see Sec. 4.4.

5.1.3. Determining the optimum ramp time

To determine the optimum ramp time for a linear driving ramp, we perform a spin-echo phase spectroscopy employing delocalization of the matter wave for different ramp times $\tau_{\lambda/2}$. The settling time of $\delta t = 2\,\mu$s and a π-pulse duration of $\tau = 8\,\mu$s correspond to typical values employed in our transport sequences, while trap depth, trapping frequencies and exposure times of fluorescence images are similar to those used in microwave (see Sec. 3.2.3) and static spin-echo spectroscopy, see Sec. 3.3.3. Similar to the latter, the spin-echo contrast $C(\tau_{\lambda/2})$ and the deviation of the fringe phase $\delta\Phi(\tau_{\lambda/2})$ from the expected macroscopic phase are inferred from a fit of

$$\widetilde{P}_{|1\rangle}(\phi_{\mathrm{rf}}, \tau_{\lambda/2}) = \frac{p_{\mathrm{sur}}(\tau_{\mathrm{img}})}{2}\left\{1 + C(\tau_{\lambda/2})\cos[\phi_{\mathrm{rf}} + \pi - \delta\Phi(\tau_{\lambda/2})]\right\} \tag{5.10}$$

to the Ramsey fringes, where $p_{\mathrm{sur}}(\tau_{\mathrm{img}})$ denotes the survival probability of the atoms in the optical lattice during the time period between the acquisition of the initial and final image. We stress that $C(\tau_{\lambda/2})$ and $\delta\Phi(\tau_{\lambda/2})$ incorporate both, the contributions from the excitations between vibrational states and the transport-independent (static) contributions discussed in Sec. 3.3.3. For the ramp times of interest, the latter play only a marginal role. Furthermore, since some excitation processes yield deviations of the fringe phase rather than a significant decrease of the spin-echo contrast, both quantities are equally considered for deducing an optimum ramp time.

tions of these states. The latter may comprise a contribution from the initial state. In that case, there is a finite overlap with the unexcited matter wave component.

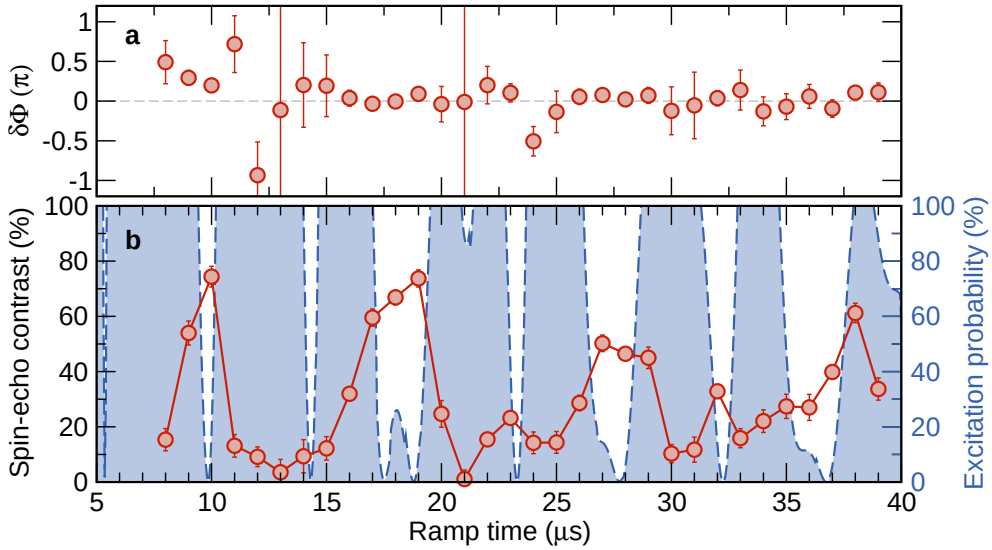

Figure 5.3.: Spin-echo contrast and deviation of the macroscopic phase (open dots in (**b**) and (**a**)) as a function of ramp time for a spin-echo sequence comprising splitting and delocalization of atomic matter waves over two neighboring lattice sites. Shaded curve in (**b**) indicate the probability to excite a matter wave component from the axial vibrational ground state to the next higher state, as inferred from a calculation which takes the entire sequence into account.

In Figure 5.3, the resulting spin-echo contrast and deviation of the macroscopic phase from the expected zero value as a function of ramp time are shown, together with the theoretical excitation probability based on the first-order perturbation theory, see Sec. 4.4. In contrast to Sec. 4.4, in which the analysis has been focused on a single ramp, here, the entire sequence has been taken into account for the calculation, including delays between both ramping up and ramping down operations. In general, these delays significantly affect the excitation probabilities. On the other hand, we abstain from incorporating technical imperfection of the polarization control system by employing the measured transfer function for two reasons: First, the transfer function has been only measured for a frequency range of 2 MHz. Therefore, numerical artifacts due to truncation of the frequency range in the numerical calculation of the inverse Fourier transform may introduce unphysical artifacts. Second, artifacts in the measured transfer function arising from the measuring process itself may additionally bias the theoretical results. While for a single ramp, such artifacts marginally affect the numerical result, they become increasingly noticeable for sequences composed of several piecewise defined ramps. Finally, since we are mainly interested in the parameter regions of excitation minima, it suffices to restrict our calculation to atoms in the axial vibrational ground state.

The positions of the maxima of the measured spin-echo contrast reasonably co-

incide with the position of the minima of the calculated excitation probability, see Fig. 5.3. We conclude from this fact that excitations between axial vibrational states during the shift indeed destroy the matter wave interference and thus may give rise to homogeneous dephasing. Deviations for increasing ramp times and the systematical shift of the maxima positions towards higher ramp times can be attributed to the limited bandwidth of the polarization control setup, see Sec. 4.3. The same applies for some minima in the excitation, which most likely are smeared out and thus suppressed in the measured spin-echo contrast. Besides a maximum at the predicted excitation minimum at $\tau_{\lambda/2} \approx 19\,\mu$s, a further maximum in the spin-echo contrast surprisingly occurs at $\tau_{\lambda/2} \approx 10\,\mu$s. This maximum can be most likely attributed to coherent excitations of both matter wave components to the same vibrational state, as discussed in case (II), see above. This hypothesis is partially supported by a finite macroscopic phase $\delta\Phi(\tau_{\lambda/2})$, see Fig. 3.10(a), which reveals an imperfect rephasing process at this ramp time. Perfect rephasing ($\delta\Phi(\tau_{\lambda/2}) \approx 0$), in turn, can be observed for $\tau_{\lambda/2} \approx 19\,\mu$s, restricting our search for optimum ramp time to this region.

To precisely adjust the optimum ramp time, we usually scan the region of interest with a higher resolution. Once an optimum ramp time is found, a spin-echo contrast of up to 84% is typically obtained, which is lower than for a static optical lattice. Analogous to the reduced transport efficiency (see Sec. 4.6), this fact can be partially attributed to a limited transfer efficiency of the rephasing π-pulse and the recombining $\pi/2$-pulse in a dynamic configuration.

5.2. Delocalizing of a matter wave over several lattice sites

The spin-echo sequence employed so far allows to completely reverse inhomogeneous dephasing of shifted thermal atoms while the homogeneous dephasing due to excitations between vibrational states remains. However, by repeating the entire delocalization process after the rephasing π-pulse also the position-dependent accumulation of phase is reversed, see below. Consequently, one of the most interesting application of a single atom interferometer, namely the probing of spatial differences in external fields in the trapping region, cannot be performed by such a sequence. Instead, just another interferometer sequence is required which is sensitive to position-dependent changes in environmental fields, while still reversing inhomogeneous dephasing by employing spin-echo techniques.

Following the idea of Sec. 4.5, such sequence can be realized by delocalizing the atomic matter wave only once, but over distances comprising an even multiple of lattice sites, see e.g. Fig. 5.4. This sequence inherently comprises the required number of rephasing π-pulses to reverse position-independent inhomogeneous dephasing. To investigate the properties of this class of interferometer sequences, for

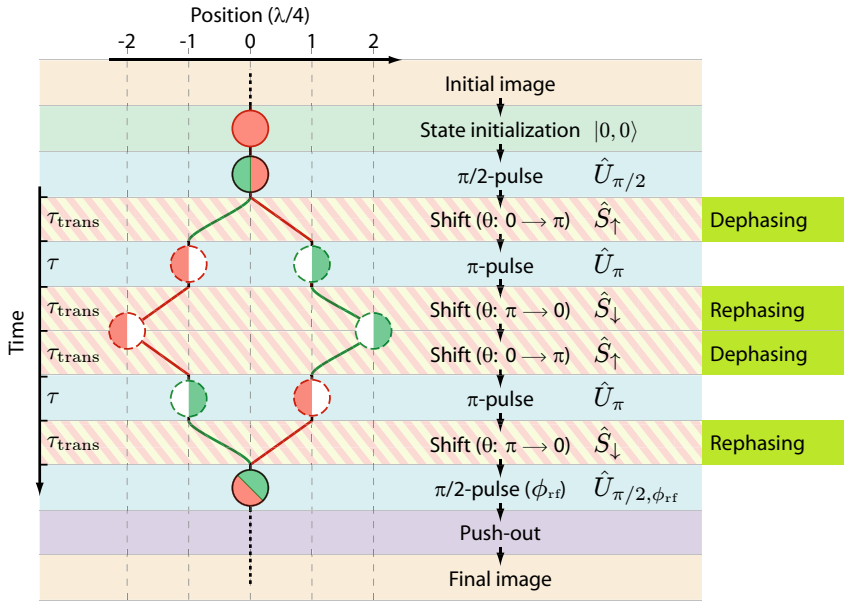

Figure 5.4.: Extended spin-echo atom interferometer sequence to probe spatial changes of external fields in the trapping region for distances of next-nearest lattice site. Symbols, paths and colors are identical to those in Fig. 5.1. π-pulses in the sequence rephase position-independent dephasing arising from both, the state-selective transport and free evolution of the phase. After being delocalized over the maximum preset distance both matter wave components are immediately remerged by reversing the order of the initially applied operators, see list on the right. Note that in the ideal case, at the position of maximal delocalization and just prior the recombination by the final $\pi/2$-pulse, all position-independent dephasing contributions are completely rephased.

simplicity, we redefine the shift operators $\hat{S}_{\uparrow}$ and $\hat{S}_{\downarrow}$ as

$$\hat{S}_{\uparrow}: \begin{cases} |0,k\rangle & \rightarrow & e^{i\chi^{(k,k+1)}_{|0\rangle,\mathbf{n}}}|0,k+1\rangle \\ |1,k\rangle & \rightarrow & e^{i\chi^{(k,k-1)}_{|1\rangle,\mathbf{n}}}|1,k-1\rangle \end{cases} \tag{5.11}$$

and

$$\hat{S}_{\downarrow}: \begin{cases} |0,k\rangle & \rightarrow & e^{i\chi^{(k,k-1)}_{|0\rangle,\mathbf{n}}}|0,k-1\rangle \\ |1,k\rangle & \rightarrow & e^{i\chi^{(k,k+1)}_{|1\rangle,\mathbf{n}}}|1,k+1\rangle \end{cases}, \tag{5.12}$$

where in contrast to Eqs. (4.43) and (4.44), the phase $\chi^{(k,k\pm1)}_{|j\rangle,\mathbf{n}}$ comprises both position-dependent and position-independent phase contributions, including the free phase evolution $\Phi(\tau_{\mathrm{trans}})$ and the contribution from state-dependent evolution of trapping frequencies and potential depth, see Sec. 5.1. The same is done for

the π-pulse operator

$$\hat{U}_\pi : \begin{cases} |0,k\rangle & \rightarrow & ie^{i\xi_{\mathbf{n}}^{(k)}}|1,k\rangle \\ |1,k\rangle & \rightarrow & ie^{-i\xi_{\mathbf{n}}^{(k)}}|0,k\rangle \end{cases} , \tag{5.13}$$

taking into account that position-dependent changes of $|0\rangle \leftrightarrow |1\rangle$ transition frequency lead to a finite detuning from the preset pulse frequency. Here, we restrict to detunings much lesser than the Rabi frequency which primarily affect the phase rather than population transfer efficiency between states $|0\rangle$ and $|1\rangle$. The effect of the latter on the Ramsey contrast is discussed in Sec. 5.2.2.

5.2.1. Accumulation of phase

To illustrate the process of phase accumulation in both interferometer arms defined by paths of the matter wave components, we first focus on a simple interferometer sequence in which atoms are temporarily delocalized over two next-nearest lattice sites ($2\lambda/2$), see Fig. 5.4. The starting point of this sequence is again a single atom initialized in $|0,0\rangle$ and prepared in a superposition state $\frac{1}{\sqrt{2}}(|0,0\rangle + i|1,0\rangle)$ using a $\pi/2$-pulse. After applying a sequence of operations, comprising a shift $\hat{S}_\uparrow$, a π-pulse $\hat{U}_\pi$ and finally a shift $\hat{S}_\downarrow$, we obtain

$$\begin{aligned} &\frac{1}{\sqrt{2}}(|0,0\rangle + i|1,0\rangle) \\ &\quad \xrightarrow{\hat{S}_\uparrow} \frac{1}{\sqrt{2}}(|0,1\rangle + ie^{-i\left[\chi_{|0\rangle,\mathbf{n}}^{(0,1)} - \chi_{|1\rangle,\mathbf{n}}^{(0,-1)}\right]}|1,-1\rangle) \\ &\quad \xrightarrow{\hat{U}_\pi} \frac{1}{\sqrt{2}}(|0,-1\rangle - ie^{i\left[\left(\chi_{|0\rangle,\mathbf{n}}^{(0,1)} - \chi_{|1\rangle,\mathbf{n}}^{(0,-1)}\right) - \left(\xi_{\mathbf{n}}^{(1)} - \xi_{\mathbf{n}}^{(-1)}\right)\right]}|1,1\rangle) \\ &\quad \xrightarrow{\hat{S}_\downarrow} \frac{1}{\sqrt{2}}(|0,-2\rangle - ie^{i\left[\left(\chi_{|0\rangle,\mathbf{n}}^{(0,1)} - \chi_{|1\rangle,\mathbf{n}}^{(0,-1)}\right) - \left(\chi_{|0\rangle,\mathbf{n}}^{(-1,-2)} - \chi_{|1\rangle,\mathbf{n}}^{(1,2)}\right) - \left(\xi_{\mathbf{n}}^{(1)} - \xi_{\mathbf{n}}^{(-1)}\right)\right]}|1,2\rangle) \\ &\quad =: |\psi_{\mathrm{del}}\rangle , \end{aligned} \tag{5.14}$$

where for the sake of clarity, global phases are factored out and ignored while remaining contributions have been ordered according to the qubit state. Particular attention should be paid to the alternating signs in the amplitudes and phases introduced by the rephasing π-pulse. After being delocalized over two next-nearest lattice sites, the atomic matter wave is immediately merged, i.e. the sequence is reversed by applying the respective operators in a reverse order, see Fig. 5.4. We obtain

$$|\psi_{\mathrm{del}}\rangle \xrightarrow{\hat{S}_\uparrow \hat{U}_\pi \hat{S}_\downarrow} \frac{1}{\sqrt{2}}(|0,0\rangle + ie^{i\Xi_{\mathrm{tot}}}|1,0\rangle) =: |\psi_{\mathrm{mer}}\rangle \tag{5.15}$$

with a total accumulated phase difference

$$\begin{aligned} \Xi_{\mathrm{tot}}(2) = &+ \left[(\chi_{|0\rangle,\mathbf{n}}^{(0,1)} + \chi_{|0\rangle,\mathbf{n}}^{(1,0)}) - (\chi_{|1\rangle,\mathbf{n}}^{(0,-1)} + \chi_{|1\rangle,\mathbf{n}}^{(-1,0)})\right] \\ &- \left[(\chi_{|0\rangle,\mathbf{n}}^{(-1,-2)} + \chi_{|0\rangle,\mathbf{n}}^{(-2,-1)}) - (\chi_{|1\rangle,\mathbf{n}}^{(1,2)} + \chi_{|1\rangle,\mathbf{n}}^{(2,1)})\right] . \end{aligned} \tag{5.16}$$

Note that in the absence of temporal drifts of experimental parameters, the phase contributions $\xi_{\mathbf{n}}^{(\pm 1)}$ arising from possibly detuned π-pulses ideally cancel out since each contribution appears twice but with a different sign in this sequence. Finally, a $\pi/2$-pulse with a preset Ramsey phase ϕ_{rf} recombines again both matter wave components and probes its accumulated phase difference, yielding a Ramsey fringe contribution of

$$P_{\mathrm{a},|1\rangle}(\phi_{\mathrm{rf}}) = |\langle 0,1|U_{\pi/2,\phi_{\mathrm{rf}}}|\psi_{\mathrm{mer}}\rangle|^2 = \frac{1}{2}\left\{1+\cos\left(\phi_{\mathrm{rf}}-\Xi_{\mathrm{tot}}(2)\right)\right\} . \tag{5.17}$$

The results obtained so far can be generalized to a sequence in which the matter wave is split and delocalized over $2K\lambda/2$ ($K \in \mathbb{N}_{>0}$) lattice sites before being subsequently merged and recombined at the initial lattice site. The contribution to the Ramsey fringe is then given by

$$P_{\mathrm{a},|1\rangle}(\phi_{\mathrm{rf}},2K) = \left|\langle 0,1|\hat{U}_{\pi/2,\phi_{\mathrm{rf}}}\hat{\mathcal{D}}_{2K}\hat{U}_{\pi/2}|0,0\rangle\right|^2 \tag{5.18}$$

$$= \frac{1}{2}\left\{1+\cos\left(\phi_{\mathrm{rf}}-\Xi_{\mathrm{tot}}(2K)\right)\right\} \tag{5.19}$$

with

$$\hat{\mathcal{D}}_{2K} = \left(\hat{S}_{\downarrow}\hat{U}_{\pi}\hat{S}_{\uparrow}\hat{U}_{\pi}\right)^{K}\left(\hat{U}_{\pi}^{-1}\hat{U}_{\pi}^{-1}\right)\left(\hat{U}_{\pi}\hat{S}_{\downarrow}\hat{U}_{\pi}\hat{S}_{\uparrow}\right)^{K}, \tag{5.20}$$

where the inverse operators $\hat{U}_{\pi}^{-1}$ ($\hat{U}_{\pi}^{-1}\hat{U}_{\pi}=1$) have been artificially introduced to shorten the notation. Note that there is no π-pulse between the end of the delocalization sequence and the beginning of the reverse process. By direct calculation, it can be shown that the accumulated phase difference is given by

$$\Xi_{\mathrm{tot}}(2K) = \sum_{k=0}^{2K-1}(-1)^k\left[(\chi_{|0\rangle,\mathbf{n}}^{(\sigma_k,\sigma_k')}+\chi_{|0\rangle,\mathbf{n}}^{(\sigma_k',\sigma_k)})-(\chi_{|1\rangle,\mathbf{n}}^{(-\sigma_k,-\sigma_k')}+\chi_{|1\rangle,\mathbf{n}}^{(-\sigma_k',-\sigma_k)})\right] \tag{5.21}$$

with the starting and final position index $\sigma_k=(-1)^k k$ and $\sigma_k'=(-1)^k(k+1)$, respectively.

In absence of temporal drifts of experimental parameters, all remaining phase contributions can be regarded as time-invariant. This means that, even though they depend on the transport time τ_{trans}, it is irrelevant at which time they appear in the sequence. In that case, according to Eq. (5.21), position-independent contributions to the phase cancel out, including those from the free evolution and those from shifting of atoms.[4] Consequently, it suffices to focus only on position-dependent contributions. The latter can be written as

$$\chi_{|j\rangle,\mathbf{n}}^{(\sigma_k,\sigma_k')} = \frac{1}{\hbar}\int_0^{\tau_{\mathrm{trans}}}\Delta\mathcal{U}_{|j\rangle,\mathbf{n}}(z_{|j\rangle}^{(\sigma_k,\sigma_k')}(t))\mathrm{d}t$$

$$+\frac{1}{\hbar}\int_0^{\tau_{\mathrm{trans}}}\left[\Delta\mathcal{U}_{|0\rangle,\mathbf{n}}(z_{|j\rangle}^{(\sigma_k,\sigma_k')}(t))-\Delta\mathcal{U}_{|1\rangle,\mathbf{n}}(z_{|j\rangle}^{(\sigma_k,\sigma_k')}(t))\right]\mathrm{d}t \tag{5.22}$$

[4] This fact becomes immediately obvious just by removing the position-dependent indices in Eq. (5.21).

with the energy difference

$$\Delta\mathcal{U}_{|j\rangle,\mathbf{n}}(z) = \mathcal{U}_{|j\rangle,\mathbf{n}}(z) - \mathcal{U}_{|j\rangle,\mathbf{n}}(0)\,, \tag{5.23}$$

and the position of the matter wave component during a shift from σ_k to σ_k', given by

$$z_{|j\rangle}^{(\sigma_k,\sigma_k')}(t) = \left[\sigma_k + (\sigma_k' - \sigma_k)s_{|j\rangle}(t)\right]\frac{\lambda}{4}\,, \tag{5.24}$$

where the shift is parameterized by a continuous function $s_{|j\rangle}(t)$, similar to that of Eq. (4.28).[5] The first term in Eq. (5.22) considers changes in the energy offset of each matter wave component in a state-selective trapping potential and a position-dependent environment, characterized by $\mathcal{U}_{|j\rangle,\mathbf{n}}(z)$. The second term, in turn, takes the evolution of the $|0\rangle \leftrightarrow |1\rangle$ transition frequency of each individual component into account.

Possible spatial inhomogeneities in external fields in the trapping region of our experimental setup are expected from magnetic field or light shift gradients. The latter, for instance, may be attributed to the intensity profile of the light field generated by two counterpropagating Gaussian beams, especially if the trapping region is displaced from the common focus, see Sec. 5.2.2. To demonstrate the effect of such gradients on the accumulated phase, for simplicity, we assume the slope of this gradient being constant over the trapping region, yielding a linear position-dependence of the energy contribution along the lattice axis

$$\mathcal{U}_{|j\rangle,\mathbf{n}}(z) = \beta_{|j\rangle} z \tag{5.25}$$

with an arbitrary constant $\beta_{|j\rangle} \in \mathbb{R}$. The resulting accumulated phase difference can be directly calculated. It is given by

$$\Xi_{\mathrm{tot}}(2K) = K^2(3\beta_{|0\rangle} - \beta_{|1\rangle})\frac{\lambda\tau_{\mathrm{trans}}}{\hbar}\,, \tag{5.26}$$

irrespective of the choice of the shift function $s_{|j\rangle}(t)$, as long as excitations between vibrational states are negligible. Consequently, it quadratically scales with K and thus with the maximum delocalization distance $2K\lambda/2$ between both matter wave components. Results for further basic energy contributions are listed in Tab. 5.1.

5.2.2. Experimental results

In the following, we experimentally investigate coherence properties of the interferometer sequence for different number of transport steps ($4K$) defining the delocalization distance ($2K\lambda/2$), and determine the accumulated phase difference between both matter wave components. To reveal temporary drifts of experimental parameters which may affect the $|0\rangle \leftrightarrow |1\rangle$ transition frequency, we apply this sequence for $K = \{1, 2, \ldots, 7\}$ in a random order. Since an interferometer sequence of $4K$

[5] $s_{|j\rangle} : [0, \tau_{\mathrm{trans}}] \to \mathbb{R}$ constrained by $s_{|j\rangle}(0) = 0$ and $s_{|j\rangle}(\tau_{\mathrm{trans}}) = 1$.

Energy contribution	Accumulated phase difference
$\mathcal{U}_{\|j\rangle,\mathbf{n}}(z) = \alpha_{\|j\rangle} = \text{const}$	$\Xi_{\text{tot}}(2K) = 0$
$\mathcal{U}_{\|j\rangle,\mathbf{n}}(z) = \beta_{\|j\rangle} z$	$\Xi_{\text{tot}}(2K) = K^2(3\beta_{\|0\rangle} - \beta_{\|1\rangle})\dfrac{\lambda\tau_{\text{trans}}}{\hbar}$
$\mathcal{U}_{\|j\rangle,\mathbf{n}}(z) = \gamma_{\|j\rangle} z^2$	$\Xi_{\text{tot}}(2K) = K^2(\gamma_{\|1\rangle} - \gamma_{\|0\rangle})\dfrac{\lambda^2\tau_{\text{trans}}}{4\hbar}$

Table 5.1.: Accumulated phase difference for basic energy contributions as obtained for the interferometer sequence of Eq. (5.20) for an arbitrary choice of shift function $s_{|j\rangle}(t)$.

transport steps comprises $2(2K-1)$ π-pulses, such drifts may not only affect the accumulated phase difference but also decrease the fringe contrast by reducing the population transfer efficiency of the π-pulses, see below. Finally, we check the reliability and reproducibility of our results by repeating our measurements on a random basis. To reduce errors in determining the accumulated phase difference, especially for Ramsey fringes with a low contrast, all fringes are recorded on an equidistantly sampled phase interval of $[0, 6\pi]$ comprising 50 sampling points, see Fig. 5.6(c). Each sampling point is measured on an atomic ensemble with on average 20 atoms using six repetitions.

Pulse amplitude or pulse duration errors in the initial and final $\pi/2$-pulse of the sequence do not only affect the amplitudes of delocalized matter wave components and their recombining, they also may suppress the measured fringe contrast. Analogous to Sec. 4.6, such errors can be represented by biased operators $\hat{U}_{\pi/2+\varepsilon}$ and $\hat{U}_{\pi/2+\varepsilon',\phi_{\text{rf}}}$ with $|\varepsilon| < \pi/2$ and $|\varepsilon'| < \pi/2$. For $\varepsilon \neq \varepsilon'$, the Ramsey fringe contrast of the interferometer sequence decreases by a factor of

$$C^{\text{err}}_{\pi/2} = \frac{\cos(\varepsilon)\cos(\varepsilon')}{1 - \sin(\varepsilon)\sin(\varepsilon')}\,. \tag{5.27}$$

Otherwise, in case of $\varepsilon = \varepsilon'$, it is $C^{\text{err}}_{\pi/2} = 1$, and the fringe contrast remains effectively unaffected, even if the fringe amplitude

$$A(2K) = \frac{1}{2}(\widetilde{P}_{|1\rangle,\text{max}}(2K) - \widetilde{P}_{|1\rangle,\text{min}}(2K)) \tag{5.28}$$

decreases by a factor of $A^{\text{err}}_{\pi/2} = \cos^2(\varepsilon)$. In other words, as long as both "$\pi/2$"-pulses of the sequence are identical, the fringe contrast does not depend on the amplitudes of the delocalized matter wave components which in turn define the balance between both interferometer arms. For practical reasons, however, large fringe amplitudes should be always preferred since they provide a better "signal-to-noise ratio" and thus simplify the subsequent analysis. Consequently, we aim to reduce pulse errors ε and ε' down to a marginal value.

Imperfect transfer efficiency of π-pulses, $\bar{P}_{|1\rangle}$, on the other hand, affects not only the rephasing process, but also the transport efficiency (see Sec. 4.5) and thus as

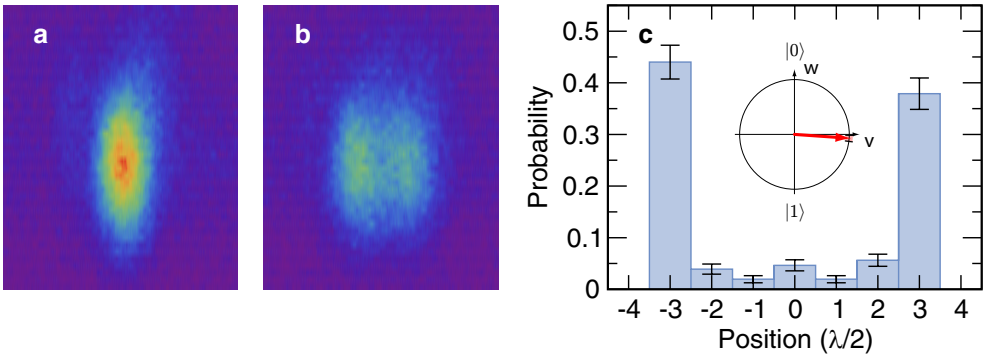

Figure 5.5.: Average over 50 initial (**a**) and final images (**b**) of atoms delocalized over $6\lambda/2$ lattice sites ($K = 3$). The respective probability histogram of relative positions (**c**) shows two dominant peaks at $\pm 3\lambda/2$, from which the pulse error ε and the balance between both interferometer arms can be inferred. Result of the erroneous pulse operation is indicated by the Bloch vector (red arrow) in the vw-plane of the Bloch sphere. For an ideal $\pi/2$-pulse the Bloch vector should coincide with the v-axis.

such, the probability to merge both matter wave components on the initial lattice site. It therefore imposes an upper limit on the fringe contrast, which can be estimated by

$$C(2K) \leq C_{\pi}^{\mathrm{err}}(2K) = (\bar{P}_{|1\rangle})^{4(2K-1)} \,. \tag{5.29}$$

For this reason, fine-aligning of both, pulse parameters and settling time of the state-selective transport require particular care, utilizing the entire spectrum of preparatory calibration measurements discussed in Sec. 4.5. The same applies for fine-alignment of the optimum transport time (see Sec. 5.1), taking into account, that the probability to excite an atom or its matter wave component to a different vibrational state increases with the number of transport steps. Here, we use a linear driving ramp (see Eq. (4.34)) with a measured optimum ramp time of $\tau_{\lambda/2} = 18.6\,\mu$s and a settling time of $\delta t = 2\,\mu$s, resulting in a total transport time for a single shift of $\tau_{\mathrm{trans}} = 20.6\,\mu$s. For a π-pulse duration of $\tau = 8\,\mu$s and $K \leq 7$, the time elapsed between splitting, delocalizing and recombining of the matter wave is still far below the elongated homogeneous dephasing time $\widetilde{T}_2'$ of a static lattice configuration, see Sec. 3.3.4. Thus, homogenous dephasing mechanisms already appearing in a static lattice configuration should only marginally affect coherence properties of the employed interferometer sequence.

To check the balance between both interferometer arms, infer the transport efficiency and the related population transfer efficiency of π-pulses in the dynamic configuration, in a preparatory measurement, we apply a truncated version of the interferometer sequence. In this sequence, both matter wave components are maximally delocalized but not merged on the initial lattice site. Instead, a fluorescence image is subsequently acquired, yielding a collapse of the delocalized matter wave to a single site of the optical lattice, ideally at a relative distance of $+K\lambda/2$ or

$-K\lambda/2$. From images acquired at the beginning and the end of the sequence, we determine the relative positions of the atoms, see Sec. 4.5.3.

In Figure 5.5(c) a probability histogram of relative positions in terms of lattice sites is exemplarily shown for $K = 3$. The histogram clearly reveals two dominant peaks of almost equal heights at the expected delocalization positions $\pm K\lambda/2$. The same becomes apparent just by averaging over all final fluorescence images centered at the initial position of the atoms, see Fig. 5.5(b). Both, the histogram and the averaged fluorescence images nicely demonstrate the splitting and delocalization of the matter wave over distances which can be resolved by our imaging optics (here $6\lambda/2 \approx 2.6\,\mu$m). Even though no conclusions regarding coherence of this process can be drawn from such a histogram, the $\pi/2$-pulse error ε or the balance between both interferometer arms can be directly deduced from the ratio of the measured probabilities P_{-2K} and P_{2K} (see Eq. (4.49)):

$$\varepsilon = \arcsin\left(\frac{P_{-2K} - P_{2K}}{P_{-2K} + P_{2K}}\right) . \tag{5.30}$$

From the probability histogram in Fig. 5.4(c), we deduce a $\pi/2$-pulse error of $\varepsilon = (0.07 \pm 0.05)$ providing a balance of 54 : 46 between the "negative" and "positive" interferometer arm. The pulse amplitude or pulse duration error is therefore sufficiently small, decreasing the fringe amplitude by only 0.5% assuming that the error of the final recombining $\pi/2$-pulse is identical.

The transport efficiency is given by the sum of probability contributions at $\pm K\lambda/2$ in the histogram. From this, the population transfer efficiency of the π-pulses can be estimated, using

$$\bar{P}_{|1\rangle} = (P_{-2K} + P_{2K})^{\frac{1}{2K-1}} . \tag{5.31}$$

Here, we obtain $\bar{P}_{|1\rangle} = (96 \pm 1)\%$, which agrees reasonably well with the value inferred in Sec. 4.6.

Once the transport efficiency and the balance between both interferometer arms is checked, we proceed with the main interferometer sequences, by recording Ramsey fringes for different delocalization distances $2K\lambda/2$. Some of them are exemplarily shown in Fig. 5.6(c). From each Ramsey fringe, we determine the fringe contrast $C(2K)$ and the fringe phase, corresponding the total accumulated phase difference $\Xi_{\mathrm{tot}}(2K)$, from a fit of

$$\widetilde{P}_{|1\rangle}(2K) = \frac{\widetilde{p}_{\mathrm{sur}}(\tau_{\mathrm{img}})}{2}\left\{1 + C(2K)\cos[\phi_{\mathrm{rf}} - \Xi_{\mathrm{tot}}(2K)]\right\} . \tag{5.32}$$

Note that in case of imbalanced interferometer arms, either intended or due to $\pi/2$-pulse errors, the survival probability $\widetilde{p}_{\mathrm{sur}}(\tau_{\mathrm{img}})$ inferred from a fit is biased. Its proper value is rather given by $p_{\mathrm{sur}}(\tau_{\mathrm{img}}) = \widetilde{p}_{\mathrm{sur}}(\tau_{\mathrm{img}})\{1 - \sin(\varepsilon)\sin(\varepsilon')\}$, supposed that both parameters ε and ε' are known. Since we are mainly interested in the fringe contrast and the phase, the biased survival probability can be regarded just as a free parameter of the fit.

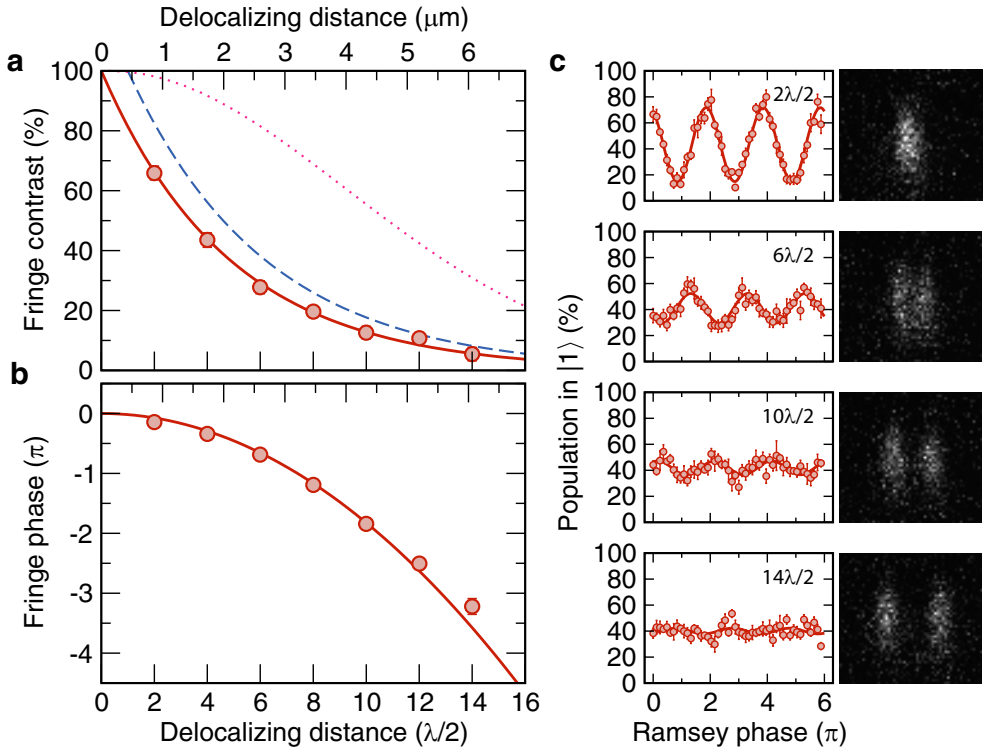

Figure 5.6.: (**a**) Fringe contrast of Ramsey fringes recorded for interferometer sequences with $K = \{1, 2, \ldots, 7\}$, corresponding to delocalization distances of $2K\lambda/2$. Some Ramsey fringes and the respective fits (solid lines) are exemplarily shown in (**c**). For illustration purposes, fluorescence images of two atoms separated by the respective delocalization distance are shown on the right side. The dotted line in (**a**) indicates the fringe contrast as inferred from the elongated homogeneous dephasing time $\widetilde{T}_2'$ in a static lattice configuration, see Sec. 3.3.4. The dashed line shows the upper limit of the contrast imposed by the probability to merge and recombine both matter wave components, see Eq. (5.29). The latter has been estimated from the measured transfer efficiency of the π-pulses. The solid line shows a fit of Eq. (5.33), from which the fraction of coherence after two transport steps is inferred. (**b**) Accumulated phase difference as inferred from the phase of the Ramsey fringes. Since the phase is a modulo 2π quantity, for fitting purposes, an offset of 2π and 4π is subtracted from the inferred values for $K = \{4, 5, 6\}$ and $K = 7$, respectively. The solid line shows a fit of Eq. (5.35), revealing a characteristic quadratic dependency.

In Figure 5.6(a,b), fit results of the fringe contrast and the accumulated phase difference are shown, both plotted as a function of maximum delocalization distance. As expected, the fringe contrast decreases with the delocalization distances, always remaining below the limit imposed by the probability to merge both matter wave components for imperfect π-pulses (see Eq. (5.29)) and the elongated coherence time $\widetilde{T}_2'$. We primarily attribute the additional decrease of fringe contrast

to excitations between axial vibrational states (homogeneous dephasing during the transport) and imperfect rephasing. The latter may be additionally affected by spatial inhomogeneities of environmental fields in the trapping region, see below. Both, the effect of excitation and imperfect rephasing cannot be distinguished from the fringe contrast alone. Modeling of the former turns out to be non-trivial, especially if both coherent and incoherent excitations over intermediate states are involved. For this reason, we abstain from a heuristic model of the fringe contrast. Instead, analogous to the pulse error model of Eq. (4.52), it appears obvious to assume the contrast to decrease progressively every second transport step

$$C_{\mathrm{tot}}(2K) = (C_{\mathrm{two}})^{2K}\,, \tag{5.33}$$

where C_{two} denotes the fraction of coherence after two transport steps. This quantity may be regarded as coherence fidelity of the state-selective transport for an even number of transport steps. For odd numbers of steps in turn, besides technical limitations (see Sec. 4.5), inhomogeneous dephasing of thermal atoms arising from different evolution of state-selective potentials during the shift would strongly suppress the fringe contrast, see Sec. 5.1. From a fit of Eq. (5.33) to the measured fringe contrast, we finally infer

$$C_{\mathrm{two}} = (81.3 \pm 0.3)\%\,. \tag{5.34}$$

Because the measured fringe contrast always refers to a delocalized *and* merged matter wave, its value at the maximum delocalization distance of both matter wave components is rather given by $\sqrt{C_{\mathrm{tot}}(2K)}$. From this, we infer a fraction of coherence of 23% at a delocalization distance of $14\lambda/2 \approx 6\,\mu$m, whereas for $10\lambda/2 \approx 4\,\mu$m, even a fraction of $36\% \approx 1/e$ is obtained. Since the latter value has been used to define our dephasing times (see Sec. 3.3), following this convention, our measurement reveals a coherent splitting and delocalization of a single atom matter wave over distances of up to 10 lattice sites. This fact should be kept in mind in the context of the quantum walks, see Chap. 6.

The total accumulated phase difference on the other hand, reveals a quadratic dependency on the delocalization distance, see Fig. 5.6(b). At first sight, according to preliminary considerations summarized in Tab. 5.1, such trend indicates spatial differences in the trapping region with at least a linear position-dependency of the relevant energy contributions. From a fit of

$$\Xi_{\mathrm{tot}}(2K) = aK^2 \tag{5.35}$$

to the measured fringe phase, we infer $a = -(0.206 \pm 0.007)$, yielding

$$(3\beta_{|0\rangle} - \beta_{|1\rangle})/\hbar = -2\pi \times (1.83 \pm 0.06)\,\mathrm{kHz}/\mu\mathrm{m}\,. \tag{5.36}$$

This value, however, is too large to be solely attributed to spatial gradients of the light field or magnetic field in the trapping region, see below. Irrespective of this fact, in the following, we list and specify some possible contributions which can in principle be investigated using the above interferometer sequence.

Magnetic field gradient along the lattice axis Suppose there is a magnetic field gradient B'_z along the optical lattice axis, which is permanently present during the entire interferometer sequence. Its position-dependent energy contributions to the accumulated phases in Eq. (5.22) can be written as

$$\mathcal{U}_{|j\rangle,\mathbf{n}}(z) = \beta_{|j\rangle} z + \delta_{j,0}\hbar\omega_0 \tag{5.37}$$

with

$$\beta_{|j\rangle} = \mu_\mathrm{B} g_{4-j} B'_\mathrm{z}\,, \tag{5.38}$$

where g_3 and g_4 denote the Landé factors for the $F = 3$ and $F = 4$ ground states, respectively, and μ_B the Bohr magneton. Assuming that the result in Eq. (5.36) is solely attributed to this field gradient, its strength would be given by $B'_\mathrm{z} = -(3.5 \pm 0.1)\,\mathrm{G/cm}$, which turns out to be too large to be unnoticed otherwise. Such gradient would result in a position-dependent $|0\rangle \leftrightarrow |1\rangle$ transition frequency in the trapping region with $\omega'(z)/2\pi = (0.86 \pm 0.02)\,\mathrm{kHz}/\mu\mathrm{m}$, see e.g. Sec. 3.4.1. Therefore, it would be rather noticed in a broadening of any preparatory microwave spectrum, while significantly decreasing its maximum population in state $|1\rangle$. We conclude from this fact that a magnetic field gradient cannot solely explain the measured difference in accumulated phase.

Light shift gradient along the lattice axis Suppose the trapping region does not coincide with the position of the waist w_0 of both superimposed counterpropagating Gaussian beams, generating the optical lattice, but is axially offset by a distance Δz. Depending on this offset, the divergence of the Gaussian beams may yield a noticeable intensity gradient of the light field in the trapping region. This gradient directly translates into a position-dependent light shift, affecting both, the trap depth and the trapping frequencies. To estimate the effect of such gradient, we first restrict to the dominant contribution — the trap depth, the position-dependency of which can be written as

$$U_{0,|j\rangle}(z) = U_{0,|j\rangle}\frac{w_0^2}{w^2(z+\Delta z)} = \frac{U_{0,|j\rangle}}{1+(z+\Delta z)^2/z_0^2} \tag{5.39}$$

$$\approx \underbrace{\frac{U_{0,|j\rangle}}{1+\Delta z^2/z_0^2}}_{=:\alpha_{|j\rangle}} + \underbrace{\frac{-2U_{0,|j\rangle}\Delta z}{(1+\Delta z^2/z_0^2)^2}}_{=:\beta_{|j\rangle}}\cdot z\,, \tag{5.40}$$

where $U_{0,|j\rangle}$ denotes the depth at the waist and z_0 the Rayleigh length. Furthermore, we have used a Taylor series expansion, employing $z \ll z_0$, so that the position-dependent energy contribution can be written in the well-known from

$$\mathcal{U}_{|j\rangle,\mathbf{n}}(z) = \alpha_{|j\rangle} + \beta_{|j\rangle} z + \delta_{j,0}\hbar\omega_0\,. \tag{5.41}$$

According to Tab. 5.1, only the linear term contributes to the total accumulated phase difference. For perfectly overlapping Gaussian beams, a maximum slope in the intensity gradient is expected at $\Delta z = \pm z_0/\sqrt{3}$, yielding

$$\left|(3\beta_{|0\rangle} - \beta_{|1\rangle})/\hbar\right| < 2\pi \times 1.5\,\mathrm{kHz}/\mu\mathrm{m} \tag{5.42}$$

for typical experimental parameters of the interferometer sequence. Hence, irrespective of the axial displacement, the measured value in Eq. (5.36) cannot be reached. By incorporating state-selective potential dynamics in the calculation, including vibrational contributions with position-dependent axial and radial trapping frequencies

$$\Omega_{\mathrm{ax},|j\rangle}(z) = \Omega_{\mathrm{ax},|j\rangle}\frac{w_0}{w(z+\Delta z)}\,, \tag{5.43}$$

$$\Omega_{\mathrm{rad},|j\rangle}(z) = \Omega_{\mathrm{rad},|j\rangle}\frac{w_0^2}{w^2(z+\Delta z)}\,, \tag{5.44}$$

analogue to the dephasing model of Eq. (5.3), the deviation from the measured value becomes even larger. Furthermore, in the presence of a light field gradient, dephasing arising from state-selective transport becomes position-dependent, and thus for this reason alone, it cannot be fully reversed by rephasing π-pulses in the interferometer sequence. Consequently, the Ramsey contrast is expected to decrease. For the maximum intensity gradient at $\Delta z = \pm z_0/\sqrt{3}$, our simulations provide a Ramsey contrast which is inconsistent with the measured data, falling far below the measured values. Irrespective of this fact, similar to the magnetic field gradient, such intensity gradient would be rather noticed in any preparatory microwave spectrum. Therefore, axial displacement of the trapping region from the position of the beam waist and the resulting intensity gradient cannot solely explain the measured difference in the accumulated phase.

Gravity in a tilted optical lattice Another eligible external field, which in principle may contribute to the measured phase difference, is earth's gravity. Even though this field does not affect the $|0\rangle \leftrightarrow |1\rangle$ transition frequency, for an optical lattice, whose axis is not perpendicular to the field direction, but tilted by an angle φ, it provides a phase difference between both components of the delocalized matter wave. The respective energy contribution can be written as

$$\mathcal{U}_{|j\rangle,\mathbf{n}}(z) = \beta_{|j\rangle} z + \delta_{j,0}\hbar\omega_0 \tag{5.45}$$

with

$$\beta_{|j\rangle} = m_{\mathrm{Cs}} g \sin\phi\,, \tag{5.46}$$

where m_{Cs} denotes the mass of the atom and g the local acceleration due to gravity. Suppose that the result in Eq. (5.36) is solely attributed to the tilted optical lattice, we would deduce a tilt angle of $\phi = -(16.1 \pm 0.5)^\circ$. Such tilt angle, however, is unrealistic, not least by the limited optical access. Since all mounting elements for the lattice beams optics are fixed to a preset height of 5 cm above the optical table, the optical lattice axis can be assumed to be parallel to the table. The latter in turn is well balanced by a spirit level. From a geometrical estimation, a maximum reasonable tilt angle of $\pm 2^\circ$ is inferred. Consequently, gravity cannot solely explain the measured difference

in the accumulated phase. It should be noted, that gravity neither affects the $|0\rangle \leftrightarrow |1\rangle$ transition frequency of both matter wave components nor the dephasing or rephasing process. Therefore, unlike the above field gradients, its contribution cannot be noticed in a microwave spectrum or a decrease of Ramsey contrast.

In summary, from the quantitative analysis, it can be stated that non of the discussed field gradients can solely explain the accumulated phase difference shown in Fig. 5.6. Furthermore, since for all discussed field gradients the phase difference depends quadratically on the delocalization distance, their individual contributions cannot be distinguished from the phase alone. Therefore, further investigations are required, which aim to clarify and identify the origin of the measured phase, especially for applications requiring full control over the phase.

There are some characteristic features which may be solely attributed to a certain class of field gradients: Field gradients which spatially change the trap parameters may noticeably affect the Ramsey contrast, since they disturb the rephasing process in our sequence. The same applies for field gradients which introduce a significant spatial change of the $|0\rangle \leftrightarrow |1\rangle$ transition frequency and thus a spatial detuning from the initial preset pulse frequency. They would decrease the contrast due to a reduced population transfer efficiency of the rephasing π-pulse, see Eq. (5.29).

In general, high-precision atom interferometers are highly customized, i.e. designed from scratch to measure only one selected field gradient while being shielded or compensated against other fields [153]. Our single atom interferometer, in turn, can be regarded as an versatile but open system, which may suffer from systematical drifts, see below. Therefore, it is only suited to deduce the fields of interest from relative changes of the respective parameters, assuming that remaining (unshielded) contributions are constant over the course of the measurement. The local gravity, for instance, could be deduced from the dependency of $\beta_{|j\rangle}$ on the tilt angle ϕ. Similar applies for magnetic field gradients, the strength of which can be tuned by external coils.

Drifts of experimental parameters

So far temporal drifts of experimental parameters affecting the trapped atoms have been neglected, allowing us to derive simple analytical expressions for the accumulated phase difference of the interferometer sequence. However, such drifts can never be completely excluded and may indeed indistinguishably affect the measured phase. In the worst case, they can even provide a quadratic dependency of accumulated phase difference on the delocalization distance $2K\lambda/2$, and thus be wrongly assigned to a spatial field gradient in the trapping region. While random long-term drifts of experimental parameters can be identified by checking the reproducibility of the measured data at certain time intervals and thus excluded for the obtained results, contributions from systematical drifts, i.e. those which are reproducible in each iteration of the interferometer sequence are indistinguishable from other

contributions to the measured phase, unless these drifts can be noticed otherwise.

The only reasonable systematical drift with a well-defined dependency on the number of transport steps and thus the transport distance is expected from the polarization control setup. Suppose that the overlap of both orthogonally circularly polarized standing waves during application of rephasing pulses decreases with the number of transport steps (e.g. due to a drifting offset voltage of the high-voltage amplifier). Then, the $|0\rangle \leftrightarrow |1\rangle$ transition frequency is expected to shift from one transport step to another. In that case, each *detuned* π-pulse would introduce an additional phase contribution which would not be cancelled anymore. Such stepwise changing detuning, however, would also affect the population transfer efficiency and the rephasing properties of the microwave pulses which would be rather noticed in the measured Ramsey contrast. Our simulations reveal that it is impossible to model a "drift function" which can reproduce both, the measured fringe contrast and the accumulated phase difference of Fig. 5.6. Furthermore, using microwave spectroscopy in dynamic configuration, similar to that for adjusting the settling time and the half-wave voltage of the EOM (see Sec. 4.5.2), we have checked that the polarization purity and the transition frequency is identical in each step of the sequence.

5.3. Conclusion

In this chapter, I have investigated coherence properties of the state-selective transport using two types of single atom interferometer sequences: A Ramsey-type sequence comprising splitting and delocalization of atomic matter wave components over two neighboring lattice sites, and its spin-echo extended version which uses a rephasing π-pulse to reverse inhomogeneous dephasing including that from state-selective transport of thermal atoms. I have introduced a simplified dephasing model which takes the different potential dynamics during the transport into account. This model sufficiently captures the dominant inhomogeneous dephasing mechanisms of the state-selective transport and reasonably explain the measured Ramsey contrast in regions in which other decoherence sources are negligible. Two approaches to overcome or decrease inhomogeneous dephasing during the transport have been proposed.

By extending the Ramsey-type sequence by a spin-echo, I have demonstrated that shift-induced inhomogeneous dephasing can be in principle reversed. The resulting atom interferometer sequence is then sensitive to irreversible homogeneous dephasing. By comparing calculated excitation probabilities to the measured data, I have shown that excitation between axial vibrational states during the state-selective transport disturb interference between two initially delocalized matter wave components and the rephasing process giving rise to homogeneous dephasing. The spin-echo sequence is therefore ideally suited to experimentally determine optimum ramp times in which such excitations are marginal.

Finally, I have investigated coherence properties of a two-arm single atom inter-

ferometer in which matter wave components of a single atom are delocalized over distances of up to $6\,\mu$m and subsequently merged on the initial lattice site. This interferometer sequence can be used to probe spatial differences in external fields in the trapping region. I have investigated the effect of experimental imperfections on the measured Ramsey contrast. From the latter, a coherence fidelity of the state-selective transport for an even number of transport steps has been inferred. Our measured data reveal a coherent splitting and delocalization of a single atom over distances of up to $10\lambda/2 \approx 4\,\mu$m lattice sites with a coherence fraction of $1/e \approx 36\%$. Furthermore, the measured accumulated phase difference between matter wave components quadratically scales with the maximum delocalization distance or the number of transport steps. I have derived analytical expressions for the accumulated phase difference, showing that already a linear energy gradient along the lattice axis may explain the measured scaling. A list of possible energy gradients has been compiled and discussed in detail, albeit non of the them can solely explain the measured phase difference. Further investigations are thus required to clarify and identify the origin of this phase difference. For this purpose, two possible directions should be followed in the future: First, the contribution of possible excitations between vibrational states to the accumulated phase difference should be investigated in detail. Suppose that each of the two delocalized matter wave components changes its vibrational state during the interferometer sequence. Then, if both of them end up in the same vibrational state or in a superposition of vibrational states with a final overlap before being recombined, we expect a systematical contribution to the measured Ramsey phase. Since excitation processes are expected to gradually increase with the number of transport steps they may indeed introduce a quadratic scaling of the accumulated phase difference even for a thermal ensemble of atoms. To theoretically check this hypothesis, an extended model incorporating both, coherent and incoherent excitation processes is required. It would be also preferable to repeat the interferometer measurements with atoms cooled to the motional ground state. By this, potential models could be simplified while the number of model parameters reduced. Second, we should look for potential geometrical phases which are also referred to as Berry phases [155].

6. Quantum walks in position space

Interference phenomena with microscopic particles are a direct consequence of their quantum-mechanical wave nature [156–160]. The prospect to fully control quantum properties of atomic systems has stimulated ideas to engineer quantum states that would be useful for applications in quantum information processing, for example, and also would elucidate fundamental questions, such as the quantum-to-classical transition [161]. A prominent example of state engineering by controlled multipath interference is the quantum walk of a particle [3, 4]. Its classical counterpart, the random walk, is relevant in many aspects of our lives, providing insight into diverse fields: It forms the basis for algorithms [8], describes diffusion processes in physics or biology [8, 10], such as Brownian motion, or has been used as a model for stock market prices [11]. Similarly, the quantum walk is expected to have implications for various fields, for instance, as a primitive for universal quantum computing [5], systematic quantum algorithm engineering [50], or for deepening our understanding of the efficient energy transfer in biomolecules for photosynthesis [162].

Quantum walks have been proposed to be observable in several physical systems [50, 163, 164]. Special realizations have been reported in either the populations of nuclear magnetic resonance samples [165, 166] or in optical systems, in either frequency space of a linear optical resonator [167], with beam splitters [168], or in the continuous tunneling of light fields through waveguide lattices [169]. Recently, quantum walks in the phase space of trapped ions have been reported [51, 52]. However, the coherent walk of an individual quantum particle in position space with controllable internal states, as originally proposed by Feynman [170], has so far not been observed.

In this chapter, I present the experimental realization of such a single quantum particle walking in a one-dimensional lattice in position space. This basic example of a walk provides all of the relevant features necessary to understand the fundamental properties and differences of the quantum and classical regimes. For example, the atomic wave function resulting from a quantum walk exhibits delocalized coherence, which reflects the underlying quantum interference. Simultaneous detection of internal state and the atomic position in the lattice by our imaging techniques allows for local quantum state tomography of the wave function. This is an important requirement to realize applications in quantum information science, such as the quantum cellular automaton [17, 18, 171].

6.1. Random walk and quantum walk on a line

The quantum walk is a quantum mechanical analogue of the classical random walk with remarkably different properties [3, 4], which arise from its particular ability of quantum interference. This characteristic ability is primarily used to design quantum algorithms which mostly outperform their classical counterparts for the same problem [7, 172]. Both, random and quantum walks can be defined either in continuous or discrete time. An overview of the distinct types of walks and their properties can be found in Ref. [173] and references therein. Throughout this chapter, we only focus on a subclass of walks, namely random and quantum walks in discrete time on a line. We shortly introduce both walks, highlight their substantial differences and compile their characteristic properties and quantities, which will be used later to discuss experimental results.

6.1.1. Random walk on a line

Consider an infinite line with allowed integer positions $k \in \mathbb{Z}$ and a particle — the "walker", which is initially located at position $k_0 = 0$. In the classical random walk on a line, a coin is tossed in each time step. Depending on the outcome (heads or tails), the walker takes one step to the left or to the right. Let p_c be the probability of tossing head, and $1-p_\mathrm{c}$ the probability of tossing tail, accordingly. After N time steps, the probability $P_N^\mathrm{R}(k)$ of finding the walker at a certain position k on the line follows then a binomial distribution

$$P_N^\mathrm{R}(k) = \begin{cases} \binom{N}{\frac{1}{2}(N+k)} p_\mathrm{c}^{\frac{1}{2}(N+k)} (1-p_\mathrm{c})^{\frac{1}{2}(N-k)} & \text{for} \quad \frac{1}{2}(N+k) \in \{0, 1, \dots N\}\,, \\ 0 & \text{else}\,, \end{cases} \tag{6.1}$$

with an expectation value (mean) $E(N) = (2p_\mathrm{c} - 1)N$ and a variance $\sigma^2(N) = 4p_\mathrm{c}(1-p_\mathrm{c})N$. Note that if N is even (odd), only even (odd) positions are occupied.

For a fair (unbiased) coin, $p_\mathrm{c} = 1/2$, the probability distribution in Eq. (6.1) becomes symmetric, i.e. $P_N^\mathrm{R}(-k) = P_N^\mathrm{R}(k)$, with $E(N) = 0$ and $\sigma^2(N) = N$. The standard deviation of this distribution is thus $\sigma(N) = \sqrt{N}$, implying a spreading time of the walk proportional to $\sqrt{N}$. The most probable position of the walker after N time steps is its initial position, whereas the probability of finding the walker at a distance of order N from the origin decreases exponentially with N. Furthermore, it can even be shown that for this particular one-dimensional random walk the walker returns with probability 1 to its initial position and hence to every possible position infinitely many times, if the random walk continues indefinitely. We refer this particular walk as *symmetric* random walk.

The random walk is obviously a stochastic process. It is also a Markov chain, i.e. each step depends only upon the immediately previous step, and not on any of the earlier steps [12].

6.1.2. Quantum Walk on a line

In a quantum-mechanical analogue of the classical random walk on a line, the quantum walker evolves in a coherent superposition of going to the left or to the right. Since quantum mechanics requires this evolution to be deterministic and unitary, an internal state has to be added to the walker [174], providing an additional degree of freedom, which can be used to control the system. Regarding our experimental system, we consider the walker to be a two-level quantum particle with internal qubit basis states $|0\rangle$ and $|1\rangle$ spanning the Hilbert space $\mathcal{H}_{\text{qbit}} = \mathbb{C}^2$. The walker is moving in position space on an infinite line with allowed integer positions, e.g. sites of an optical lattice. The corresponding total Hilbert space of its states is thus given by $\mathcal{H}_{\text{ext}} = \mathcal{H}_{\text{qbit}} \otimes \mathcal{H}_{\text{pos}}$ with $\mathcal{H}_{\text{pos}} = l_2(\mathbb{Z})$ spanned by position basis states $\{|k\rangle | k \in \mathbb{Z}\}$, see Sec. 4.5.1. In this Hilbert space, the quantum walk can be described as follows:
Consider the quantum walker to be initially located at position k_0 and prepared in a general qubit state $|\psi_0\rangle$ (not necessarily a basis state), resulting in an initial state $|\Psi_0\rangle = |\psi_0\rangle \otimes |k_0\rangle$ on $\mathcal{H}_{\text{ext}}$. Analogous to the random walk, in every time step of the quantum walk, the unitary coin operator $\hat{C}$, which acts on $\mathcal{H}_{\text{qbit}}$ and takes on the coin toss of its classical counterpart, brings each qubit basis state into a coherent superposition of the two states. Each coin operation is subsequently followed by a conditional shift, the unitary operator of which is defined by[1]

$$\hat{S} : \begin{cases} |0,k\rangle & \rightarrow & |0,k+1\rangle \\ |1,k\rangle & \rightarrow & |1,k-1\rangle \end{cases} , \tag{6.2}$$

moving the walker in state $|0\rangle$ ($|1\rangle$) one step to the right (left) or delocalizing its matter wave components and thus entangling the internal state with the position of the walker. Finally, after N time steps, the quantum state of the walker reads

$$|\Psi_N\rangle = [\hat{S}(\hat{C} \otimes \hat{\mathbb{1}})]^N |\Psi_0\rangle . \tag{6.3}$$

The probability of observing the walker at position k is then given by

$$P_N^{\text{Q},|\Psi_0\rangle}(k) = \langle \Psi_N | \hat{P}_k | \Psi_N \rangle \tag{6.4}$$

with $\hat{P}_k = |0,k\rangle\langle k,0| + |1,k\rangle\langle k,1|$.

To expose the differences between the quantum walk and its classical counterpart, we illustrate its evolution for few time steps with a concrete example:
Consider the walker in a qubit state $|\psi_0\rangle = |0\rangle$, which is initially located at position $k_0 = 0$, i.e. $|\Psi_0\rangle = |0,0\rangle$. From the variety of unitary coin operators acting on $\mathcal{H}_{\text{qbit}}$, we chose a frequently used, unbiased coin — the so-called Hadamard coin, which is defined by

$$\hat{C}_{\text{H}} : \begin{cases} |0\rangle & \rightarrow & \frac{1}{\sqrt{2}}(|0\rangle + |1\rangle) \\ |1\rangle & \rightarrow & \frac{1}{\sqrt{2}}(|0\rangle - |1\rangle) \end{cases} . \tag{6.5}$$

[1] Here, again a short-hand notation of the product states $|j,k\rangle \equiv |j\rangle \otimes |k\rangle \in \mathcal{H}_{\text{ext}}$ ($j = \{0,1\}$) is used.

Random walk

N \ k	-6	-5	-4	-3	-2	-1	0	1	2	3	4	5	6
0							1						
1						$\frac{1}{2}$		$\frac{1}{2}$					
2					$\frac{1}{4}$		$\frac{1}{2}$		$\frac{1}{4}$				
3				$\frac{1}{8}$		$\frac{3}{8}$		$\frac{3}{8}$		$\frac{1}{8}$			
4			$\frac{1}{16}$		$\frac{1}{4}$		$\frac{3}{8}$		$\frac{1}{4}$		$\frac{1}{16}$		
5		$\frac{1}{32}$		$\frac{5}{32}$		$\frac{5}{16}$		$\frac{5}{16}$		$\frac{5}{32}$		$\frac{1}{32}$	
6	$\frac{1}{64}$		$\frac{3}{32}$		$\frac{15}{64}$		$\frac{5}{16}$		$\frac{15}{64}$		$\frac{3}{32}$		$\frac{1}{64}$

Quantum walk

N \ k	-6	-5	-4	-3	-2	-1	0	1	2	3	4	5	6
0							1						
1						$\frac{1}{2}$		$\frac{1}{2}$					
2					$\frac{1}{4}$		$\frac{1}{2}$		$\frac{1}{4}$				
3				$\frac{1}{8}$		$\frac{1}{8}$		$\frac{5}{8}$		$\frac{1}{8}$			
4			$\frac{1}{16}$		$\frac{1}{8}$		$\frac{1}{8}$		$\frac{5}{8}$		$\frac{1}{16}$		
5		$\frac{1}{32}$		$\frac{5}{32}$		$\frac{1}{8}$		$\frac{1}{8}$		$\frac{17}{32}$		$\frac{1}{32}$	
6	$\frac{1}{64}$		$\frac{5}{32}$		$\frac{5}{64}$		$\frac{1}{8}$		$\frac{13}{64}$		$\frac{13}{32}$		$\frac{1}{64}$

Figure 6.1.: Left: Probability of finding the walker at position k after N time steps of the classical, symmetric random walk on the line starting in $k = 0$. Empty fields indicate zero probability. **Right:** The respective probability of a quantum walk using a Hadamard coin and starting with the initial state $|\Psi_0\rangle = |0, 0\rangle$. Shaded fields indicate deviations of the probabilities from the classical counterpart.

Then, the quantum state of the walker for the first three time steps reads

$$|\Psi_1\rangle = \frac{1}{\sqrt{2}} \left(|1, -1\rangle + |0, 1\rangle\right) , \tag{6.6a}$$

$$|\Psi_2\rangle = \frac{1}{\sqrt{2}} \left(-|1, -2\rangle + |1, -2\rangle + |0, 0\rangle + |1, 0\rangle + |0, 2\rangle\right) , \tag{6.6b}$$

$$|\Psi_3\rangle = \frac{1}{2\sqrt{2}} \left(|1, -3\rangle - |0, -1\rangle + 2|0, 1\rangle + |1, 1\rangle + |0, 3\rangle\right) . \tag{6.6c}$$

The corresponding spatial probability distributions are listed in Fig. 6.1 up to the sixth time step and compared to the respective distributions of the classical symmetric random walk.

After the first step, the probability of finding the walker at $k = \pm 1$ is given by $P_1^{\mathrm{Q},|0,0\rangle}(\pm 1) = 1/2$, and thus identical to that of the symmetric random walk, see Eq. (6.1). The same applies for the second step, i.e. $P_2^{\mathrm{Q},|0,0\rangle}(k) = P_2^{\mathrm{R}}(k)$ for all $k \in \mathbb{Z}$. After the third step, however, the distribution induced by the quantum walk partly differs from the classical one, due to quantum interference, which affects the walk for the first time: Two initially delocalized parts of the walker are recombined at a common position ($k = 0$). Being in different internal states, they cannot interfere. The next coin operator, however, deterministically mixes the internal states and removes the which-way information, which gives rise to quantum interference of the two overlapping parts. Further steps result in a multipath interference, which then alters the properties of the quantum walk as compared to the classical random walk.

One of these characteristic and distinguishing properties is the influence of internal states on the quantum walk. While the spatial probability distribution of

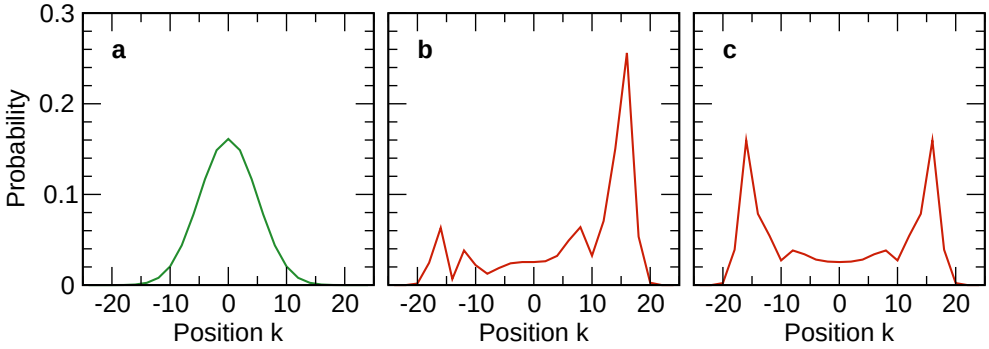

Figure 6.2.: (**a**) Probability distribution $P_N^{\mathrm{R}}(k)$ of a symmetric random walk starting at $k_0 = 0$ after $N = 24$ time steps, plotted only at the even points, since the odd points have probability zero. (**b**) The respective probability distribution $P_N^{\mathrm{Q},|\Psi_0\rangle}(k)$ of a quantum walk with Hadamard coin starting in $|\Psi_0\rangle = |0,0\rangle$, and (**c**) in $|\Psi_0\rangle = \frac{1}{\sqrt{2}}(|0,0\rangle + i|1,0\rangle)$. The latter initial state yields a symmetric distribution, see text.

the random walk is fully determined by the balance of the coin (see Eq. (6.1)), the quantum walk distribution depends also on the initial qubit state $|\psi_0\rangle$ of the walker and can be either strongly asymmetric, as shown in our example (see Fig. 6.1 and 6.2(b)) or symmetric for one and the same coin operator, see Fig. 6.2(c). In case of the Hadamard coin, the asymmetry for $|\psi_0\rangle = |0\rangle$ arises from a different treatment of the qubit basis states [4], multiplying the phase by -1 only in the case of $|1\rangle$ (see Eq. (6.6)), and thus inducing more cancellations for paths going rightwards (destructive interference), whereas particles moving to the left interfere constructively. A symmetric distribution is obtained using the initial qubit state $|\psi_0\rangle = \frac{1}{\sqrt{2}}(|0\rangle + i|1\rangle)$. In this particular case, the contributions from the qubit state $|0\rangle$ to the walker's state remain real, whereas those from $|1\rangle$ are purely imaginary. Hence, they do not interfere with each other. The total probability distribution is then given by the sum of the individual distributions, i.e. $P_N^{\mathrm{Q},|\Psi_0\rangle}(k) = \frac{1}{2}[P_N^{\mathrm{Q},|0,0\rangle}(k) + P_N^{\mathrm{Q},i|1,0\rangle}(k)]$. Because of $P_N^{\mathrm{Q},|0,0\rangle}(k) = P_N^{\mathrm{Q},i|1,0\rangle}(-k)$, this distribution is symmetric as shown in Fig. 6.2(c).

Besides the influence on the initial qubit state, there are further characteristic properties which distinguish the quantum walk from its classical counterpart. In particular, the standard deviation of the probability distribution of a quantum walk scales proportional to N, as in a ballistic transport, in contrast to the diffusive $\sqrt{N}$ scaling of the random walk, see Sec. 6.1.1. Consequently, the quantum walk propagates quadratically faster. Furthermore, in the symmetric case, it spreads roughly uniformly over the positions in the interval $[-N/\sqrt{2}, N/\sqrt{2}]$ as shown in Ref. [175], whereas the symmetric random walk is peaked at the initial position. Unlike the classical random walk, the quantum walk is fully deterministic and unitary. Hence, the multipath interference can be in principle reversed by inverting coin and shift operations, see Sec. 6.3.3.

Finally, it should be noted that neither the random walk nor the quantum walk on the line are restricted to a single particle, a single coin or position space. Quantum walks on a line, for instance have been also investigated for two entangled particles [52, 176], a sequence of different coins [177] or in frequency space [51, 52, 163]. All of them provide signatures of quantum interference, deterministic and unitary evolution in time and noticeable differences in probability distributions or related quantities compared to their classical counterparts. We will focus on these key properties in the investigation of experimental results of our quantum walk.

6.2. Experimental realization

The first proposal to implement a discrete time quantum walk on a line using neutral atoms in state-selective optical lattices appeared in 2002 [50]. In contrast to other proposals at that time, which relied on ion traps [163] and microwave cavities [178], it provided a quantum walk in position space as originally proposed by Feynman [170] and augured implementations with up to several hundred steps. Being able to determine positions of atoms in an optical lattice, coherently manipulate their internal states, and finally, coherently and state-selectively shift the atoms from one lattice site to another, all ingredients are in principle available to implement such a walk. However, technical limitations, decoherence and experimental imperfections require modifications of the originally proposed sequence, resulting in some deviations from the previously presented textbook example.

6.2.1. Effect of limitations imposed by the state-selective transport

Our realization of a quantum walk mainly faces two problems, both arising from our implementation of the state-selective transport, which takes over the role of the conditional shift: The first problem arises from the state-dependent shift dynamics, resulting in a state-dependent accumulation of phases of the matter wave components, which need to be given special consideration. The second problem arises from the polarization of the retro-reflected beam forming the optical lattice, which cannot be rotated infinitely, see Sec. 4.5. Hence, instead of only one, two shift operators $\hat{S}_\uparrow$ and $\hat{S}_\downarrow$, defined in Eqs. (4.43) and (4.44), respectively, need to be alternately applied in a quantum walk sequence. Under certain circumstances, both problems may affect the quantum state and the probability distribution of a walk, significantly changing its sensitivity to inhomogeneous dephasing as discussed in Sec. 5.1.1.

Suppose that there is solely the problem of state-dependent accumulation of phase while polarization of the retro-reflected beam is assumed to rotate infinitely so that the shift operator can be written as

$$\hat{S}_\mathrm{p} : \begin{cases} |0,k\rangle & \rightarrow & e^{i\varphi_{|0\rangle,\mathbf{n}}}|0,k+1\rangle \\ |1,k\rangle & \rightarrow & e^{i\varphi_{|1\rangle,\mathbf{n}}}|1,k-1\rangle \end{cases} , \tag{6.7}$$

where excitations between vibrational states contributing to shift-induced homogeneous dephasing are neglected. Then, the spatial probability distribution of the corresponding quantum walk is identical to that of the textbook example with the shift operator $\hat{S}$ defined in Eq. (6.2), irrespective of the phases $\varphi_{|0\rangle,\mathbf{n}}$ and $\varphi_{|1\rangle,\mathbf{n}}$, albeit the quantum states of both walks are different [179]. Consequently, possible inhomogeneous dephasing arising from shifting of thermal atoms (see Sec. 5.1.1) would not affect the distribution of the walk.[2] The situation, however, is different if both problems arise simultaneously and two shift operators, $\hat{S}_\uparrow$ and $\hat{S}_\downarrow$, have to be alternately applied in a sequence. The quantum state of the walker then reads

$$|\Psi_{2N'}^{\uparrow\downarrow}\rangle = [\hat{S}_\downarrow(\hat{C}\otimes\hat{\mathbb{1}})\hat{S}_\uparrow(\hat{C}\otimes\hat{\mathbb{1}})]^{N'}|\Psi_0\rangle\,, \tag{6.8}$$

where technical limitations restricting the walk to even numbers of transport steps (see Sec. 4.5) have already been taken into account. In that case, the probability distribution may indeed become sensitive to the accumulated phase during the shift. With regard to the experimental data presented later in this chapter, we demonstrate this fact by evolving such quantum walk for $2N' = 6$ steps for the initial state $|\Psi_0\rangle = |1,0\rangle$ and the coin operator

$$\hat{C}_\mathrm{E} : \begin{cases} |0\rangle & \rightarrow & \frac{1}{\sqrt{2}}(|0\rangle - |1\rangle) \\ |1\rangle & \rightarrow & \frac{1}{\sqrt{2}}(|0\rangle + |1\rangle) \end{cases} \quad . \tag{6.9}$$

The contributions to the resulting spatial probability distribution

$$P_{2N'}^{\mathrm{Q},\uparrow\downarrow,|\Psi_0\rangle}(k) = \langle\Psi_{2N'}^{\uparrow\downarrow}|\hat{P}_k|\Psi_{2N'}^{\uparrow\downarrow}\rangle \tag{6.10}$$

are shown in Tab. 6.1 and compared to those of a textbook example $P_{2N'}^{\mathrm{Q},|\Psi_0\rangle}(k)$ with the same coin operator $\hat{C}_\mathrm{E}$ and a single shift operator $\hat{S}$. In the following, we distinguish between two cases: $\Delta\varphi_\mathbf{n} \equiv \varphi_{|0\rangle,\mathbf{n}} - \varphi_{|1\rangle,\mathbf{n}} = 0$ and $\Delta\varphi_\mathbf{n} \neq 0$.

For $\Delta\varphi_\mathbf{n} = 0$, we can write $\hat{S}_\uparrow = e^{i\varphi_{|0\rangle,\mathbf{n}}}\cdot\hat{S}$ and $\hat{S}_\downarrow = e^{\varphi_{|0\rangle,\mathbf{n}}}\cdot\hat{S}^{-1}$. Consequently, both shift operators only introduce a global phase, which however, is indistinguishable in a measurement of the resulting quantum state $|\psi_{2N'}^{\uparrow\downarrow}\rangle$. Hence, neither the quantum state nor the corresponding probability distribution provide a measurable dependency on the accumulated phase $\varphi_{|0\rangle,\mathbf{n}}$, making the walk insensitive to inhomogeneous dephasing discussed in Sec. 5.1.1. For this reason, it would be valuable to avoid a state-dependent accumulation of phase during the shift, e.g. by using other qubit basis states and a different characteristic wavelength, as proposed in Sec. 5.1.1. Irrespective of this fact, the probability distribution of a quantum walk

[2] Throughout this chapter, we focus mainly on shift-induced inhomogeneous dephasing discussed in Sec. 5.1.1, which is expected to be the most dominant dephasing source. Each atom of the thermal ensemble performs thus an quantum walk with undisturbed quantum interference for all time steps, whereas homogenous dephasing, e.g. from excitations between vibrational states would destroy this interference with a certain probability. Homogeneous dephasing has been extensively studied in Refs. [50, 180, 181] and references therein.

k	$P_6^{\mathrm{Q},\lvert 1,0\rangle}(k) \times 2^6$	$P_6^{\mathrm{Q},\uparrow\downarrow,\lvert 1,0\rangle}(k) \times 2^6$ $(\Delta\varphi_{\mathbf{n}} \neq 0)$	$P_6^{\mathrm{Q},\uparrow\downarrow,\lvert 1,0\rangle}(k) \times 2^6$ $(\Delta\varphi_{\mathbf{n}} = 0)$
-6	1	1	1
-4	26	$6 + 4\cos(2\Delta\varphi_{\mathbf{n}})$	10
-2	13	$11 - 2\cos(4\Delta\varphi_{\mathbf{n}}) - 4\cos(2\Delta\varphi_{\mathbf{n}})$	5
0	8	$12 - 4\cos(4\Delta\varphi_{\mathbf{n}})$	8
$+2$	5	$19 + 6\cos(4\Delta\varphi_{\mathbf{n}}) - 12\cos(2\Delta\varphi_{\mathbf{n}})$	13
$+4$	10	$14 + 12\cos(2\Delta\varphi_{\mathbf{n}})$	26
$+6$	1	1	1

Table 6.1.: Contributions to the spatial probability distribution of various quantum walks, the coin operator $\hat{C}_{\mathrm{E}}$ (see Eq. (6.9)) and initial state $|\Psi_0\rangle = |1,0\rangle$ of which are identical, while their shift operators differ. For details, see text.

with two alternately applied shift operators $\hat{S}_\uparrow$ and $\hat{S}_\downarrow$ differs from that with a single operator $\hat{S}$ or $\hat{S}_{\mathrm{p}}$. For our particular case with the initial state $|\Psi_0\rangle = |0,0\rangle$, the distribution is mirror-inverted, yielding

$$P_M^{\mathrm{Q},\uparrow\downarrow,|1,0\rangle}(k) = P_M^{\mathrm{Q},|1,0\rangle}(-k) = P_M^{\mathrm{Q},|0,0\rangle}(k) \tag{6.11}$$

for all $k \in \mathbb{Z}$ and $M \in \mathbb{N}$. The same applies for the initial state $|\Psi_0\rangle = |0,0\rangle$, so that

$$P_M^{\mathrm{Q},\uparrow\downarrow,|0,0\rangle}(k) = P_M^{\mathrm{Q},|0,0\rangle}(-k) = P_M^{\mathrm{Q},|1,0\rangle}(k)\,. \tag{6.12}$$

Even though this mirror-inversion is not universally valid, as can be exemplarily shown for $|\Psi_0\rangle = \frac{1}{\sqrt{2}}(|0,0\rangle + |1,0\rangle)$, it should be kept in mind when discussing experimental results.

For $\Delta\varphi_{\mathbf{n}} \neq 0$, which rather corresponds to our experimental implementation, both the quantum state and the corresponding probability distribution depend on the accumulated phases $\varphi_{|0\rangle,\mathbf{n}}$ and $\varphi_{|1\rangle,\mathbf{n}}$, see e.g. Tab. 6.1. In that case, the quantum walk is sensitive to inhomogeneous dephasing during the shift. According to our dephasing model of Sec. 5.1.1, we expect the measured probability distribution to be given by

$$\bar{P}_{2N'}^{\mathrm{Q},\uparrow\downarrow,|\Psi_0\rangle}(k) = \sum_{n=0}^{\infty} \varrho_{\mathrm{ax}}^{(n)} \sum_{m,m'=0}^{\infty} \varrho_{\mathrm{rad}}^{(m,m')} P_{2N'}^{\mathrm{Q},\uparrow\downarrow,|\Psi_0\rangle}(k) \tag{6.13}$$

with the axial and radial occupation probability $\varrho_{\mathrm{ax}}^{(n)}$ and $\varrho_{\mathrm{rad}}^{(m,m')}$ defined in Eq. (5.4). For the particular case, presented in Tab. 6.1, such dephasing would partially smear out the characteristic features of the distribution and shift its weight from the outer to the inner positions. The same applies for the initial state $|\Psi_0\rangle = |0,0\rangle$ and therefore also for the superposition state $|\Psi_0\rangle = \frac{1}{\sqrt{2}}(|0,0\rangle + i|1,0\rangle)$, since the distribution of the latter is just given by the sum of the contributions of the individual basis states, see Sec. 6.1.2.

An alternative approach to directly reverse inhomogeneous dephasing, not only that arising from shifting of thermal atoms, involves an extended version of the shift operator which comprises two shifts $\hat{S}_\uparrow$ and $\hat{S}_\downarrow$, and a rephasing spin-echo π-pulse in between

$$\hat{S}^{(1)}_{\mathrm{ext}} \equiv \hat{S}_\downarrow \hat{U}_\pi \hat{S}_\uparrow : \begin{cases} |0,k\rangle & \rightarrow & ie^{i(\varphi_{|0\rangle,\mathbf{n}}+\varphi_{|1\rangle,\mathbf{n}})}|1,k+2\rangle \\ |1,k\rangle & \rightarrow & ie^{i(\varphi_{|0\rangle,\mathbf{n}}+\varphi_{|1\rangle,\mathbf{n}})}|0,k-2\rangle \end{cases} . \tag{6.14}$$

Since this operator introduces only a global phase, the same statements as for $\Delta\varphi_{\mathbf{n}} = 0$ can be made, albeit the matter wave components are transported over twice as large distances. Because $\hat{S}^{(1)}_{\mathrm{ext}}$ swaps the qubit basis states, the probability distributions of a walk with the coin operator $\hat{C}_{\mathrm{E}}$ are mirror-inverted for both, the initial state $|0,0\rangle$ and $|1,0\rangle$. This mirror-inversion, however, can be in principle fixed by extending the shift operator by an additional π-pulse, yielding

$$\hat{S}^{(2)}_{\mathrm{ext}} \equiv \hat{U}_\pi \hat{S}^{(1)}_{\mathrm{ext}} = -e^{i(\varphi_{|0\rangle,\mathbf{n}}+\varphi_{|1\rangle,\mathbf{n}})} \cdot \hat{S}^2 . \tag{6.15}$$

Apart from a scaled position axis, the resulting distribution is then identical to that of the textbook example. This statement is valid irrespective of the choice of the coin or the initial state. Furthermore, using $\hat{S}^{(1)}_{\mathrm{ext}}$ or $\hat{S}^{(2)}_{\mathrm{ext}}$, quantum walks with an odd number of time steps can be realized. However, besides all the advantages, there is a major drawback of this approach: Shift operators employing additional rephasing pulses suffer from their imperfect population transfer efficiency which already has been shown to limit the transport efficiency. This problem has thus to be weighed against the inhomogeneous dephasing problem of the previous approach. Preliminary measurements have shown that imperfect π-pulses are far more problematic than dephasing arising from shifting of thermal atoms. For this reason, we oppose the use of extended shift operators in our quantum walk sequences.

Remarks on the random walk

So far, we have investigated the properties of a particular quantum walk with alternately applied shift operators $\hat{S}_\uparrow$ and $\hat{S}_\downarrow$. For the random walk, this situation corresponds to an alternately changed moving direction for the outcome of a coin toss. Although such changes obviously do not affect the probability distribution for a fair (unbiased) coin, i.e. $P^{\mathrm{R},\uparrow\downarrow}_{2N'}(k) = P^{\mathrm{R}}_{2N'}(k)$ for $p_{\mathrm{c}} = 1/2$, the situation changes for the biased coin ($p_{\mathrm{c}} \neq 1/2$). In general, it is then $P^{\mathrm{R},\uparrow\downarrow}_{2N'}(k) \neq P^{\mathrm{R}}_{2N'}(k)$ while the resulting distribution is symmetric ($P^{\mathrm{R},\uparrow\downarrow}_{2N'}(k) = P^{\mathrm{R},\uparrow\downarrow}_{2N'}(-k)$). This fact is immediately obvious when two alternated coins instead of alternated shifts are equivalently used, which corresponds to a random walk with a single three-sided dice tossed every second time step, providing three outcomes: walk two steps to the left, walk two steps to the right, each with a probability of $p_{\mathrm{c}}(1-p_{\mathrm{c}})$, and remain on place with a probability of $p_{\mathrm{c}}^2 + (1-p_{\mathrm{c}})^2$. In that sense, the dice is symmetric since walking in both directions is equally probable, yielding a symmetric spatial distribution, the width of which is defined by the bias of the initial coin.

The above considerations only hold for an ideal coin toss which does not dependent on the walker's internal "state". Experimentally, such coin toss is difficult to implement using microwave pulses which rather induce a unitary evolution of the quantum state. To mimic a stochastic process a measurement destroying the state after each time step of the walk is required which can be realized by photon scattering. After each measurement, however, the atom has to be brought back to the qubit's Hilbert space again using optical pumping prior to the next microwave operation.[3] In case of a random walk with more then ten time steps, only a small fraction of atoms would survive such procedure. For this reason, we follow another approach: Instead of destroying the qubit state by photon scattering, we merely destroy its phase relation by introducing a delay of the order of the homogeneous dephasing time. The evolution of the walk must therefore be described by a density operator

$$\hat{\rho}(t+1) = \hat{G}_{-1,t}\hat{\rho}(t)\hat{G}^{\dagger}_{-1,t} + \hat{G}_{+1,t}\hat{\rho}(t)\hat{G}^{\dagger}_{+1,t} \tag{6.16}$$

with the time evolution operators

$$\hat{G}_{\pm 1,t} = \begin{cases} (\hat{D}_{\pm 1} \otimes \hat{\mathbb{1}})\hat{S}_{\uparrow}(\hat{C} \otimes \hat{\mathbb{1}}) & \text{for } t \text{ even} \\ (\hat{D}_{\pm 1} \otimes \hat{\mathbb{1}})\hat{S}_{\downarrow}(\hat{C} \otimes \hat{\mathbb{1}}) & \text{for } t \text{ odd} \end{cases}, \tag{6.17}$$

and the projector operators

$$\hat{D}_{\pm 1} : \begin{cases} |0\rangle & \rightarrow & \frac{1}{2}(1 \pm i)|0\rangle \\ |1\rangle & \rightarrow & \frac{1}{2}(1 \mp i)|1\rangle \end{cases}, \tag{6.18}$$

which remove all off-diagonal entries of $\hat{\rho}(t)$ emulating decoherence. For an unbiased coin ($p_c = 1/2$), the resulting spatial probability distribution recovers a symmetric binomial distribution of the random walk, irrespective of the initial state. Otherwise, for $p_c \neq 1/2$, the distribution indeed depends on the initial state of the walker and can even be asymmetric. Hence, for our experimental realization of a random walk, errors in the coin manifest themselves in deviation of the measured probability distribution from the classical distribution of a random walk.

6.2.2. Experimental sequence

To reduce the statistical error in subsequent analysis, the experimental sequence of a quantum walk is usually applied on multiple atoms which do not overlap during their walk. The sequence basically consists of three parts: In the first part, the initial state $|\Psi_0\rangle = |\psi_0\rangle \otimes |k_0\rangle = |\psi_0, k_0\rangle$ of each walker is prepared. For this purpose, we load on average eight atoms into the optical lattice, adjusting the parameters of the MOT in such a way that atoms are widely distributed over the lattice sites ensuring a sufficiently wide walking space on both sides. From an initial fluorescence image, the initial position of each atom (the walker) is extracted, defining its reference zero

[3] Since optical pumping involves photon scattering, it can also take over the role of the destructive measurement at the same time.

position in the lattice ($|k_0\rangle \equiv |0\rangle$). The atoms are subsequently molasses cooled before the lattice depth is adiabatically lowered to $k_\mathrm{B} \times 80\,\mu$K — the typical depth for initializing and manipulating the atom's qubit states, see Sec. 3.1.1. Finally, the atoms are optically pumped into the qubit basis state $|\psi_0\rangle = |0\rangle$, whereas for other initial qubit states, a microwave pulse is subsequently applied, e.g. a $\pi/2$-pulse for $|\psi_0\rangle = \frac{1}{\sqrt{2}}(|0\rangle + i|1\rangle)$ or a π-pulse for $|\psi_0\rangle = |1\rangle$, see Tab. 3.1 in Sec. 3.2.1.

In the second part of the sequence, the actual quantum walk for a preset number of time steps ($2N'$) is performed by alternately applying the coin and the shift operators $\hat{S}_\uparrow$ and $\hat{S}_\downarrow$, the order of which is defined in Eq. (6.8). The shift operators are implemented by the state-selective transport with a linear driving ramp, an adjusted optimum ramp time of $\tau_{\lambda/2} = 18.5\,\mu$s and a settling time of $\delta t = 2\,\mu$s, resulting in a total transport time for a single shift of $\tau_\mathrm{trans} = 20.5\,\mu$s. For demonstration purposes, we use the unbiased coin operator $\hat{C}_\mathrm{E}$ defined in Eq. (6.9), which is implemented by a $3\pi/2$-pulse with a pulse duration of $12\,\mu$s and a phase of $\phi_\mathrm{rf} = \pi/2$ with respect to the first pulse, i.e. $\hat{C}_\mathrm{E} = \hat{U}_{3\pi/2,\pi/2}$, see Tab. 3.1. Intuitively, an implementation of an unbiased coin employing a $\pi/2$-pulse, which corresponds to the Hadamard coin $\hat{C}_\mathrm{H} = \hat{U}_{\pi/2,\pi/2}$ of Eq. (6.5), would be a more appropriate choice, since $\pi/2$-pulses are in general more robust to frequency detuning than $3\pi/2$-pulses of equal Rabi frequency. However, preliminary experiments have shown that quantum walks employing such coin implementation experience more decoherence than those using $3\pi/2$-pulses. We thus suspect additional rephasing processes when $3\pi/2$-pulses are used, which however cannot be explained just from evolution of the respective operators. The presence of rephasing processes is partially supported by experimental results which reveal comparable coherence properties to those obtained with spin-echo techniques employed in the sequences. Further theoretical investigations are planed in the future, taking a more extensive decoherence and dephasing model into account compared to that presented in this thesis. Finally, to emulate an unbiased coin toss of a random walk, a $\pi/2$-pulse with a phase shift of $\phi_\mathrm{rf} = \pi/2$ is used to intentionally omit possible rephasing. Furthermore, an additional delay of $400\,\mu$s between each coin and the subsequent shift operation is introduced, so that the phase relation between subsequent steps of the walk is destroyed.

In the third part of the sequence, the final atom distribution is probed by fluorescence imaging, determining the relative position of each atom with respect to its initial (zero) position, see Sec. 4.5.3. Optionally, we extract information on the internal state populations and relative phase by *local* quantum state tomography. The latter is based on site-resolved, state-selective detection combined with single-particle operations and projection measurements employing the push-out technique. For details, see Sec. 3.2.4. The local state tomography provides a population distribution for each eigenstate of the Pauli spin operators defining the u-, v- and w-axis of the Bloch sphere. From these distributions, the final state (the Bloch vector) at each relative position of the walker can be reconstructed providing a partial insight into coherence properties of the walk, see below.

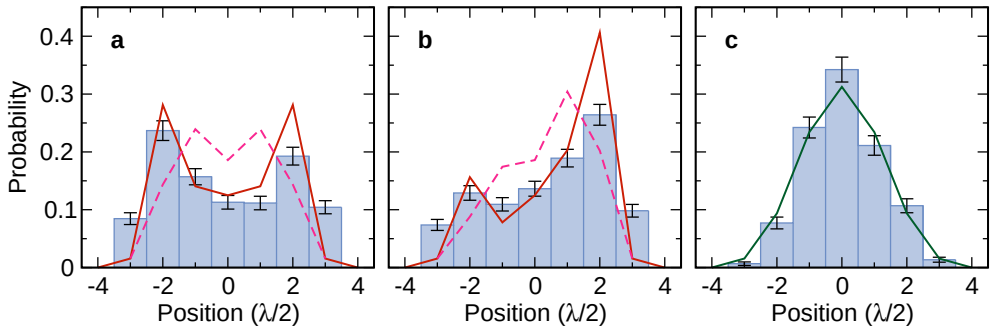

Figure 6.3.: Spatial probability distribution of a six-step quantum walk for (**a**) the initial state $|\Psi_0\rangle = \frac{1}{\sqrt{2}}(|0,0\rangle + i|1,0\rangle)$ and (**b**) the initial state $|\Psi_0\rangle = |1,0\rangle$, each inferred from approximately 800 identical realizations. Measured data are shown as a histogram. Solid lines show the theoretical expectation for the ideal case; dashed lines results of the dephasing model of Eq. (6.13). Error bars indicate the statistical error. (**c**) Spatial probability distribution of the analogous random walk.

6.3. Experimental results

We apply the quantum walk sequence for $2N' = 6$ time steps on atoms initialized in state $|\Psi_0\rangle = |1,0\rangle$ and $|\Psi_0\rangle = \frac{1}{\sqrt{2}}(|0,0\rangle + i|1,0\rangle)$, respectively. In addition, for comparison, we perform an analogous random walk in which the phase relation between subsequent steps is destroyed by intentionally introducing decoherence, see Sec. 6.2.2.

In Figure 6.3, the resulting spatial probability distributions are shown and compared to the theoretical expectations for an ideal case (no decoherence), characterized by $\Delta\varphi_{\mathbf{n}} = 0$ for the quantum walk, and $p_c = 1/2$ for its random counterpart. Both measured quantum walk distributions reasonably well reproduce the theoretical results: For $|\Psi_0\rangle = \frac{1}{\sqrt{2}}(|0,0\rangle + i|1,0\rangle)$, the characteristic two-peak splitting of the quantum walk is recovered, see Fig. 6.3(a), albeit both peaks are partially smeared out while the distribution reveals a slight asymmetry. Smearing-out of the characteristic peaks can be attributed to decoherence introduced through either the coin or the shifting operations, whereas the slight asymmetry and especially the transferred weight of the distribution to the outermost positions ($\pm 3\lambda/2$) most likely arise from systematical errors of the coin. The measured distribution for $|\Psi_0\rangle = |1,0\rangle$ in Fig. 6.3(b), reveals the characteristic asymmetry with a pronounced peak at $+2\lambda/2$, and a smaller peak at $-2\lambda/2$, in good agreement with the theoretical prediction. Here as well, a smearing-out of the peaks and a transfer of their weight to the outermost relative positions can be observed.

Both measured distributions seem to better match with the theoretical results for the ideal case rather than the estimations from the dephasing model of Eq. (6.13). This fact may have various reasons: First, the real experimental values of the average vibrational occupation numbers in the model may be lower than our typical

values $\bar{n}_{\mathrm{ax}} = 1.2$ and $\bar{m}_{\mathrm{mrad}} = 200$ which have been used for the calculation. This is the case when the temperature of the atoms lies below the typical value of $10\,\mu$K.[4] Second, the shift dynamics of the state-selective potentials which enter the dephasing model may improperly describe the real experimental situation. This can be the case, when retardation components in the polarization control setup introduce additional distortion which may partially decrease differences in potential dynamics and thus the amount of inhomogeneous dephasing as well. Third, possible rephasing processes may appear which are not considered in our model. Fourth, pulse errors in frequency duration and phase affecting the coin operation, excitations between motional states affecting the interference properties and position-dependent accumulation of phase due to an inhomogeneous environment (see Sec. 5.2) may affect the spatial probability distributions. Coin and shift operations can even change from one time step to another due to drifts of experimental parameters over the course of the measurement, giving rise to homogeneous dephasing. Finally, external perturbations such as fluctuations of the ambient magnetic field, laser power, beam pointing, or spontaneous emission processes, introduce additional decoherence even in the absence of a quantum walk sequence, see Sec. 3.3. In general, it is nearly impossible to unambiguously extract coin or shift errors or estimate the amount of decoherence just from a single measured distribution, since the number of unknown parameters exceeds the number of data points. The interplay of different decoherence sources together with systematic errors makes it also difficult to model experimental imperfections and quantitatively extract the respective contributions from the measured data. Consequently, throughout this thesis, we abstain from a quantitative analysis of these imperfections and rather qualitatively discuss their possible effects.

By intentionally introducing decoherence in the quantum walk sequence (see Sec. 6.2.2), the spatial distribution of the random walk is recovered, see Fig. 6.3, irrespective of the choice of the initial qubit state $|\psi_0\rangle$. The measured distribution is well symmetric and agrees reasonably well with the binomial distribution of Eq. (6.1) for $p_{\mathrm{c}} = 1/2$. We observe merely a slightly increased weight at the initial position which may arise from atoms wrongly initialized into internal states lying outside the qubit's Hilbert space before the walk starts. In that case, atoms are insensitive to microwave operations. Hence, for an even number of time steps, they are shifted back and forth to the initial position, see Sec. 4.6.

6.3.1. Quantum-to-classical transition

Reproducing spatial probability distributions of a quantum walk with its characteristic features and dependency on the internal state of the walker, but also the ability to recover its classical counterpart just by introducing decoherence, provides

[4] Note that this temperature value relies on a measurement which has been performed long before quantum walks have been investigated. Since then, several methods improving alignment of experimental setup and fine-adjusting experimental parameters, including molasses cooling have been developed.

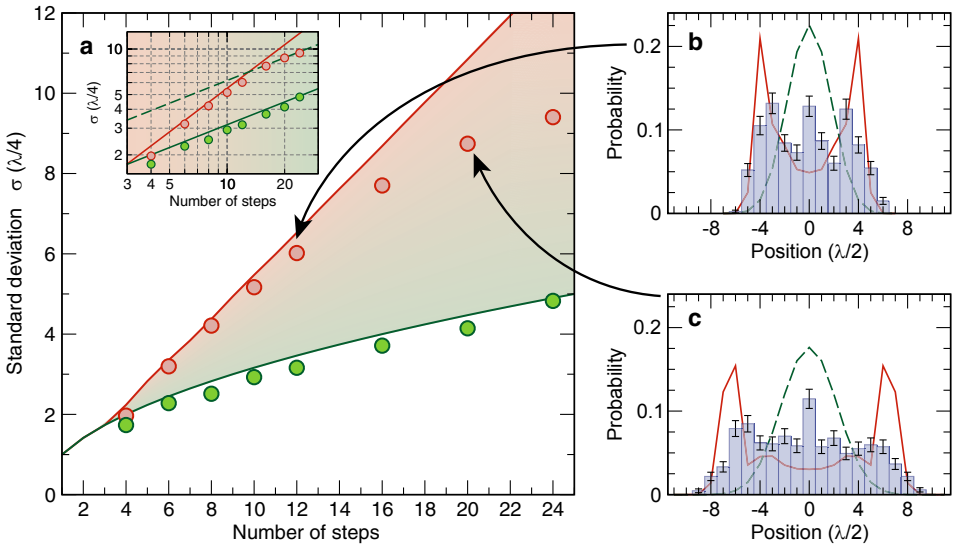

Figure 6.4.: (**a**) Scaling of the standard deviation of the measured spatial probability distributions on a linear and double logarithmic scale (inset) for a quantum walk (red) and random walk (green). The solid lines indicate the expectations for the ideal cases. Error bars are smaller than the size of symbols. The measured quantum walks follow the ideal linear behavior until, because of decoherence, they gradually turn into a random walk. The dashed line in the inset indicates an offset shifted square-root scaling. The probability distributions for $2N' = 12$ (**b**) and $2N' = 20$ (**c**) show a gradual change from the quantum to a classical shape. The theoretical prediction is shown as a solid line for the pure quantum walk and as a dashed line for the random walk.

strong evidence of multipath quantum interference. There are, however, further characteristic properties distinguishing the quantum walk from the random walk, see Sec. 6.1.2. The most prominent of them is the scaling of the standard deviation of the probability distribution with the number of time steps. From this scaling, we anticipate an insight into the quantum-to-classical transition initiating the breakdown of multipath quantum interference.

To investigate the scaling of standard deviations for the random and quantum walk, we again apply both sequences for $2N' = \{2, 4, 6, \ldots, 24\}$ time steps on atoms initialized in $|\Psi_0\rangle = \frac{1}{\sqrt{2}}(|0,0\rangle + i|1,0\rangle)$. For each resulting distribution $\widetilde{P}_{2N'}(k)$, we calculate the standard deviation using

$$\sigma(2N') = \sqrt{\sum_{k=-N'}^{N'} [k\lambda/4 - \mu_{2N'}]^2 \widetilde{P}_{2N'}(k)} \tag{6.19}$$

with the expectation value defined by

$$\mu_{2N'} = \sum_{k=-N'}^{N'} (k\lambda/4) \cdot \widetilde{P}_{2N'}(k)\,. \tag{6.20}$$

In Figure 6.4(a), standard deviations for both walks and different numbers of time steps are shown. For the quantum walk, the standard deviation follows closely the expected linear behavior for up to ten time steps. The subsequent deviation is due to decoherence, which asymptotically turns the quantum walk into a classical random walk. This quantum-to-classical transition is particularly noticeable in the double logarithmic plot (see inset of Fig. 6.4(a)), revealing a transition from one straight line to another, the slopes of which correspond to the expected exponents one and one-half, respectively. For the random walk, the typical square-root scaling is recovered. The fact, that the measured values lie slightly below the theoretical curve is most likely attributed to atoms the internal states of which lie outside the qubit's Hilbert space before the walk starts. These atoms give rise to an increased probability of finding an atom at its initial position (see above), which in case of a symmetric distribution do not contribute to the standard deviation. Furthermore, a bias of the coin can also decrease the standard deviation of the probability distribution. Both effects, however, cannot be distinguished from the probability distribution of a random walk alone.

The quantum-to-classical transition can be partially observed in the measured spatial probability distributions of the walk, see Fig. 6.4(b,c). They reveal a gradual recovering of the characteristic central peak of the random walk with increased number of time steps, while the characteristic two-peak distribution of the quantum walk is stepwise suppressed. Similar transitions in spatial distributions have been theoretically predicted for various decoherence models relying on homogeneous dephasing, see e.g. Refs. [50,180,181] and reference therein, albeit not for the particular case of alternating shift operators.

6.3.2. Quantum state reconstruction

To get a more detailed characterization of the wave function prepared by a six-step quantum walk sequence for atoms initialized in $|\Psi_0\rangle = \frac{1}{\sqrt{2}}(|0,0\rangle + i|1,0\rangle)$, we extract information on the internal state populations and relative phases by local quantum state tomography. For this, after the second part of the quantum walk sequence, we apply a series of projection measurements in the qubit states $|u_+\rangle = \frac{1}{\sqrt{2}}(|0\rangle + |1\rangle)$, $|v_+\rangle = \frac{1}{\sqrt{2}}(|0\rangle + i|1\rangle)$ and $|w_+\rangle = |0\rangle$, and their orthogonal complements $|u_-\rangle = \frac{1}{\sqrt{2}}(|0\rangle - |1\rangle)$, $|v_-\rangle = \frac{1}{\sqrt{2}}(|0\rangle - i|1\rangle)$ and $|w_-\rangle = |1\rangle$, respectively. From the resulting, state-dependent probability distributions $\widetilde{P}^{\mathrm{Q},\uparrow\downarrow,|\Psi_0\rangle}_{6,|u_+\rangle}(k)$, $\widetilde{P}^{\mathrm{Q},\uparrow\downarrow,|\Psi_0\rangle}_{6,|v_+\rangle}(k)$, etc., at each lattice site, the internal quantum state is reconstructed and represented by a vector on the Bloch sphere. For details on reconstructing the Bloch vector see Sec. 3.2.4.

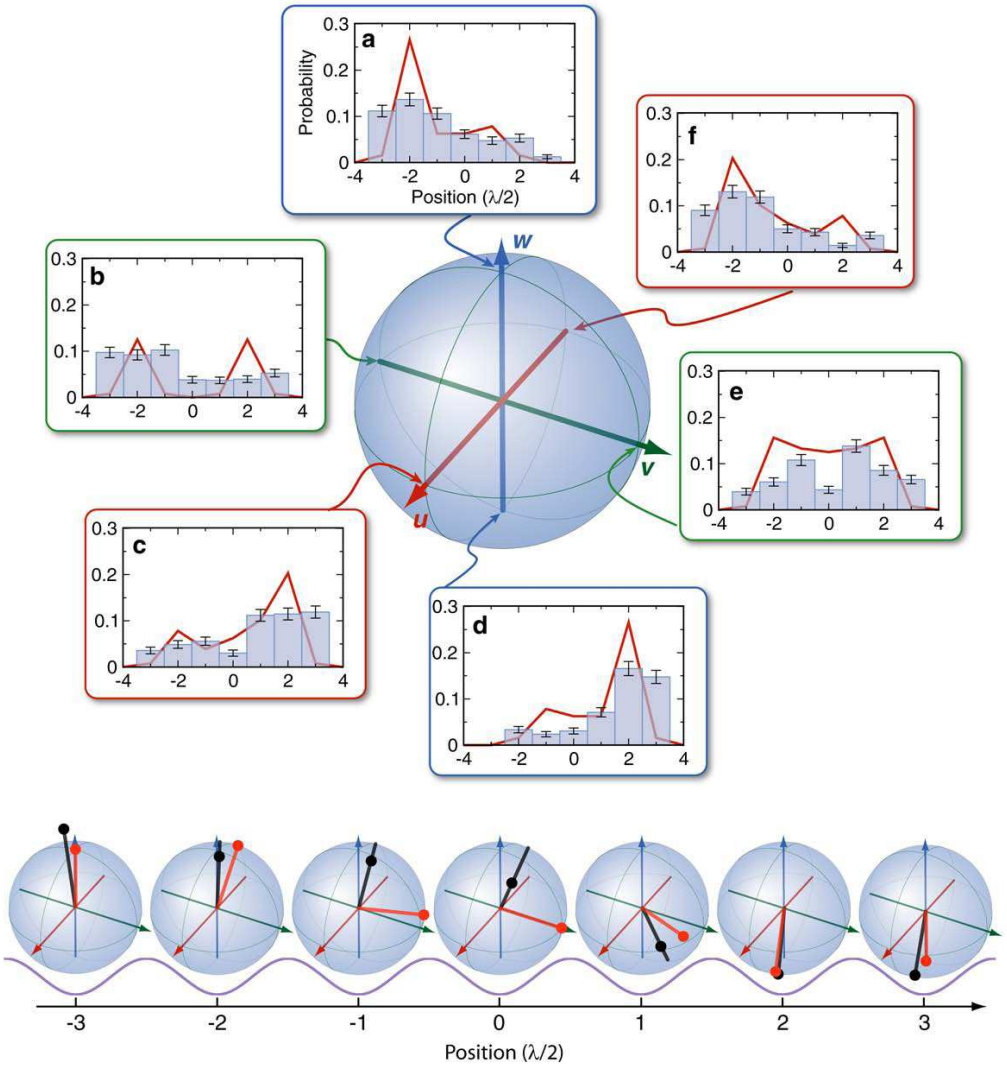

Figure 6.5.: Local quantum state tomography of the atomic wave function after a six-step quantum walk for $|\Psi_0\rangle = \frac{1}{\sqrt{2}}(|0,0\rangle + i|1,0\rangle)$. The distributions show the contributions of the qubit states $|w_+\rangle$ (**a**, $+w$-axis), $|v_-\rangle$ (**b**, $-v$-axis), $|u_+\rangle$ (**c**, $+u$-axis), $|w_-\rangle$ (**d**, $-w$-axis), $|v_+\rangle$ (**e**, $+v$-axis), and $|u_-\rangle$ (**f**, $-u$-axis). Reconstructed Bloch vectors at each relative position in the lattice are shown below. The tips of the reconstructed and ideally expected Bloch vectors are shown as black and red dots, respectively. The lines for Bloch vectors extend to the surface of the Bloch sphere to guide the eye; deviations from the surface illustrate the effect of decoherence and measurement errors.

In Figure 6.5, the state-dependent probability distributions (a-f) and the reconstructed Bloch vectors at each relative position are shown, together with the theoretical prediction for the ideal case. The measured distributions qualitatively

recover the main features of the theoretical results, including symmetry and positions of the characteristic peaks, albeit noticeable deviations are visible. The same applies for the reconstructed Bloch vectors which fit well to the theoretical prediction at the edges of the distribution, but they show increasing deviations in a region close to the initial position of the walk. In this region, matter wave interference occurs at almost every step during the sequence, which makes the respective positions more sensitive to decoherence compared to those further apart. Such behavior can partially be inferred from the calculated contributions of the distribution for $\Delta\varphi_{\mathbf{n}} \neq 0$ in Tab. 6.1, which reveal an increasingly dominant dependency on $\Delta\varphi_{\mathbf{n}}$ close to the initial position,[5] indicating a higher sensitivity to inhomogeneous dephasing in this region. The increasing decoherence close to the initial position can be read out just from the decreasing length of the respective Bloch vectors (see Sec. 3.2.4). Deviations in their pointing directions are partially attributed to systematical coin and shift errors but also to technical limitations of our experimental setup, in particular concerning the long-term stability as the measurement of each spatial probability distributions takes approximately 30 minutes in our case. Striking evidence for long-term instabilities manifest themselves by the lengths of the reconstructed Bloch vectors which at $-3\lambda/2$ is larger than one.

Finally, to check whether the measured tomography data is consistent within itself, we calculate the sum of probability distributions for each pair of complementary states. This sum should obey

$$\widetilde{P}_6^{\mathrm{Q},\uparrow\downarrow,|\Psi_0\rangle}(k) = \widetilde{P}_{6,|X_+\rangle}^{\mathrm{Q},\uparrow\downarrow,|\Psi_0\rangle}(k) + \widetilde{P}_{6,|X_-\rangle}^{\mathrm{Q},\uparrow\downarrow,|\Psi_0\rangle}(k) \tag{6.21}$$

with the overall, independently measured probability distribution $\widetilde{P}_6^{\mathrm{Q},\uparrow\downarrow,|\Psi_0\rangle}(k)$. However, we infer merely an agreement within 2.5, 3.0, 2.1 times the statistical error for $X = u$, v, w, respectively, indicating problems in long-term stability of the experiment over the course of the tomography measurement.

In order to perform not only local but full quantum state tomography, also the off-diagonal elements of the position space density matrix of the final state have to be measured. This can in principle be done by applying j shifting operations prior to the last coin operator which then allows to perform local measurements of the off-diagonal elements which have the form $|k\rangle\langle k+j|$. This scheme, however, is challenging in our case, as the sequence involves several shifting operations even for small quantum walk distributions, leading to significant decoherence.

6.3.3. Reversing the quantum walk

The local tomography does not yield information about the off-diagonal elements of the position space density matrix, which essentially contain information about the phase relation between the wave function at different lattice sites rather than at each site. To demonstrate the spatial coherence of the state over all populated

[5] Even though the distribution in Tab. 6.1 has been calculated for $|\Psi_0\rangle = |1,0\rangle$, similar conclusions can be drawn for the initial state $|\Psi_0\rangle = \frac{1}{\sqrt{2}}(|0,0\rangle + i|1,0\rangle)$.

lattice sites, we aim to reverse the multipath interference by (partially) inverting the respective operations in the sequence. For this, we invert the coin operation

$$\hat{C}_{\mathrm{E}}^{-1} = \hat{U}_{3/2\pi,3/2\pi} : \begin{cases} |0\rangle & \rightarrow & \frac{1}{\sqrt{2}}(|0\rangle + |1\rangle) \\ |1\rangle & \rightarrow & \frac{-1}{\sqrt{2}}(|0\rangle - |1\rangle) \end{cases} . \tag{6.22}$$

and swap the shifting directions of the shift operations. Note that full inversion of $\hat{S}_{\uparrow}$ and $\hat{S}_{\downarrow}$ is only possible for $\Delta\varphi_{\mathbf{n}} = 0$, since in that particular case it is $(\hat{S}_{\uparrow,\downarrow})^{-1} = \hat{S}_{\downarrow,\uparrow}$. Otherwise, unequal accumulation of phases cannot be reversed in our particular sequence, preventing a full inversion of the shift operators. We continue then the previous walk for six additional time steps, so that

$$|\Upsilon_{2\cdot 6}^{\uparrow\downarrow}\rangle = [(\hat{C}_{\mathrm{E}}^{-1} \otimes \hat{\mathbb{1}})\hat{S}_{\downarrow}(\hat{C}_{\mathrm{E}}^{-1} \otimes \hat{\mathbb{1}})\hat{S}_{\uparrow}]^3 \cdot [\hat{S}_{\downarrow}(\hat{C}_{\mathrm{E}} \otimes \hat{\mathbb{1}})\hat{S}_{\uparrow}(\hat{C}_{\mathrm{E}} \otimes \hat{\mathbb{1}})]^3 |\Psi_0\rangle . \tag{6.23}$$

Being only interested in the spatial probability distribution of this "reversed" walk

$$P_{2\cdot 6}^{\mathrm{Q}^{-1},\uparrow\downarrow,|\Psi_0\rangle}(k) = \langle \Upsilon_{2\cdot 6}^{\uparrow\downarrow} | \hat{P}_k | \Upsilon_{2\cdot 6}^{\uparrow\downarrow} \rangle \tag{6.24}$$

the very last coin operation can be omitted in the sequence. In the ideal case, for $\Delta\varphi_{\mathbf{n}} = 0$, negligible drifts of experimental parameters defining the coin and shifts, and perfect inversion of the coin operations, the quantum walk is expected to be perfectly reversed, i.e. all matter wave components of the walker are merged on the initial lattice site, yielding a refocused distribution $P_{2\cdot 2N'}^{\mathrm{Q}^{-1},\uparrow\downarrow,|\Psi_0\rangle}(k) = \delta_{k,0}$.

In Figure 6.6, the measured "refocused" distribution is shown, revealing a pronounced spike at the initial position superimposed with a binomial-like distribution. To explain the shape of the measured distribution, we distinguish two possible types of dephasing considering each of them separately: Pure, homogeneous dephasing of the coin while $\Delta\varphi_{\mathbf{n}} = 0$, following the model of Refs. [177, 181], and inhomogeneous dephasing arising from shifting of thermal atoms in state-dependent potentials ($\Delta\varphi_{\mathbf{n}} \neq 0$) using our dephasing model, see e.g. Eq. (6.13).

Suppose that our reversed quantum walk suffers solely from homogeneous dephasing of the coin. Following the dephasing model of Refs. [177, 181], which considers decoherence in the form of randomly-occurring uncorrelated non-unitary events characterized by the probability p_{dec} and added to the quantum walk dynamics, the calculated probability distribution reveals then a characteristic shape: a spike at the initial position superimposed with a binomial-like distribution, which we refer to as the background. By increasing the amount of dephasing (p_{dec}), the central spike is gradually suppressed, its weight is transferred to the background which becomes increasingly dominant, until finally the binomial distribution of the random walk is fully recovered. In that extreme case, both the coin operator $\hat{C}_{\mathrm{E}}$ and its inverse $\hat{C}_{\mathrm{E}}^{-1}$ act identically as a classical unbiased coin toss. Hence, there is no reversion at all and the random walk is just continued with one omitted coin toss. To incorporate possible systematical errors of the coin, we consider the most

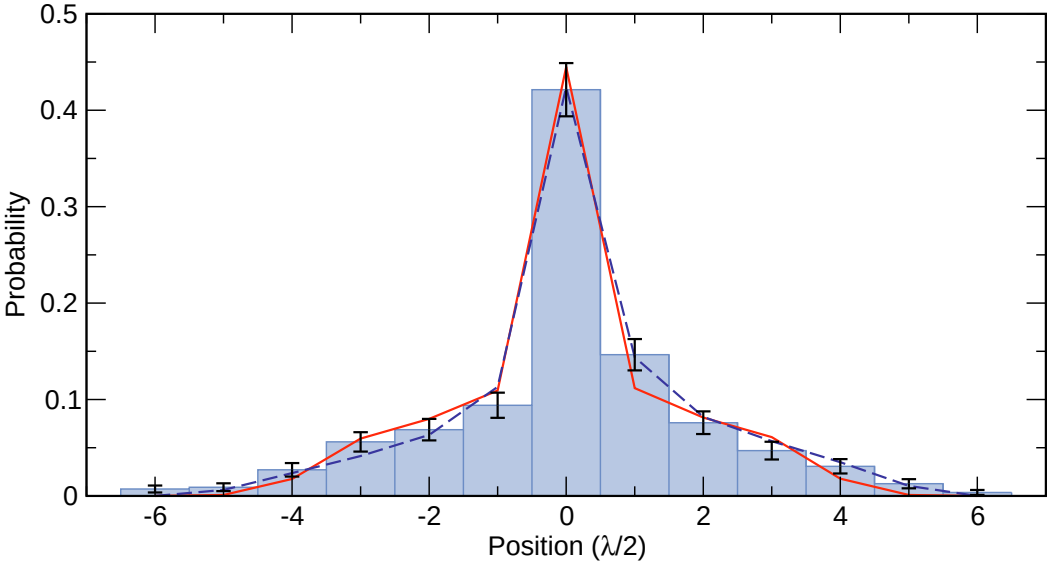

Figure 6.6.: Measured spatial probability distribution of time-reversing sequence to refocusing the delocalized state of a six-step quantum walk. The distribution shows a pronounced peak at the center, to where, ideally, the amplitude should be fully refocused, surrounded by a binomial-like background. Solid line shows a fit of the homogeneous dephasing model of the coin. Dashed line shows a calculated distribution which solely assumes inhomogeneous dephasing due to shifting of thermal atoms.

general coin on $\mathcal{H}_{\mathrm{qbit}}$,

$$\hat{C}_{p_\mathrm{c},\alpha,\beta} : \begin{cases} |0\rangle & \rightarrow & \sqrt{p_\mathrm{c}} \cdot |0\rangle + \sqrt{1-p_\mathrm{c}} \cdot e^{i\alpha}|1\rangle \\ |1\rangle & \rightarrow & \sqrt{1-p_\mathrm{c}} \cdot e^{i\beta}|0\rangle - \sqrt{p_\mathrm{c}} \cdot e^{i(\alpha+\beta)}|1\rangle \end{cases} , \tag{6.25}$$

with $0 \leq p_\mathrm{c} \leq 1$ defining its bias and $0 \leq \alpha, \beta \leq \pi$. In the dephasing model of the coin, the refocused distribution for the initial state $|\Psi_0\rangle = \frac{1}{\sqrt{2}}(|0\rangle + i|1\rangle)$ is symmetric for any choice of p_dec and p_c, and does not depend on β at all. For $p_\mathrm{dec} > 0$ and $p_\mathrm{c} \neq 1/2$, the coin bias gradually transfers weight from the background to the central peak until finally for the trivial cases $p_\mathrm{c} = 0$ or $p_\mathrm{c} = 1$, i.e. no pulses or π-pulses, respectively, only the central peak remains, irrespective of the dephasing since there is no multipath interference at all while π-pulses only introduce a global phase. Asymmetry in the background appears for $\beta \neq 0$ and $\beta \neq \pi$. For our particular coin $\hat{C}_\mathrm{E}$, it is $p_\mathrm{c} = 1/2$, $\beta = 0$ and $\alpha = \pi$. From a fit of the distribution inferred from the homogeneous dephasing model to the measured data, we obtain $p_\mathrm{c} = (0.78 \pm 0.01)$ and $\alpha = (0.90 \pm 0.01)\pi$ with a coherence fraction of $(66 \pm 1)\%$ per time step ($p_\mathrm{dec} = (34 \pm 1)\%$). The inferred bias of the coin, however, seems to be too large to be unnoticed in the preparatory measurements. It is also strongly correlated to the coherence fraction, i.e. fixing the parameter to $p_\mathrm{c} = 1/2$ would result in a coherence fraction of $(76 \pm 1)\%$, which, albeit still too small, would be

rather consistent with the scaling of the standard deviation, see Sec. 6.3.1. Hence, even though the model seems to reasonably fit our measured data, it is unclear whether it can solely explain the dominant decoherence process of the walk, see below.

Neglecting homogeneous dephasing, for $0 < \Delta\varphi_{\mathbf{n}} < \pi$,[6] the distribution still reveals a spike at the initial position. However, the distribution is asymmetric while the background provides a complex shape comprising sub-peak features. The refocusing process is therefore distorted just by the accumulation of phase during the shift. Taking additionally inhomogeneous dephasing by averaging over the thermal ensemble into account, we obtain a probability distribution which seems to perfectly recover the measured data, see Fig. 6.6. This agreement, however, should be regarded with reservations: First, we have solely considered inhomogeneous dephasing of the shift in this calculation while the duration of the inverted quantum walk sequence ($390\,\mu$s) already exceeds the inhomogeneous dephasing $T_2^* \approx 200\,\mu$s (see Tab. 3.2) in the absence of any walk. Thus, if no rephasing processes are involved, we would rather expect a stronger deviation from the measured data. Even in the presence of rephasing processes, the extended homogeneous dephasing time $\widetilde{T}_2' \approx 900\,\mu$s is still of the order of the duration of the sequence (in the static case, i.e. without transport, see Tab. 3.3). For this reason, homogeneous dephasing cannot be ignored and should noticeably affect the measured distribution. Taking additionally excitations between motional states and drifts of experimental parameters into account, we would rather expect a more binomial-like refocused distribution. Since bias of the coins can be excluded,[7] we conclude that the dephasing contribution from the shift is overestimated by our model since it should not solely explain the measured data. Furthermore, rephasing processes must be present during the measurement. Finally, since each of the two different dephasing models alone fits to the measured distribution, we can hardly distinguish between both dephasing processes. Further investigations and extended theoretical models are therefore required in the future.

6.4. Conclusion

In this chapter, I have experimentally demonstrated a discrete time quantum walk on a line using single neutral atoms in a one-dimensional optical lattice. I have discussed substantial differences between the typical textbook example of a quantum and random walk on a line and our particular implementation of both walks. Due to technical limitations imposed by the state-selective transport, our quantum walk sequences require application of alternating shift operations which among others make the spatial probability distribution of the walk sensitive to inhomogeneous

[6] We focus only on the relevant interval. The same applies for $\Delta\varphi'_{\mathbf{n}} = \Delta\varphi_{\mathbf{n}} + j\pi$ with $j \in \mathbb{Z}$.

[7] We have carefully measured the coin operators and performed several consistency checks, including Ramsey and single atom interferometry sequences in dynamic configuration besides the standard method of recording the Rabi oscillations.

dephasing. On the other hand, the limited population transfer efficiency of the microwave pulses prevents the use of spin-echo pulses in each shift which in principle could counteract the inhomogeneous dephasing.

For a six-step quantum walk sequence, the measured spatial probability distributions recovers the characteristic distributions of a quantum walk, revealing the dependency on the initial state and the characteristic two-peak structures. They agree reasonably well with the theoretical results, indicating the presence of quantum interference. We also observe clear signs of experimental imperfections and decoherence. By intentionally introducing decoherence in the quantum walk sequence, quantum interference is destroyed and the spatial probability distribution of the random walk is recovered, irrespective of the initial state.

By increasing the number of time steps, we observe a quantum-to-classical transition in the scaling of the standard deviation of the measured distributions but also in their characteristic features. The former shows a clear transition from a linear scaling of a quantum walk to a square-root scaling of the random walk, clearly supporting the presence of quantum interference. For the random walk sequence, the typical square-root scaling is recovered.

To get a more detailed characterization of the wave function prepared by a six-step quantum walk sequence, I have extract information on the internal state populations and relative phases by local quantum state tomography. The reconstructed Bloch vectors at each final position of the walker fit well to the theoretical prediction at the outermost positions, but they show increasing deviations in regions which are particularly sensitive to inhomogeneous dephasing.

Finally, I have investigated the spatial probability distribution of a (partially) reversed six-step quantum walk. The resulting distribution reveals a pronounced spike at the initial position in which the delocalized walker is expected to refocus. This spike is superimposed with a binomial-like distribution, which can be attributed to both inhomogeneous and homogeneous dephasing. Both, a model solely considering homogeneous dephasing and our dephasing model which takes only inhomogeneous dephasing during the shift into account, can in principle explain the measured data. The fact that the distribution does not fully recover the binomial distribution of the random walk provides a striking evidence of high fraction of coherence of the walk.

All results presented in this chapter make one thing clear: From the measured data, it is nearly impossible to unambiguously extract experimental imperfections, distinguish between homogeneous and inhomogeneous dephasing and estimate their amount. For this reason, further investigations are required relying on sequences with much higher number of time steps and advanced theoretical models. Both strategies are planed in the future.

7. Controlled two-atom collisions

Controlled on-site interactions between individual atoms or their matter wave components in an optical lattice allow for a variety of applications ranging from efficient production of ultracold molecules [182–185], realization of fundamental quantum gates [16, 53, 55] to creation of large-scale entanglement [37, 54]. In the last decade, the respective experiments have been usually performed on large atomic ensembles starting from a Mott insulating phase of an ultracold atomic quantum gas. Apart from ideal starting conditions, this approach, however, currently suffers from the lack of control and detection of individual atoms in the lattice.

In another approach, which has also been systematically followed in our research group over the past years, systems of atoms are designed atom-by-atom, aiming on full control over each individual particle [43, 46, 47, 89] and their interactions [34–36]. Parts of this "bottom-up" approach have been perfected during this thesis, permitting single-site detection and generation of arbitrary patterns of atoms, see Sec. 2.4 and Sec. 3.4.4. Inserting two selected atoms into a common lattice site has so far been only achieved using optical tweezers [186]. The success rate of this approach has been indirectly inferred from light-induced atom losses, appearing when two atoms are irradiated with near-resonant laser light on a common site. Such light-induced atom losses have been partially observed in Sec. 2.4.3.

In this chapter, I follow an alternative approach which uses the state-selective transport to bring two atoms together to a single lattice site. In contrast to optical tweezers, the state-selective transport offers additional advantages which enlarge its range of possible applications: First, once two atoms have been brought together, it allows us to subsequently separate and displace them to adjacent lattice sites where their quantum states can be separately manipulated or detected. The entire process, however, has to be performed within the coherence time. Second, utilizing the delocalizing capability of the sate-selective transport (see Sec. 5.1), it additionally allows us to investigate on-site interactions between delocalized matter wave components. This ability has been proposed to generate multi-particle entanglement [37, 54] and has been recently demonstrated on a large scale [41], albeit the initial and resulting state of the large atomic ensemble could not be fully characterized so far. We aim to close this gap in the future getting a detailed insight on a variety of on-site interactions at the most fundamental two-atom level.

In the following, I experimentally demonstrate how previously introduced techniques, including generation of atom patterns, position-dependent manipulation of qubit states and state-selective transport can be used to bring two atoms together into contact. The success rate of this approach is inferred from atom losses due to light-induced collisions. The purpose of this chapter is to give an overview over the

experimental realization and its limitations rather than investigating different collision processes. The latter have been extensively studied in the past [63,67,112–114]. For a general review see Ref. [187] and references therein.

7.1. State-selective transport in a magnetic field gradient

To state-selectively transport two atoms towards each other, both atoms have to be prepared in orthogonal qubit basis states, i.e. one atom in $|0\rangle$, the other in $|1\rangle$. Furthermore, because of the limited transport efficiency (see Sec. 4.6), high success rates in bringing two atoms together are only achievable if both atoms are initially separated by only few lattice sites. For this reason, position-selective manipulation of their qubit states requires a strong magnetic field gradient. Such field gradient, however, cannot be switched off just before the transport since the decay time of the magnetic field is of the order of the T_1 relaxation time. Hence, all transport operations have to be performed in a magnetic field gradient, imposing some limits in practice.

Transporting atoms over several lattice sites requires microwave π-pulses, the frequencies of which have to be resonant with the $|0\rangle \leftrightarrow |1\rangle$ transition of the respective atom, see Sec. 4.5. For regular π-pulses employed in this thesis, already small detuning from this frequency would significantly decrease the population transfer efficiency and thus, according to Eq. (4.51), the transport efficiency as well. In presence of a magnetic field gradient, the transition frequency is position-dependent and thus changes while atoms are shifted along the lattice. However, since atoms are stepwise shifted from site to site, knowing the axial gradient strength $B'(I)$ and the shift direction, the microwave frequency could be in principle stepwise adjusted, once the initial position of the atom and the corresponding $|0\rangle \leftrightarrow |1\rangle$ transition frequency $\omega_0(\boldsymbol{r}, I)$, see Eq. (3.60), are known. Alternatively, by employing the patterning sequence prior the state-selective transport, this initial position and the transition frequency can be even preset, see Sec. 3.4.4. For $2K$ transport steps the adjusted frequency would then read

$$\omega_k = \omega_0(\boldsymbol{r}, I) \pm k \cdot \omega'(I)\lambda/4\,, \tag{7.1}$$

where $k = 1, \ldots, 2K-1$ denotes the number of completed transport steps and $\omega'(I) = \gamma B'(I)$ is defined in Eq. (3.60). The sign in Eq. (7.1) has to be inferred from preliminary measurements, since it depends on a number of parameters, including the initial qubit basis state, the direction of polarization rotation and the sign of $B'(I)$ in Eq. (3.60).

There are several technical problems facing the above approach: First, to stepwise adjust the microwave frequency within a typical transport time of $\approx 20\,\mu$s, the RF signal generator (see Sec. 3.2.2) has to be operated in frequency modulation mode. This operation mode, however, provides a lower frequency stability compared to the usually used fixed frequency operation. Second, since for $B'(I = 45A) = -123\,\mathrm{G/cm}$ the pulse bandwidth of a regular π-pulse corresponds

to an axial distance of less than $1\,\mu$m in position space, the transport efficiency may suffer from drifts of the quadrupole field with respect to the optical lattice during the transport. This does not hold for drifts appearing in the time interval between repetitions of the transport sequence, as long as the initial position and transition frequency of the atom are previously defined by the patterning sequence. Finally, for two atoms transported to a common lattice site, a π-pulse adjusted for one atom may unintentionally affect the qubit state of the adjacent atom, unless efficient and selective π-pulses with single-site resolution can be ensured. Since the current status of the experiment cannot ensure such resolution, the above approach is not suitable for bringing two atoms into contact.

For this reason, another approach is followed in this thesis: Instead of using regular π-pulses, broadband composite pulses, namely $90_0225_{180}315_0$-pulses are employed in the transport sequence, see Sec. 3.5 and also Sec. 4.6. By this, the frequency of these pulses does not need to be changed and can be kept fixed for the entire transport sequence. The maximum number of transport steps in the sequence depends on the axial gradient strength $B'(I)$ and is limited by the bandwidth of the pulses. This approach, however, allows us to operate the RF signal generator in the stable fixed frequency mode. Furthermore, due to an extended bandwidth of the $90_0225_{180}315_0$-pulse, the transport efficiency is less sensitive to drifts of the quadrupole field relative to the optical lattice.

The center frequency of the composite pulses has to be adjusted to the desired transport distance. For transporting a single atom over a distance of $K\lambda/2$, it is ideally preset to

$$\omega_{\mathrm{CP}}(K) = \omega_0(\boldsymbol{r}, I) \pm K \cdot \omega'(I)\lambda/4\,. \tag{7.2}$$

For $B'(45\,\mathrm{A})$, the bandwidth of the $90_0225_{180}315_0$-pulse currently permits a transport within a region comprising up to $K = 7$ lattice sites, see Sec. 3.5. Since for efficiency reasons large transport distances are anyway avoided, the size of this region suffices for our purpose. The initial separation between two atoms which have to be brought together to a single site should therefore be smaller than $7\lambda/2 \approx 3\,\mu$m.

7.1.1. Experimental sequence

To investigate the transport efficiency of the composite pulses approach for the maximum available axial field gradient strength $B'(45\,\mathrm{A}) = -123\,\mathrm{G/cm}$, we prepare a single atom with a preset position and transition frequency ω_0 in the optical lattice using the patterning technique, see Sec. 3.4.4. The preparation is typically performed in a lattice depth of $k_\mathrm{B} \times 80\,\mu$K and an axial gradient strength of $B'(45\,\mathrm{A})$ using a single Gaussian π-pulse with the frequency ω_0, a $1/\sqrt{e}$ pulse half-width of $\sigma_t = 15\,\mu$s and a pulse duration of $t = 100\,\mu$s. To improve the effective selectivity of the pulse, we repeat the inner sequence core of the patterning sequence by a total of $M = 3$ times, yielding a $1/\sqrt{e}$ spectral half-width of $\sigma_\omega(3) = (4.34 \pm 0.03)\,\mathrm{kHz}$. By this, in most cases only a single or no atom at all remains on the desired position. Only in very rare cases two neighboring atoms will remain. The magnetic field gradient is then temporarily switched off and the lattice depth raised for fluorescence

imaging to $k_\mathrm{B} \times 0.4\,\mathrm{mK}$. After acquiring an initial image of the atom with an exposure time of 800 ms, the lattice depth is lowered to $k_\mathrm{B} \times 80\,\mu\mathrm{K}$ and the magnetic field gradient is switched on again. The atom is then optically pumped into the qubit state $|0\rangle$ before the state-selective transport is applied, see Sec. 4.5.

The transport sequence comprises $90_0 225_{180} 315_0$-pulses and $2K$ transport steps with $K = \{1, 2, \ldots, 9\}$ corresponding to a transport distance of $K\lambda/2$. The pulse frequency is preset to

$$\omega_\mathrm{CP}(K) = \begin{cases} \omega_0(\boldsymbol{r}, I) + K\omega'(I)\lambda/4 & \text{for} \quad K \text{ even}\,, \\ \omega_0(\boldsymbol{r}, I) + (K-1)\omega'(I)\lambda/4 & \text{for} \quad K \text{ odd}\,. \end{cases} \tag{7.3}$$

For each transport step, a linear driving ramp with an optimum ramp time of $\tau_{\lambda/2} = 19\,\mu\mathrm{s}$ and a settling time of $\delta t = 2\,\mu\mathrm{s}$ is employed. Finally, we switch off the field gradient, rise the lattice depth and acquire a final fluorescence image of the atom. For each preset value of K, the entire sequence is repeated $500 - 1000$ times.

7.1.2. Revealing drifts of the magnetic quadrupole field

From the initial images of the atoms, long-term drifts of the selectivity region of the patterning pulse arising from drifts of the quadrupole field can be deduced. For this, the initial positions of the atoms with respect to the imaging optics are plotted as a function of sequence shot (sequence repetition).

In Figure 7.1, the resulting plot is exemplarily shown. The initial positions of the atoms are approximately distributed along equidistant parallel stripes, the separation of which corresponds to the periodicity of the optical lattice. These stripes thus represent positions of the lattice sites which obviously drift linearly in time with respect to the imaging optics from shot to shot. The drift velocity, however, is negligible on the timescale of a single sequence repetition with a duration of $\approx 2.7\,\mathrm{s}$. Furthermore, we observe alternating regions with atoms distributed almost over a single lattice site and over two neighboring sites. The former regions correspond to the case in which the selectivity region of the patterning pulse overlaps with a single site. In between, the selectivity region is spread over two neighboring lattice sites, affecting atoms on both sites so that each of them may remain in the lattice with a finite probability after patterning. By connecting the overlap regions, a drift of the selectivity region with respect to the optical lattice and the imaging optics can be revealed. This drift is attributed to a drifting quadrupole field arising from thermal expansion of the anti-Helmholtz coils, since it is only observable when the coils are operated with high currents for a long time. The drift of the quadrupole field, however, is also negligible on the relevant timescale of a single transport sequence with a duration of less than 1 ms.

7.1.3. Transport efficiency in a magnetic field gradient

Analogous to the previous analysis of the state-selective transport, we infer the transport efficiency P_{2K} in a magnetic field gradient from the probability histograms

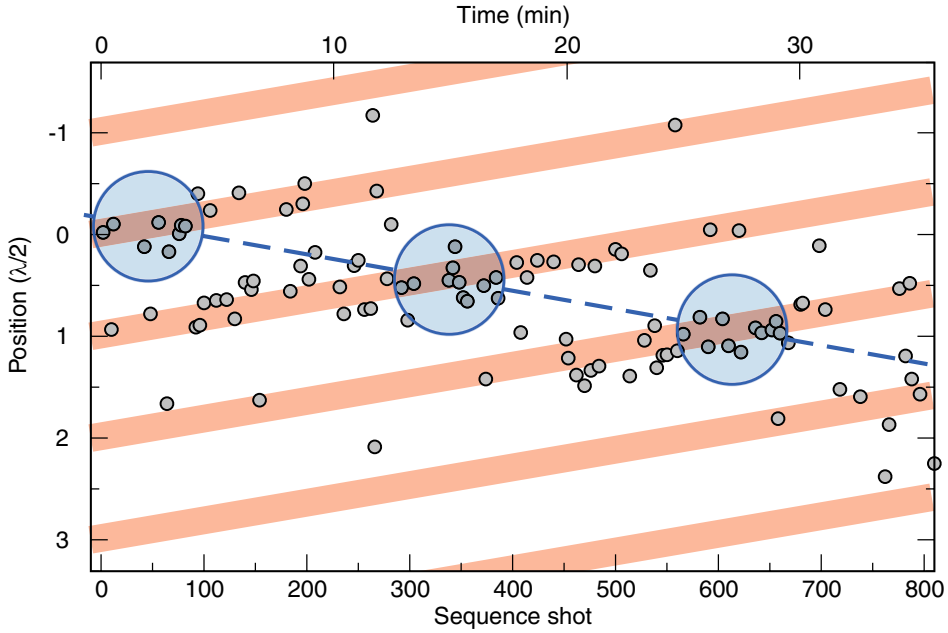

Figure 7.1.: Initial position of an atom prepared using the patterning technique with a fixed frequency as a function of sequence shot. The distribution of atomic positions reveals the relative drift between the imaging optics (reference system), sites of the optical lattice (shaded stripes) and the selectivity region of the patterning pulse (dashed line). Encircled regions approximately indicate an overlap between the selectivity region and a single lattice site.

of relative positions of the atoms for different number of transport steps, see Sec. 4.6. The transport efficiency stepwise decreases with the number of transport steps, see Fig. 7.2. For $K \leq 7$, it reveals a similar decay behavior to that of a transport in absence of the field gradient, whereas the abrupt drop for $K > 7$ arises from the transport distance which exceeds the region limited by the bandwidth of the composite pulses. The decay behavior is assumed to arise from the limited transfer efficiency of the microwave pulses $\bar{P}_{|1\rangle,\mathrm{gr}}$. This transfer efficiency can be inferred from a fit of the model function

$$P_{2K}^{\mathrm{err}} = \bar{P}_{|1\rangle,\mathrm{gr}} \cdot \prod_{k=1}^{2K-1} P_{|1\rangle}(\omega_k - \omega_{\mathrm{CP}}(K))\,, \tag{7.4}$$

where ω_k and $\omega_{\mathrm{CP}}(K)$ are defined in Eqs. (3.60) and (7.3), respectively, and $P_{|1\rangle}(\delta)$ denotes the theoretical microwave spectrum of the $90_0225_{180}315_0$-pulse (see e.g. Fig. 3.24) as inferred from solving the optical Bloch equations. This model function fits well to the measured data, confirming our assumption and yielding

$$\bar{P}_{|1\rangle,\mathrm{gr}} = (96.0 \pm 0.5)\%\,, \tag{7.5}$$

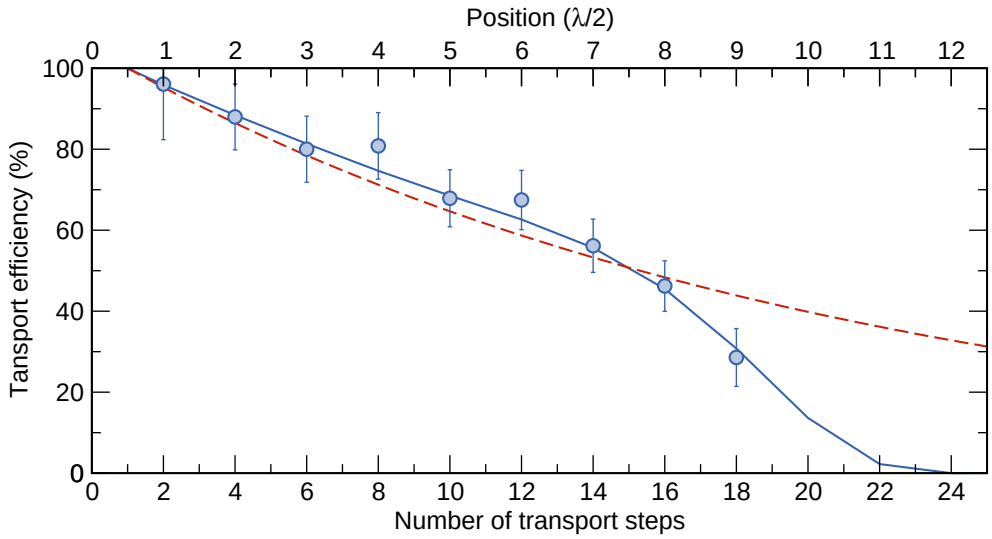

Figure 7.2.: Transport efficiency P_{2K} as a function of number of transport steps $2K$ in a magnetic field gradient for a linear driving ramp with $\tau_{\lambda/2} = 19\,\mu$s and $\tau_{\mathrm{trans}} = 21\,\mu$s, employing $90_0225_{180}315_0$-pulses in the transport sequence. The solid line shows a fit of the model function of Eq. (7.4) to the data. For comparison, the dashed lines indicate the decay of the transport efficiency in absence of a magnetic field gradient, see Fig. 4.10.

which even slightly exceeds the corresponding value inferred in absence of the magnetic field gradient, see Eq. (4.54). We conclude from this fact, that the magnetic field gradient does not noticeably affect the efficiency of displacing atoms from one lattice site to another. So far, no statements can yet be made regarding the coherence properties of the transport in the gradient. Such statements would require further investigations relying on single atom interferometry (see Sec. 5.1), which are planed in the future.

7.2. Transporting atoms to a common lattice site

The experimental sequence to bring two atoms together to a single lattice site basically comprises three stages: preparation of an atom pair with a predefined separation, addressing of atoms in orthogonal qubit basis states and finally applying the state-selective transport with a proper number of steps, defined by the initial separation of the atoms. To determine the success rate of this approach, an initial and final fluorescence image is acquired before the second and after the third stage, respectively. The lattice depths for preparation, transport and fluorescence imaging are similar to those used in previous section.

In contrast to previous experiments presented in this thesis, we now use two RF signal generators: one for frequency modulated pulses, used in the patterning sequence (secondary signal generator, see Sec. 3.2.2), the other for the composite

pulses, i.e. phase modulated pulses (primary signal generator).

The atom pair is prepared using the patterning sequence in a magnetic field gradient with $B'(45\,\mathrm{A}) = -123\,\mathrm{G/cm}$. We choose an atom pair separation of $4\lambda/2$, so that on the one hand, efficient selective manipulation of the qubit states of both individual atoms is ensured, while on the other hand, only four transport steps are required to bring both atoms into contact. The patterning sequence comprises two subsequently applied Gaussian pulses separated by a dwell time of $40\,\mu\mathrm{s}$. Each Gaussian pulse has a $1/\sqrt{e}$ pulse half-width of $\sigma_t = 15\,\mu\mathrm{s}$ and a pulse duration of $t = 100\,\mu\mathrm{s}$. The preset pulse frequencies are given by

$$\omega_{0,\mathrm{L}} = \omega_\mathrm{c} + 2 \cdot \omega'(45\,\mathrm{A})\lambda/2 \tag{7.6}$$

for the left hand atom in the image plane, and

$$\omega_{0,\mathrm{R}} = \omega_\mathrm{c} - 2 \cdot \omega'(45\,\mathrm{A})\lambda/2 \tag{7.7}$$

for the right hand atom, respectively. The center frequency ω_c has been previously adjusted so that patterning of both atoms is performed in a lattice region, in which high filling factors are expected. The inner sequence core of the patterning sequence is repeated by a total of $M = 3$ times.

After the patterning sequence, the magnetic field gradient is temporarily switched off while the lattice depth is raised to acquire the initial fluorescence image of the atoms with an exposure time of 800 ms. We subsequently lower the lattice depth, switch on the magnetic field gradient and optically pump the atoms into the qubit state $|0\rangle$. Then, a Gaussian π-pulse with the frequency $\omega_{0,\mathrm{R}}$, a $1/\sqrt{e}$ pulse half-width of $\sigma_t = 6\,\mu\mathrm{s}$ and a pulse duration of $t = 100\,\mu\mathrm{s}$ is applied to flip the qubit state of the right hand atom from $|0\rangle$ to $|1\rangle$.[1] Since both atoms are expected to be separated by a distance of $4\lambda/2$, we intentionally use a less selective π-pulse for this operation which provides a slightly higher population transfer efficiency ($\bar{P}_{|1\rangle} = (96 \pm 1)\%$) compared to the π-pulses employed in the patterning sequence, see Eq. (3.65).

Finally, we apply four steps of the state-selective transport using $90_0 225_{180} 315_0$-pulses with a fixed pulse frequency of $\omega_\mathrm{CP} = \omega_\mathrm{c}$. For each transport step, a linear driving ramp with an optimum ramp time of $\tau_{\lambda/2} = 19\,\mu\mathrm{s}$ and a settling time of $\delta t = 2\,\mu\mathrm{s}$ is employed. After transporting the atoms, we switch off the field gradient, rise the lattice depth and acquire a final fluorescence image. During the imaging process, atoms are irradiated with near-resonant laser light. Hence, we expect to observe light-induced atom losses whenever two atoms occupy a common lattice site after the transport. The entire sequence is repeated 7250 times.

[1] As presented in previous sections, the state-selective transport shifts the atoms in state $|0\rangle$ from left to the right in the image plane, whereas atoms in state $|1\rangle$ are shifted in opposite direction. Therefore, the right hand atom has to be initialized in state $|1\rangle$ to bring two atoms together into contact.

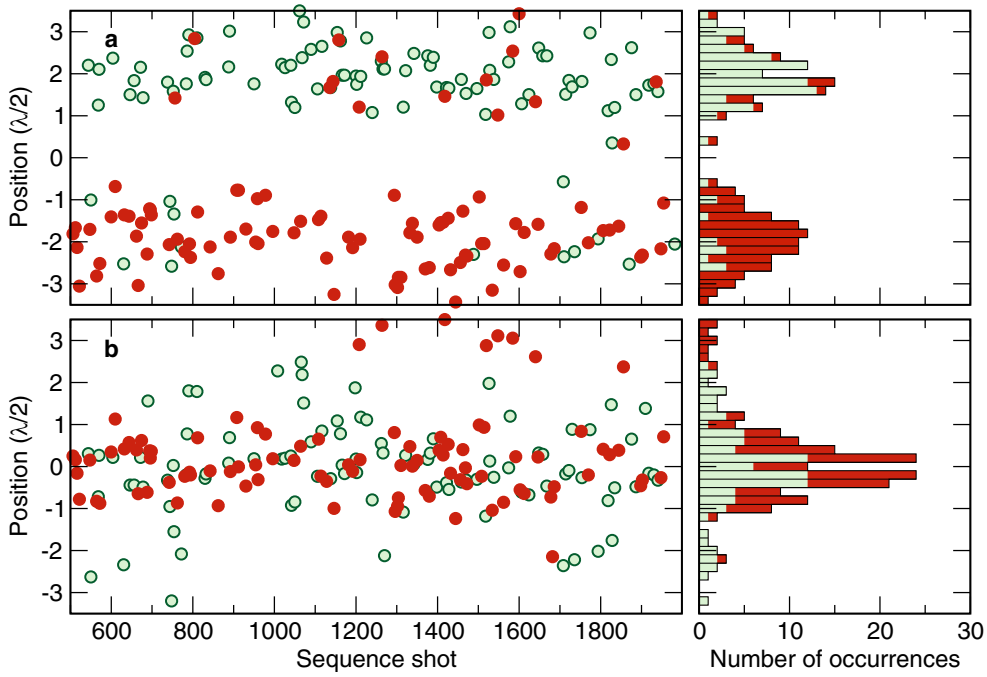

Figure 7.3.: (**a**) Initial positions and estimated qubit states of atoms as a function of sequence shot (left). Filled red and open green dots correspond to state $|0\rangle$ and $|1\rangle$, respectively. The same colors are used to indicate the respective contributions to the histogram of initial positions (right). From the stripe-like distribution of atomic positions, the positions of drifting lattices sites can be deduced. (**b**) Final positions of atoms after a state-selective transport comprising four transport steps (left) and the corresponding histogram (right). Dots and colors indicate the initial qubit state of the transported atoms.

7.2.1. Experimental results

From the acquired pairs of initial and final images, in principle all relevant information regarding the efficiency of each stage of the experimental sequence can be directly inferred. For this, we first post-select image pairs, the initial image of which show only a single atom. Since we expect a uniform filling of the lattice in the region of interest prior the patterning, the probabilities of finding single left hand and right hand atoms should be identical. This expectation is supported by the histogram of initial positions, see Fig. 7.3(a), calculated from a subset of post-selected image pairs, in which drifts of the selectivity region of the patterning pulses with respect to the imaging optics are negligible. The zero position in the histogram has been set to the position of the center frequency ω_c in the image plane.

The histogram in Figure 7.3(a) shows two almost identical peaks, separated by the predefined distance of $4\lambda/2$. It reveals a proper setting of the pulse frequencies in the patterning sequence. Since this histogram is calculated from atomic positions

measured on a time interval of 90 min, substructures revealing the periodicity of the optical lattice are smeared-out due to lattice drifts. Positions of the drifting lattice sites can be determined from the stripe-like distribution of atomic positions, similar to that in Fig. 7.1. From the slope of these stripes, we infer a drift velocity of 8 nm/s which is negligible on the time scale of a single sequence shot with a duration of 3.7 s.

State-selective detection using state-selective transport

The initial qubit basis state of atoms contributing to the histogram in Fig. 7.3(a) can be estimated from their relative positions after the state-selective transport. For this, we employ the fact that the transport direction of the atoms depends on their initial states. Neglecting tunneling between lattice sites, this approach provides in principle a detection reliability of 100% if only a single transport step is employed. Otherwise, the detection reliability is decreased due to imperfections of π-pulses used for transporting atoms over several sites. In that case, the reliability can be roughly estimated from a probability histogram of relative positions inferred from state-selectively transported atoms, see e.g. Fig. 4.9 in Sec. 4.6. Suppose that atoms are efficiently prepared in the qubit basis state $|0\rangle$ prior the transport, for $2K$ transport steps the estimated reliability then reads

$$F_{\mathrm{qbit}}(2K) \approx \sum_{l=1}^{K} h_{2l}\,, \tag{7.8}$$

where h_{2l} denotes the histogram value at the relative position $l\lambda/2$. For the four-step transport in a magnetic field gradient, we typically obtain $F_{\mathrm{qbit}}(4) \approx 92\%$. From the probability histogram of relative position calculated from the post-selected image pairs (not shown), the four-step transport efficiency is finally inferred, yielding $P_4 = (82 \pm 2)\%$.

Employing the above state detection method, we estimate the qubit state of each atom contribution to the histogram in Fig. 7.3(a). From the state-dependent contributions, we deduce that $p_{\mathrm{L}} \approx 87\%$ of the left hand atoms and $p_{\mathrm{R}} \approx 85\%$ of the right hand atoms are initialized in the predefined qubit state $|0\rangle$ and $|1\rangle$, respectively. However, since both values are estimated with a reliability of only 92%, they should be considered with reservations.

Finally, to check whether single left hand atoms and right hand atoms are transported to a common lattice, we determine the final positions of the atoms from the same subset of post-selected image pairs, see Fig 7.3(b). The corresponding histogram reveals indeed a single pronounced peak at the zero position in the vicinity of which the common lattice site is expected. However, drifts of the optical lattice and the resulting broadening of the central peak prevent a direct estimation of the success rate of bringing two atoms from both sides together to a single lattice site. For this reason, analogous to Ref. [186], we estimate this success rate from light-induced atom losses.

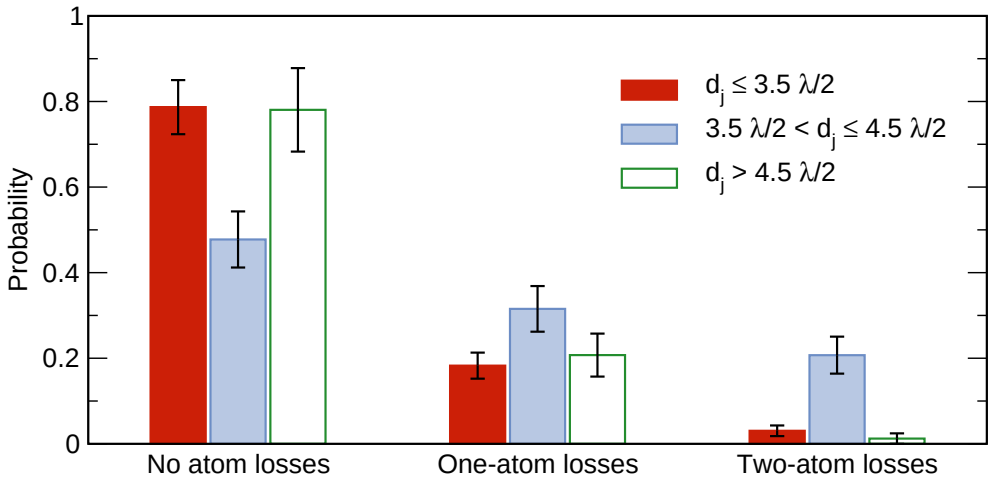

Figure 7.4.: Histograms of atom losses inferred for different subsets of initial atom pair separations d_j after a four-step state-selective transport and subsequent irradiation of atoms with near-resonant laser light.

Success rate of bringing two atoms together to a single lattice site

We analyze the previous data set again, this time post-selecting those image pairs with two atoms in the initial image. From the resulting data set comprising 390 image pairs, we determine the initial separations $d_{j\in\mathbb{N}}$ between both atoms using the parametric deconvolution, see Sec. 2.4.3. The post-selected image pairs are then further subdivided into three subsets: The first subset $D_<$ comprises 197 image pairs, for which the initial separations obey $d_j \leq 3.5\,\lambda/2$. They belong to sequence repetitions in which two atoms are separated by three or less lattice sites prior the transport. Hence, considering the transport efficiency, there is only a marginally probability that both atoms end up in a common lattice site. The second subset $D_=$, in turn, comprises 111 image pairs with $3.5\lambda/2 < d_j \leq 4.5\,\lambda/2$. The respective sequence repetitions provide two atoms properly separated by the predefined separation of four lattice sites. In that case, we expect a noticeable probability of bringing both atoms together to a single lattice site. Finally, the third subset $D_>$ comprises the remaining 82 image pairs, i.e. those with $d_j > 4.5\lambda/2$. They correspond to sequence repetitions in which two atoms are too far away to be brought into contact using only four transport steps.

From each final image of the subsets, we determine the number of atoms which remain in the optical lattice after the state-selective transport and the subsequent irradiation with near-resonant laser light. By this, we infer whether no atom, a single atom or two atoms got lost during the sequence.

In Figure 7.4, the resulting histograms of atom losses are separately shown for each of the three subsets. For $D_>$, i.e. those sequence repetitions in which two atoms never met, the probability of losing one atom out of two is given by

$p^{>}_{1\text{-a}} = (21 \pm 5)\%$. This value reasonably agrees with $\binom{2}{1}\widetilde{p}_{1\text{-a}}(1-\widetilde{p}_{1\text{-a}}) = (15 \pm 3)\%$, where $\widetilde{p}_{1\text{-a}} = (8 \pm 2)\%$ denotes the probability of uncorrelated one-atom losses in the time interval between acquisition of the image pairs. This probability is inferred from a previous analysis of post-selected single atom images. The probability of losing two atoms out of two is given by $p^{>}_{2\text{-a}} = (1 \pm 1)\%$ in well agreement with the expected value $(\widetilde{p}_{1\text{-a}})^2 = (0.6 \pm 0.3)\%$, whereas in $p^{>}_{0\text{-a}} = (78 \pm 10)\%$ of sequence repetitions no atom losses occur.

Almost similar results are obtained for $D_{<}$, namely $p^{<}_{0\text{-a}} = (79 \pm 6)\%$, $p^{<}_{1\text{-a}} = (18 \pm 3)\%$ and $p^{<}_{2\text{-a}} = (3 \pm 1)\%$. The probability of two-atom losses is slightly increased and does not agree with the expected value inferred from uncorrelated one-atom losses within the error bars. This fact might be a first indication for light-induced losses of atoms unintentionally transported to a common lattice site due to the imperfect transport. According to the initial atom separations such cases are in principle possible, albeit they are extremely improbable for the given transport efficiency. Due to the statistical error, however, we cannot infer a precise statement from this data set.

Significant deviations from previous results are obtained for $D_{=}$, i.e. for atoms properly separated to be brought together to a single lattice site. Here, the probability that no atom get lost after the transport and near-resonant irradiation drops to a value of $p^{=}_{0\text{-a}} = (48 \pm 7)\%$, i.e. by $\approx 38\%$ compared to $p^{>}_{0\text{-a}}$ and $p^{<}_{0\text{-a}}$, indicating additional atom losses. We attribute this losses to light-induced on-site interactions. From $p^{=}_{0\text{-a}}$ and the probability of uncorrelated atom losses $\widetilde{p}_{1\text{-a}}$,[2] the success rate of bringing two atoms to a common lattice site can be deduced

$$P_{\text{suc}} = (1-\widetilde{p}_{1\text{-a}})^2 - p^{=}_{0\text{-a}} = (37 \pm 8)\% \,. \tag{7.9}$$

This value agrees reasonably well with the success rate, estimated from the preparation efficiency of the qubit states and the transport efficiency of the atoms

$$P^{\text{est}}_{\text{suc}} = (1-\widetilde{p}_{1\text{-a}})^2 \cdot p_{\text{L}} \cdot p_{\text{R}} \cdot (P_4)^2 \approx 42\% \,. \tag{7.10}$$

Furthermore, it becomes evident that by increasing both efficiencies the success rate can be significantly increased. Alternatively, the selectivity of the preparation pulses could be improved, allowing us to perform the same sequence with an initial atom separation of two lattice sites instead of four, and thus employing only two transport steps. By this, assuming the same preparation efficiency and population transfer efficiency of the composite pulses during the transport, we could obtain $P_2 = (P_4)^{1/3} = (94 \pm 1)\%$, yielding a success rate of $P^{\text{est}}_{\text{suc}}(2) = 55\%$.

The histogram in Figure 7.4 reveals a further interesting detail. For $D_{=}$, we observe an increase in both, the probability of losing a single atom $p^{=}_{1\text{-a}} = (32 \pm 5)\%$ and the probability of losing two atoms $p^{=}_{2\text{-a}} = (21 \pm 4)\%$. The respective contributions of the on-site interactions are given by

$$p^{\text{ons}}_{1\text{-a}} = p^{=}_{1\text{-a}} - 2\widetilde{p}_{1\text{-a}}(1-\widetilde{p}_{1\text{-a}}) = (17 \pm 6)\% \tag{7.11}$$

[2] Note that, we intentionally refer to the probability of uncorrelated atom losses $\widetilde{p}_{1\text{-a}}$ rather than to the respective histogram values from $D_{<}$ and $D_{>}$ since the former provides a smaller error.

and

$$p_{2\text{-a}}^{\text{ons}} = p_{2\text{-a}}^{=} - (\widetilde{p}_{1\text{-a}})^2 = (20 \pm 4)\% \,. \tag{7.12}$$

Thus, for two atoms occupying the same lattice site and being irradiated with near-resonant laser light, the ratio between light-induced one-atom and two-atom losses is 46 : 54. Experimental evidence that light-induced collisions can also lead to one-atom losses have so far been observed and distinguished in a MOT [63], albeit with a significantly lower fraction of one-atom losses. Further investigations are therefore required to get a more detailed insight into these losses and their dependency on experimental parameters, e.g. depth of the optical lattice, irradiation power, etc.

7.3. Conclusion

In this chapter, I have experimentally demonstrated how previously introduced techniques, including generation of atom patterns, position-dependent manipulation of qubit states and state-selective transport can be used to bring two atoms together to a single lattice site. Due to technical limitations the state-selective transport has to be performed in the presence of a magnetic field gradient. For this purpose, two approaches have been proposed: One relying on a stepwise adjustment of the microwave frequency during the transport, the other using broadband composite pulses with a fixed frequency. Currently, only the latter approach allows us to bring two atoms together into contact.

In principle, drifts of the magnetic quadrupole field during the transport may significantly decrease its efficiency. I have demonstrated a method, which allows us to reveal such drifts. In our case, these drifts turned out to be negligibly slow compared to the duration of the transport sequence.

I have investigated the efficiency of the state-selective transport in the presence of the currently maximum available axial gradient strength $B'(45\,\text{A}) = -123\,\text{G/cm}$. Similar to the transport in absence of a magnetic field gradient, the transport efficiency is limited by the population transfer efficiency of the employed π-pulses, here the $90_0225_{180}315_0$-pulses. It turns out that the magnetic field gradient does not noticeably affect the transport efficiency.

Employing the above approaches and techniques, I have experimentally demonstrated that two atoms can indeed be deterministically brought together to a single lattice site. I have presented how the efficiency of each stage of the experimental sequence can be deduced just from acquired fluorescence images. Furthermore, a new detection method of the qubit basis states $|0\rangle$ and $|1\rangle$ relying on the state-selective transport has been introduced and the reliability of this method has been estimated.

Finally, I have inferred the success rate of bringing two atoms together into contact from atom losses due to light-induced collisions, appearing when two atoms occupying the same lattice site are irradiated with near-resonant laser light. The success rate is given by $P_{\text{suc}} = (37 \pm 8)\%$ and agrees reasonably well with the theoretical prediction. It can be in principle increased up to $P_{\text{suc}} \approx 55\%$ by decreasing

the initial separation of the atoms from four to two lattice sites.

The experimental results reveal that our method is capable of distinguishing between light-induced one-atom losses and two-atom-losses, opening up new opportunities for investigation of on-site interaction on a two-atom level.

8. Perspectives

In this thesis, I have presented the realization and investigation of the state-selective transport of single neutral cesium atoms in a one-dimensional optical lattice and its applications, including a single atom interferometer, a quantum walk and controlled two-atom collisions. Further methods to determine the atomic positions with sub-micrometer precision, reliably infer the separation of atoms down to neighboring lattice sites and individually manipulate and detect their internal states have been discussed in detail. The methods and results presented in this thesis pave the way for a wide range of interesting applications. In the following, I briefly outline some future prospects and suggestions.

8.1. Anderson localization in disordered quantum walks

The one-dimensional quantum walk of a single atom in an optical lattice can be used to observe localization phenomena similar to those described by Anderson in Ref. [188], in which imperfect crystals are modeled by an independent and identically distributed random potential. Investigation of such walks may be classified as a kind of quantum simulation of simple transport phenomena in solid-state physics. For this purpose, the walker has to be subjected to disorder induced by a random position-dependent coin [189]. Such coin can be realized by applying a sequence of microwave pulses in the presence of a magnetic field gradient, by stepwise adjusting the pulse frequency to the position-dependent $|0\rangle \leftrightarrow |1\rangle$ transition frequency of each lattice site in the walking region. Spatial randomness can be introduced by alternating pulse phases during the pulse sequence, which are read from a previously generated list of random values with a predefined distribution. However, since for N time steps the walking region comprises $2N + 1$ lattice sites, a sequence of $2N - 1$ microwave pulses have to be applied in each time step of the walk, significantly extending the duration of the single repetition of the sequence far above our current homogeneous dephasing time. Such quantum walk would therefore increasingly suffer from decoherence, resulting in a classical distribution.

For this reason, we rather prefer another approach: Instead of using a sequence of randomized coins in a magnetic field gradient and thus a well-defined environment, a single coin in a (quasi-)random spatially distorted environment can be equivalently used, suppose that this distortion translates into a random position-dependent $|0\rangle \leftrightarrow |1\rangle$ transition frequency or the accumulated phase of the matter wave components during coin operations. Such random spatially distorted environment can be formed by superimposing the optical lattice with additional standing wave light fields generated by far-detuned counterpropagating laser beams ($\lambda_{\mathrm{add}} \gg \lambda$). The

amount of spatial randomness can be increased by intentionally introducing optical aberrations in the incident beams before they are coupled in along the lattice axis and retro-reflected. The magnitude of the resulting potential distortion can be adjusted by the power of these beams. The additional standing wave light fields can be fast switched on whenever distortion is required, i.e. prior to each coin operation of the walk, and switched off during the transport or preparation of the walker's initial qubit state. Since drifts of the optical lattice have been proven to be negligible on the time scale of a single repetition of a quantum walk sequence, the interference patterns of the additional light fields must not be necessarily stabilized with respect to the optical lattice. Drifts from one sequence repetition to another would give rise to inhomogeneous dephasing, which however is expected to play a marginal role in the localization phenomena [190].

8.2. Implementation of a two-qubit gate

One of the most interesting applications of the state-selective transport is the realization of a fundamental two-qubit gate relying on coherent cold collisions between matter wave components [37, 41]. Besides improving coherence properties of our system, full control over accumulation of phases is required. For this reason, atoms have to be prepared in the purest possible quantum state by cooling them to the motional ground state. Cooling of atoms to the ground state of axial motion has recently been implemented in our experimental setup [68, 129]. Further steps focusing on cooling to the ground state of radial motion are underway. Once we are able to prepare the atoms in the motional ground state, the following scheme can be applied to experimentally realize fundamental two-qubit gates.

Consider two neighboring atoms at positions $k_0 = \pm 1$ in the lattice, each initialized into qubit basis state $|0\rangle$, i.e. atom "1" in state $|0,-1\rangle_1$ and atom "2" in state $|0,1\rangle_2$. This initial configuration can be written as a product state $|0,-1\rangle_1|0,1\rangle_2$. Using a $\pi/2$-pulse both atoms are brought into an superposition of the qubit basis states $|0\rangle$ and $|1\rangle$, resulting in the initial state

$$|\Psi_{\mathrm{ini}}\rangle = \frac{1}{2}\left(|0,-1\rangle_1|0,1\rangle_2 + i|0,-1\rangle_1|1,1\rangle_2 + i|1,-1\rangle_1|0,1\rangle_2 - |1,-1\rangle_1|1,1\rangle_2\right) . \tag{8.1}$$

By successively applying a single step of the state selective transport (here $\hat{S}_\uparrow$, see Eq. (4.43)), the matter wave components of both atoms are delocalized, each accumulating a state-dependent phase $\varphi_{|j\rangle}$ ($j = \{0,1\}$) during the shift[1] until finally two components are brought together to common lattice site $k = 0$, see Fig. 8.1(a). Due to collisional interaction [37], they acquire an additional distinct phase, given

[1] Since we consider both atoms in the motional ground state, the multiple index vector $\boldsymbol{n} = \mathbf{0}$ in the phase has been dropped.

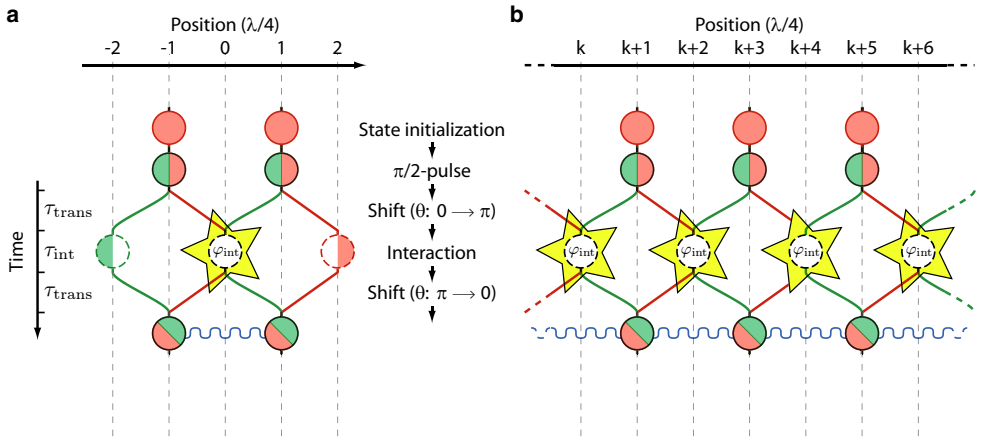

Figure 8.1.: (**a**) Schematic sequence of a two-qubit gate employing state-selective transport and coherent cold collisions [37] resulting in a collisional phase φ_{int}, see Eq. (8.2). Symbols, paths and colors are identical to those in Fig. 3.7. (**b**) Extension for generation of entangled clusters of neighboring atoms, which form the basis of a quantum cellular automata [17, 18].

by

$$\varphi_{\mathrm{int}} = \frac{1}{\hbar} \int_0^{\tau_{\mathrm{int}}} \Delta E(t)\, \mathrm{d}t\,, \tag{8.2}$$

where τ_{int} denotes the interaction time and

$$\Delta E(t) = \frac{4\pi a_{\mathrm{s}} \hbar^2}{m_{\mathrm{Cs}}} \int |\psi_1(\boldsymbol{r}, t)|^2 |\psi_2(\boldsymbol{r}, t)|^2 \, \mathrm{d}\boldsymbol{r} \tag{8.3}$$

the time-dependent energy shift with the s-wave scattering length a_{s} and the ground state wave functions $\psi_1(\boldsymbol{r})$ and $\psi_2(\boldsymbol{r})$ of atoms in the common potential well of the lattice. Finally, by recombining the delocalized matter waves of both atoms on the initial lattice sites, the respective contributions to the initial state transform as follows

$$|0,-1\rangle_1 |0,1\rangle_2 \to e^{4i\varphi_{|0\rangle}} |0,-1\rangle_1 |0,1\rangle_2 \tag{8.4a}$$
$$|0,-1\rangle_1 |1,1\rangle_2 \to e^{i(2\varphi_{|0\rangle}+2\varphi_{|1\rangle})+i\varphi_{\mathrm{int}}} |0,-1\rangle_1 |1,1\rangle_2 \tag{8.4b}$$
$$|1,-1\rangle_1 |0,1\rangle_2 \to e^{2i(\varphi_{|0\rangle}+\varphi_{|1\rangle})} |1,-1\rangle_1 |0,1\rangle_2 \tag{8.4c}$$
$$|1,-1\rangle_1 |1,1\rangle_2 \to e^{4i\varphi_{|1\rangle}} |1,-1\rangle_1 |1,1\rangle_2\,. \tag{8.4d}$$

This transformation corresponds to a fundamental two-qubit gate [191]. The single qubit phases $\varphi_{|j\rangle}$ can be precompensated either in the preparation of the initial state or by extending the shift operation by a spin-echo rephasing π-pulse (see Eq. (6.14))

while starting the sequence with next-nearest neighboring atoms ($k_0 = \pm 2$). Alternatively, other qubit basis states can be used as proposed in Sec. 5.1.1.

The above scheme is scalable to a larger number of qubits (see Fig. 8.1(b)), paving the way for generation of multi-particle entangled clusters of neighboring atoms. Sequential operations of one and two-qubit gate operations with predefined interaction phases can be used to experimentally realize a quantum cellular automata [17, 18] in the future.

A. Software

A part of this thesis has been devoted to the development of computer software which has to deal with different types of tasks, ranging from control of experimental processes over acquisition of fluorescence images up to real-time or post-analysis of the acquired data. In the following sections, a short overview over the most important self-developed software is given.

A.1. Control Center

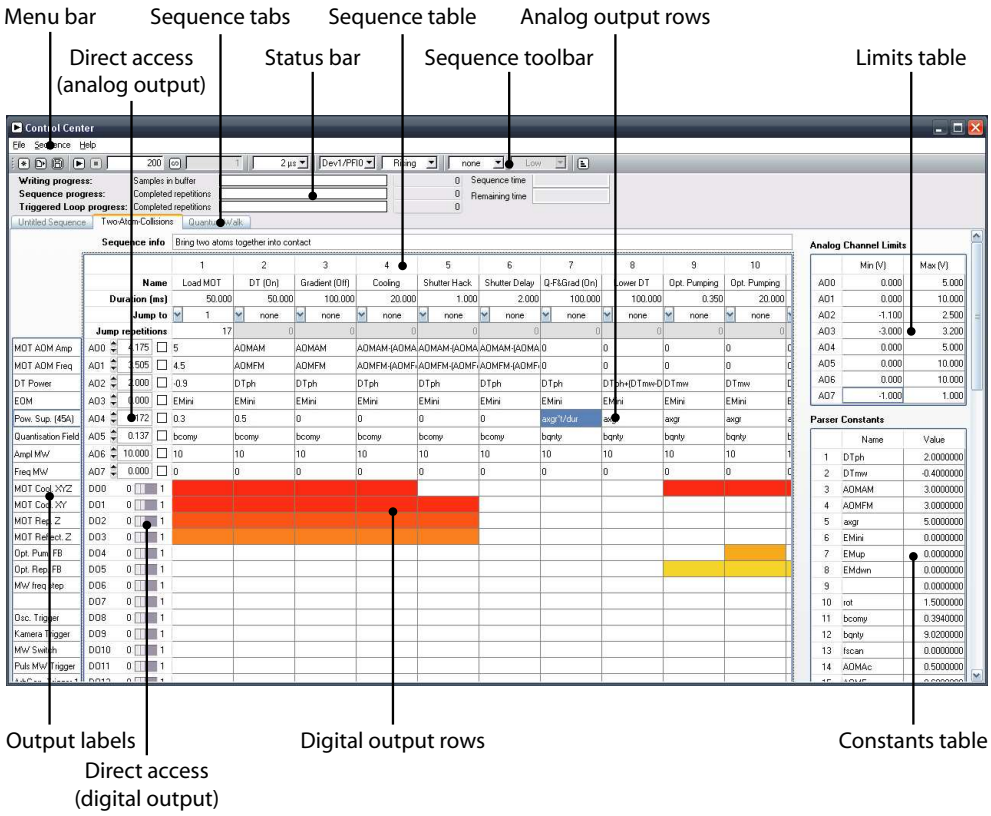

Figure A.1.: Graphical user interface of the software "Control Center". For details, see text.

Most experimental parameters or processes are voltage controlled by multiple analog or digital signals which are joined together in complex sequences. To rapidly design

and precisely control any arbitrary sequence, a software called "Control Center" has been developed. The software is written in ANSI C using LabWindows/CVI 8.5 (National Instruments) — an integrated development environment (IDE) which provides a set of programming tools for graphical user interface (GUI) and the DAQmx function library (National Instruments) to access the multifunction data acquisition boards, see Sec. 1.3. The Control Center provides a graphical user interface for sequence design which consists of a main window containing a menu bar, a toolbar, a status bar, several buttons, fields and parameter tables and finally a spreadsheet panel, see Fig. A.1. In the following, functions of the respective GUI elements are shortly summarized.

Sequence toolbar The sequence toolbar contains buttons and fields for accessing common commands and global parameters of the sequence. Details are shown in Fig. A.2.

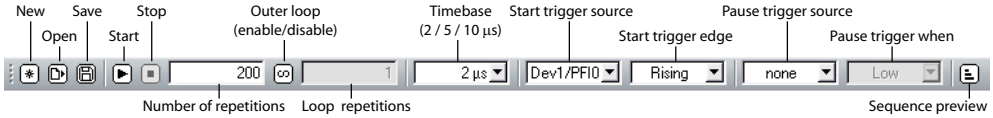

Figure A.2.: Sequence toolbar for accessing common commands and global parameters of the sequence.

Sequence table The columns of the spreadsheet panel define the sequence blocks, which subdivide the experimental sequence into separate logical parts of simultaneous output signals from the 8 analog and 64 digital channels. The signal of each channel is defined in the respective row of the spreadsheet, which for overview reason can be individually labeled. The subdivision of the sequence into blocks depends primarily on the digital signals, which can either be set to a high or to a low level for the total duration of the block, whereas analog signals are arbitrarily defined using mathematical expressions entered in the respective fields of the spreadsheet and parsed by a mathematical parser. A built-in preview function, allows to directly check the parsed signal, see Fig. A.3.

The mathematical parser supports numbers, arbitrary self-defined constants[1] with up to 5 characters entered in fields of the constants table (see Fig. A.1) and the four basic arithmetic operations (`+`, `-`, `*`, `/`) evaluated in the order of precedence. It is case-insensitive and supports parenthesis and standard mathematical expressions, including the square-root function `sqrt()`, the absolute value `abs()`, the sign function `sign()`, the natural logarithm `ln()`, the exponential function `exp()`, the trigonometric functions `sin()`, `cos()`, `tan()`, `cot()` and their inverses `asin()`, `acos()`, etc. Hyperbolic functions `sinh()`, `cosh()`, `tanh()`, `coth()` and their inverses `asinh()`, `acosh()`, etc.,

[1] Some constants are already predefined, e.g. the mathematical constant `pi`.

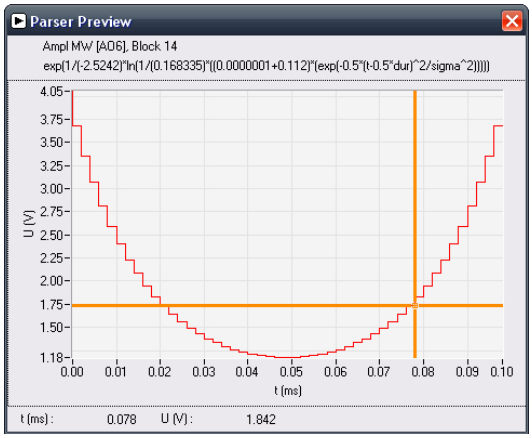

Figure A.3.: Parser preview. The preview window shows a signal parsed from a mathematical expression of a selected field in the spreadsheet panel.

are also supported. The parser comprises a list of predefined variables which are dynamically adjusted during sequence design or a running sequence, including the block duration `dur`, the current sequence repetition `rep` and the total number of sequence repetitions `numrep`. The control variable in each block is `t`, defining the time in milliseconds elapsed since the beginning of the block ($\texttt{t} \in [0, \texttt{dur}]$).

In the spreadsheet panel, blocks can be added, deleted, duplicated, copied and pasted at any position. The same holds for any entry in their fields. Furthermore, simultaneous selection and manipulation of multiple fields are permitted, allowing for instance, to change the level of several digital channels over multiple sequence blocks at once.

Once the sequence is precompiled, loaded into computer's memory and started, the sequence blocks are successively played from left to right. Optionally, for each sequence block, a "jump to" operation and its number of repetitions can be defined, permitting jumps to any previous sequence block. By this, arbitrary inner sequence loops with a preset number of loop repetitions can be defined. Such loops, for instance, have been employed in the patterning sequence, see Sec. 3.4.4. It should be noted that the duration of a single sequence repetition is limited by the computer's memory.

Sequence tabs The Control Center provides a tabbed sequence interface, allowing to work with multiple sequences in a single window.

Status bar The status bar displays the status of a running sequence, including the number of sampling points, current sequence repetition, total sequence duration and an estimation of remaining sequence time.

Limits table In the limits table, upper and lower voltage limits for each analog

output channel can be defined. These limits are usually used to prevent the controlled devices from overvoltage. Analog signals, the output voltage of which lie outside the respective limits are just clipped at the level of the limits.

Direct access panels Direct access panels permit a direct access to any analog or digital channel without starting the sequence, switching them on and off or setting the required voltage.

A.2. iXacq

To acquire, analyze, display and store fluorescence images of atoms in real-time, a self-developed software called "iXacq" is used. This software is also written in ANSI C using LabWindows/CVI 8.5 and a software development kit (SDK, Andor, version 2.77[2]) which provides a suite of functions to access our EMCCD camera, see Sec. 2.2.1. The imaging software provides a multiple document interface (MDI) with freely scalable windows within a single parent window, see Fig. A.4. It is modularly designed to be easily extended in the future. Similar to the Control Center, the imaging software also provides typical user interface elements, including menu bars, toolbars, status bars and parameter tables. In the following, functions of the most important elements are shortly summarized.

Device settings The most common settings to configure and control the EMCCD camera are gathered and clearly structured in a settings table embedded in a side-panel of the parent window. The setting table can be saved to and loaded from a predefined configuration file, employing the standard INI format.

Device information The device information side-panel provides all relevant information, parts of which are regularly read out from the camera, e.g. detector temperature, but also information about the CCD chip, the controller, the firmware and driver version. They are all gathered in a clearly structured table.

Deconvolution settings The deconvolution settings side-panel comprises a table with all relevant settings used for the parametric deconvolution, see Sec. 2.3.5.

Imaging widow The freely movable and resizable imaging window displays acquired images and the respective horizontal and vertical intensity distributions either binned or determined along both orthogonal lines of a cross line cursor in real-time. It provides a build-in zoom in, zoom out and zoom selection function and can optionally display results of image segmentation, atom number estimation and positions of the atoms obtained from the parametric deconvolution.

[2]Note that there are some incompatibility issues with newer versions of the Andor SDK, which could not be solved so far.

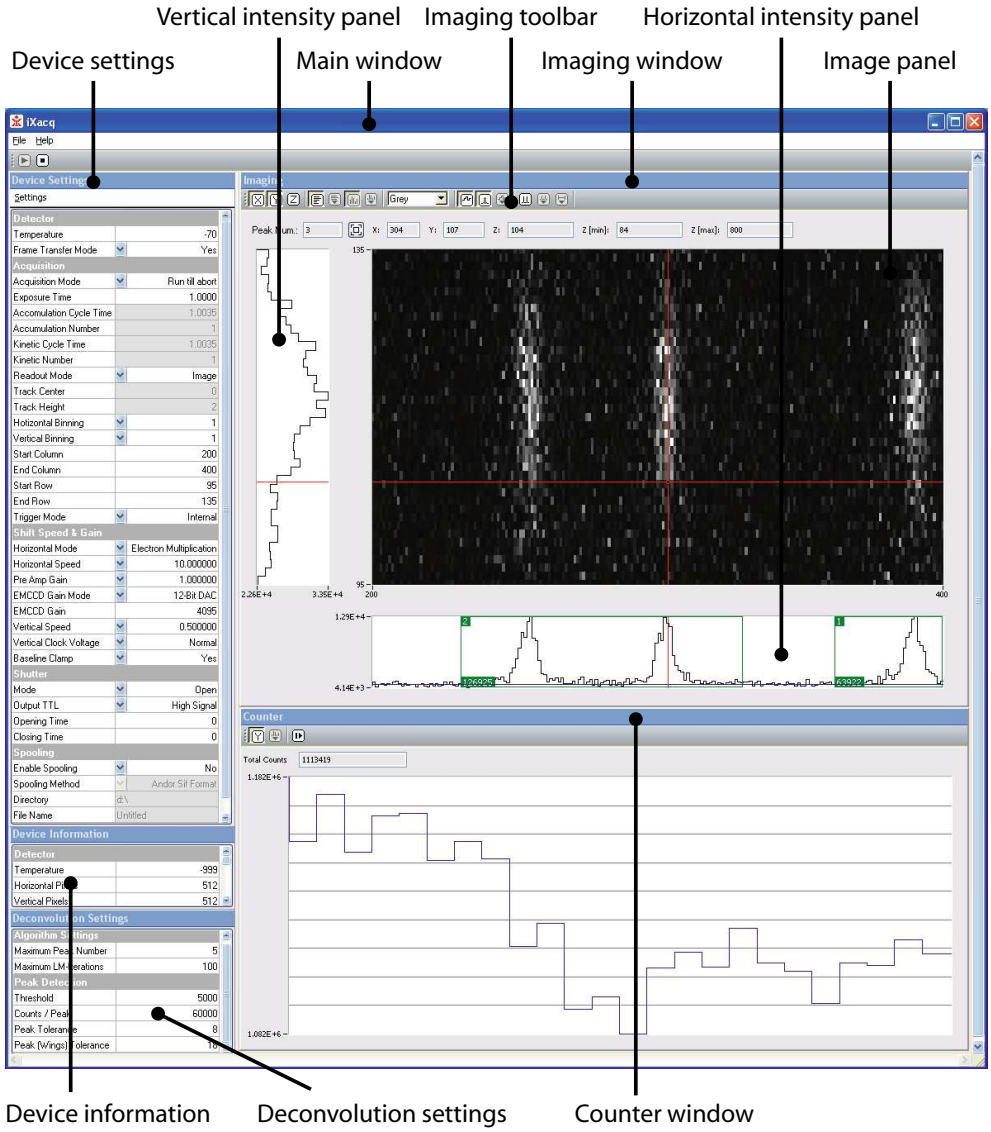

Figure A.4.: Multiple document interface of the imaging software "iXacq". For details, see text.

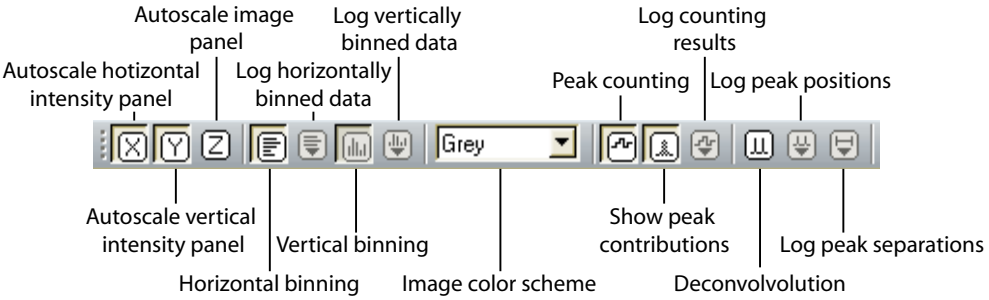

Figure A.5.: Imaging window toolbar.

Besides a status bar displaying the intensity level of a pixel at the cursor position, the imaging window provides a separate toolbar with buttons and fields for accessing display and image analysis settings. Details of this toolbar are shown in Fig. A.5.

Counter window The counter window displays the total fluorescence signal in the region of interest as a function of acquired image. This features is typically used for investigations employing a large number of atoms providing a high fluorescence signal level, e.g. atoms in a MOT. It can be also used to monitor drifts in the background signal level.

The acquired images are usually stored in an Andor SIF multi-channel image file which can be opened and converted into other file formats using "Andor Solis" — a software supplied with the EMCCD camera, or the self-developed software called "Post Deconvolution", see App. A.4. The latter provides additional features to post-analyze fluorescence images of atoms. Results of real-time analyzed data are optionally stored into dedicated, separated files in ASCII[3] format, together with device settings and additional information which allow to easily reconstruct the acquisition process afterwards.

A.3. WaveGen

Timing-critical applications require that driving ramps of the EOM amplifier (see Sec. 4.3) and microwave pulse triggers (see Sec. 3.2.2) are rather controlled by arbitrary waveform generators than by multifunction data acquisition boards of the computer, since the former provide a higher bandwidth (80 MHz for Agilent 33250A) or (20 MHz for Agilent 33220A) compared to the latter (500 kHz). To rapidly design, modify and transfer arbitrary waveforms and pulse sequences, and control the generators from the computer, a software called "WaveGen" has been developed. It is written in ANSI C using LabWindows/CVI 8.5, employing standard commands for programmable instruments (SCPI) for the data transfer over GPIB.

[3] ASCII: American Standard Code for Information Interchange.

The software provides a graphical user interface containing a spreadsheet panel,

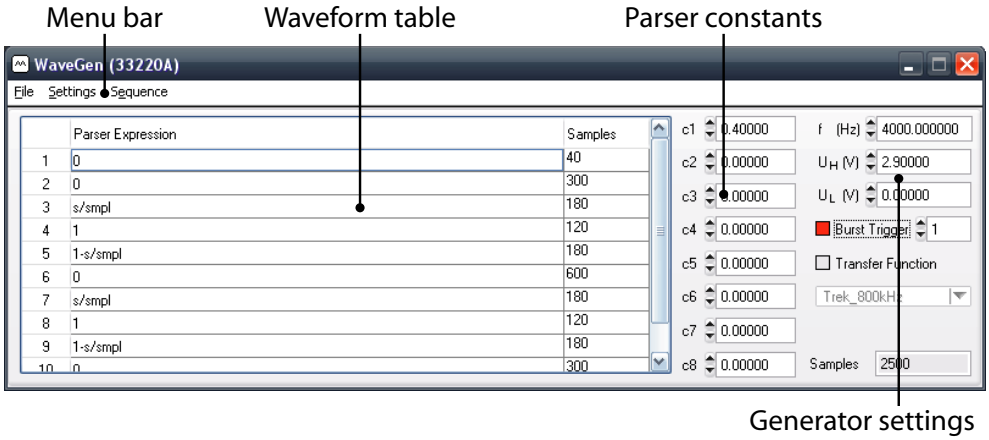

Figure A.6.: Graphical user interface of the software "WaveGen".

see Fig. A.6. Analogous to the Control Center, the waveform is compiled from sequence blocks which are defined in rows of the spreadsheet (waveform table) using mathematical expressions. The latter are then parsed by a mathematical parser, which supports the same functions as that of the Control Center, albeit with some differences arising from the operation principle of the generators: First, the control variable in each block `s` and the block duration variable `smpl` are entered in units of samples. The duration of a sample is defined by

$$\Delta s = \frac{1}{N \cdot \nu} \tag{A.1}$$

where N denotes the total number of samples and ν the operating frequency of the generator entered in a dedicated numeric field. Second, the codomain of a parameterized waveform function $f(s)$ is restricted to the interval $[-1, 1] \subset \mathbb{R}$, i.e. $f : S \subset \mathbb{R} \to [-1, 1]$, $s \mapsto f(s)$. For $f(s) > 1$ and $f(s) < -1$ the function value is clipped, i.e. it is subsequently set to $+1$ and -1, respectively. The parameter function is then transformed into an output voltage signal according to

$$U(s) = \begin{cases} \dfrac{U_\mathrm{H} - U_\mathrm{L}}{f_\mathrm{max} - f_\mathrm{min}}(f(s) - f_\mathrm{min}) + U_\mathrm{L} & \text{for} \quad f_\mathrm{max} \neq f_\mathrm{min}\,, \\ 0 & \text{else}\,, \end{cases} \tag{A.2}$$

where $f_\mathrm{max} = \max\{f(s)|s \in S\}$, $f_\mathrm{min} = \min\{f(s)|s \in S\}$, while U_L and U_H denote the lower and upper voltage level, respectively. Both voltage levels can be preset in the respective fields of the generator settings, see Fig. A.6. Finally, only eight predefined parser constants `c1`, ..., `c8` are supported.

Waveforms can be saved to and loaded from a file in ASCII format, together with the configuration of the generator and the respective GPIB address. Furthermore,

the software provides a build-in feature allowing to generate an output signal with precompensated influence of the transfer function of a linear, time-invariant system. A list of transfer functions can be directly loaded from multiple ASCII files.

A.4. Post Deconvolution

In most cases, it is more advantageous to post-analyze the acquired fluorescence images rather then inferring the results in real-time. This is especially important when the line spread function or other deconvolution parameters are not precisely known before the acquisition process and need to be inferred from the images afterwards. For this purpose a software called "Post Deconvolution" has been developed. Just like any other software in this thesis, this software is also written in ANSI C using LabWindows/CVI 8.5, whereas parts of numerical algorithms are adopted from Numerical Recipes [109]. The software provides a graphical user interface with a display panel for results of the parametric deconvolution. This is particularly useful for adjusting the threshold level and the wings of each atom's distribution, see Sec. 2.3.1. Furthermore, it provides a preview of the estimated baseline, the regions

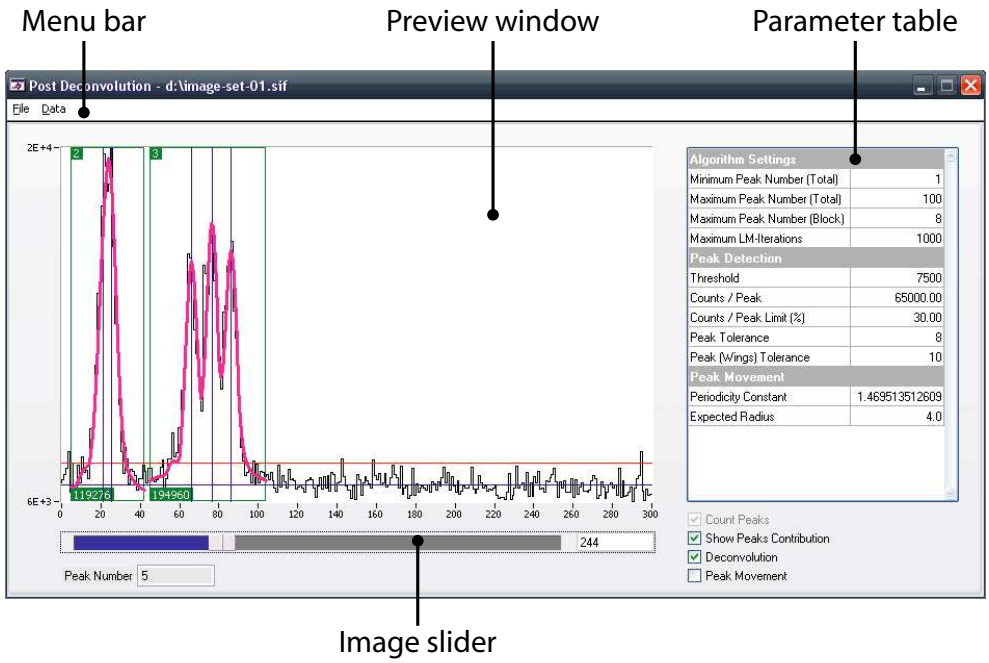

Figure A.7.: Graphical user interface of the software "Post Deconvolution".

of interest (ROIs), the number of atoms and the atomic positions, see Fig. A.7. The deconvolution settings are clearly structured in a dedicated parameter table. An image slider allows to browse between the acquired images. In addition, the software permits to automatically analyze transport data, calculating the relative positions of the atoms while considering uniqueness issues discussed in Sec. 4.5.3.

The post-deconvolution software supports the Andor SIF multi-channel image file format, allowing to directly access the raw data as inferred from the EMCCD camera. Besides the analysis of a single selected file, it also provides a batch operation mode which permits to successively analyze multiple files at different locations. For this, the names and paths of the SIF files have to be entered in a batch file, which is then processed by the software. Results of the analyzed data are stored at the same location as the original SIF file in dedicated ASCII files with a characteristic suffix:

[SIF file]_num_post.dat In this file, the estimated numbers of atoms are stored.

[SIF file]_ppos_post.dat This file contains the calculated positions of atoms in units of pixels. Each result is preceded with comment lines starting with the character `#`. These comment lines provide information on the image number, the background baseline value, positions and sizes of the ROIs from which the atom positions have been inferred and the chi-squared fitting error. Besides positions of the atoms, their fluorescence contributions are also stored. Erroneous results, which fail the reliability criterion (see Sec. 2.3.7) are marked with a preceding comment `#ERROR`, so that they can be easily found in the file for root cause analysis.

[SIF file]_dist_post.dat In this file, calculated separations between atoms in units of pixels are stored. Results are preceded with a comment line which indicates the respective image number.

[SIF file]_trans.dat This file contains the relative positions of transported atoms in both, units of pixels and lattice sites as inferred from successively acquired image pairs. A preceded comment line indicates the image numbers of the respective image pair.

[SIF file]_settings.log In this file, settings from the parameter table (see Fig. A.7) are stored, to easily reconstruct the deconvolution process afterwards.

Note that names, formats and contents of files stored by the real-time analysis module of the software "iXacq" are similar to those presented above, only the suffix "_post" is missing for distinction purposes.

Bibliography

[1] R. P. Feynman, *Quantum Mechanical Computers*, Opt. News **11**, 11–20 (1985)

[2] S. Lloyd, *Almost Any Quantum Logic Gate is Universal*, Phys. Rev. Lett. **75**, 346–359 (1995)

[3] Y. Aharonov, L. Davidovich, and N. Zagury, *Quantum random walks*, Phys. Rev. A **48**, 1687–1690 (1993)

[4] J. Kempe, *Quantum random walks: an introductory overview*, Contemp. Phys. **44**, 307–327 (2003)

[5] A. M. Childs, *Universal Computation by Quantum Walk*, Phys. Rev. Lett. **102**, 180501 (2009)

[6] N. B. Lovett, S. Cooper, M. Everitt, M. Trevers, and V. Kendon, *Universal quantum computation using the discrete time quantum walk*, arXiv:0910.1024 (2009)

[7] A. M. Childs, R. Cleve, E. Deotto, E. Farhi, S. Gutmann, and D. A. Spielman, *Exponential algorithmic speedup by a quantum walk*, in *STOC '03: Proceedings of the thirty-fifth annual ACM symposium on Theory of computing*, 59–68, ACM Press, New York, NY, USA (2003)

[8] M. Barber, *Random and Restricted Walks: Theory and Applications*, Gordon and Breach, New York, 1st edition (1970)

[9] J. B. Anderson, *Quantum chemistry by random walk.*, J. Chem. Phys. **65**, 4121–4127 (1976)

[10] H. C. Berg, *Random Walks in Biology*, Princeton University Press, revised edition (1993)

[11] E. F. Fama, *Random Walks in Stock Markets*, Financ. Anal. J **21**, 55–59 (1965)

[12] M. Rosenblatt, *Random Processes*, Oxford University Press (1962)

[13] L. K. Grover, *Quantum Mechanics Helps in Searching for a Needle in a Haystack*, Phys. Rev. Lett. **79**, 325–328 (1997)

[14] P. W. Shor, *Polynomial-Time Algorithms for Prime Factorization and Discrete Logarithms on a Quantum Computer*, SIAM J. Comput. **26**, 1484–1509 (1997)

[15] A. Ekert and R. Jozsa, *Quantum computation and Shor's factoring algorithm*, Rev. Mod. Phys. **68**, 733–753 (1996)

[16] R. Raussendorf and H. J. Briegel, *A One-Way Quantum Computer*, Phys. Rev. Lett. **86**, 5188–5191 (2001)

[17] R. Raussendorf, *Quantum cellular automaton for universal quantum computation*, Phys. Rev. A **72**, 022301 (2005)

[18] D. J. Shepherd, T. Franz, and R. F. Werner, *Universally Programmable Quantum Cellular Automaton*, Phys. Rev. Lett. **97**, 020502 (2006)

[19] D. P. DiVincenzo, *The Physical Implementation of Quantum Computation*, Fortschr. Phys. **48**, 771–783 (2000)

[20] D. Leibfried, R. Blatt, C. Monroe, and D. Wineland, *Quantum dynamics of single trapped ions*, Rev. Mod. Phys. **75**, 281–324 (2003)

[21] L. M. K. Vandersypen and I. L. Chuang, *NMR techniques for quantum control and computation*, Rev. Mod. Phys. **76**, 1037–1069 (2005)

[22] Y. Makhlin, G. Schön, and A. Shnirman, *Quantum-state engineering with Josephson-junction devices*, Rev. Mod. Phys. **73**, 357–400 (2001)

[23] Q. A. Turchette, C. S. Wood, B. E. King, C. J. Myatt, D. Leibfried, W. M. Itano, C. Monroe, and D. J. Wineland, *Deterministic Entanglement of Two Trapped Ions*, Phys. Rev. Lett. **81**, 3631–3634 (1998)

[24] C. A. Sackett, D. Kielpinski, B. E. King, C. Langer, V. Meyer, C. J. Myatt, M. Rowe, Q. A. Turchette, W. M. Itano, D. J. Wineland, and C. Monroe, *Experimental entanglement of four particles*, Nature **404**, 256–259 (2000)

[25] S. Gulde, M. Riebe, G. P. T. Lancaster, C. Becher J. Eschner, H. Häffner, F. Schmidt-Kaler, I. L. Chuang, and R. Blatt, *Implementation of the Deutsch-Jozsa algorithm on an ion-trap quantum computer*, Nature **421**, 48–50 (2003)

[26] I. L. Chuang, N. Gershenfeld, and M. Kubinec, *Experimental Implementation of Fast Quantum Searching*, Phys. Rev. Lett. **80**, 3408–3411 (1998)

[27] L. M. K. Vandersypen, M. Steffen, G. Breyta, C. S. Yannoni, M. H. Sherwood, and I. L. Chuang, *Experimental realization of Shor's quantum factoring algorithm using nuclear magnetic resonance*, Nature **414**, 883–887 (2001)

[28] R. Grimm, M. Weidemüller, and Y. B. Ovchinnikov, *Optical dipole traps for neutral atoms*, Adv. At. Mol. Opt. Phys. **42**, 95–170 (2000)

[29] M. Lewenstein, A. Sanpera, V. Ahufinger, B. Damski, A. Sen, and U. Sen, *Ultracold atomic gases in optical lattices: mimicking condensed matter physics and beyond*, Adv. Phys. **56**, 243–379 (2007)

[30] I. Bloch, J. Dalibard, and W. Zwerger, *Many-body physics with ultracold gases*, Rev. Mod. Phys. **80**, 885–964 (2008)

[31] T. Pellizzari, S. A. Gardiner, J. I. Cirac, and P. Zoller, *Decoherence, Continuous Observation, and Quantum Computing: A Cavity QED Model*, Phys. Rev. Lett. **75**, 3788–3791 (1995)

[32] A. Rauschenbeutel, G. Nogues, S. Osnaghi, P. Bertet, M. Brune, J. M. Raimond, and S. Haroche, *Coherent Operation of a Tunable Quantum Phase Gate in Cavity QED*, Phys. Rev. Lett. **83**, 5166–5169 (1999)

[33] L. You, X. X. Yi, and X. H. Su, *Quantum logic between atoms inside a high-Q optical cavity*, Phys. Rev. A **67**, 032308 (2003)

[34] D. Jaksch, J. I. Cirac, P. Zoller, S. L. Rolston, R. Côté, and M. D. Lukin, *Fast Quantum Gates for Neutral Atoms*, Phys. Rev. Lett. **85**, 2208–2211 (2000)

[35] L. Isenhower, E. Urban, X. L. Zhang, A. T. Gill, T. Henage, T. A. Johnson, T. G. Walker, and M. Saffman, *Demonstration of a Neutral Atom Controlled-NOT Quantum Gate*, Phys. Rev. Lett. **104**, 010503 (2010)

[36] T. Wilk, A. Gaëtan, C. Evellin, J. Wolters, Y. Miroshnychenko, P. Grangier, and A. Browaeys, *Entanglement of Two Individual Neutral Atoms Using Rydberg Blockade*, Phys. Rev. Lett. **104**, 010502 (2010)

[37] D. Jaksch, H.-J. Briegel, J. I. Cirac, C. W. Gardiner, and P. Zoller, *Entanglement of Atoms via Cold Controlled Collisions*, Phys. Rev. Lett. **82**, 1975–1978 (1999)

[38] D. Jaksch, C. Bruder, J. I. Cirac, C. W. Gardiner, and P. Zoller, *Cold Bosonic Atoms in Optical Lattices*, Phys. Rev. Lett. **81**, 3108–3111 (1998)

[39] M. Greiner, O. Mandel, T. Esslinger, T. W. Hänsch, and I. Bloch, *Quantum phase transition from a superfluid to a Mott insulator in a gas of ultracold atoms*, Nature **415**, 39–44 (2002)

[40] O. Mandel, M. Greiner, A. Widera, T. Rom, T. W. Hänsch, and I. Bloch, *Coherent Transport of Neutral Atoms in Spin-Dependent Optical Lattice Potentials*, Phys. Rev. Lett. **91**, 010407 (2003)

[41] O. Mandel, M. Greiner, A. Widera, T. Rom, T. W. Hänsch, and I. Bloch, *Controlled collisions for multi-particle entanglement of optically trapped atoms*, Nature **425**, 937–940 (2003)

[42] D. P. DiVincenzo, *Quantum Computation*, Science **270**, 255–261 (1995)

[43] I. Dotsenko, W. Alt, M. Khudaverdyan, S. Kuhr, D. Meschede, Y. Miroshnychenko, D. Schrader, and A. Rauschenbeutel, *Submicrometer Position Control of Single Trapped Neutral Atoms*, Phys. Rev. Lett. **95**, 033002 (2005)

[44] T. Gericke, P. Würtz, D. Reitz, T. Langen, and H. Ott, *High-resolution scanning electron microscopy of an ultracold quantum gas*, Nat. Phys. **4**, 949–953 (2008)

[45] P. Würtz, T. Langen, T. Gericke, A. Koglbauer, and H. Ott, *Experimental Demonstration of Single-Site Addressability in a Two-Dimensional Optical Lattice*, Phys. Rev. Lett. **103**, 080404 (2009)

[46] S. Kuhr, W. Alt, D. Schrader, I. Dotsenko, Y. Miroshnychenko, W. Rosenfeld, M. Khudaverdyan, V. Gomer, A. Rauschenbeutel, and D. Meschede, *Coherence Properties and Quantum State Transportation in an Optical Conveyor Belt*, Phys. Rev. Lett. **91**, 213002 (2003)

[47] D. Schrader, I. Dotsenko, M. Khudaverdyan, Y. Miroshnychenko, A. Rauschenbeutel, and D. Meschede, *Neutral Atom Quantum Register*, Phys. Rev. Lett. **93**, 150501 (2004)

[48] M. Khudaverdyan, W. Alt, I. Dotsenko, L. Förster, S. Kuhr, D. Meschede, Y. Miroshnychenko, D. Schrader, and A. Rauschenbeutel, *Adiabatic quantum state manipulation of single trapped atoms*, Phys. Rev. A **71**, 031404(R) (2005)

[49] Stefan Kuhr, *A controlled quantum system of individual neutral atoms*, Ph.D. thesis, Rheinische Friedrich-Wilhelms-Universität Bonn (2003)

[50] W. Dür, R. Raussendorf, V. M. Kendon, and H.-J. Briegel, *Quantum walks in optical lattices*, Phys. Rev. A **66**, 052319 (2002)

[51] H. Schmitz, R. Matjeschk, Ch. Schneider, J. Glueckert, M. Enderlein, T. Huber, and T. Schaetz, *Quantum Walk of a Trapped Ion in Phase Space*, Phys. Rev. Lett. **103**, 090504 (2009)

[52] F. Zähringer, G. Kirchmair, R. Gerritsma, E. Solano, R. Blatt, and C. F. Roos, *Realization of a Quantum Walk with One and Two Trapped Ions*, Phys. Rev. Lett. **104**, 100503 (2010)

[53] G. K. Brennen, C. M. Caves, P. S. Jessen, and I. H. Deutsch, *Quantum Logic Gates in Optical Lattices*, Phys. Rev. Lett. **82**, 1060–1063 (1999)

[54] H. J. Briegel and R. Raussendorf, *Persistent Entanglement in Arrays of Interacting Particles*, Phys. Rev. Lett. **86**, 910–913 (2001)

[55] G. K. Brennen, I. H. Deutsch, and C. J. Williams, *Quantum logic for trapped atoms via molecular hyperfine interactions*, Phys. Rev. A **65**, 022313 (2002)

[56] T. W. Hänsch and A. L. Schawlow, *Cooling of gases by laser radiation*, Opt. Commun. **13**, 68–69 (1975)

[57] S. Chu, L. Hollberg, J. E. Bjorkholm, A. Cable, and A. Ashkin, *Three-dimensional viscous confinement and cooling of atoms by resonance radiation pressure*, Phys. Rev. Lett. **55**, 48–51 (1985)

[58] E. L. Raab, M. Prentiss, A. Cable, S. Chu, and D. E. Pritchard, *Trapping of Neutral Sodium Atoms with Radiation Pressure*, Phys. Rev. Lett. **59**, 2631–2634 (1987)

[59] G. A. Askaryan, *Effects of the gradient of a strong electromagnetic beam on electrons and atoms*, Sov. Phys. JETP **15**, 1088 (1962)

[60] V. S. Letokhov, *Doppler line narrowing in a standing light wave*, JETP Lett. **7**, 272 (1968)

[61] S. Chu, J. E. Bjorkholm, A. Ashkin, and A. Cable, *Experimental Observation of Optically Trapped Atoms*, Phys. Rev. Lett. **57**, 314–317 (1986)

[62] D. Haubrich, A. Höpe, and D. Meschede, *A simple model for optical capture of atoms in strong magnetic quadrupole fields*, Opt. Commun. **102**, 225–230 (1993)

[63] B. Ueberholz, S. Kuhr, D. Frese, D. Meschede, and V. Gomer, *Counting cold collisions*, J. Phys. B: At. Mol. Opt. Phys. **33**, 135–142 (2000)

[64] D. Frese, B. Ueberholz, S. Kuhr, W. Alt, D. Schrader, V. Gomer, and D. Meschede, *Single Atoms in an Optical Dipole Trap: Towards a Deterministic Source of Cold Atoms*, Phys. Rev. Lett. **85**, 3777–3780 (2000)

[65] W. Alt, D. Schrader, S. Kuhr, M. Müller, V. Gomer, and D. Meschede, *Single atoms in a standing-wave dipole trap*, Phys. Rev. A **67**, 033403 (2003)

[66] S. Kuhr, W. Alt, D. Schrader, I. Dotsenko, Y. Miroshnychenko, A. Rauschenbeutel, and D. Meschede, *Analysis of dephasing mechanisms in a standing-wave dipole trap*, Phys. Rev. A **72**, 023406 (2005)

[67] L. Förster, W. Alt, I. Dotsenko, M. Khudaverdyan, D. Meschede, Y. Miroshnychenko, S. Reick, and A. Rauschenbeutel, *Number-triggered loading and collisional redistribution of neutral atoms in a standing wave dipole trap*, New J. Phys. **8**, 259 (2006)

[68] Leonid Förster, *Microwave control of atomic motion in a 1D optical lattice*, Ph.D. thesis, Rheinische Friedrich-Wilhelms-Universität Bonn (2010)

[69] D. J. Wineland and W. M. Itano, *Laser cooling of atoms*, Phys. Rev. A **20**, 1521–1540 (1979)

[70] R. J. Cook, *Quantum-Mechanical Fluctuations of the Resonance-Radiation Force*, Phys. Rev. Lett. **44**, 976–979 (1980)

[71] J. Dalibard and C. Cohen-Tannoudji, *Laser cooling below the Doppler limit by polarization gradients: simple theoretical models*, J. Opt. Soc. Am. B **6**, 2023–2045 (1989)

[72] D. Haubrich, H. Schadwinkel, F. Strauch, B. Ueberholz, R. Wynands, and D. Meschede, *Observation of individual neutral atoms in magnetic and magneto-optical traps*, Europhys. Lett. **34**, 663–668 (1996)

[73] L. Ricci, M. Weidemüller, T. Esslinger, A. Hemmerich, C. Zimmermann, V. Vuletic, W. König, and T. W. Hänsch, *A compact grating-stabilized diode laser system for atomic physics*, Opt. Commun. **117**, 541–549 (1995)

[74] Florian Grenz, *Ein System zur entarteten Raman-Seitenbandkühlung einzelner Cäsium-Atome*, Master's thesis, Rheinische Friedrich-Wilhelms-Universität Bonn (2008)

[75] C. Wieman and T. W. Hänsch, *Doppler-Free Laser Polarization Spectroscopy*, Phys. Rev. Lett. **36**, 1170–1173 (1976)

[76] C. P. Pearman, C. S. Adams, S. G. Cox, P. F. Griffin, D. A. Smith, and I. G. Hughes, *Polarization spectroscopy of a closed atomic transition: applications to laser frequency locking*, J. Phys. B: At., Mol. Opt. Phys. **35**, 5141–5151 (2002)

[77] Wolfgang Alt, *Optical control of single neutral atoms*, Ph.D. thesis, Rheinische Friedrich-Wilhelms-Universität Bonn (2004)

[78] Daniel Döring, *Ein Experiment zum zustandsabhängigen Transport einzelner Atome*, Master's thesis, Rheinische Friedrich-Wilhelms-Universität Bonn (2007)

[79] Dominik Schrader, *A neutral atom quantum register*, Ph.D. thesis, Rheinische Friedrich-Wilhelms-Universität Bonn (2004)

[80] J. D. Jackson, *Classical Electrodynamics*, Wiley, New York, 2nd edition (1962)

[81] R. N. Palmer, C. Moura Alves, and D. Jaksch, *Detection and characterization of multipartite entanglement in optical lattices*, Phys. Rev. A **72**, 042335 (2005)

[82] Jaeyoon Cho, *Addressing Individual Atoms in Optical Lattices with Standing-Wave Driving Fields*, Phys. Rev. Lett. **99**, 020502 (2007)

[83] A. V. Gorshkov, L. Jiang, M. Greiner, P. Zoller, and M. D. Lukin, *Coherent Quantum Optical Control with Subwavelength Resolution*, Phys. Rev. Lett. **100**, 093005 (2008)

[84] K. D. Nelson, X. Li, and D. S. Weiss, *Imaging single atoms in a three-dimensional array*, Nat. Phys. **3**, 556–560 (2007)

[85] R. Scheunemann, F. S. Cataliotti, T. W. Hänsch, and M. Weitz, *Resolving and addressing atoms in individual sites of a CO_2-laser optical lattice*, Phys. Rev. A **62**, 051801 (2000)

[86] J. W. Goodman, *Introduction to Fourier Optics*, McGraw-Hill, New York (1996)

[87] L. Rayleigh, *Investigations in Optics, with special reference to the Spectroscope*, Phil. Mag. **8**, 261–274, 403–411, 477–486 (1879)

[88] J. L. Starck, E. Pantin, and F. Murtagh, *Deconvolution in Astronomy: A Review*, Publications of the Astronomical Society of the Pacific **114**, 1051–1069 (2002)

[89] Y. Miroshnychenko, W. Alt, I. Dotsenko, L. Förster, M. Khudaverdyan, D. Meschede, D. Schrader, and A. Rauschenbeutel, *Quantum engineering: An atom-sorting machine*, Nature **442**, 151 (2006)

[90] Wolfgang Alt, *An objective lens for efficient fluorescence detection of single atoms*, Optik **113**, 142–144(3) (2002)

[91] *CCD97-00 Front Illuminated 2-Phase IMO Series, Electron Multiplying CCD Sensor*, e2v technologies limited, Waterhouse Lane, Chelmsford, England (2003)

[92] D. J. Burt and R. T. Bell, *CCD Imagers with multiplication register* (2004)

[93] M. S. Robbins and B. J. Hadwen, *The noise performance of electron multiplying charge-coupled devices*, IEEE Transactions on Electron Devices **50**, 1227–1232 (2003)

[94] *Low Light Technical Note 5, An Overview of the Ageing Characteristics of L3Vision Sensors*, e2v technologies limited, Waterhouse Lane, Chelmsford, England (2006)

[95] David Dussault and Paul Hoess, *Noise performance comparison of ICCD with CCD and EMCCD cameras*, Proc. SPIE **5563**, 195–204 (2004)

[96] *Low-Light Technical Note 4, Dark Signal and Clock-Induced Charge in L3VisionTM CCD Sensors*, e2v technologies limited, Waterhouse Lane, Chelmsford, England (2004)

[97] Warren J. Smith, *Modern Optical Engineering: The Design of Optical Systems*, McGraw-Hill, New York, 3rd edition (2000)

[98] K. Fliegel, *Modeling and Measurement of Image Sensor Characteristics*, Radioengineering **13**, 27–34 (2004)

[99] H. H. Hopkins, *The Frequency Response of a Defocused Optical System*, Proc. R. Soc. Lond. A **231**, 91–103 (1955)

[100] P. A. Stokseth, *Properties of a Defocused Optical System*, J. Opt. Soc. Am. **59**, 1314–1321 (1969)

[101] K. R. Castleman, *Digital Image Processing*, Prentice Hall Professional Technical Reference, 1st edition (1979)

[102] J. Li, P. Agathoklis, F. Peet, G. Jensen, and T. Sahota, *Measurement and analysis of defocused point spread functions and optical transfer functions of a microscope*, in *Proceedings of IEEE Pacific Rim Conference on Communications, Computers, and Signal Processing*, 407–410 (1995)

[103] L. Li and T. P. Speed, *Parametric deconvolution of positive spike trains*, Ann. Statist. **28**, 1279–1301 (2000)

[104] K. Levenberg, *A Method for the Solution of Certain Problems in Least Squares*, Quart. Appl. Math. **2**, 164–168 (1944)

[105] D. W. Marquardt, *An Algorithm for Least-Squares Estimation of Nonlinear Parameters*, SIAM Journal on Applied Mathematics **11**, 431–441 (1963)

[106] Åke Björck, *Numerical Methods for Least Squares Problems*, Society for Industrial and Applied Mathematics, Philadelphia, PA, USA (1996)

[107] A. G. Basden, C. A. Haniff, and C. D. Mackay, *Photon counting strategies with low-light-level CCDs*, Mon. Not. R. Astron. Soc. **345**, 985–991 (2003)

[108] E. Lantz, J.-L. Blanchet, L. Furfaro, and F. Devaux, *Multi-imaging and Bayesian estimation for photon counting with EMCCDs*, Mon. Not. R. Astron. Soc. **386**, 2262–2270 (2008)

[109] W. H. Press, S. A. Teukolsky, W. T. Vetterling, and B. P. Flannery, *Numerical Recipes in C: The Art of Scientific Computing*, Cambridge University Press, 2nd edition (1992)

[110] Igor Dotsenko, *Single atoms on demand for cavity QED experiments*, Ph.D. thesis, Rheinische Friedrich-Wilhelms-Universität Bonn (2007)

[111] Y. Miroshnychenko, W. Alt, I. Dotsenko, L. Förster, M. Khudaverdyan, A. Rauschenbeutel, and D. Meschede, *Precision preparation of strings of trapped neutral atoms*, New J. Phys. **8**, 191 (2006)

[112] A. Gallagher and D. E. Pritchard, *Exoergic collisions of cold Na^*-Na*, Phys. Rev. Lett. **63**, 957–960 (1989)

[113] M. T. DePue, C. McCormick, S. L. Winoto, S. Oliver, and D. S. Weiss, *Unity Occupation of Sites in a 3D Optical Lattice*, Phys. Rev. Lett. **82**, 2262–2265 (1999)

[114] D. Sesko, T. Walker, C. Monroe, A. Gallagher, and C. Wieman, *Collisional losses from a light-force atom trap*, Phys. Rev. Lett. **63**, 961–964 (1989)

[115] A. K. Ekert, *Quantum cryptography based on Bell's theorem*, Phys. Rev. Lett. **67**, 661–663 (1991)

[116] N. Gisin, G. Ribordy, W. Tittel, and H. Zbinden, *Quantum cryptography*, Rev. Mod. Phys. **74**, 145–195 (2002)

[117] H. J. Briegel, W. Dür, J. I. Cirac, and P. Zoller, *Quantum Repeaters: The Role of Imperfect Local Operations in Quantum Communication*, Phys. Rev. Lett. **81**, 5932–5935 (1998)

[118] L.-M. Duan, M. D. Lukin, J. I. Cirac, and P. Zoller, *Long-distance quantum communication with atomic ensembles and linear optics*, Nature **414**, 413–418 (2001)

[119] W. Rakreungdet, J. H. Lee, K. F. Lee, B. E. Mischuck, E. Montano, and P. S. Jessen, *Accurate microwave control and real-time diagnostics of neutral-atom qubits*, Phys. Rev. A **79**, 022316 (2009)

[120] L. Allen and J. H. Eberly, *Optical Resonance and Two-Level Atoms*, Dover Publications (1987)

[121] J. Cavanagh, W. J. Fairbrother, A. G. Palmer III, M. Rance, and N. J. Skelton, *Protein NMR Spectroscopy: Principles and Practice*, Academic Press (2006)

[122] Arne Härter, *Ein Aufbau zur kohärenten Manipulation und zum zustandsabhängigen Transport einzelner Atome*, Master's thesis, Rheinische Friedrich-Wilhelms-Universität Bonn (2007)

[123] D. F. V. James, P. G. Kwiat, W. J. Munro, and A. G. White, *Measurement of qubits*, Phys. Rev. A **64**, 052312 (2001)

[124] M. Beck and M. Raymer, *Quantum State Estimation*, in Matteo Paris and Jaroslav Rehacek, eds., *Experimental Quantum State Tomography of Optical Fields and Ultrafast Statistical Sampling*, volume 649 of *Lecture Notes in Physics*, 235–295, Springer (2004)

[125] M. A. Nielsen and I. L. Chuang, *Quantum Computation and Quantum Information*, Cambridge University Press (2000)

[126] Z. Hradil and J. Řeháček, *Efficiency of Maximum-Likelihood Reconstruction of Quantum States*, Fortschr. Phys. **49**, 1083–1088 (2001)

[127] N. F. Ramsey, *Molecular Beams*, Oxford University Press, London (1956)

[128] N. F. Ramsey, *The method of successive oscillatory fields*, Phys. Today **33**, 25–30 (1980)

[129] L. Förster, M. Karski, J.-M. Choi, A. Steffen, W. Alt, D. Meschede, A. Widera, E. Montano, J. H. Lee, W. Rakreungdet, and P. S. Jessen, *Microwave Control of Atomic Motion in Optical Lattices*, Phys. Rev. Lett. **103**, 233001 (2009)

[130] E. L. Hahn, *Spin Echoes*, Phys. Rev. **80**, 580–594 (1950)

[131] M. F. Andersen, A. Kaplan, and N. Davidson, *Echo Spectroscopy and Quantum Stability of Trapped Atoms*, Phys. Rev. Lett. **90**, 023001 (2003)

[132] H. Y. Carr and E. M. Purcell, *Effects of Diffusion on Free Precession in Nuclear Magnetic Resonance Experiments*, Phys. Rev. **94**, 630–638 (1954)

[133] S. Meiboom and D. Gill, *Compensation for pulse imperfections in Carr-Purcell NMR experiments*, Rev. Sci. Instrum. **29**, 688–691 (1958)

[134] G. D. Grier, *A revolution in optical manipulation*, Nature **424**, 810–816 (2003)

[135] J. Fortagh and C. Zimmermann, *Magnetic microtraps for ultracold atoms*, Rev. Mod. Phys. **79**, 235–289 (2007)

[136] C. G. Townsend, N. H. Edwards, C. J. Cooper, K. P. Zetie, C. J. Foot, A. M. Steane, P. Szriftgiser, H. Perrin, and J. Dalibard, *Phase-space density in the magneto-optical trap*, Phys. Rev. A **52**, 1423–1440 (1995)

[137] M. H. Levitt, *Encyclopedia of Nuclear Magnetic Resonance*, chapter Composite Pulses, 1396–1411, Wiley (1996)

[138] Z. Starčuk and V. Sklenář, *Composite Pulse Sequences with Variable Performance*, J. Magn. Reson. **62**, 113 (1985)

[139] F. Schwabl, *Quantenmechanik - QMI*, Springer, Heidelberg, 6th edition (2002)

[140] D. A. Steck, *Cesium D Line Data*, Technical report, Los Alamos National Laboratory (1998)

[141] W. Hänsel, J. Reichel, P. Hommelhoff, and T. W. Hänsch, *Trapped-atom interferometer in a magnetic microtrap*, Phys. Rev. A **64**, 063607 (2001)

[142] D. Hucul, M. Yeo, W. K. Hensinger, J. Rabchuk, S. Olmschenk, and C. Monroe, *On the transport of atomic ions in linear and multidimensional ion trap arrays*, QIC **8**, 501–578 (2008)

[143] G. De Chiara, T. Calarco, M. Anderlini, S. Montangero, P. J. Lee, B. L. Brown, W. D. Phillips, and J. V. Porto, *Optimal control of atom transport for quantum gates in optical lattices*, Phys. Rev. A **77**, 052333 (2008)

[144] Y. Shin, M. Saba, T. A. Pasquini, W. Ketterle, D. E. Pritchard, and A. E. Leanhardt, *Atom Interferometry with Bose-Einstein Condensates in a Double-Well Potential*, Phys. Rev. Lett. **92**, 050405 (2004)

[145] T. Schumm, S. Hofferberth, L. M. Andersson, S. Wildermuth, S. Groth, I. Bar-Joseph, J. Schmiedmayer, and P. Kruger, *Matter-wave interferometry in a double well on an atom chip*, Nat. Phys. **1**, 57–62 (2005)

[146] Y.-J. Wang, D. Z. Anderson, V. M. Bright, E. A. Cornell, Q. Diot, T. Kishimoto, M. Prentiss, R. A. Saravanan, S. R. Segal, and S. Wu, *Atom Michelson Interferometer on a Chip Using a Bose-Einstein Condensate*, Phys. Rev. Lett. **94**, 090405 (2005)

[147] C. R. Ekstrom, J. Schmiedmayer, M. S. Chapman, T. D. Hammond, and D. E. Pritchard, *Measurement of the electric polarizability of sodium with an atom interferometer*, Phys. Rev. A **51**, 3883–3888 (1995)

[148] J. P. Davis and F. A. Narducci, *A proposal for a gradient magnetometer atom interferometer*, J. Mod. Opt. **55**, 3173–3185 (2008)

[149] M. J. Snadden, J. M. McGuirk, P. Bouyer, K. G. Haritos, and M. A. Kasevich, *Measurement of the Earth's Gravity Gradient with an Atom Interferometer-Based Gravity Gradiometer*, Phys. Rev. Lett. **81**, 971–974 (1998)

[150] A. Peters, K. Y. Chung, and S. Chu, *High-precision Gravity Measurements Using Atom Interferometry*, Metrologia **38**, 25–61 (2001)

[151] D. S. Weiss, B. C. Young, and S. Chu, *Precision measurement of the photon recoil of an atom using atomic interferometry*, Phys. Rev. Lett. **70**, 2706–2709 (1993)

[152] T. L. Gustavson, P. Bouyer, and M. A. Kasevich, *Precision Rotation Measurements with an Atom Interferometer Gyroscope*, Phys. Rev. Lett. **78**, 2046–2049 (1997)

[153] A. D. Cronin, J. Schmiedmayer, and D. E. Pritchard, *Optics and interferometry with atoms and molecules*, Rev. Mod. Phys. **81**, 1051 (2009)

[154] D. F. Walls and G. J. Milburn, *Quantum Optics*, Springer-Verlag, New York (1994)

[155] M. V. Berry, *Quantal Phase Factors Accompanying Adiabatic Changes*, Proc. R. Soc. Lond. A **392**, 45–57 (1984)

[156] G. Möllenstedt and H. Düker, *Beobachtungen und Messungen an Biprisma-Interferenzen*, Z. Phys. A Hadrons Nucl. **145**, 377–397 (1956)

[157] O. Carnal and J. Mlynek, *Young's double-slit experiment with atoms: A simple atom interferometer*, Phys. Rev. Lett. **66**, 2689–2692 (1991)

[158] M. S. Chapman, T. D. Hammond, A. Lenef, J. Schmiedmayer, R. A. Rubenstein, E. Smith, and D. E. Pritchard, *Photon Scattering from Atoms in an Atom Interferometer: Coherence Lost and Regained*, Phys. Rev. Lett. **75**, 3783–3787 (1995)

[159] M. Weitz, T. Heupel, and T. W. Hänsch, *Multiple Beam Atomic Interferometer*, Phys. Rev. Lett. **77**, 2356–2359 (1996)

[160] L. Hackermuller, K. Hornberger, B. Brezger, A. Zeilinger, and M. Arndt, *Decoherence of matter waves by thermal emission of radiation*, Nature **427**, 711–714 (2004)

[161] M. A. Schlosshauer, *Decoherence and the Quantum-To-Classical Transition*, Springer Berlin Heidelberg, 1st edition (2007)

[162] J. R. Sension, *Biophysics: Quantum path to photosynthesis*, Nature **446**, 740–741 (2007)

[163] B. C. Travaglione and G. J. Milburn, *Implementing the quantum random walk*, Phys. Rev. A **65**, 032310 (2002)

[164] P. L. Knight, E. Roldán, and J. E. Sipe, *Quantum walk on the line as an interference phenomenon*, Phys. Rev. A **68**, 020301(R) (2003)

[165] J. Du, H. Li, X. Xu, M. Shi, J. Wu, X. Zhou, and R. Han, *Experimental implementation of the quantum random-walk algorithm*, Phys. Rev. A **67**, 2003 (2003)

[166] C. A. Ryan, M. Laforest, J. C. Boileau, and R. Laflamme, *Experimental implementation of a discrete-time quantum random walk on an NMR quantum-information processor*, Phys. Rev. A **72**, 062317 (2005)

[167] D. Bouwmeester, I. Marzoli, G. P. Karman, W. Schleich, and J. P. Woerdman, *Optical Galton board*, Phys. Rev. A **61**, 013410 (1999)

[168] B. Do, M. L. Stohler, S. Balasubramanian, D. S. Elliott, C. Eash, E. Fischbach, M. A. Fischbach, A. Mills, and B. Zwickl, *Experimental realization of a quantum quincunx by use of linear optical elements*, J. Opt. Soc. Am. B **22**, 499–504 (2005)

[169] H. B. Perets, Y. Lahini, F. Pozzi, M. Sorel, R. Morandotti, and Y. Silberberg, *Realization of Quantum Walks with Negligible Decoherence in Waveguide Lattices*, Phys. Rev. Lett. **100**, 170506 (2008)

[170] R. P. Feynman and A. R. Hibbs, *Quantum Mechanics and Path Integrals*, McGraw-Hill, New York (1965)

[171] K. G. H. Vollbrecht and J. I. Cirac, *Reversible universal quantum computation within translation-invariant systems*, Phys. Rev. A **73**, 012324 (2006)

[172] A. M. Childs, E. Farhi, and S. Gutmann, *An Example of the Difference Between Quantum and Classical Random Walks*, Quantum Information Processing **1**, 35–43 (2002)

[173] A. M. Childs, *On the Relationship Between Continuous- and Discrete-Time Quantum Walk*, Commun. Math. Phys. **294**, 581–603 (2010)

[174] D. A. Meyer, *On the absence of homogeneous scalar unitary cellular automata*, Phys. Lett. A **223**, 337–340 (1996)

[175] A. Ambainis, E. Bach, A. Nayak, A. Vishwanath, and J. Watrous, *One-dimensional quantum walks*, in *Proceedings of the 33rd Annual ACM Symposium on Theory of Computing*, 37–49 (2001)

[176] Y. Omar, N. Paunković, L. Sheridan, and S. Bose, *Quantum walk on a line with two entangled particles*, Phys. Rev. A **74**, 042304 (2006)

[177] T. A. Brun, H. A. Carteret, and A. Ambainis, *Quantum to Classical Transition for Random Walks*, Phys. Rev. Lett. **91**, 130602 (2003)

[178] B. C. Sanders, S. D. Bartlett, B. Tregenna, and P. L. Knight, *Quantum quincunx in cavity quantum electrodynamics*, Phys. Rev. A **67**, 042305 (2003)

[179] A. Werner and A. Ahlbrecht, *Private communication.*

[180] V. Kendon and B. Tregenna, *Decoherence can be useful in quantum walks*, Phys. Rev. A **67**, 042315 (2003)

[181] V. Kendon, *Decoherence in quantum walks — a review*, Math. Struct. Comp. Sci. **17**, 1169–1220 (2007)

[182] T. Rom, T. Best, O. Mandel, A. Widera, M. Greiner, T. W. Hänsch, and I. Bloch, *State Selective Production of Molecules in Optical Lattices*, Phys. Rev. Lett. **93**, 073002 (2004)

[183] T. Stöferle, H. Moritz, K. Günter, M. Köhl, and T. Esslinger, *Molecules of Fermionic Atoms in an Optical Lattice*, Phys. Rev. Lett. **96**, 030401 (2006)

[184] G. Thalhammer, K. Winkler, F. Lang, S. Schmid, R. Grimm, and J. H. Denschlag, *Long-Lived Feshbach Molecules in a Three-Dimensional Optical Lattice*, Phys. Rev. Lett. **96**, 050402 (2006)

[185] T. Volz, N. Syassen, D. M. Bauer, E. Hansis, S. Dürr, and G. Rempe, *Preparation of a quantum state with one molecule at each site of an optical lattice*, Nat. Phys. **2**, 692–695 (2006)

[186] Y. Miroshnychenko, W. Alt, I. Dotsenko, L. Förster, M. Khudaverdyan, D. Meschede, S. Reick, and A. Rauschenbeutel, *Inserting Two Atoms into a Single Optical Micropotential*, Phys. Rev. Lett. **97**, 243003 (2006)

[187] J. Weiner, V. S. Bagnato, S. Zilio, and P. S. Julienne, *Experiments and theory in cold and ultracold collisions*, Rev. Mod. Phys. **71**, 1–85 (1999)

[188] P. W. Anderson, *Absence of Diffusion in Certain Random Lattices*, Phys. Rev. **109**, 1492–1505 (1958)

[189] A. Werner, A. Ahlbrecht, and V. Scholz, *On Localization of Disordered Quantum Walks*, To be published. (2010)

[190] A. Ahlbert and V. Scholz, *Private communication.*

[191] D. P. DiVincenzo, *Two-bit gates are universal for quantum computation*, Phys. Rev. A **51**, 1015–1022 (1995)